Advanced electromagnetic non-destructive testing on creep degraded high chromium ferritic steels : Characterization, Modelling and physical interpretation

Bhaawan Gupta

N°d'ordre NNT : 2019LYSEI074

THESE de DOCTORAT DE L'UNIVERSITE DE LYON

opérée au sein de

Institut National des Sciences Appliquées de Lyon (INSA-Lyon)

En cotutelle internationale avec

Tohoku University

Ecole Doctorale N° 162
Mécanique-Energétique-Génie Civil-Acoustique (ED MEGA)

Spécialité : Génie Mécanique

Soutenue publiquement le 23/09/2019, par :

Bhaawan GUPTA

Advanced Electromagnetic Non-Destructive Testing on Creep Degraded High Chromium Ferritic Steels: Characterization, Modelling and Physical Interpretation

Devant le jury composé de :

President of Jury: **Professor Laurent Daniel**

Rapporteur		
Lebouc, Afef	Professor/ CNRS Research Director, Grenoble, France	
Daniel, Laurent	Professor/ CentraleSuplec, Paris, France	
Examinateur		
Szielasko, Klaus	Dr.-Ing. / Head of Department / Fraunhofer IZFP, Germany	
Skarlatos, Anastasios	Dr./ Scientific Researcher/CEA LIST, Paris, France	
Advising Committee		
Sebald, Gael	Professor / ELyTMaX/INSA-Lyon, France	Directeur
Uchimoto, Tetsuya	Professor / Tohoku University, Japan	Co-directeur
Ducharne, Benjamin	Associate Professor / LGEF / INSA-Lyon, France	Co-Advisor

Département FEDORA – INSA Lyon - Ecoles Doctorales – Quinquennal 2016-2020

SIGLE	ECOLE DOCTORALE	NOM ET COORDONNEES DU RESPONSABLE
CHIMIE	**CHIMIE DE LYON** **http://www.edchimie-lyon.fr** Sec. : Renée EL MELHEM Bât. Blaise PASCAL, 3e étage **secretariat@edchimie-lyon.fr** INSA : R. GOURDON	M. Stéphane DANIELE Institut de recherches sur la catalyse et l'environnement de Lyon IRCELYON-UMR 5256 Équipe CDFA 2 Avenue Albert EINSTEIN 69 626 Villeurbanne CEDEX **directeur@edchimie-lyon.fr**
E.E.A.	**ÉLECTRONIQUE, ÉLECTROTECHNIQUE, AUTOMATIQUE** **http://edeea.ec-lyon.fr** Sec. : M.C. HAVGOUDOUKIAN **ecole-doctorale.eea@ec-lyon.fr**	M. Gérard SCORLETTI École Centrale de Lyon 36 Avenue Guy DE COLLONGUE 69 134 Écully Tél : 04.72.18.60.97 Fax 04.78.43.37.17 **gerard.scorletti@ec-lyon.fr**
E2M2	**ÉVOLUTION, ÉCOSYSTÈME, MICROBIOLOGIE, MODÉLISATION** **http://e2m2.universite-lyon.fr** Sec. : Sylvie ROBERJOT Bât. Atrium, UCB Lyon 1 Tél : 04.72.44.83.62 INSA : H. CHARLES **secretariat.e2m2@univ-lyon1.fr**	M. Philippe NORMAND UMR 5557 Lab. d'Ecologie Microbienne Université Claude Bernard Lyon 1 Bâtiment Mendel 43, boulevard du 11 Novembre 1918 69 622 Villeurbanne CEDEX **philippe.normand@univ-lyon1.fr**
EDISS	**INTERDISCIPLINAIRE SCIENCES-SANTÉ** **http://www.ediss-lyon.fr** Sec. : Sylvie ROBERJOT Bât. Atrium, UCB Lyon 1 Tél : 04.72.44.83.62 INSA : M. LAGARDE **secretariat.ediss@univ-lyon1.fr**	Mme Emmanuelle CANET-SOULAS INSERM U1060, CarMeN lab, Univ. Lyon 1 Bâtiment IMBL 11 Avenue Jean CAPELLE INSA de Lyon 69 621 Villeurbanne Tél : 04.72.68.49.09 Fax : 04.72.68.49.16 **emmanuelle.canet@univ-lyon1.fr**
INFOMATHS	**INFORMATIQUE ET MATHÉMATIQUES** **http://edinfomaths.universite-lyon.fr** Sec. : Renée EL MELHEM Bât. Blaise PASCAL, 3e étage Tél : 04.72.43.80.46 **infomaths@univ-lyon1.fr**	M. Luca ZAMBONI Bât. Braconnier 43 Boulevard du 11 novembre 1918 69 622 Villeurbanne CEDEX Tél : 04.26.23.45.52 **zamboni@maths.univ-lyon1.fr**
Matériaux	**MATÉRIAUX DE LYON** **http://ed34.universite-lyon.fr** Sec. : Stéphanie CAUVIN Tél : 04.72.43.71.70 Bât. Direction **ed.materiaux@insa-lyon.fr**	M. Jean-Yves BUFFIÈRE INSA de Lyon MATEIS - Bât. Saint-Exupéry 7 Avenue Jean CAPELLE 69 621 Villeurbanne CEDEX Tél : 04.72.43.71.70 Fax : 04.72.43.85.28 **jean-yves.buffiere@insa-lyon.fr**
MEGA	**MÉCANIQUE, ÉNERGÉTIQUE, GÉNIE CIVIL, ACOUSTIQUE** **http://edmega.universite-lyon.fr** Sec. : Stéphanie CAUVIN Tél : 04.72.43.71.70 Bât. Direction **mega@insa-lyon.fr**	M. Jocelyn BONJOUR INSA de Lyon Laboratoire CETHIL Bâtiment Sadi-Carnot 9, rue de la Physique 69 621 Villeurbanne CEDEX **jocelyn.bonjour@insa-lyon.fr**
ScSo	**ScSo*** **http://ed483.univ-lyon2.fr** Sec. : Véronique GUICHARD INSA : J.Y. TOUSSAINT Tél : 04.78.69.72.76 **veronique.cervantes@univ-lyon2.fr**	M. Christian MONTES Université Lyon 2 86 Rue Pasteur 69 365 Lyon CEDEX 07 **christian.montes@univ-lyon2.fr**

*ScSo "Histoire, Géographie, Aménagement, Urbanisme, Archéologie, Science politique, Sociologie, Anthropologie

Advanced Electromagnetic Nondestructive Testing on Creep Degraded High Chromium Ferritic Steels: Characterization, Modelling and Physical Interpretation

Bhaawan GUPTA

Abstract

All ferromagnetic materials reflect changes in their magnetic behavior corresponding to the mechanical changes that occur in the materials. Under constant high temperatures and pressure, the material undergoes mechanical creep degradation which leads to microstructural changes. These microstructural changes if not monitored on time, can lead to some serious incidents such as in power plants. In order to monitor these microstructural changes in the materials, the material has to be shaped in a certain specific shape and size in order to get the analysis using the imaging techniques such as Scanning electron microscopy (SEM), Electron backscatter diffraction (EBSD) etc. However, these techniques involve destroying the integrity of the sample under test which is not applicable for on-site Non-Destructive Testing (NDT) operations. Additionally, such experiments involve high equipment cost. There have been a lot of research done to understand the creep and its evolution in different kinds of steels. Creep being a complex phenomenon hinders in making concrete conclusions about its evolution. All the studies so far have tried to understand creep from materials science point of view, that is, by performing SEM, EBSD etc. and rarely have been studies on relating microstructure with the magnetic signatures of the materials which could reveal significant information about the condition of the materials. Although, on one hand, low alloy steels have been investigated using NDT techniques, there is a lack of correlating the magnetic signatures of the materials to the microstructure of the materials and on the other hand, high alloy steels on the contrary have rarely been studied from Electromagnetic NDT point of view.

The main objective of this thesis work is to determine the evolution of microstructural changes (Precipitations, Dislocations) in Creep Degraded High Chromium Ferritic Steels, from the NDT signatures. To achieve this objective, the main objective is divided into two sub-objectives. The first sub-objective is to screen different electromagnetic techniques to correlate the NDT signals with the microstructural changes for 12%Cr-Mo-W-V Creep degraded Ferritic samples. Under this sub-objective, three different empirical approaches are applied to the test samples, namely, Magnetic Incremental Permeability (MIP), Hysteresis measurements (B(H)) and Magnetic Barkhausen noise (MBN). This sub-objective reveals how the magnetic parameters evolve in the creep degraded samples with different rupture levels and each of this technique reveals its sensitivity as well. Combining micro-structure analysis to the micro-magnetic tests enable to target which experimental parameter is the most representative for the creep phenomena. To further quantify the results obtained in the first sub-objective, the second sub-objective is to develop a physical model and interpret the modelling parameters in terms of microstructure. The physical model is adapted to simulate the signals derived from each technique mentioned in the first sub-objective. Each modelling technique gives access to few model parameters that are assessed in terms of microstructure. Post to the derivation of these model parameters, the most sensitive parameter(s) is/are established for each technique used. The modelling

technique will help in overcoming the issue of lack of standards in NDT, irrespective of the experimental set-up involved.

This thesis is divided into 6 chapters including the conclusion. In chapter 1, the state of the art for the electromagnetic NDT is detailed. Several commercially applied non-destructive testing methods have been described in detail along with the advantages and their limitation on applicability to detect flaws like residual stress, creep etc. Additionally, a short background on the hysteresis modelling has been illustrated.

In chapter 2, the microstructure analysis of 12% chromium steel subjected to creep is investigated, for different temperature and stress levels. Investigations reveal that the behavior of these samples is opposite in case of lower and higher temperature treated samples. Properties like Hardness, Grain size are evaluated against the data derived from microstructural analysis (Precipitation number/Average of KAM). Further to this, the microstructural properties are also studied in terms of the mechanical factors like Creep life fraction as well as Larson Miller Parameter.

Chapter 3 focusses on understanding the kind of microstructural changes with effect to different treatments of the high chromium creep test steel samples. For a deeper investigation, an advanced technique 'Magnetic Incremental Permeability'(MIP) is implemented to analyze the same set of samples. This technique helps to extract some magnetic parameters from the typical MIP curve from each sample. These parameters are then assessed with respect to the microstructural parameters (Number of precipitates, Average of KAM (Kernel Average Misorientation)). Various assessments are formalized based on multiple mechanical / microstructural / magnetic parameters to interpret the behavior of the differently treated samples. From the microstructural point of view, the precipitation number shows a very good correlation with the magnetic parameters. It is revealed that the evolution of magnetic parameters for lower temperature samples is entirely opposite to the evolution of these parameters in case of high temperature samples. On the other hand, it is also observed that Average of KAM exhibits a good correlation to the magnetic parameters only in case of high temperature samples and the variation is much higher within the same set of samples as compared to the lower temperature treated samples. After the implementation of MIP technique, the same set of samples are examined by standard Hysteresis measurements. Since, hysteresis is global measurement, there are not much distinct variations observed in different samples within the same category. This chapter reveals that MIP being a local measurement technique is much more useful and adapted in order to detect the effects of degradation due to creep.

The chapter 4 focuses on modelling MIP signals based on Jiles-Atherton model to understand more deeply the creep phenomenon in high chromium steel. The model derives three parameters which are investigated against the microstructure of the materials. Correlations between specific J-A parameters and the number of precipitates (Pearson correlation coefficient of 0.82), the Kernel Average Misorientation (0.70), the hardness (0.70), and grain size (0.65) are obtained. Following to the modelling of MIP curves, the Hysteresis curves are also modelled adapting the J-A model to B(H) measurements.

The Chapter 5 aims on implementing Magnetic Barkhausen Noise method for the evaluation of the micro-structural state of the same set of samples. In this study, instead of following the classic approach which consist on working directly from the raw signal, MBN_{energy} hysteresis cycles have been reconstructed and simulated. Working with these

hysteresis cycles limit the reproducibility and the sensitivity issues by providing a magnetic signature which can easily be simulated using the classic hysteresis models like Jiles-Atherton. Once all the experimental tests and simulations are performed, a fine analysis has been done in order to find correlations between the magnetic parameters, the J-A simulation parameters and the micro-structural properties.

Since, all the three techniques mentioned above are based on different principles and provide information at different levels, all these techniques are then compared in Chapter 6 to find which is the most efficient method to characterize creep degraded High Chromium Ferritic Steel samples. In addition to that, it is also concluded that which parameter based on each technique is the most sensitive parameter to microstructural change in the materials.

Advanced Electromagnetic Non-Destructive Testing on Creep Degraded High Chromium Ferritic Steels: Characterization, Modelling and Physical Interpretation

Bhaawan GUPTA

Résumé

Le comportement magnétique des matériaux ferromagnétiques varie en fonction des paramètres mécaniques. Sous des températures et des pressions élevées constantes, le matériau subit une dégradation mécanique par fluage qui entraîne notamment des changements microstructuraux. Ces changements microstructuraux, s'ils ne sont pas surveillés à temps, peuvent être à l'origine de dégradation au niveau des matériaux de structure, et potentiellement devenir une source importante d'incidents (centrales électriques). Pour déterminer leur microstructure, les échantillons doivent être préparés dans une forme et une taille spécifique permettant l'utilisation de méthodes d'imagerie telles que la microscopie électronique à balayage (MEB), la diffraction de rétrodiffusion électronique (EBSD), etc. En revanche, ces méthodes, impliquant la destruction de l'échantillon testé, ne permettent pas un suivi des matériaux de structure dans le temps, contrairement aux méthodes de contrôle non destructif (CND). De plus, elles impliquent des coûts d'équipement élevés, ce qui constitue une deuxième limitation. De nombreuses recherches ont été menées pour comprendre le fluage et son évolution, ceci pour différents types d'aciers. Toutefois, aucune conclusion concrète ne fait consensus en raison de la complexité du phénomène. Jusqu'à présent, tous les travaux effectués ont tenté de comprendre le fluage du point de vue de la science des matériaux, à partir d'images MEB, EBSD. Etudier la relation entre la microstructure et la signature magnétique des matériaux pourrait révéler des informations importantes sur l'état des matériaux, et complémentaires aux travaux déjà effectués.

Bien que les aciers faiblement alliés aient déjà fait l'objet de nombreuses études CND, il n'existe pour l'instant pas de corrélation entre les signatures magnétiques et la microstructure des matériaux. En réalité, les aciers fortement alliés ont rarement été étudiés à partir des techniques de CND électromagnétiques.

Dans cette étude, motivée par les exigences du contrôle de santé en temps réel de l'industrie de l'énergie thermique, les aciers ferritiques à haute teneur en chrome dégradés par fluage ont été étudiés. Afin de résoudre le problème des changements microstructuraux dans les matériaux dus aux conditions de pressions et de températures élevées constantes, dans ce travail de thèse trois techniques non destructives micro magnétiques ont été testée pour déterminer l'évolution des signatures magnétiques en fonction du niveau de contrainte auquel les échantillons testés ont été exposés. Il est légitime de supposer que tous les changements microstructuraux à travers le matériau vont se refléter dans les signatures magnétiques correspondantes mesurées.

Cette thèse est divisée en 6 chapitres dont la conclusion. Dans le chapitre 1, un état de l'art présentant le contrôle non destructif électromagnétique est détaillé. Plusieurs

méthodes d'essais non destructifs appliquées dans l'industrie sont présentées, de même que leurs avantages et leurs limites d'application pour la détection de défauts tels que les contraintes résiduelles, le fluage, etc. Un bref historique de la modélisation de l'hystérésis magnétique (Modèle de Preisach, modèle de Jiles-Atherton) est proposé ensuite.

Dans le chapitre 2, l'analyse micro structurelle d'un acier à haute teneur en chrome est proposée. Les matériaux testés sont soumis à des hautes températures et des contraintes de traction générant du fluage. Trois températures différentes sont notamment étudiées, ceci pour une contrainte constante mais pour différents temps de fluage. Les études révèlent que l'évolution des paramètres microstructuraux avec le temps de fluage s'inverse si on compare les cas à basses températures et à hautes températures. Les propriétés telles que la dureté et la taille des grains sont évaluées par rapport aux données dérivées de l'analyse microstructurale (nombre de précipitations / moyenne du KAM). De plus, les propriétés microstructurales sont également étudiées en termes de facteurs mécaniques comme la fraction de fluage et le paramètre de Larson-Miller (qui combine les deux facteurs mécaniques comme la contrainte et le paramètre thermique température). Les résultats analysés dans ce chapitre montrent une grande diversité dans les changements microstructuraux tels que la taille des grains, les précipités, etc. Ces informations microstructurales, lorsqu'elles sont corrélées aux signatures magnétiques des échantillons testés, pourraient permettre à terme d'estimer (au moins qualitativement) la microstructure des matériaux directement à partir des signatures magnétiques sans avoir à effectuer l'analyse microstructurale, où les échantillons doivent être dégradés.

Le chapitre 3 se concentre sur la compréhension des changements microstructuraux résultant des différents traitements des échantillons d'acier à haute teneur en chrome. Pour une investigation plus approfondie, une technique avancée de « Perméabilité Magnétique Incrémentale » (MIP pour Magnetic Incremental Permeability) est mise en œuvre pour analyser le même ensemble d'échantillons. Cette technique permet d'extraire des paramètres magnétiques issus de la courbe dite « aille de papillon » signature propre à chaque échantillon. Ces paramètres sont ensuite évalués par rapport au changement des paramètres microstructuraux (Densité de précipités, recristallisation, moyenne de KAM (Kernel Average Misorientation) correspondant aux dislocations). Différentes évaluations sont formalisées à partir de multiples paramètres mécaniques / microstructurels / magnétiques pour interpréter de façon plus approfondie le comportement des échantillons traités. Du point de vue microstructural, le nombre de précipitations montre une très bonne corrélation avec les paramètres magnétiques. Il s'avère que l'évolution des paramètres magnétiques pour les échantillons à basse température est totalement à l'opposé de celle des échantillons à haute température. D'autre part, on observe également que la moyenne du paramètre KAM ne présente une bonne corrélation avec les paramètres magnétiques que dans le cas d'échantillons à haute température et que la variation est beaucoup plus élevée dans le même ensemble d'échantillons par rapport aux échantillons traités à basse température. Après la mise en œuvre de la technique MIP, le même ensemble d'échantillons est examiné via des mesures

d'hystérésis classiques (cycle d'hystérésis de l'évolution du champ magnétique B en fonction du champ d'excitation H). Les mesures des cycles d'hystérésis donnent accès à des informations moyennes et globales contrairement au MIP qui est une mesure locale. En revanche pour ces mesures globales moyennées, les variations sont difficilement discernables entre les différents échantillons d'une même catégorie, et ceci quel que soit le niveau de fluage. Ce chapitre révèle que la localité de la mesure MIP, la rend beaucoup plus adaptée à la détection des effets de la dégradation due au fluage.

Pour quantifier davantage les résultats obtenus à partir des signatures magnétiques des matériaux, des modèles du comportement magnétiques sont mis en œuvre. En raison de son interprétation physique, un modèle issu de la théorie de Jiles-Atherton est finalement choisi pour simuler les signatures MIP. Les résultats de modélisation donnent accès à différents paramètres. Chaque paramètre a une signification physique, selon la théorie de Jiles-Atherton. La technique de modélisation peut par ailleurs aider à résoudre le problème de l'absence de normes dans les essais non destructifs, les paramètres du modèle de comportement du matériau étant par définition indépendants du dispositif expérimental utilisé. Les paramètres sont comparés pour révéler la sensibilité des techniques testées.

Le développement d'outil de modélisation est très important dans le domaine des essais non destructifs. Ces outils permettent non seulement de comprendre la physique mais encore de réduire le traitement fastidieux et coûteux des échantillons imposé par les méthodes d'imagerie. Le chapitre suivant discute des techniques de modélisation développées pour simuler la courbe « ailles de papillon » dans un premier temps et l'adapter ensuite aux données expérimentales.

Le chapitre 4 se concentre sur un modèle basé sur le modèle de Jiles-Atherton pour mieux comprendre le phénomène de fluage des aciers chromés utilisés dans les centrales thermiques. Le modèle dérive trois paramètres qui sont étudiés en fonction de la microstructure des matériaux. Dans ce chapitre, les corrélations entre les paramètres J-A spécifiques et le nombre de précipités (coefficient de corrélation de Pearson de 0,82), la moyenne de KAM (Kernel Average Misorientation) (0,70), la dureté (0,70) et la taille des grains (0,65) sont obtenues. Suite à la modélisation des courbes MIP, les courbes de l''hystérésis magnétique sont également simulées. Dans le cas de cycles d'hystérésis, seul α montre une bonne corrélation. Ensuite, l'interprétation physique de la microstructure est analysée à partir de ces paramètres. La valeur absolue de ces paramètres ne donne pas d'informations précises sur la microstructure mais la tendance et l'évolution de ces paramètres donnent une idée du fluage et de la dégradation des matériaux. Dans l'étape suivante, pour soutenir cette compréhension et cette interprétation, des tests de bruit magnétique de Barkhausen sont effectués et les mêmes paramètres sont étudiés.

Le chapitre 5 vise donc à mettre en œuvre une autre méthode micro-magnétique, le bruit magnétique de Barkhausen. Une telle analyse micro-magnétique est d'un intérêt majeur car l'état microstructural est profondément lié à la propagation des défauts dans ces aciers structuraux et à des conséquences graves si elles ne sont pas prévues. En tant

qu'image du basculement des parois des domaines magnétiques, la mesure du bruit de Barkhausen est une méthode de contrôle micro magnétique non destructif à fort potentiel et d'intérêt. Dans cette étude, au lieu de suivre l'approche classique qui consiste à travailler directement à partir du signal brut, les cycles d'hystérésis MBNenergy(H) ont été reconstruits et simulés. Travailler avec ces cycles d'hystérésis permet d'améliorer la reproductibilité et résout les problèmes liés à la sensibilité. De même, cette signature magnétique peut être modélisée en utilisant les modèles de l'hystérésis classiques tel que celui de Jiles-Atherton qui a été utilisé dans cette étude. Une fois tous les essais expérimentaux et les simulations terminés, une analyse fine a été effectuée afin de trouver des corrélations entre les paramètres magnétiques (champ coercitif, facteur de perméabilité, etc.), les paramètres de simulation J-A et les propriétés micro-structurelles.

Les trois techniques mentionnées ci-dessus sont basées sur des principes différents, elles sont complémentaires et fournissent des informations à différents échelles. Toutes ces techniques sont comparées dans le chapitre 6 afin de déterminer la méthode la plus efficace pour caractériser les échantillons testés. En outre, il est également conclu que chaque technique permet d'affiner plus efficacement l'un ou l'autre des paramètres sensibles au changement microstructural des matériaux. Les paramètres sont finalement comparés pour révéler le paramètre le plus sensible en fonction de la technique mise en œuvre. Une conclusion est proposée pour vérifier quels sont les paramètres clés et ceci quelle que soit la méthode de CND utilisée.

Table of Contents

List of Figures

CHAPTER 1

INTRODUCTION

1. General Idea

Every known material has magnetic characteristics. Materials are not only characterized by their composition, size, geometry but their magnetic properties play a very major role in determining the state of the material. However, in some materials the magnetic effect might be extremely weak but it can certainly be measured. Magnetic permeability is the physical quantity describing material properties in the external magnetic field. This property is defined as the measure of the magnetisability of any material [Dear]. This property of materials has been widely used to find minerals in soil, rocks etc., especially Fe-bearing minerals [Dear] enabling to classify different types of materials.

Exploiting this property of the materials, it is quite convenient to study all materials to make sure its application is safe, fast and non-destructive. In ferromagnetic materials, magnetic domain walls interact with microstructure over similar mechanisms as dislocations do [Bozo, Cull, and Jile]. This fundamental observation is the basis of micro-magnetic materials characterization. The correlation between micro magnetic parameters and the mechanical hardness, strength and stress has been thoroughly studied to date, and there are commercial non-destructive testing devices for solving the inverse problem of measured quantity estimation using micro magnetic testing parameters as input. Coupling between the stress and magnetic field is the main and important feature of the ferromagnetic materials consisting of various small magnetic domains in its microstructure [Pete]. Hence, it means that extent of magnetization might even result in the dimension variation of ferromagnetic materials and vice versa, i.e., the amount of stress also affects the magnetization of the ferromagnetic materials for which the magnetic non-destructive testing (NDT) has always paid special attention to. To understand the applicability of magnetism in the field of NDT, the following sections in this chapter cover the basics of magnetism and the current state of the art for the electromagnetic non-destructive testing methods.

1.2. Basics of magnetism

1.2.1. Magnetic field and its generation

Consider two parallel current carrying electric wires. If the direction of the current passing through both of them is same, the wires tend to attract each other and if the direction is opposite, the phenomenon of repulsion is observed [Nave]. This force which

leads to attraction or repulsion is called the magnetic force. The magnetic force acting on such moving charges is defined by the magnetic field. The most basic fundamental part of magnetism is Magnetic field [Bozo]. The magnetic field generated from different sources have different patterns which are briefly shown in the next section.

1.2.2. Magnetic Field Patterns

The field around a single current loop and a solenoid are similar to that of a bar magnet, where the field emerges from one end of the magnet (North pole) and passes through the air making a return path to the other end of the magnet (South pole) [Nave]. In Fig.1.1, some of the magnetic field patterns generated by different sources are shown.

1.2.3. Materials characterization based on magnetic properties

According to the Faraday's law of magnetic induction, whenever a material is placed under the influence of an alternating magnetic field, the magnetic force acting upon its electrons is always affected [Hayt]. Mathematically, it can be defined by the following expression

$$\varepsilon = -\frac{d\Phi_B}{dt} \qquad (1.1)$$

Depending on the atomic and molecular structure of the materials or the net magnetic moment associated to the atoms, every material responds quite differently to the magnetic field. The magnetic moment can be due to the change in motion of the electrons because of an external magnetic field or simply by motion of the electrons. Electrons exist in pairs in most of the atoms which spin in opposite directions as a result of which their magnetic fields get cancelled. However, materials with unpaired electrons tend to react to the external magnetic field since they have a net magnetic field. Based on this, most materials can be classified as diamagnetic, paramagnetic and ferromagnetic materials.

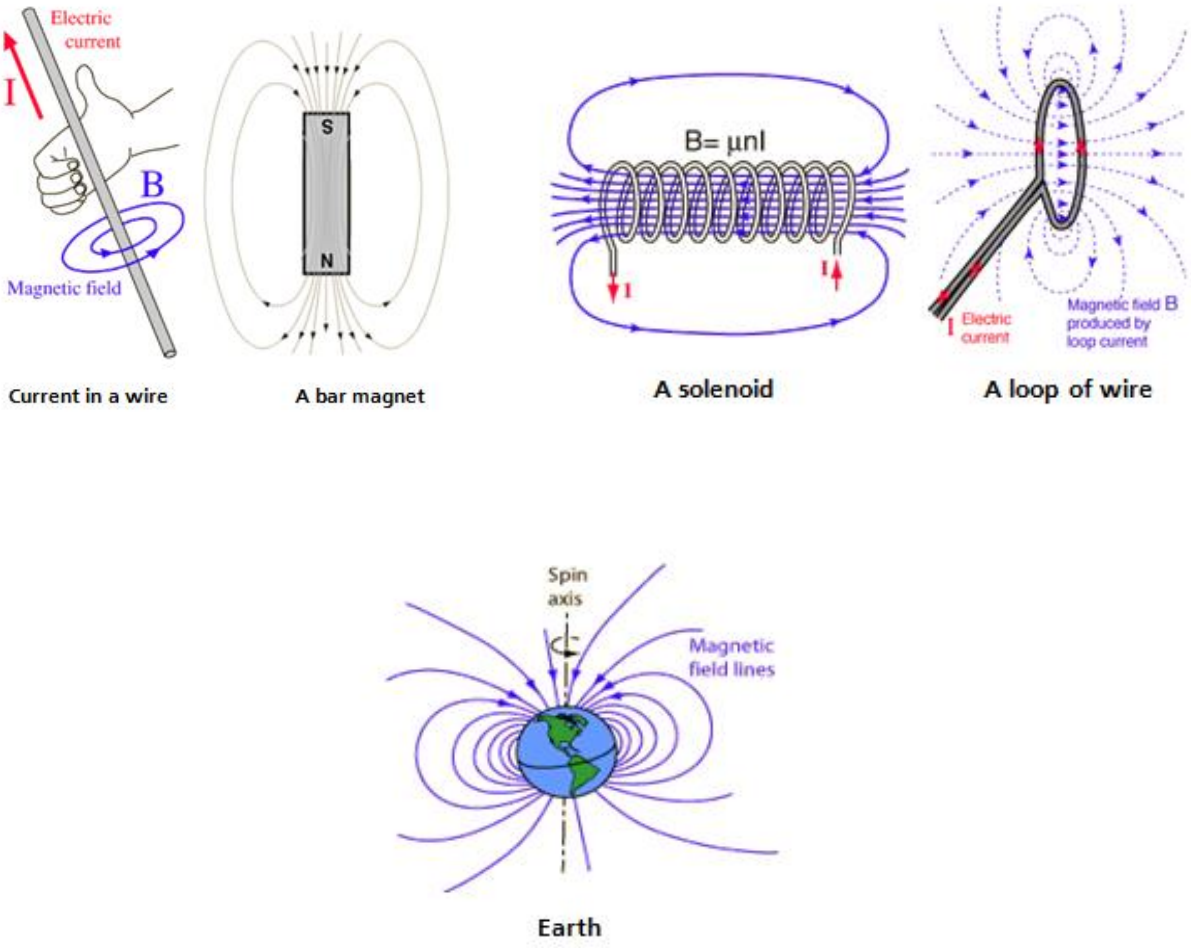

Figure 1.1. Magnetic Field Patterns[Nave]

1.2.4. Magnetic permeability

Magnetic permeability (μ) is the physical quantity of a magnetic material which describes the response of a material under the external magnetic field and it measures the amount of magnetisability of the material [Dear]. Magnetic permeability could also be defined as the constant in the proportionality relation between magnetic induction, B and magnetic field intensity, H. The magnetic permeability of the material is directly proportional to the number of lines passing through it. Higher the magnetic permeability of a material is, more are the magnetic lines of force that pass through the material. Magnetic permeability is expressed in terms of Henry per meter. The permeability of the

air or vacuum is represented by $\mu 0$ which is equal to $4\pi \times 10^{-7}$ H/m [Circ]. Mathematically, $\mu = B/H$.

Magnetic permeability is the key reason that decides whether the material is magnetized in the direction of the applied magnetic field or in the opposite direction. Magnetic permeability of a material may not be a constant value but rather is influenced by several factors such as humidity content, the medium that is used, the temperature or the strength of the applied magnetic field. Hence, magnetic permeability is generally expressed in terms of relative permeability rather than the absolute value. Pure Iron is one example of high permeable material ($\mu >> 1000$).

Depending on the value of the magnetic permeability, materials can be categorized as ferromagnetic materials, paramagnetic materials, or diamagnetic materials. Diamagnetic materials are the ones which oppose the applied magnetic field and hence result in repulsion effect. On the other hand, the paramagnetic materials are the ones that support the applied magnetic field and hence result in an attraction force. Ferromagnetic materials are strongly attracted to the applied magnetic field. Since, this thesis work is based on the ferromagnetic materials characterization and hence a short explanation of such materials is given below. However, for other categories of the materials [Gupt] could be referred to.

1.2.5. Ferromagnetism

These materials show a very strong attraction to the applied external magnetic field and for them μ is positive and quite large comparatively. Like paramagnetic materials, these materials too have unpaired electrons which result in the net magnetic moment. But in addition to it, such materials possess magnetic domains where the atomic magnetic moments are aligned parallel resulting in a strong magnetization [Bozo]. When ferromagnetic materials are heated, the thermal agitation of the atoms results in a decrease in the degree of alignment of atomic magnetic moment. At a certain temperature, called Curie temperature, the thermal agitation becomes so high that the ferromagnetic material becomes paramagnetic [Spal]. In Fig. 1.2 the magnetic domains in a ferromagnetic material are illustrated.

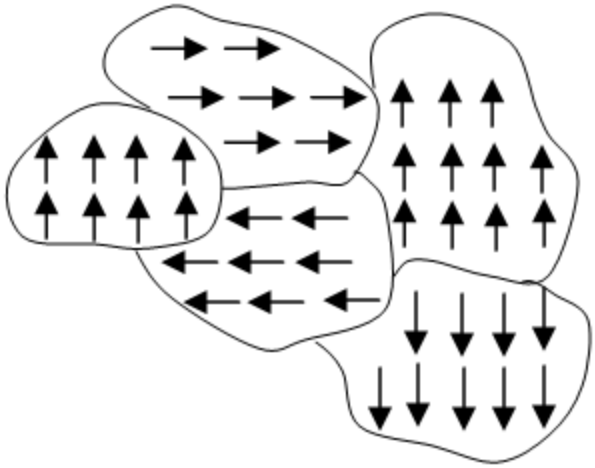

Figure 1.2. Domains in the Ferromagnetic materials at atomic level

1.3. Non-destructive Testing (NDT)

In this section, an overview of the state of the art for materials characterization in NDT, basics of measurement techniques, have been discussed.

Non-Destructive Testing and Evaluation is defined as the process of investigating, testing materials for any discontinuity, cracks or defects that affect the integrity of the material or the structure without affecting its serviceability. Consequently, the material can still be used after the test. Non-destructive testing mainly finds their applicability in the field of fabrication, manufacturing and in-situ inspections ensuring the reliability and the integrity of the product/materials, thereby controlling the manufacturing process. As a result, it leads to lower production costs by avoiding the next step of production if there is a flaw. By following a certain set of procedures, this also leads to maintaining a uniform quality level for the manufactured parts. When it comes to civil structures, NDT is used in ensuring the quality of the materials before and after their installations to make it effective and safe for the public using it. Every product goes through a cycle before manufacturing and a cycle after manufacturing starting with the raw material and, ending up with the recycling or reusing of the product. In between, the product goes through a whole series of value creation phases, including trade, transport and e-commerce. Hence, NDT becomes very important in the monitoring of these products to ensure the quality.

As a matter of fact, a material goes through many transitions in its lifecycle, some of which transitions cause physical cracks and physical discontinuities. For detecting such phenomenon, several NDT techniques are applicable. According to the American society for non-destructive testing, there are six most commonly practised techniques for non-destructive characterization of materials namely, MT (Magnetic Particle Inspection), PT (Liquid Penetrant Testing), RT (Radiographic Testing), UT (Ultrasonic Testing), ET (Electromagnetic Testing) and VT (Visual Testing). Magnetic Particle Inspection becomes a challenging technique when monitoring rough surfaces which interferes with the preparation of the test part (removal of finishes and sealant etc.). In addition to the similar issues as mentioned in MT, the Liquid penetrant technique requires high degree of cleanliness of the part post testing. The Radiographic NDT however is very useful in detecting surface as well as internal flaws, it requires large equipment and high cost. It also requires a high degree of experience and skill for exposure and interpretation depth of discontinuities that are not indicated. Ultrasonic Testing is extensively used in the field of NDT as it is a portable method and is sensitive to very small discontinuities However, to perform UT the set-ups usually are complex and requires a high level of skill to perform the measurements. Most of these techniques are applicable in case of physical cracks and defects. There are very less NDT techniques that can study the evolution of change in the materials properties before the crack occurs for which Electromagnetic Testing shows a higher potential. In the following sections, some of the electromagnetic based non-destructive methods are described.

1.3.1. Magnetic Flux Leakages (MFL)

This method is based on the principle when a strong magnetic field is exposed on to a ferromagnetic material; there is a magnetic field leakage that will leak out of the object into the air in case when there is a crack or any geometrical discontinuity in the object. The field leakage or the flux leakage can be recorded by the use of magnetic field sensors and further can be utilized in the dimension estimation of the defects. The output signal of the sensors is pre-amplified, with an appropriate gain resulting in the detection of even very small defects. The limitation of the MFL technique is that it is limited to only physical cracks and damages and not applicable until now for stress analysis or studying creep phenomenon. Fig. 1.3 below demonstrates the principle of Magnetic Flux Leakages.

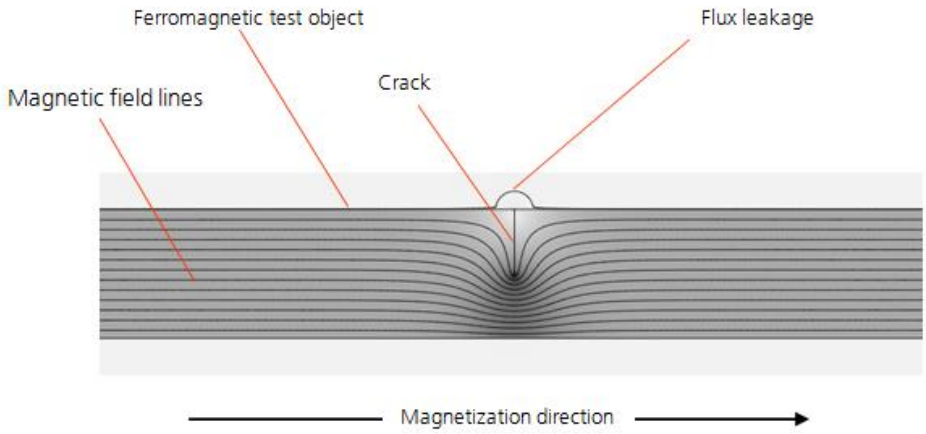

Figure 1.3. Demonstration of Magnetic Flux Leakage Technique[Izfp]

1.3.2. Magnetic Field Distortion (MFD)

The Magnetic Flux Distortion sensor setup is consisted of a permanent magnet at rather a larger distance from the surface of the material instead of a yoke as is the case in MFL. A magnetic field strength sensor such as a Hall effect sensor or a Giant Magnetoresistive (GMR) sensor close to the surface is mounted as demonstrated in Fig. 1.4. This set-up allows to have small and lightweight sensor designs, suitable also for applications where sensor arrays are required. Due to the large air gap, the flux density in the material is lower as compared to MFL. The Magnetic Flux Distortion is based on measuring the changes or distortions in the magnetic fields caused by the discontinuities on the surface of a ferromagnetic material when the magnet and sensor are placed in its proximity. It is useful in detecting the effects due to corrosion on the surface.

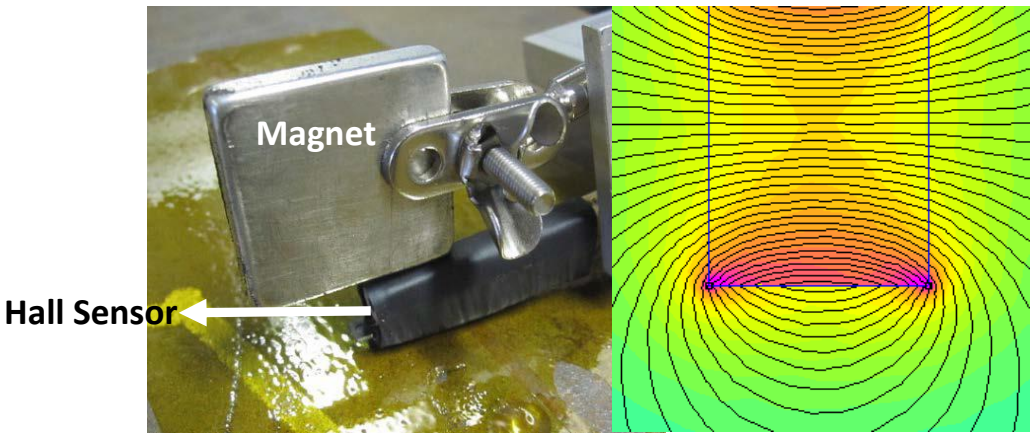

Figure 1.4. A simple Magnetic Flux Distortion set-up [Yous]

1.3.3. Magnetic Particle Inspection (MPI / MT)

Magnetic particle inspection (MPI) is used to locate discontinuities on the surface of the ferromagnetic materials. When a test object is magnetized, any discontinuity/deformity present in the direction transverse to the direction of the applied magnetic field leads to a field leakage. The presence of the leakage field due to the discontinuity/deformity could be detected by application of finely distributed magnetic particles over the surface which results in gathering of particles around the flaw due to the leakage field. These magnetic particles form an outline near the discontinuity and indicate its size, location and shape [Asmh]. Fig. 1.5 below shows a screw inspected using the standard MPI method.

Figure 1.5. A screw inspected using Magnetic Particle Inspection [Magn]

1.3.4. Eddy Current Testing (ECT)

Eddy current testing is one of the most widely used NDT methods to characterize materials non-destructively. Methods such as Magnetic Incremental Permeability (MIP), explained in section 1.4 use the principle based on Eddy current phenomenon. Fig. 1.6 below shows the principle set-up for ECT.

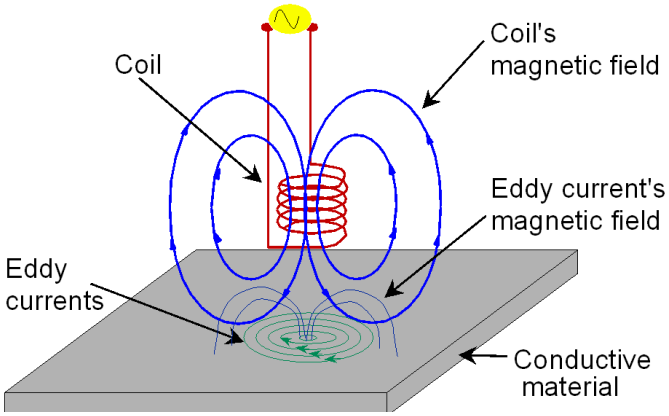

Figure 1.6. Principle description of Eddy Current Testing [Euro]

As per the Faraday's law of electromagnetic induction, whenever an alternating current is applied to a conductor (material 1) or a copper wire, an alternating magnetic field is induced in and around the conductor [Hayt]. In case, another electrically conductive material (material 2) is placed in the proximity of this alternating magnetic field, currents are induced in the material 2. These currents are known as Eddy current which follow a circular path, hence their name 'Eddy'. In case there is a flaw in the physical structure of the material 2, the path of eddy currents is affected which can be monitored (change in impedance) using a pick up coil. Hence, Eddy currents are very useful in the non-destructive testing of conductive materials.

Industrially, the Eddy Current Testing is extensively used in finding defects and making analysis of the materials' health. Generally, ECT is used to inspect relatively a smaller area and the probes are designed according to the material under test (geometry, shape etc.). Since, eddy currents is a phenomenon generated because of the alternating currents and alternating magnetic field, frequency plays an important role. When frequency is one of the factors, it also introduces the concept of skin depth. The skin depth, δ, is defined as the depth where the current density is just 1/e (about 37%) of the value at the surface. The skin depth depends on the frequency of the current and the electrical/magnetic properties of the conductor. Consequently, eddy currents inspection method is able to concentrate only on the surface of a material, hence, applicable to detect local surface and near surface defects, hence, can be considered as a micro-magnetic NDT technique.

Based on the principle of induction, Eddy currents are affected by the electrical conductivity and the magnetic response (Magnetic Permeability/Susceptibility) of the materials. Since, high temperatures can result in the change of conductivity and permeability of the materials, Eddy Currents can easily distinguish between the materials which have / have not been exposed to the high temperatures. Contrary to the other micro-magnetic NDT techniques, ECT is not restricted to only ferromagnetic materials but is applicable to all electrically conductive materials. However, in case of ferromagnetic materials, the measurements and their analysis become more complex since, other than conductivity, the permeability change also plays a role. As a major application, Eddy Currents are also used to measure the thickness of the material. This application is extremely useful in detecting damages caused by corrosion/pitting that could cause the thinning of material. Being highly informative, ECT is used to make corrosion thinning measurements on aircraft parts and on the tube walls characterization used in assemblies such as heat exchangers. Eddy current testing is also used to measure the thickness of paints and other coatings.

1.4. Micromagnetic multi-parameter microstructure and stress analysis (3MA)

3MA is a non-destructive electromagnetic testing method developed at Fraunhofer IZFP, whereby testing statistics are derived during magnetic hysteresis cycles. 3MA evaluates electrical and magnetic parameters which are influenced, for instance, by the microstructure, hardness, hardness depth, yield strength and residual stress. A 3MA probe consists of a magnetization unit (yoke core with magnetization coil) in order to magnetize the measuring sample with an alternating magnetic field, a Hall probe for measuring the time signal of the tangential magnetic field component, coil for detecting the magnetic Barkhausen noise, probe system for detecting the eddy current and the incremental permeability and a preamplifier [Izfp]. Fig. 1.7 shows the standard commercial 3MA sensor. 3MA set-up is a combination of four micromagnetic non-destructive testing methods: Magnetic Barkhausen Noise, Eddy Current Analysis, Magnetic Incremental Permeability and Harmonic Analysis of the tangential component of the magnetic field strength. EC principle has been explained in detail in the previous section 1.3.4. and the principles of Incremental Permeability and Barkhausen noise have been explained in the following section in 1.4.1. and 1.4.2. respectively. Harmonic Analysis method allows the analysis of deeper material ranges and this technique is

applicable to shallow structural and tension gradients (occurring in the surface hardened parts). Variable magnetization is generated in the specimen when a low frequency sinusoidal voltage is applied into the magnetization coil. The amplitude of the magnetization is controlled by the Hall sensor incorporated into the sensor design. This Hall sensor is used to monitor and record the entire evolution of magnetic field development during the hysteresis cycle. Eventually a Fourier analysis is performed on the recorded signal. Due to the symmetry in the hysteresis, only odd higher harmonics can be determined, the amplitudes and phase shifts of which are studied. Further details about the 3MA set-up can be referred to in [Wolt1].

Like 3MA uses multiple techniques to study microstructure and stress analysis, in this work as well, three techniques, namely, Magnetic Barkhausen Noise, Magnetic Incremental Permeability, and standard B(H) curves are used to analyse the microstructure of the material affected by Creep (explained in the section 1.5.). A short description of these techniques are given as below.

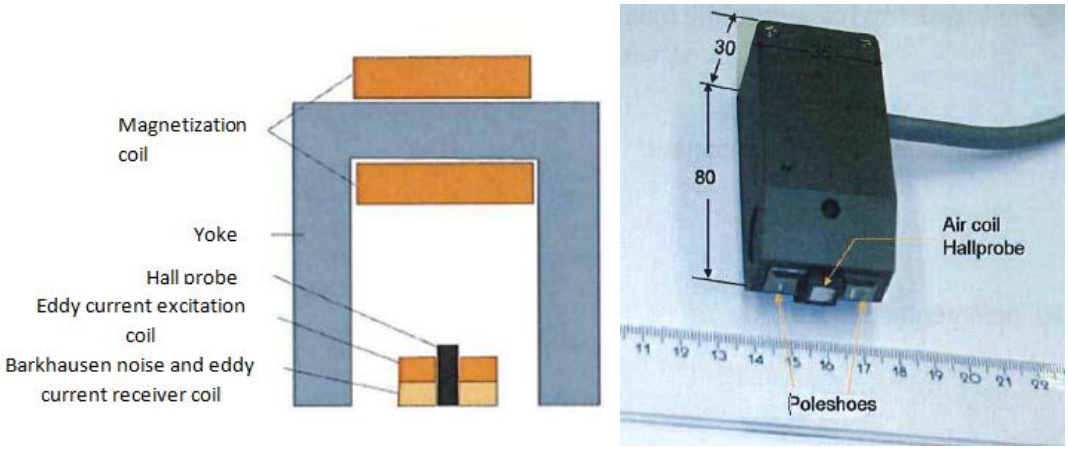

Figure 1.7. Principle set-up of 3MA and the standard 3MA probe with curved pole shoes and spring mounted sensor[Izfp]

1.4.1. Magnetic Incremental Permeability

The basis of micro-magnetic materials characterization is based on this fundamental observation of the interactions between the domain walls and the microstructure of the materials [Jile][Bozo]. Coupling between the stress and magnetic field is the main and important feature of the ferromagnetic materials consisting of various small magnetic domains in its microstructure [Cull]. ECT is the simplest way to measure electrical signals, response of the magnetization state of the material under test. Because of the simplicity of the experimental set-up and the ease to pick up the response from the coil makes it

one of the most used methods in electromagnetic NDT with some limitations of course, when a deeper investigation about the materials is needed.

To improve it, at the end of the 20th century researchers from the Fraunhofer IZFP have proposed to couple the ECT experimental setup to a quasi-static weakly varying high amplitude magnetic excitation [Yash]. This method has been named Magnetic Incremental Permeability (MIP). MIP is defined as a measure of the material's response when exposed to a steady, high amplitude quasi-static magnetic field and a small amplitude alternative magnetic excitation. Fig. 1.8 demonstrates the typical MIP curve. From a mathematical point of view, magnetic incremental permeability μ_Δ can be defined as:

$$\mu_\Delta = \frac{1}{\mu_0}.\frac{\Delta B}{\Delta H} \qquad (1.2)$$

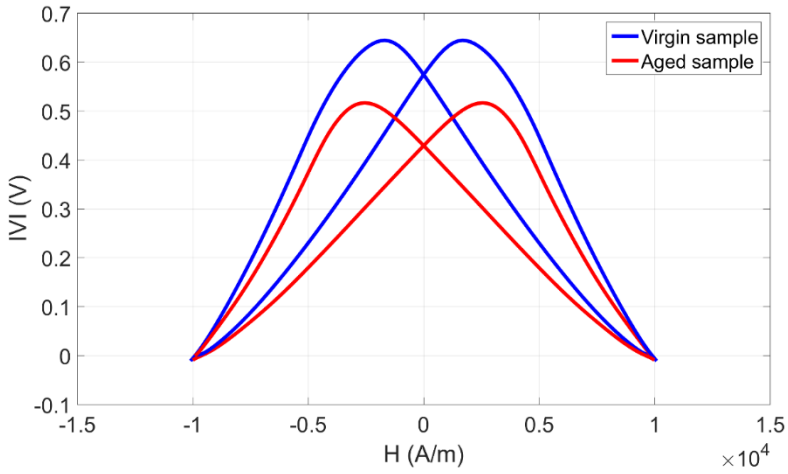

Figure 1.8. MIP Signature curve

1.4.2. Magnetic Barkhausen Noise (MBN)

The phenomenon of Barkhausen effect was first observed and studied in 1919[Bark] which is now used as one of the investigating methods in the field of non-destructive testing. It is applied to study the grain shape, hardness etc. like material properties. Interestingly, the Barkhausen effect has been used as a great tool for studying the effect of residual stress in the ferromagnetic materials [Stew, Kleb, Gaut, Yelb, Sors]. As an industrial application, in the aerospace industry (bearings) and in the automotive industry (Gear boxes), Barkhausen noise is used to inspect the local hardness uniformity after exposing the materials to exact working conditions. Like all other NDT inspection methods,

the Barkhausen noise based characterizations are also very experimental based. The operators collect a lot of data from the very well-known samples, and set certain thresholds for the samples to be approved or rejected in case of some anomalies. Consequently, in the industrial production line, the operators employ this technique for their specific materials, and check if the Barkhausen noise signature lies within the acceptance threshold or not. If not, without any further investigation, the samples are destroyed. One issue with the Barkhausen noise measurements is the stability and the reproducibility. However, if the geometry of the sample is given, the experimental conditions can be optimized (such as the Applied Magnetic field, sensor coil lift-off distance, the instrumentation involved) to deal with this issue. On the other hand, when the samples are modified in geometry or in their properties, this whole optimization process has to be repeated which is quite a cumbersome job from the industrial point of view.

The instrumentation involved in measuring the Barkhausen noise involves high amplification and filtering since, it is a noise measurement. Each step of calibration within the process is very sensitive and time consuming and hence, for small scale industries, it could really be a big challenge to implement this method which becomes a major obstacle in the expansion of use for this method, even though it yields very promising results.

Barkhausen noise is a discontinuous variation in flux density, and consists of irreversible motions of domain walls (magnetic) which break from pinning sites under the influence of varying external applied magnetic field H. Hence, the Barkhausen activities are highly dependent on the density, number and the nature of pinning sites that exist within the material. Pinning sites can be grain boundaries, dislocations or precipitates of a different phase with different magnetic properties from that of the material in which they exist. In Jiles review of magnetic methods for nondestructive evaluation from 1988, MBN is already clearly identified as an indispensable method for the evaluation of residual stress [Pasl, Jile1].

1.4.3. B(H) measurements / Hysteresis Loops

Hysteresis is the basis of understanding the behaviour of magnetic materials. It is the most fundamental property in magnetism. When a ferromagnetic material is under active

magnetization in one direction, the material will still be at a non-zero magnetic state even when the imposed magnetizing field is removed. To attain the zero magnetization, a magnetic field in the opposite direction must be applied. Hence, when an alternating magnetic field is applied to a material, the variations in induced field B with respect to the applied magnetic field, it will trace out a loop called a hysteresis loop as depicted in Fig. 1.9 below.

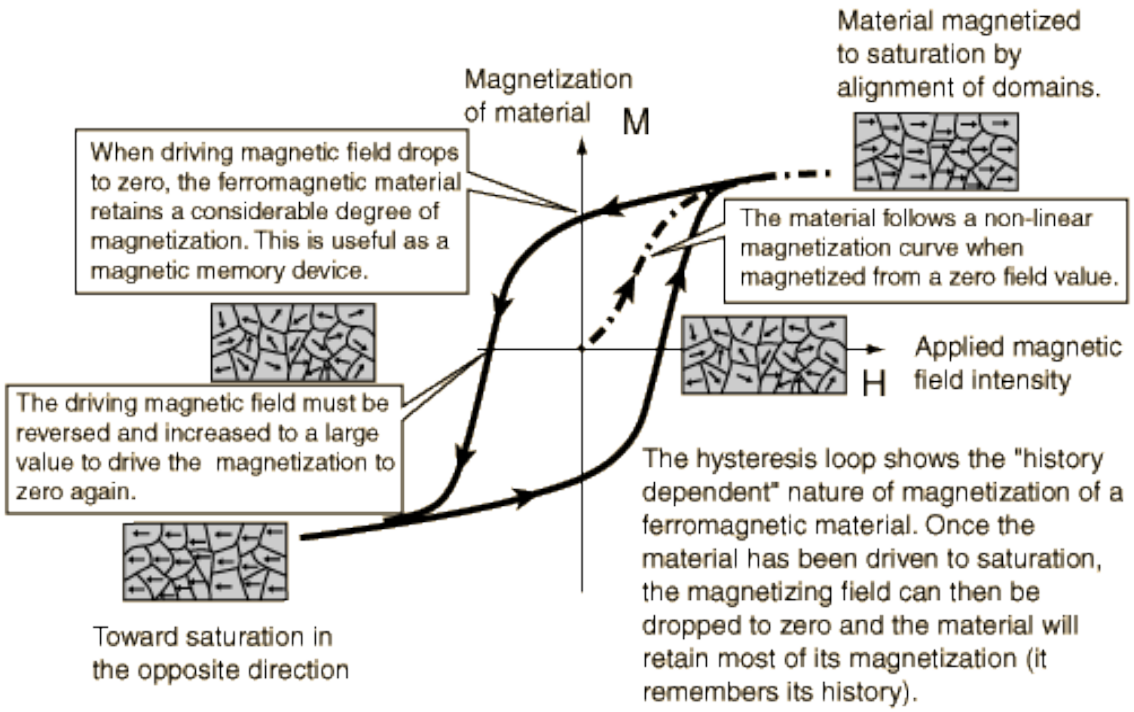

Figure 1.9. Standard Hysteresis Curve[Hype]

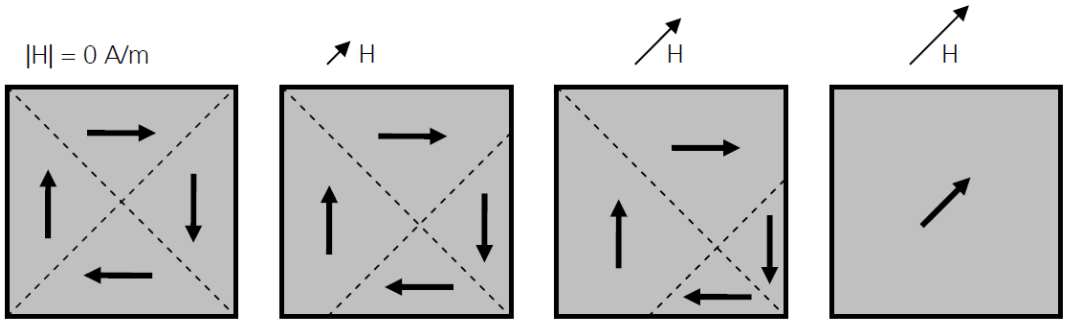

Figure 1.10. Process of change in domain size and rotation of spontaneous magnetization with increasing applied external magnetic field [Szie]

The magnetization of a ferromagnetic material is essentially due to the shifting of the Bloch walls. A Bloch wall is a narrow transition area at the boundary between the magnetic domains, over which the magnetization changes from its value/orientation in one domain to that of in the neighbouring one. When an originally demagnetized ferromagnetic material is exposed to an external field, the ferromagnetic domains tend to be magnetized towards the direction of the external field at the expense of the other domains as shown in Fig. 1.10 [Szie].

The shift of the Bloch walls is initially reversible at low field strengths (Rayleigh-Area). Irregularities in the microstructure such as grain boundaries, dislocations and precipitates hamper the movement of the Bloch walls. The transition in the movement of Bloch walls is abrupt and always happens when the applied magnetic field is high enough to overcome the transition. Consequently, when the material is saturated with a high magnetic field, it results to the formation of a single domain which is parallel to the direction of the external magnetic field. When the external magnetic field is removed, due to the presence and the obstruction caused by the Bloch wall movement, the so called remanence effect is observed, when the material fails to return to its original demagnetized state in the absence of the external magnetic field. This behavior is very well adapted to understand the microstructural properties of the materials. Now to completely bring the magnetization in the material to zero, the magnetic field is applied in the negative direction. To reach the zero magnetization, the applied field is non-zero which is the coercive point in the hysteresis curve. The obstructions caused by the Bloch wall movement and the energy required to bring back the material to its original state are the reasons behind the hysteresis effect. Fig. 1.11 below shows the typical hysteresis curves for a soft magnetic material as well as a hard magnetic material.

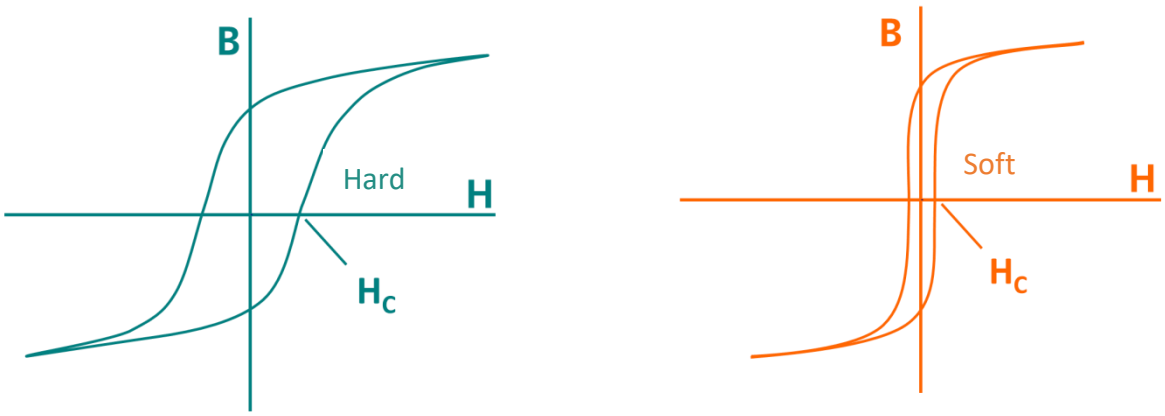

Figure 1.11. Typical Hysteresis curves for Hard as well as soft magnetic materials[Izfp]

All the techniques mentioned above are very sensitive to detecting physical cracks or anomalies in the materials. However, when it comes to detect the early stages of the crack initiation, many of such techniques have strong limitations. One such phenomenon is creep which over the time can cause to microstructural changes in the materials which can lead to fatal accidents in the power industries. The phenomenon of creep is explained as under in section 1.4.

1.5. Creep

A standardized designed material will handle the static load for an unlimited time at ordinary temperatures which is basically an ideal case but practically such conditions are next to impossible to maintain. As soon as there is an influence of external factors like exposure to the high temperatures, lifecycle of materials may be intensively limited and affected, even for loads (could be mechanical or thermal or both) which are much below the range, the material is originally designed to sustain. Under such cases, for instance, the elevated high temperatures, the materials exposed to loads might incur inelastic strain that increases with the time. This phenomenon of deformation and degradation in the materials is known as creep in the scientific community. Since this plastic deformation is a time dependent phenomenon, such a deformation caused due to the prolonged loading is known as creep deformation.

Every material that is exposed to a sustained load at a temperature that is even slightly above its recrystallization temperature, is prone to creep effects. At this temperature, the atoms become highly dynamic. Consequently, over the time, the microstructure of the material undergoes transitions.

Practically, the threshold level of elevated temperatures must be determined specifically for each category of materials since, the phenomenon happens at the microstructural level and is very complex to generalize for all materials. The American Society for Metals' Handbook (ASM, 1976), mentions that this behaviour for various metals at elevated temperature becomes significant over a wide range of temperature, for instance, 205°C for aluminium alloys, for iron-based high-temperature alloys, it is 540°C and for austenitic steels, it ranges between 980°C -1540°C for refractory metals and alloys. It also mentions that the elevated temperatures for certain kinds of plastics, concrete, lead based alloys, lie in the range between 0 to 50°C.

First study of creep: A French Engineer L. J. Vicat in 1834 [Masa] first studied the evolution of creep for hardened iron at room temperature (in this case for rope wires). Till that time, he studied only the first stage of (primary) of the classical form of the strain-time evolution as shown in Fig.12 below. His main focus was to analyse the rope wires for their use in load-carrying materials in suspension bridges. However, the entire creep curve as demonstrated in Fig. 1.12 was studied during the beginning of the 20th century. Additionally, it was studied for rope wires as well as the other materials.

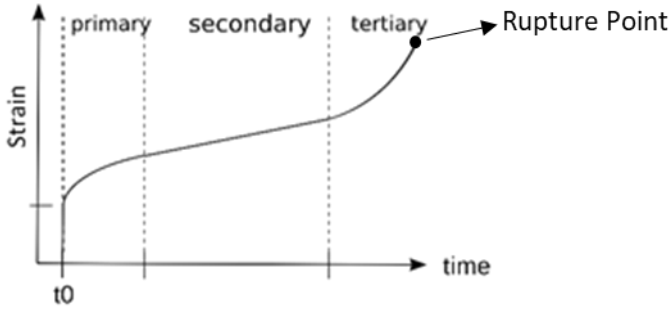

Figure 1.12. Evolution of creep vs. strain

To understand the creep, many researchers put different samples under test to check its evolution. Mostly all the metallic materials showed the similar behaviour as shown in Fig. 1.12. A creep test in general consists of a specimen subjected to constant load at the same temperature. As soon as the sample is loaded, there is an instant elastic deformation. The evolution of strain vs. time is shown in the Fig.1.12 can be categorized into three stages as follows:

Primary Stage of Creep: In this stage the strain rate is initially high relatively, but it starts to slow down as the time and strain increase but with some typical cases of creep, the strain rate increases with strain [Kass] as a result of the process that is analogous to work hardening at lower temperatures, thus making creep almost an unpredictable phenomenon.

Secondary Stage: The strain rate starts to diminish to a minimum value and ultimately becomes almost constant as soon as the secondary stage of creep commences. The reason behind this the balance between the work hardening and the annealing process (thermal softening). This secondary stage of creep is also known as "Steady-state Creep" and it is the most understood and investigated stage of the entire curve show in Fig. 12.

Since, the recovery effects rare very much concurrent with the deformation, there are hardly any significant changes that occur during this secondary stage. According to [Cour], there is hardly any material strength that is lost during the primary as well as the secondary stages of creep.

Tertiary stage: In this stage, due to the internal voids and cracks, the effective area of the specimen decrease, hence leading to an exponential increase in the strain rate with respect to the stress. As a result, the strength of the materials is rapidly degraded and lost in this stage in addition to the material's shape that is permanently deformed. The rate of creep deformation in this stage ultimately leads to the material fracture.

1.6. Study of creep using non-destructive testing techniques

Due to the complexities in understanding, creep has been investigated by many researchers. In the scientific community, the major interest in understanding creep phenomenon has been amongst the solids that are exposed to high temperatures and stress levels and hence from the industrial point of view as well, the analysis of creep becomes very essential especially for the engineering applications of such materials in the thermal/nuclear power plants etc., where the materials are constantly under high stress and temperatures. Even the blades of the turbines and the discs are frequently exposed to the creep degradation effects. In addition to this, the reinforced/non-reinforced materials are in extensive use in industry 4.0 generation and hence it becomes very significant to predict the behaviour and to draw a logical analysis of the creep effected materials in order to gain a thorough knowledge of the characteristics of creep mechanisms.

Although there have been enough studies on high chromium steels from the materials science point of view, however investigations on these materials still lack from the non-destructive testing point of view. For instance, *Eggeler et al.* studied 12% Cr-Mo-V steel samples and investigated that the mechanism of creep at higher stress levels evolve differently when compared to lower stress levels. However, this study was purely based on material science and no magnetic parameters were related to the microstructural changes. *Alexandra et al.* also studied the 9%Cr–3%Co Martensitic Steels but the major focus was to check the effect of tungsten proportion in the materials.

Electromagnetic NDT testing has been a very important technique approach to reveal the mechanical behaviour of paramagnetic as well as the ferromagnetic materials. Consequently, it can help in characterizing the materials using the physical testing and different measurement techniques on an industrial scale by optimizing and developing the industry ready inspection systems. Techniques based on Eddy current testing have been extensively used so far to characterize ferromagnetic materials to study effects like crack depths, crack initiation etc. In ferromagnetic materials, the magnetic properties of the materials can be affected by various factors. To study the effects due to creep damage and choosing a method to study creep has always been complicated. Techniques like Magnetic Barkhausen Noise have been used in the past to study creep, but due to the reproducibility issues, different results are yielded to different researchers[Spos]. Additionally, there has hardly been any study on relating the precipitations or dislocations (which are quite common during the evolution of creep) to the magnetic signatures of the materials.

From the magnetic point of view, *Mohapatra et al*. used Magnetic Barkhausen noise technique to study creep in 9Cr-1Mo steel in which they study the MBE technique to correlate the structural changes during creep of water-quenched modified 9Cr-1Mo steel [Moha]. Similar study was proposed by *Levent et al*. to study 2.25% Cr-1%Mo Steel to investigate creep damage, shot peening and case hardening again using Barkhausen Noise but the conclusions were drawn based on the electrical signals only and not the magnetic behaviour. All these studies were not detailed enough to make a concrete conclusion. Hence, in this work, three different magnetic inspection techniques are employed to study a very complex material in detail and to understand it even better, the magnetic signatures are modelled. Following section covers the work done so far in the field of modelling hysteresis losses.

1.7. Simulation of micro magnetic non-destructive testing: Introduction to the modelling techniques

A large number of micro-magnetic methods for NDT&E are available [Jile1]. Interests in this field are increasing and there is no doubt that new magnetic methods will have tremendous development in a near future. Compared to the classic NDT ultrasound method, most of these micro magnetic methods are still in their stammering and opportunities for future development and growth are numerous. The success of micro

magnetic inspection stands mainly on relatively limited required instrumentations. Since a few years now, integration in manufacturer production lines has been highly successful. Progress in electronics such as printing electronics will for sure open new perspectives. Self-supplied permanent micro-magnetic controller can be envisaged for structural health monitoring by example. All the micro-magnetic NDT&E techniques are based on local magnetic properties of ferromagnetic components. Their setups differ, which makes all of them particularly sensitive or not to given defects or mechanical properties. Coupling these methods as it has been done in the 3MA project seems the most effective compromise but it imposes the use of a single sensor which is unfortunately a restriction [Dobm, Beck, Dobm1, Altp, Thei, Beck1, and Wolt].

The current industrial use of the micro-magnetic NDT is very empirical. It relies on the obtained empirical data from samples, used for calibration, of well-known conditions (e.g. stress, hardness etc.). Thresholds of acceptance/rejection, polynomials representing the target value or databases for pattern recognition are based on these data. At this time, at the exception of the Eddy-current Testing (ECT) experimental situations, no commercial simulation software is available that would completely describe the relation between measured parameters and target material properties. The calibration effort could be significantly reduced if such tools were existing. There is a commercially available software from CEA, CIVA which is a very efficient tool in modelling NDT techniques e.g, EMAT, Ultrasonic techniques, however in terms of Eddy Current Testing, the developed model in CIVA is at a very initial level. However, at the laboratory scale, local accurate models have been developed for the coupled mechanical/magnetic behavior dedicated to numerically simulate the phenomena observable due to the micro magnetic nondestructive evaluation. Numerically simulating micro magnetic methods is possible by means of two approaches as follows.

1.8. Space discretized techniques (SDT)

Mathematically, discretization is the process of converting continuous functions, variables, equations or models into discrete form. This conversion is usually the first step toward making them suitable for numerical evaluation and its implementation on the digital platforms. Considering the case of eddy current testing method, models available are very well capable of providing the visualization of the field/flaw interactions, which in result, help in the better understanding of the procedure in case of any defects/anomalies

present. The use of theoretical models, whether numerical or analytical, helps to generate a lot of information about the defect signatures, which are normally very complex and expensive to be produced empirically. Until now, the analytical approaches that are available are able to provide information only in case of geometrically simple cases.

Due to the advancements in the technology and the computational methods, numerical methods are much more popular now, whose basis is on mathematical approach of solving differential or integral equations. However, when it comes to complex geometries, there are still limitations on finding the efficient solutions to integral equations for eddy current testing related problems [Yook]. Contrary to that, differential equations solving methods are more flexible and capable enough for addressing the issue of modeling complicated geometries. Being relatively simpler in its formulation and capable enough of modelling the non-linearity and the anisotropic properties of the materials even with complex geometries, the finite-element method (FEM) is one of the most popular numerical method for modelling ECT.

Lord et al. introduced the technique of FEM for ECT application [Lord, Hwan, Lord1 and Pala]. 2-D models and the axisymmetric models which simulate the axisymmetric coils and the currents induced, are much simpler to implement and are based on only a single component (either circumferential or vertical) Magnetic Vector Potential formulation. However, when it comes to more realistic conditions, the development of 3-D simulation methods is needed, which is not only a challenging task in terms of computational resources required to succeed but it also adds an extra degree of complexity from the theoretical point of view. [Ida, Obrk, Obr, Goto, Saba, and Zeng] highlight the developments made in the direction of implementing FEM to address the issue of 3-D simulations for ECT methods.

Finite Elements Methods (FEM), Finite Differences Methods (FDM) and in a general way all space discretized method can also be used for the simulation of other micro magnetic methods. However, because of the ferromagnetic nature of the sample tested the numerical method has to be extended with accurate scalar or vectorized data. They are performed in either dynamic or static conditions, and can consider hysteretic material laws. The latter ones are covered by different models. The best results were obtained by extending the quasi-static hysteresis models (Preisach model [Prei, Maye and Zhan], Jiles-Atherton model [Jile2, Jile3 and Zhan2] to dynamic behavior considering the separation losses technique as proposed by Bertotti [Bert, Bert1 and Bert2]. Since at least one

hysteresis model has to be associated to one element/node, the material law must be fast and light [Gabi, Gabi1 and Wolt1].

Iterative techniques such as the fixed point approach can be used to realize the combination of SDT procedures with the hysteresis models. Using this technique can lead to accurate results but still numerical convergence issues can be prominent is some particular cases [Kucz, Sait]. In order to simulate correctly the micro magnetic experimental conditions, the electromagnetic model to be used must be accurate enough to give the local as well as the time variations of both the excitation field *H* and the induced magnetic field *B*. The 2-D approach can give the evolution of both *H* and *B* via the cross section of the material under test. On the other hand, the 3-D approach gives this local information across the entire volume of the test sample. So, to tackle the numerical issue because of the fixed point/ Newton-Raphson algorithm, strong formulations (instead of using the classic approach of coupling the space discretization and the material law, by calculating for each time step, the equivalent permeability for each node of the resolution scheme with new formulations, the hysteresis model is already included in the equation solved by SDT) can be proposed to solve simultaneously the diffusion equation (macroscopic eddy currents) as well as the dynamic hysteresis model (microscopic eddy currents) [Gupt1, Duch, Duch1 and Raul] (which is basically the preliminary work done as the first step of this thesis work). In these simulations, structural defects are considered as local variations of the physical properties (magnetic permeability and electrical conductivity). Using such numerical solutions, some conclusions can be drawn concerning the influence of each contribution (macroscopic as well as the microscopic eddy currents) on the evolution of average measurable entities. The effect of the geometrical position of a microstructural defect such as micro-residual stresses can be easily studied. This approach of modelling can also be used to precisely define an excitation waveform (amplitude, frequency) that is required to study a sample.

1.9. Lump models

The lump model or lumped element model is used to simplify the behavioural description of spatially distributed physically systems into a topology that consists of discrete entities to approximate the behaviour of the system under certain assumptions. Mathematically, this simplification helps to reduce the state space of the system to a finite dimension in addition to the partial differential equation of the continuous time and space

model of the physical system into ordinary differential equations with a finite number of parameters.

As explained before, SDT can give very accurate and precise results. However, the high non-linear behavior of hysteresis phenomenon can often lead to uncertain convergences which results in numerical errors as demonstrated in [Kucz, Sait]. Moreover, SDT require a large amount of memory, and such an approach of simulating is always very time-consuming. By assuming homogeneous magnetic property in the tested area, alternative methods can be proposed. For these methods also called "lump model", the focus is to determine the measured parameters as they are observable experimentally with the experimental sensor. As the magnetic state of the tested sample is supposed to be homogeneous the lump models is typically scalar and made out of two contributions explained in the following section.

1.9.1. A quasi-static contribution

A. Scalar quasi-static hysteresis Preisach model:

Preisach model is a quasi-static model for hysteresis for which the input of the model can be reversed to B instead of H. This model has been used a lot by the researchers to interpret and understand the phenomenon of hysteresis in the ferromagnetic materials [Henr, Torr]. According to the theory of Preisach model, the magnetization of the materials can be determined by a set of elementary hysteresis curves which have a distribution function that can be represented by a Preisach triangle. In [Maye] it is illustrated that the behavior of the magnetic materials is determined by a set of elementary hysteresis curves that are defined as $h(\alpha, \beta)$ where α is the upper switching field and β is the lower switching fields with $\alpha \geq \beta$. The magnetization factor M can be calculated by the set of elementary particles that have a distribution function $\mu(\alpha, \beta)$ over the Preisach triangle as shown in Fig. 1.13.

$$M = Ms.\int_{\alpha}\int_{\beta} h(\alpha,\beta).\mu(\alpha,\beta)d\alpha d\beta \qquad (1.3)$$

with

$$\int_{\alpha}\int_{\beta} \mu(\alpha,\beta)d\alpha d\beta = 1 \quad and \quad -HS \leq \alpha \leq HS, \quad \beta \leq \alpha \qquad (1.4)$$

where Ms is the magnetization value when $H=HS$.

According to the concept of a classic Preisach model, the centered cycle of magnitude H1, H2 and H3 as shown in Fig. 1.14, is obtained by the integrating the distribution function over the triangles 1, 2 and 3 respectively as shown in Fig. 1.13.

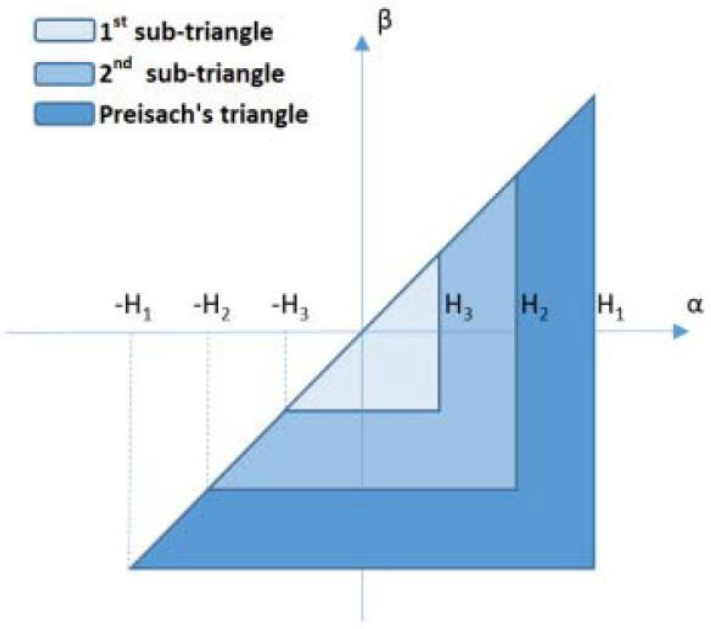

Figure 1.13. Preisach triangle, 1st and 2nd sub-triangle.

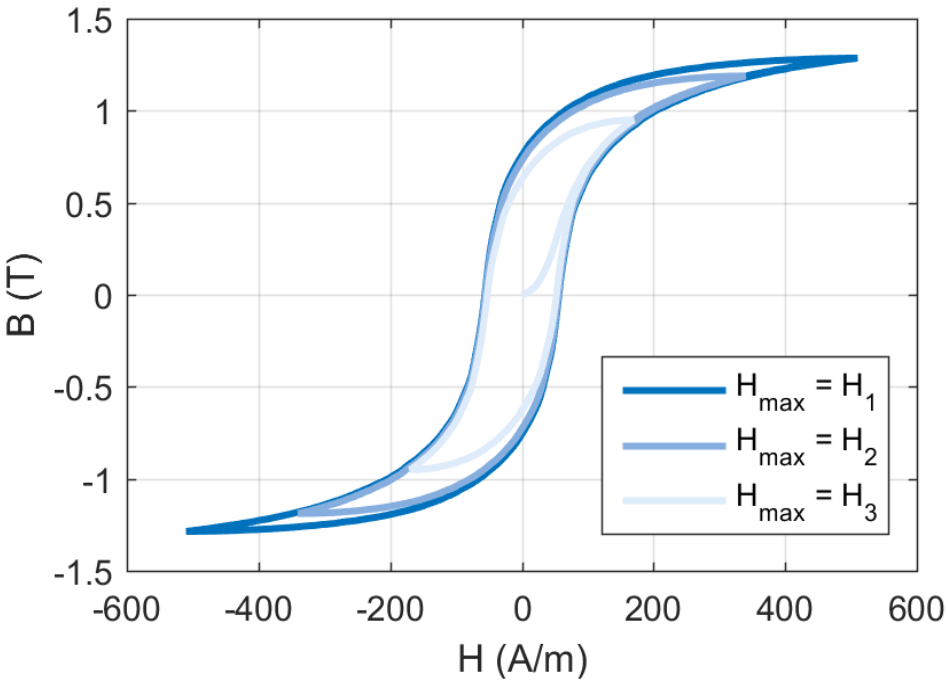

Figure 1.14. Simulated centered cycles.

In order to precisely model the behavior of the magnetic materials, it is very important to determine the distribution function very accurately from the experimental data. The first way to determine the distribution function is to assume that it has a particular form like Gaussian or Lorentzian and then determine the parameters of the selected function to illustrate the hysteretic behavior. The second way is by discretizing the distribution function into a set of finite values that can be determined by the experimental data.

Using the first technique, a lot of experimental data is needed although an accurate behavior could be achieved with a lower size of discretized distribution that simplifies the memory management. Fig. 1.15 illustrates the Preisach space discretized distribution using the Biorci method for a standard steel sample.

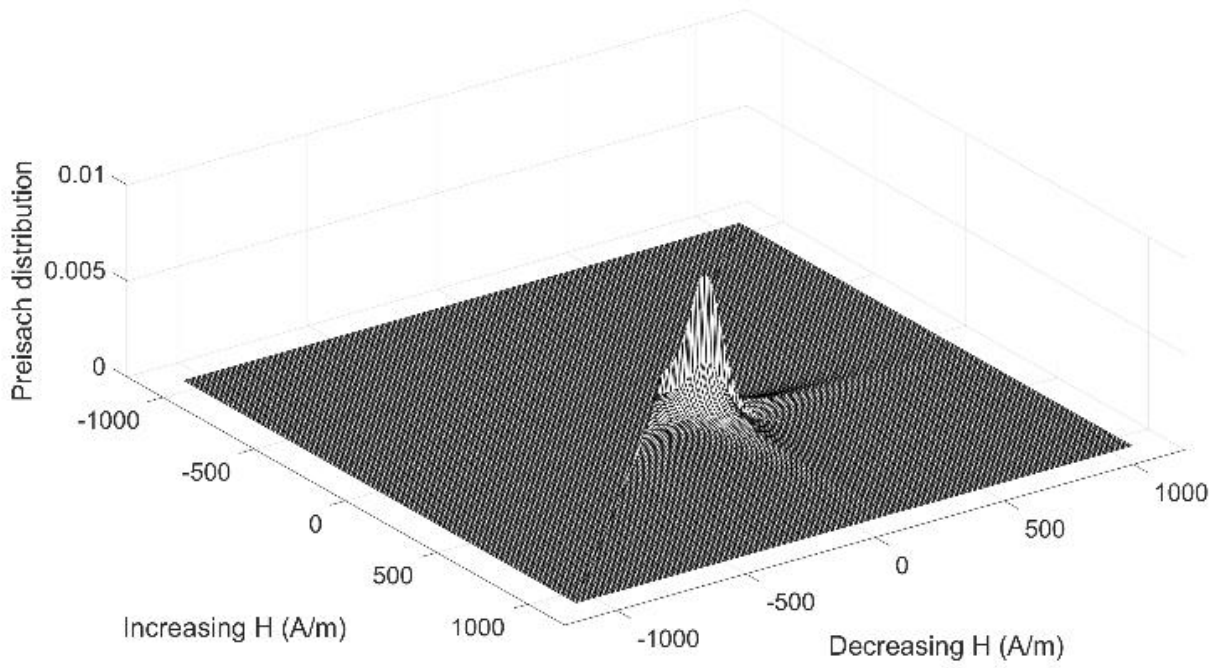

Figure1.15. Preisach distribution function.

B. Scalar quasi-static hysteresis Jiles-Atherton model:

In 1984, Jiles and Atherton proposed a quasi-static scalar mathematical model of the hysteresis mechanism in ferromagnetic materials [Jile2]. The Jiles-Atherton model is based on physical basis for the magnetization process. The Jiles-Atherton model can be defined by 5 parameters and each of these parameter has a physical meaning. This model is explained in detail in Chapter 4 since it has been used to model the results in this research work.

1.9.2. A dynamic contribution, for the frequency dependence.

When subjected to weaker frequencies, the quasi-static models can provide accurate and precise results for the evolution of Hysteresis cycles. Such external conditions represent the distribution of induction in the sample under test homogeneously which signify the homogenous distribution of losses. However, seen the simplicity of such models, as soon as there is a deviation in such conditions, huge differences in the results can be noticed. Such differences can be avoided by adding to a dynamic contribution, the product of a damping constant ρ and the time derivative of the induction B which is equivalent to the magnetizing exciting field. This can somehow provide a relative improvement although the correct simulation result can be obtained within a narrow bandwidth of frequency.

Apparently, a simple losses term dB/dt seems to lead an overestimation in the high frequency part when looking at the hysteresis loop area plotted against the frequency curve. Hence, to achieve precise simulation results over the large frequency bandwidth, instead of using a straight time derivative, fractional order derivatives can be implemented which can help in dealing with lower and higher frequency bandwidth differently Using the franctional order derivatives that represent the n fold integral, d^nB/dt^n can be added in the lump model as stated in the Grünwald Letnikov (represents the n order derivative) or Riemman-Liouville (represents the n fold integral) definitions [Grun, Riem and Liou]. In the following section, the use of the Riemman Liouville class for n ∈ [0,1] (n being the fractional order of the derivative).

$$\frac{d^n f(t)}{dt^n} = D_t^n f(t) = \frac{1}{\Gamma(1-n)} \frac{d}{dt} \int_{-\infty}^{t} (t-\tau)^{-n} f(\tau) d\tau \qquad (1.5)$$

where Γis the Euler gamma function. In the equation (Eq. 1.5), the fractional derivative of a function f(t) can also be considered as the convolution of a f(t) and $t^n/\Gamma(1-n)$. The straight time derivative expressed in the equation above illustrates the occurrence of positive argument of gamma function, Γ(.), which converges to a finite value. Observing equation (1.5), it is evident that fractional derivative also considers the previous states' memory. An interesting property of the fractional calculus is that in the frequency domain, the frequency spectrum f(ω) of f(t) is multiplied to the $(j\omega)^n$ [Guyo, Guyo1]. Consequently, the equation provides a new degree of freedom (n value) and by fine-tuning it, the experimental requirements can be fulfilled, which can help in adjusting the evolution of the hysteresis area versus frequency.

The way fractional derivatives are implemented in the lump quasi-static model is done through a dynamic contribution. The term ρ. dB/dt is therefore replaced by $\rho.d^nB/dt^n$, This term is then added to the quasi-static contribution, following to Eq. 1.6.

$$\rho.\frac{d^nB(t)}{dt^n} = H_{dyn}(t) - f_{static}^{-1}(B(t)) \qquad (1.6)$$

The parameters (ρ, n) are determined by comparing the simulations/experimental results. To get accurate behavior, a minimum of two dynamic experimental major hysteresis cycles are required (50, 200 Hz for the SV142b).

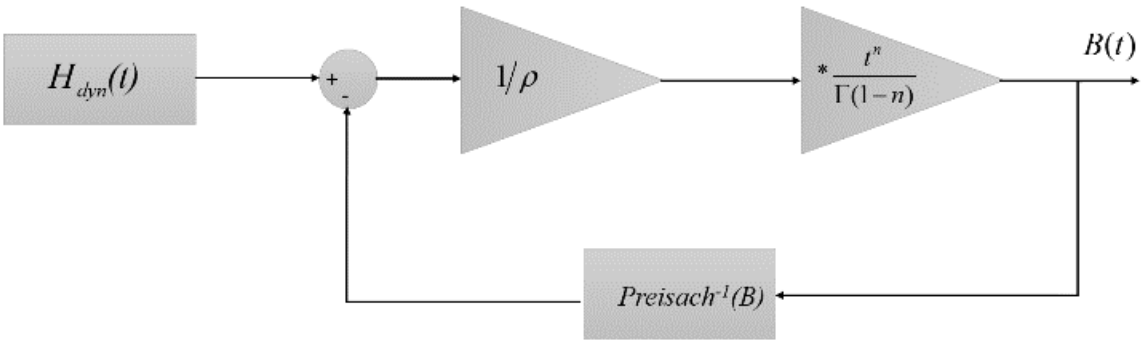

Figure 1.16. Fractional dynamic lump hysteresis model.

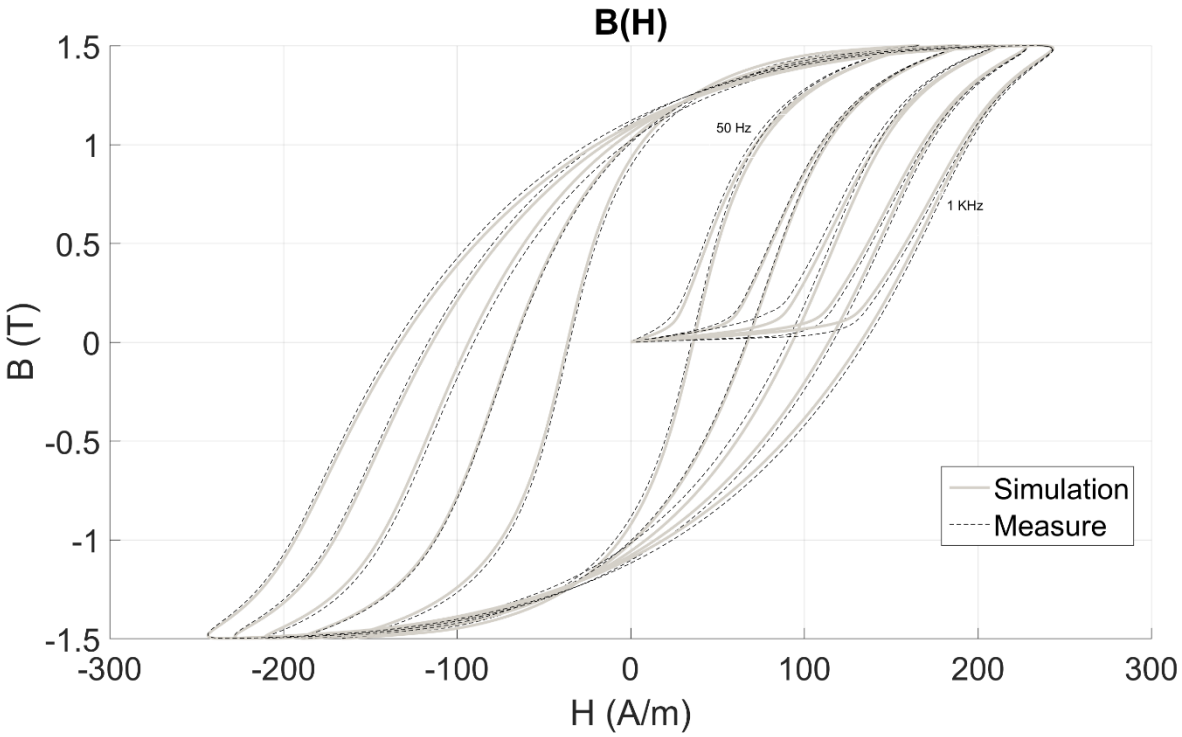

Figure 1.17. Comparison simulation/measure under dynamic state (50, 250, 500, 750 and 1000 Hz) [Zhan2]

Fig. 1.18 demonstrates the time variation of *H* from 50 Hz to 750 Hz illustrating the non-linear behavior.

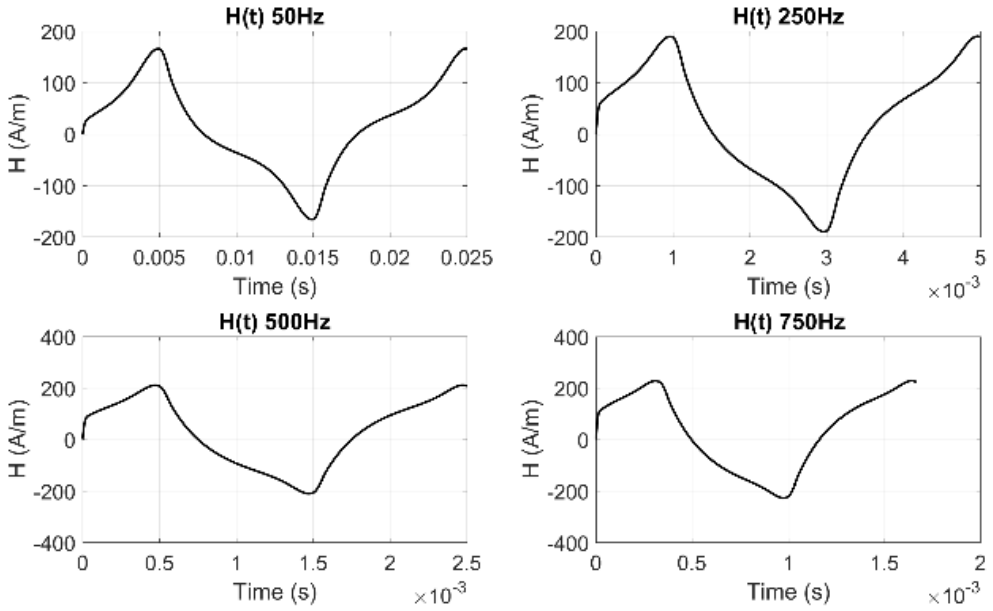

Figure 1.18. Tangent excitation field H versus time (50, 250, 500 and 750 Hz) [Zhan2]

Fig. 1.19 illustrates the behavior of the model under B imposed harmonic-type excitation (1T 50Hz + 0.8T 150Hz) and Fig. 1.20, both B and H time variations for such excitations.

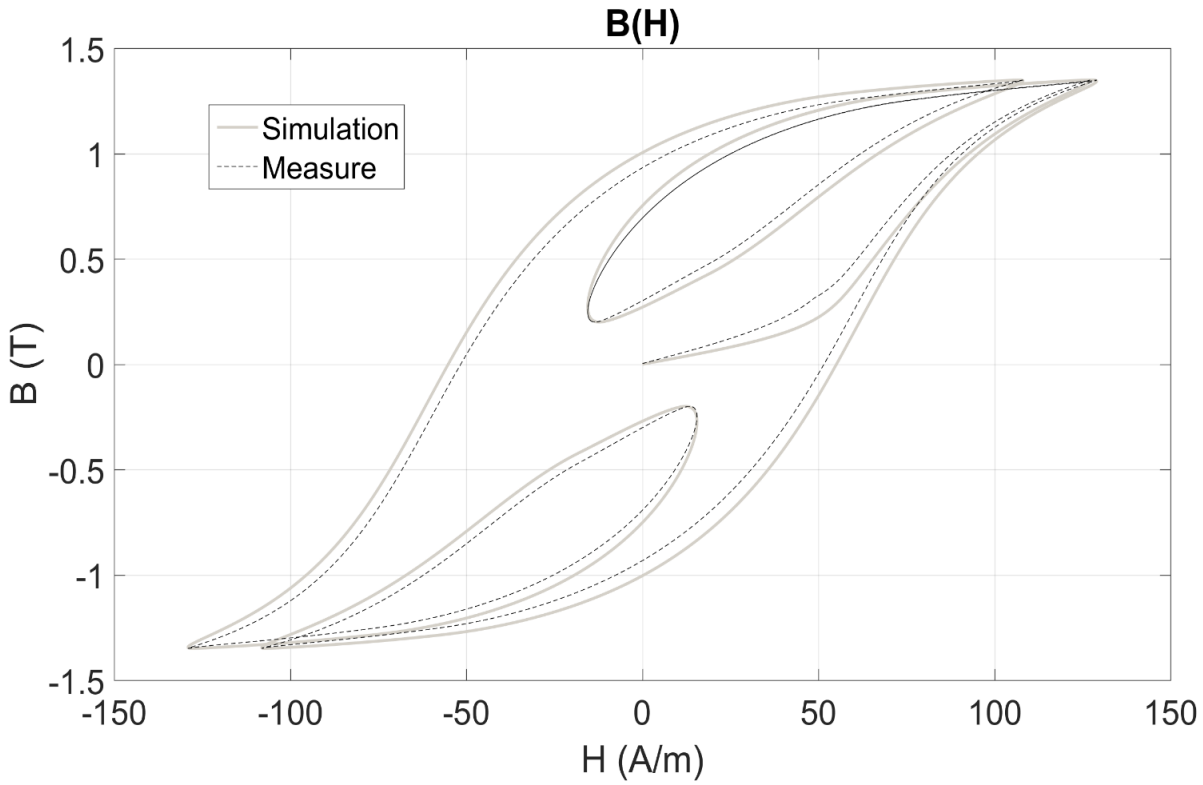

Figure 1.19. Comparison simulation/measure under dynamic harmonic type excitation[Zhan2]

With this micro-magnetic NDT simulation state of the art, we can insist on the strong need for

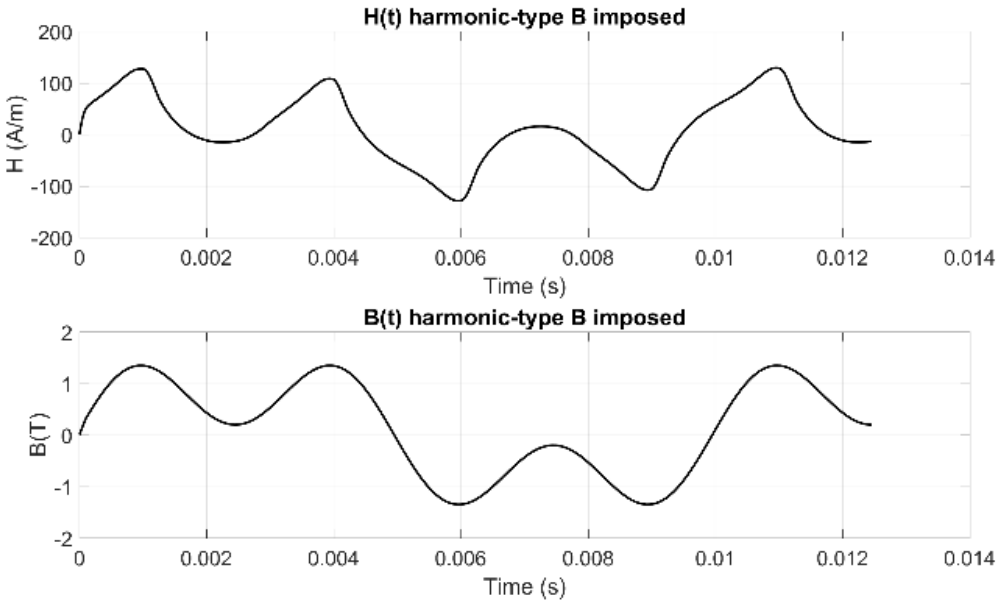

Figure 1.20. H and B versus time under harmonic-type B imposed [Zhan2]

models specifically dedicated to NDT applications. The phenomena have to be understood at a deeper level and to achieve this objective, simulations are mandatory. As explained before, a lot of theoretical research has been performed in the past in order to physically interpret the parameters of magnetic loss models, but at this time very less are published concerning their evolution as a function of ageing or fatigue of the material. Obtaining such an evolution would constitute a major step forward in the prediction of micro-residual stress, microstructural issues, and first damages in the tested components.

1.10. Objectives

In thermal power plants, it is very difficult to measure microstructure real time changes. The conditions under which the materials are exposed (constant high temperatures and pressures) lead to the introduction of creep phenomenon, first step toward rupture. To check the microstructure evolution, material samples have to be prepared in a specific shape and size to be tested using EBSD, SEM, TEM techniques. These destructive methods involve fastidious preparation time, large number of experiments and huge equipment costs. Hence, an alternative solution must be introduced to evaluate and predict the real time microstructure changing with very minimal measurements and maximum information. Electromagnetic non-destructive testing techniques can play a key role in studying the rarely investigated high chromium steel from the Magnetic NDT point of view.

Hence, the main objective of this thesis work is to determine the evolution of microstructural changes (Precipitations, Dislocations) in Creep Degraded High Chromium Ferritic Steels, from the NDT signatures. To achieve this objective, the main objective is divided into two sub-objectives. The first sub-objective is to screen different electromagnetic techniques to correlate the NDT signals with the microstructural changes for 12%Cr-Mo-W-V Creep degraded Ferritic samples. Under this sub-objective, three different empirical approaches are applied to the test samples, namely, Magnetic Incremental Permeability (MIP), Hysteresis measurements (B(H)) and Magnetic Barkhausen noise (MBN). As a first step, the MIP method is applied to the given set of samples and the corresponding signature curves are used to determine the magnetic parameters. These magnetic parameters are then evaluated against the microstructural information such as precipitations, dislocations etc. The next step is to evaluate the same set of samples using the hysteresis measurements. Furthermore, MBN technique is applied to

the same set of samples to derive the magnetic parameters and check their correlation in terms of microstructural evolution. This sub-objective reveals how the magnetic parameters evolve in the creep degraded samples with different rupture levels and each of this technique reveals its sensitivity as well. Combining micro-structure analysis to the micro-magnetic tests will enable to target which experimental parameter is the most representative for the creep phenomena.

To further quantify the results obtained in the first sub-objective, the second sub-objective is to develop a physical model and interpret the modelling parameters in terms of microstructure. The physical model is adapted to simulate the signals derived from each technique mentioned in the first sub-objective. Each modelling technique gives access to few model parameters that are assessed in terms of microstructure as well. Post to the derivation of these model parameters, the most sensitive parameter(s) are established for each technique used. Finally, a correlation factor between these parameters and the microstructural/mechanical properties is determined to check which parameter is correlated and sensitive to a particular microstructural as well as mechanical property of the samples. The modelling technique can be a tentative solution to the problem of lack of standards in the field of NDT (as the tendency of the evolution of the parameters will not change with the change in the experimental set-ups involved).

1.11. Thesis Outline

In this thesis work, the samples are provided by the industry and the raw information of the microstructure was also given. In Chapter 2, an analysis based on the microstructure given is performed. In chapter 3, the Magnetic Incremental Permeability inspection method is applied to evaluate the samples. The typical MIP butterfly curves are obtained for each sample. These curves give access to magnetic parameters which are then correlated to the microstructure to interpret the evolution of magnetic behavior. In addition to this the experimental analysis based on Hysteresis curves has also been investigated. Following to this, in chapter 4, different modelling principles to simulate MIP curves have been illustrated along with their limitations and reasons to choose Lump models to model the same. In this chapter, lump based model is developed and tested based on Preisach model and Jiles-Atherton theory. Since, Jiles-Atherton model is a physical model and each parameter has a physical meaning, it is finally adapted to model

the magnetic signatures obtained in Chapter 3. The modelling parameters are then studied in relation to the microstructure. Additionally, in this chapter, the hysteresis cycles studies in Chapter 3 are also studied from the modelling point of view for the same set of samples and their corresponding modelling has been performed. At the end of this chapter, based on the method applied, the most sensitive parameters are demonstrated. The third technique based on Magnetic Barkhausen Noise (MBN) is applied to the samples in Chapter 5. Using the raw data, MBN_{energy} cycles are plotted for each sample providing a magnetic signature related to the domain wall movements. This makes it easy to model the curves and derive the modelling parameters which are then studied with respect to the microstructure of the samples. Finally, the thesis is concluded in Chapter 6 with the comparisons of the three techniques briefing which parameter is relevant for each technique and with the physical interpretation of the magnetic as well as the modelling parameters.

References

[Alle] W. Allen, R.G. Mahroter, Investigation into the electrical conductivity and mechanical properties of aluminum alloys subjected to elevated temperature exposure,USNaval report no.NAEC-AIVIL- 2083, Aeronautical Materials Laboratory, November (1964)

[Altp] I. Altpeter, G. Dobmann, W.A. Theiner, "Quantitative hardening-depth-measurements up to 4 mm by means of micromagnetic microstructure multiparameter analysis-3MA", Rev. Prog. Quant. Nondestruct. Eval. 1987, 7B, 1471–1475.

[Bark] H. Barkhausen, "Two phenomena revealed with the hekp of new amplifiers", Phys. Z, vol. 29, pp. 401, 1919

[Beck] R. Becker, G. Dobmann, C. Rodner, "Quantitative eddy current variants for micromagnetic microstructure multiparameter analysis-3MA", Rev. Prog. Quant. Nondestruct. Eval. 1987, 7B, 1703–1707. 23.

[Beck1] R. Becker, G. Dobmann, W.A. Theiner, "Progress in the micromagnetic multiparameter microstructure and stress analysis—3MA", In Nondestructive Characterization of Materials III, Proceedings of the

International Symposium on Nondestructive Characterization of Materials, Saarbruecken, Germany, 3–6 October 1988.

[Bert] G. Bertotti, "General properties of power losses in soft ferromagnetic materials," IEEE Trans. on Mag.., 24, pp. 621-630, 1988.

[Bert1] G. Bertotti, "Physical interpretation of eddy current losses in ferromagnetic materials. I. Theoretical considerations", J. Appl. Phys., vol. 57, no. 6, p. 2110, Mar. 1985.

[Bert2] G. Bertotti, "Space-time correlation properties of the magnetization process and eddy current losses: Applications. I. Fine wall spacing," J. Appl. Phys., vol. 55, no. 12, p. 4339, Jun. 1984.

[Bozo] R.M. Bozorth; Ferromagnetism. Van Nordstrand, Princeton.1951.

[Circ] Basics of Magnetism, URL:https://circuitglobe.com/magnetic-permeability.htm, as of January 2019.

[Cour] T.H. Courtney (2005). Mechanical behavior of materials. Waveland Press. ISBN 9781577664253. OCLC 894800884.

[Cull] B. D. Cullity.; Introduction to magnetic materials. Addison-Wesley. 1972.

[Dear] J.A. Dearing; Environmental magnetic susceptibility.1994. URL:http://gmw.com/magnetic_properties/pdf/Om0409%20J_Dearing_Handbook_iss7.pdf, as of January 2015.

[Dobm] G. Dobmann, "Physical basics and industrial applications of 3MA—Micromagnetic multiparameter microstructure and stress analysis", In Proceedings of the 10th European Conference on Nondestructive Testing, ECNDT 2010, Moscow, Russia, 7–11 June 2010.

[Dobm1] G. Dobmann, H. Pitsch, "Magnetic tangential field-strength-inspection, a further ndt-tool for 3MA", In Proceedings of the 3rd International Symposium on Nondestructive Characterization of Materials, Saarbrücken, Germany, 3–6 October 1988; pp. 636–643.

[Duch] B. Ducharne, G. Sebald, D. Guyomar, G. Litak, "Fractional model of magnetic field penetration into a toroidal soft ferromagnetic sample", Int. J. of Dyn. And Cont., pp. 1-8, 2017.

[Duch1] B. Ducharne, G. Sebald, D. Guyomar, G. Litak "Dynamics of magnetic field penetration into soft ferromagnets", Journal of Applied Physics, pp. 243907, 2015.

[Euro] Eddy Current Testing, http://www.eurondt.com/EDDY%20CURRENT.html, as of March 2019.

[Gabi] Y. Gabi, B. Wolter, A. Gerbershagen, M. Ewen, P. Braun, O. Martins, "FEM simulations of incremental permeability signals of a multi-layer steel with consideration of the hysteretic behaviour of each layer", IEEE Trans. Magn., vol. 50, pp. 1–4, 2014.

[Gabi1] Y. Gabi, O. Martins, B. Wolter, B. Strass, "Combination of electromagnetic measurements and FEM simulations for nondestructive determination of mechanical hardness", AIP Adv., vol. 8, 2017.

[Gaut] J. Gauthier, T.W. Krause, D.L. Atherton, "Measurement of residual stress in steel using the magnetic Barkhausen noise technique", NDT&E Int. vol. 31, iss. 1, pp. 23-31, 1998.

[Goto] Y. Gotoh, N. Takahashi, "Three-dimensional FEM analysis of electromagnetic inspection of outer side defects on steel tube using inner coil", IEEE Trans. Magn., vol. 43, no. 4, pp. 1733-1736, Apr. 2007.

[Grun] A.K. Grünwald, "Ueber begrenzte derivationen und deren Anwendung", Zeitschrift für mathematik und physik, XII(6), pp.441-480, 1867.

[Gupt] B. Gupta., K. Szielasko, Magnetic Sensor Principle for Susceptibility Imaging of Para- and Diamagnetic Materials, Journal of Nondestructive Evaluation. 2016.

[Gupt1] B. Gupta, B. Ducharne, G. Sebald, T. Uchimoto, "A space discretized ferromagnetic model for non-destructive eddy current evaluation", IEEE Trans. on. Mag, vol. 54 Iss. 3, 2018.

[Guyo] D.Guyomar, B.Ducharne, G.Sebald, "Dynamical hysteresis model of ferroelectric ceramics under electric field using fractional derivatives", J. Phys.D: Appl.Phys., 2007.

[Guyo1] D.Guyomar, B.Ducharne, G.Sebald, "The use of fractional derivation in modeling ferroelectric dynamic hysteresis behavior over large frequency bandwidth", J. Appl. Phys., 2010, vol.107, Iss. 11, n° 114108.

[Hayt] W. H. Hayt, Engineering electromagnetics, McGraw-Hill. 1989.

[Henr] F. Henrotte, 'Modeling ferromagnetic materials in 2D finite element problems using Preisach's model,' IEEE Trans. Mag., pp. 2614–2616, Sept. 1992.

[Hwan] J. H. Hwang, W. Lord, "Finite element modeling of magnetic field/defect interactions", ASNT J. Test. Eval., vol. 3, no. 1, pp. 21-25, 1975.

[Hype] Hysteresis Loop, HyperPhysics, URL: http://hyperphysics.phy-astr.gsu.edu/hbase/Solids/hyst.html, as of June 2019.

[Idan] N. Ida, Three Dimensional Finite Element Modeling of Electromagnetic NDT Phenomena, 1983.

[Izfp] Fraunhofer institute of non-destructive testing, Saarbrücken, personal communication.

[Jile] D.C. Jiles; Introduction to magnetism and magnetic materials.Chapman and Hall.1991.

[Jile1] D.C. Jiles, "Review of magnetic methods for nondestructive evaluation", NDT Int., vol. 21, n°5, 1988.

[Jile2] D.C. Jiles, D. L. Atherton, "Theory of ferromagnetic hysteresis". J. of App. Phys., vol. 55, iss. 6, pp. 2115, 1984.

[Jile3] D. C. Jiles, "A self-consistent generalized model for the calculation of minor loop excursions in the theory of hysteresis," IEEE Trans. Magn., vol. 28, no. 5, pp. 2602–2604, Sep. 1992.

[Kass] M.E. Kassner, Fundamentals of Creep in Metals and Alloys.

[Kleb] X. Kleber, A. Vincent, "On the role of residual internal stresses and dislocation on Barkhausen in plastically deformed steel", NDT&E Int., vol. 37, iss. 6, pp. 439-445, 2004.

[Kucz] M. Kuczmann, A. Iványi, 'The Finite Element Method in magnetics', Budapest, Academic Press, 2008.

[Liou] J.Liouville, "Mémoire sur le calcul des différentielles à indices quelconques", J. Ecole Polytech. , vol.13(21), pp. 71-162, 1832.

[Lord] W. Lord, R. Palanisamy, "Development of theoretical models for NDT eddy current phenomena", Proc. Symp. Eddy Curr. Charact. Mater. Struct. NBS, 1979-Sep.

[Lord1] W. Lord, R. Palanisamy, "Magnetic probe inspection of steam generator tubing", Mater. Eval., vol. 38, no. 5, pp. 478-485, May 1980.

[Masa] Masateru Ohnami, Fracture and Society, IOS Press.

[Magn] Magnaflux, URL: https://www.qualitymag.com/articles/90976-magnetic-particle-powder-performance, as of March 2019.

[Maye] I.D. Mayergoyz "Mathematical models of hysteresis", Phys. Rev. Lett, 56, pp1518-21, 1986.

[Moha] Magnetic Non-destructive Evaluation of Creep Behavior in Water-Quenched Modified 9Cr1Mo Steel. Available from: https://www.researchgate.net/publication/253177678_Magnetic_Nondestructive_Evaluation_of_Creep_Behavior_in_Water-Quenched_Modified_9Cr1Mo_Steel [accessed Mar 04 2019].

[Nave] Nave Rod; Magnetic field. URL: http://hyperphysics.phyastr.gsu.eu/hbase/magnetic/magfile.html, as of December 2018.

[Obrk] O. Br, K. Preis, "On the use of the magnetic vector potential in the finite element analysis of three-dimensional eddy currents", IEEE Trans. Magn., vol. 25, no. 4, pp. 3145-3159, Jul. 1989.

[Obr1] O. Br, "Edge element formulations of eddy current problems", Comput. Methods Appl. Mech. Eng., vol. 169, pp. 391-405, 1999.

[Pala] R. Palanisamy, Finite Element Modeling of Eddy Current Nondestructive Testing Phenomena, 1980.

[Pasl] R.L. Pasley, "Barkhausen effect an indication of stress", Mater. Eval., vol. 28, pp. 157, 1970.

[Prei] F. Preisach, "Über die magnetische Nachwirkung". Zeitschrift für Physik, 94: 277-302, 1935.

[Raul] M. A. Raulet, B. Ducharne, J.P. Masson, and G. Bayada, "The magnetic field diffusion equation including dynamic hysteresis: a linear formulation of the problem", IEEE Transactions on Magnetics, vol. 40, n° 2, pp. 872 – 875, 2004.

[Riem] B.Riemann, "Gesammelte werke", 1892.

[Saba] R. V. Sabariego, P. Dular, "A perturbation approach for the modeling of eddy current nondestructive testing problems with differential probes", IEEE Trans. Magn., vol. 43, no. 4, pp. 1289-1292, Apr. 2007.

[Sait] J. Saitz, IEEE Trans. Magn., pp. 1398–1401, May 1999.

[Scha] H. Schaumburg: Werkstoffe. Teubner-Verlag, Stuttgart. 1990.

[Sors] A. Sorsa, K. Leiviskä, S. Santa-aho, T. Lepistö, "Quantitative prediction of residual stress and hardness in case-hardened steel based on the Barkhausen noise measurement", NDT&E Int. vol. 46, pp. 100-106, 2012.

[Spal] Spaldin N.A.; Magnetic materials: fundamentals and applications. Cambridge: Cambridge University Press. 2010.

[Stew] D.M. Stewart, K.J. Stevens, A.B. Kaiser, "Magnetic Barkhausen noise analysis of stress in steel", Cur. App. Phys., pp. 308-311, 2004.

[Szie] K. Szielasko, Entwicklung messtechnischer Module zur mehrparametrischen Elektromagnetischen Werkstoffcharakterisierung und –prüfung, Doctoral Thesis, https://d-nb.info/996406999/34.

[Thei] W.A. Theiner, P. Deimel, "Non-destructive testing of welds with the 3MA-analyzer", Nuclear Eng. Des. 1987, 102, 257–264.

[Torr] E. Della Torre, "Parameter identification of the complete-moving-hysteresis model using major loop data'', IEEE Trans. Magn.,Vol. 30, pp. 4987-5000, 1994.

[Wolt] B. Wolter, W.A. Theiner, R. Kern, R. Becker, C. Rodner, P. Kreier, P. Ackeret,"Detection and quantification of grinding damage by using EC and 3MA techniques", In Proceedings of the ICBM4—4th International Conference on Barkhausen Noise and Micromagnetic Testing, Brescia, Italy, 3–4 July 2003.

[Wolt1] B. Wolter, Y. Gabi, C. Conrad, Nondestructive Testing with 3MA—An Overview of Principles and Applications, Applied Sciences 9(6):1068.

[Yash] A. Yashan, G. Dobmann, "Measurements and semi-analytical modeling of incremental permeability using eddy current coil in the presence of magnetic hysteresis", Electromagnetic nondestructive evaluation (VI), IOS press, 2002.

[Yelb] H.I. Yelbay, I. Cam, C.H. Gür, "Non-destructive determination of residual stress state in steel weldments by magnetic Barkhausen noise technique", NDT&E Int. vol. 43, iss. 1, pp. 29-33, 2010.

[Yook] J. G. Yook, Electromagnetic Modeling of High-Speed High-Frequency Interconnects, 1996.

[Yous] S. Youssef, K. Szielasko, A. Sourkov, B. Gupta, A. Youssef, Surface Inspection and Remanence Imaging with Magnetic Field Distortion Measurement, WCNDT 2016.

[Zeng] Z. Zeng, X. Liu, Y. Deng, L. Udpa, L. Xuan, W. C. L. Shih, G. L. Fitzpatrick, "A parametric study of magneto-optic imaging using finite-element analysis applied to aircraft rivet site inspection", IEEE Trans. Magn., vol. 42, no. 11, pp. 3737-3744, Nov. 2006.

[Zhan] B. Zhang, B. Gupta, B. Ducharne, G. Sebald, T. Uchimoto, "Preisach's model extended with dynamic fractional derivation contribution", IEEE Trans. on. Mag, vol. 54 iss. 3, 2017.

[Zhan2] B. Zhang, B. Gupta, B. Ducharne, G. Sebald, T. Uchimoto, "Dynamic magnetic scalar hysteresis lump model, based on JilesAtherton quasi-static hysteresis model extended with dynamic fractional derivative contribution", IEEE Trans. on. Mag, iss. 99, pp. 1-5, 2018.

CHAPTER 2

MATERIAL OF INTEREST AND MICROSTRUCTURE ANALYSIS

In this chapter, the material characterization based on microstructure is studied and investigated. A lot of literature is available on the creep analysis on different kinds of steel [Spos, Garo, Lupi, Kass, Shib] but all studies have been entirely on the low alloy based steel. There is not much evaluation been done till date on high alloy steel and hence, this study focuses on the evaluation of high alloy steel non-destructively. The research is motivated from the industrial requirement from a thermal power plant to study high chromium steel that has undergone creep. It is very important to detect creep in its primary stage since; the crack grows very rapidly as the rupture is near [Praj]. Hence, it is very beneficial to predict the microstructural changes which may lead to creep evolution, from the magnetic signatures at different test times.

2.1. Sample description

The sample used in this study is high chromium steel '12% Cr-Mo- W-V Steel' which is a representative martensitic stainless steel. This type of steels is used as a high-temperature material particularly for gas turbines, steam turbines and boilers. As illustrated in Table 2.1, the general composition of this particular alloy is provided in [Muto]. Although, the percentage of the elements present in the steels studied in this work might slightly differ to that of the percentages mentioned in Table 2.1, the magnetic properties of the material will not be effected significantly.

The 12 Cr-Mo-W-V high-chromium creep steel samples investigated in this work find their application in the thermal power plants. Fig. 2.1 below can be referred to for the raw sample's schematic diagram). As illustrated in the figure, the sample in its initial state is in the form of a rod. After the creep test, the grip part at the edges is cut. Post to this treatment, the surface of the sample is then machined as shown in the left-hand side of Fig 2.1. The ultimate polishing powder is used at #8,000.

Table 2.1: General composition for 12% Cr-Mo-W-V Steel [Muto1992]

Material	C	Si	Mn	P	S	Ni	Cr	Mo	V	W	Co	Sn	Al	Ti
12 Cr-Mo-W-V Steel	0.23	0.9	0.70	0.021	0.001	0.67	11.21	0.93	0.23	0.95	0.02	0.01	0.01	0.01

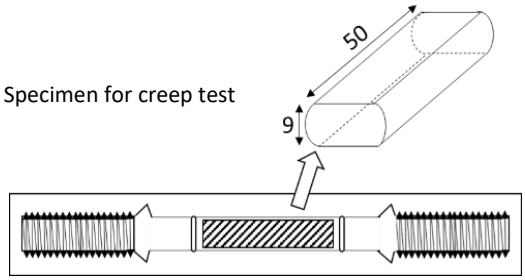

Figure 2.1. Samples with the sensor probe used.

Table 2.2 below displays the set of samples, investigated in this study. These samples are classified into three different categories based on their treatment. Sample 0 is a damage free (i.e., virgin) sample that has not undergone any treatment. The first category of the samples is based on their temperature treatment of 550°C and exposure of 343 MPa stress level (hereafter referred to as Sample 1,2 &3). Each of these three samples within this category has different testing times. Sample 3 however, which has the testing time of 2205.7 hours, is a ruptured sample. Sample 4, 5 & 6 have a temperature treatment of 600°C with an exposure to stress level of 201 MPa. In this category, sample 6 is the ruptured one. The last category of samples (Sample 7,8 & 9) have a temperature treatment of 650°C and an exposure to stress level of 98 MPa. In this category, sample 9 is the ruptured one.

Table 2.2. High-chromium steel samples subjected to different treatments.

Sample number	Stress [MPa]	Temp [°C]	Test time [h]	Rupture level Ruptured:1
0	—	—	—	—
1	343	550	281.8	0.13
2	343	550	785.6	0.36
3	343	550	2205.7	**1.00**
4	201	600	255.6	0.15
5	201	600	763.9	0.44
6	201	600	1725.9	**1.00**
7	98	650	256.3	0.15
8	98	650	789.6	0.46
9	98	650	1736.8	**1.00**

2.2. Microstructural Analysis

In this study to analyze the microstructure of the samples mentioned in Table 2.2, microstructure imaging techniques like SEM (Scanning Electron Microscopy) and EBSD (Electron backscatter diffraction) have been used. In order to implement these techniques on the samples, the surface of the materials has to be very carefully prepared. In this research work, Ar ion-milling method has been used to prepare the samples. During this process, the Ar ions are accelerated and then focused to form a beam which collides with the sample's surface (the sample is placed in a vacuum) as illustrated in Fig. 2.2 below. These ion beams are then directed towards the sample which are used in abrading the sample via atomic-sputtering. This procedure can help in removing strain hardening that is associated with the preliminary steps of mechanical preparation. Furthermore, it helps in exposing the precipitates by using different sputtering rates in each material. The bright-contrast regions in the Secondary-Electron mode correspond to the precipitates that remain on the surface of the sample as also demonstrated in Figures 2.3-2.12. These figures show the number of grains in bright-contrast per unit area (/mm^2). For more details about the procedures to perform microstructural analysis [Trea, Wood] could be referred.

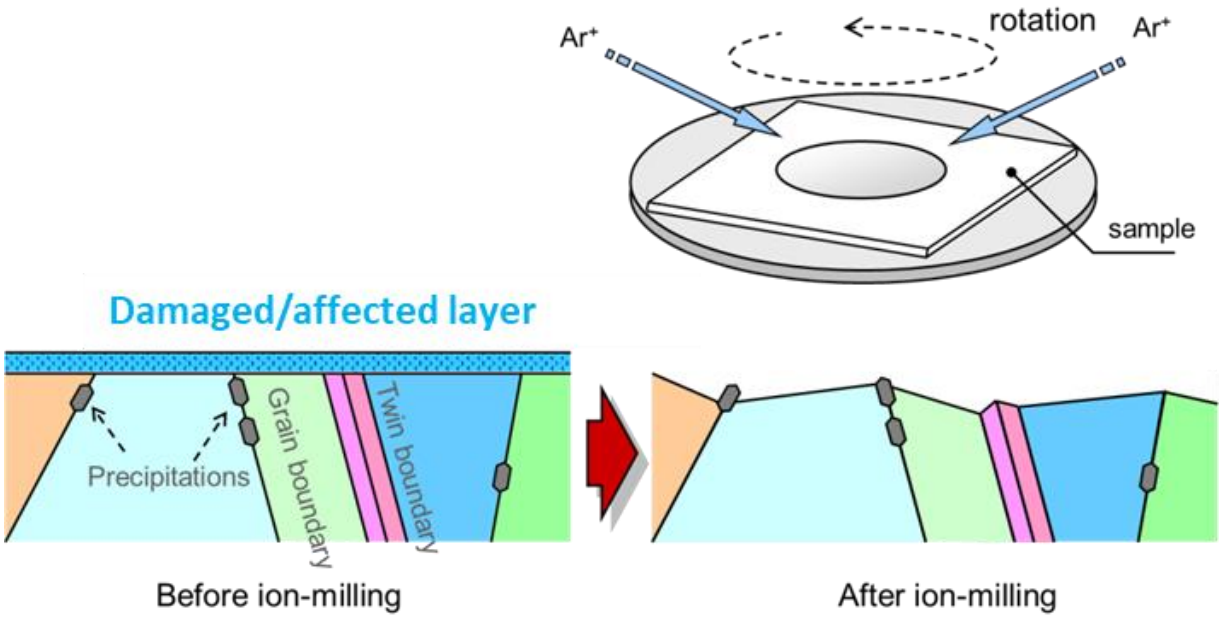

Figure 2.2. Schematic showing sample preparation for SEM and EBSD.

Kernel Average Misorientation (KAM) data are obtained by using the imaging technique EBSD as mentioned in the previous section. The KAM can be defined as the average misorientation angle of a give point with respect to all its neighbors [Mous]. On plastic deformation, the crystalline lattice of the material tries to rearrange itself in order to compensate for the changes in the geometry of the material. Consequently, as a result of the rearrangements of the crystal lattice, leads to the introduction of line defects which are also referred to as dislocations in the material structure [Mous].

Effects due to creep are dependent on both time and temperature. There exists a number of statistical parameters which take into consideration rupture time as well as the temperature effects. One of such parameters is the Larson-Miller Parameter (LMP) that enables comparisons between materials with different treatments. The LMP can be determined as follows [Lars].

$$LMP = T(C + \log t), \qquad (2.1)$$

Where, C, t, and T are a material specific constant, often approximated as 20, the time (h), and the temperature (K), respectively.
Table 2.3 below shows the LMP values calculated using Eq. (2.1) and the values of different test times (t) and the temperature (T) listed in Table 2.2.

Table 2.3. LMP values of different samples based on the formula given in Eq. (2.1).

Sample Number	Larson Miller Parameter (LMP)
0	–
1	18479
2	18446
3	19215
4	19565
5	19980
6	20289
7	20686
8	21137
9	21453

2.2.1. Scanning Electron Microscopic and Kernel Average Misorientation Analysis of each sample

In this section the SEM and EBSD images are shown and the corresponding data is given. These images are derived by the procedure explained in the section 2.2. To summarize the evaluation, three categories of samples are investigated. In the lower temperature samples, as the rupture increases, the number of the precipitates increase although the size of these precipitates is smaller. However, in case of the higher temperature treated samples, the number of precipitates decrease as the rupture increase but the size of the precipitates increase. As far as the misorientation is concerned, the degree of the misorientation decrease in all the samples as the rupture level increases. This implies that the number of dislocations in the sample reduce as the rupture increase. This is probably due to the fact that the when the rupture increases, although the sample is subject to damage, there is a degree of freedom that is added to the material structure which helps the crystalline structure to reorient itself thereby leading to less dislocations. However, the rate of decrease in the misorientation is much higher in case of higher treated samples.

Figures 2.3 – 2.12 show the microstructural images for all the samples studied in this work. Each sub-figure in the following figures has 3 SEM images with different magnification factor (x2000, x5000 and x10000). In addition to the SEM images, EBSD image for every sample is also demonstrated. For the lower temperature treated samples, there are higher number of red points observed in the image that correspond to the maximum degree of misorientation which 5° in this case. However, for the higher temperature samples blue color is significantly present highlighting the minimum degree of misorientation.

Table 2.4. Microstructural data for Sample 0

Microstructural Property	Value
Hardness(HV)	322
Grain Size (μm^2)	29.75
Average of KAM [degrees]	1.2942
Number of Precipitates($/mm^2$)	20
Level of Rupture (t_r)	0
Creep Life Fraction (t/t_r)	N/A

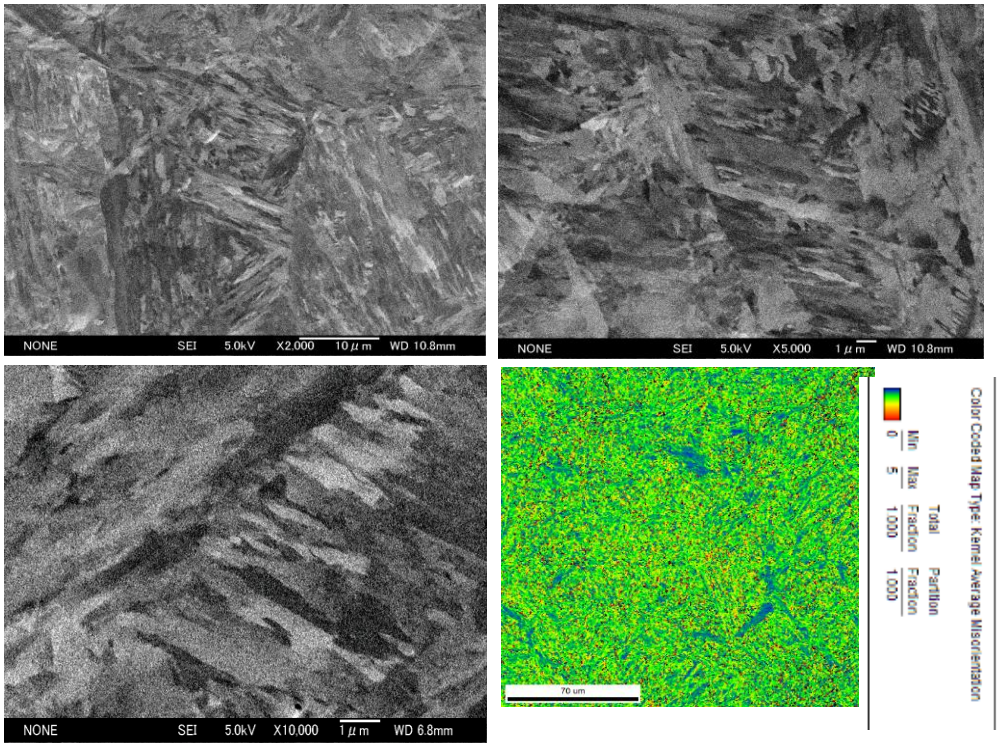

Figure 2.3. SEM Images for Virgin sample and corresponding EBSD Image (bottom right)

Table 2.5. Microstructural data for Sample 1

Microstructural Property	Value
Hardness(HV)	315
Grain Size (μm^2)	37.93
Average of KAM [degrees]	1.2965
Number of Precipitates(/mm^2)	1307546
Level of Rupture (t_r)	281.8 hours
Creep Life Fraction (t/t_r)	0.13
Temperature (°C)	550
Stress (MPa)	343

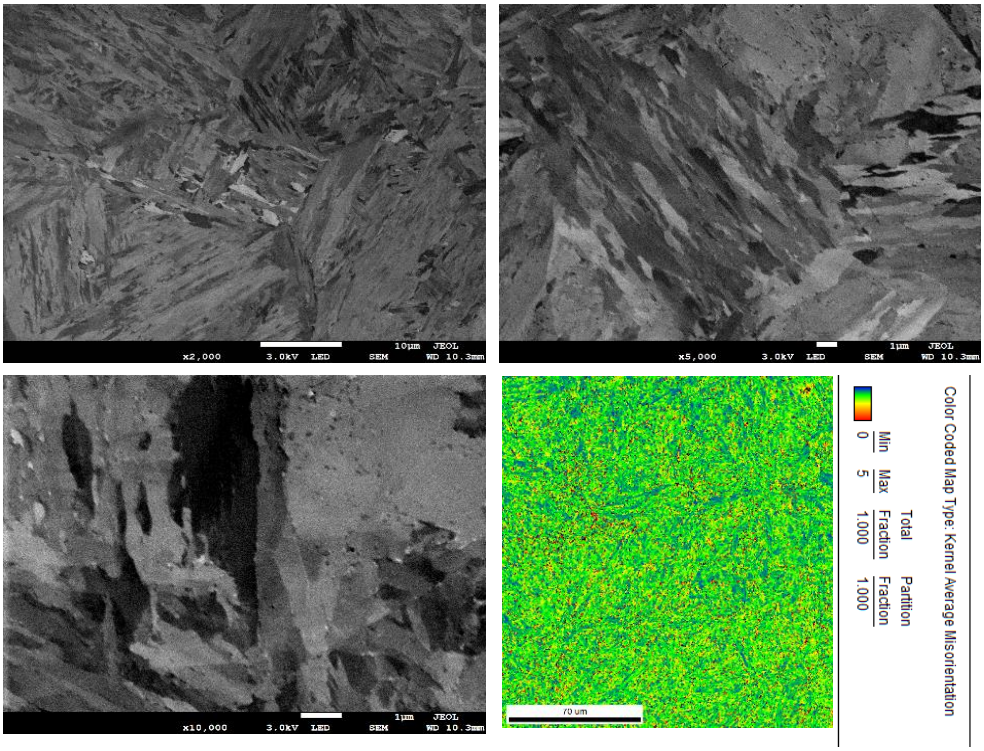

Figure 2.4. SEM Images for Sample 1 and corresponding EBSD Image (bottom right)

Table 2.6. Microstructural data for Sample 2

Microstructural Property	Value
Hardness(HV)	310
Grain Size (μm^2)	31.4
Average of KAM [degrees]	1.1962
Number of Precipitates($/mm^2$)	1491833
Level of Rupture (t_r)	785.6 hours
Creep Life Fraction (t/t_r)	0.36
Temperature (°C)	550
Stress (MPa)	343

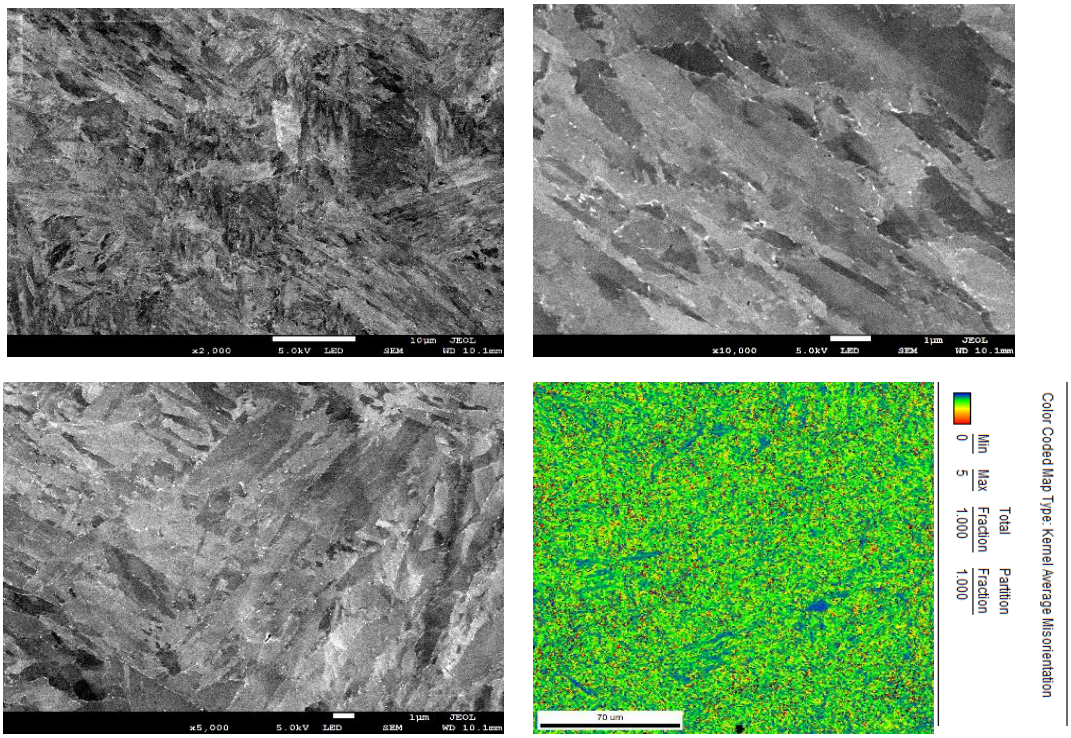

Figure 2.5. SEM Images for Sample 2 and corresponding EBSD Image (bottom right)

Table 2.7. Microstructural data for Sample 3

Microstructural Property	Value
Hardness(HV)	294
Grain Size (μm^2)	31.4
Average of KAM [degrees]	1.1973
Number of Precipitates($/mm^2$)	1949725
Level of Rupture (t_r)	2205.7 hours
Creep Life Fraction (t/t_r)	1 (Ruptured)
Temperature (°C)	550
Stress (MPa)	343

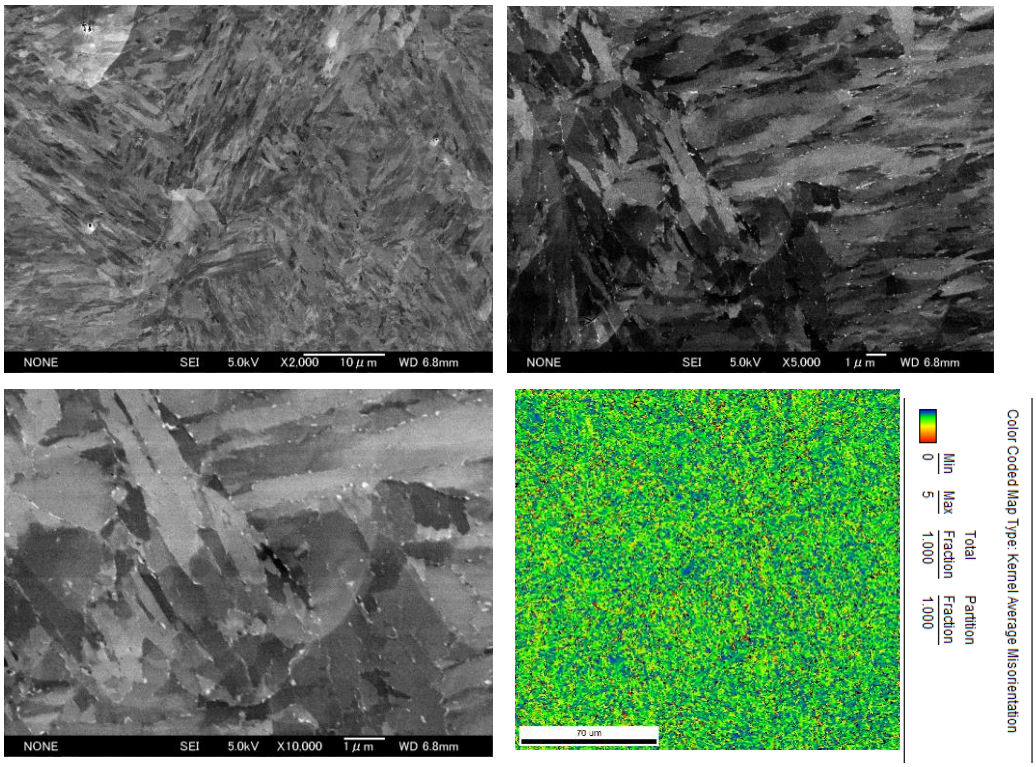

Figure 2.6. SEM Images for Sample 3 and corresponding EBSD Image (bottom right)

Table 2.8. Microstructural data for Sample 4

Microstructural Property	Value
Hardness(HV)	312
Grain Size (μm^2)	42.87
Average of KAM [degrees]	1.1553
Number of Precipitates(/mm^2)	717590
Level of Rupture (t_r)	255.6 hours
Creep Life Fraction (t/t_r)	0.15
Temperature (°C)	600
Stress (MPa)	201

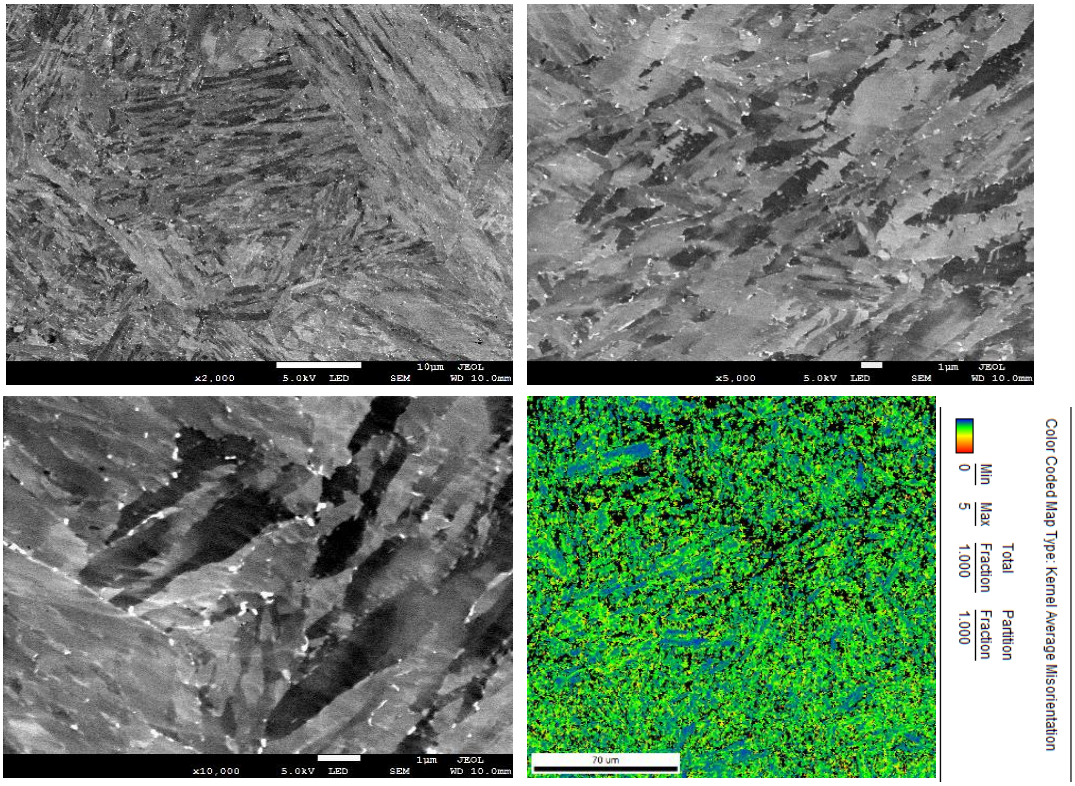

Figure 2.7. SEM Images for Sample 4 and corresponding EBSD Image (bottom right)

Table 2.9. Microstructural data for Sample 5

Microstructural Property	Value
Hardness(HV)	304
Grain Size (μm^2)	30.77
Average of KAM [degrees]	1.0929
Number of Precipitates($/mm^2$)	774242
Level of Rupture (t_r)	763.9 hours
Creep Life Fraction (t/t_r)	0.44
Temperature (°C)	600
Stress (MPa)	201

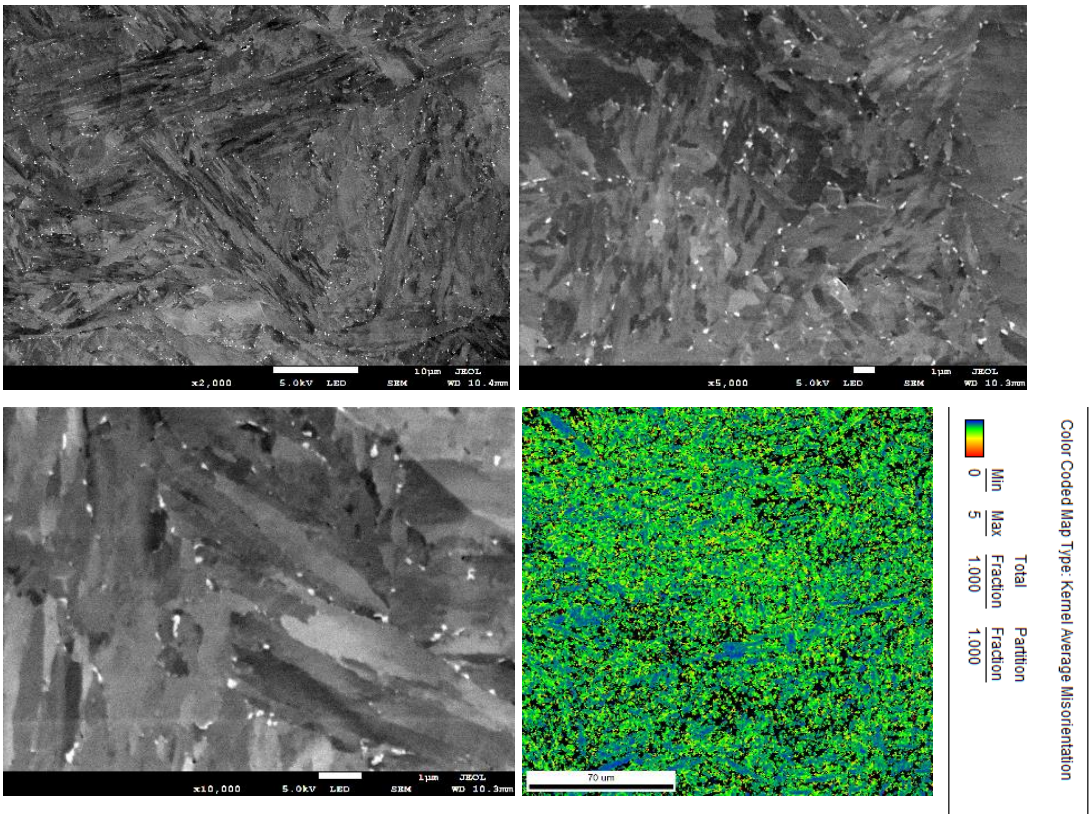

Figure 2.8. SEM Images for Sample 5 and corresponding EBSD Image (bottom right)

Table 2.10. Microstructural data for Sample 6

Microstructural Property	Value
Hardness(HV)	252
Grain Size (μm^2)	32.82
Average of KAM [degrees]	1.0727
Number of Precipitates($/mm^2$)	665245
Level of Rupture (t_r)	1725.9 hours
Creep Life Fraction (t/t_r)	1 (Ruptured)
Temperature (°C)	600
Stress (MPa)	201

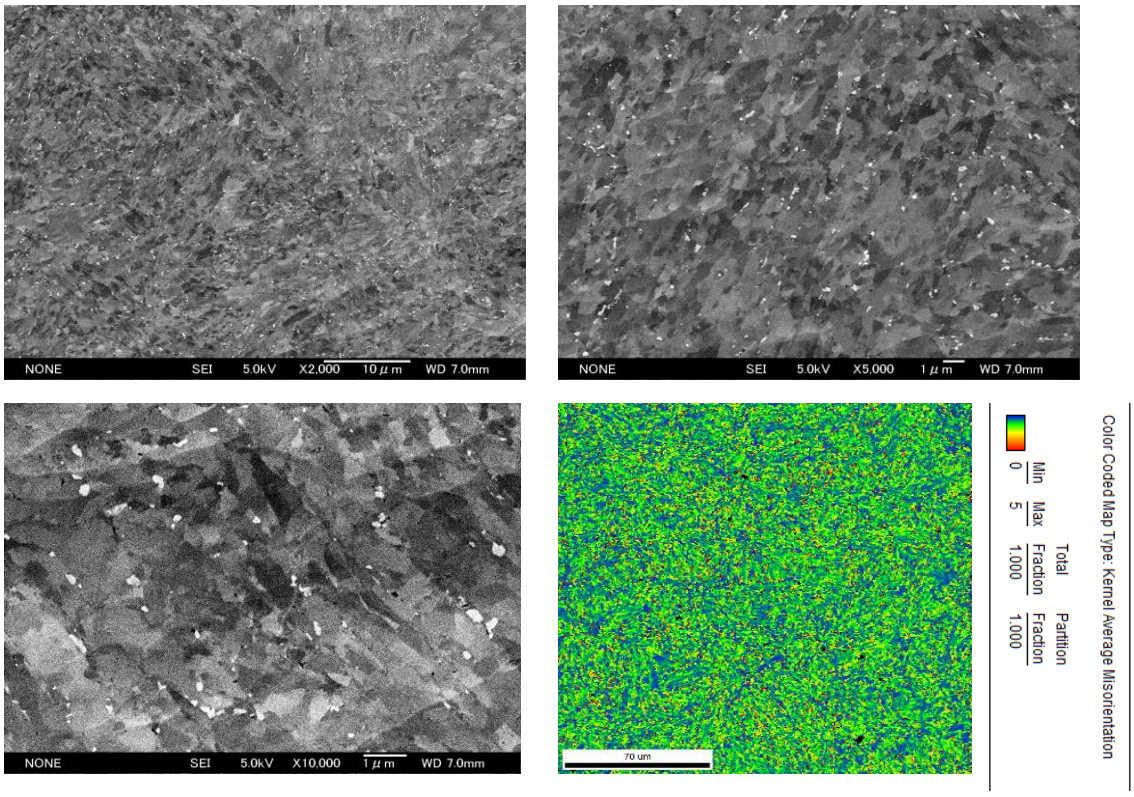

Figure 2.9. SEM Images for Sample 6 and corresponding EBSD Image (bottom right)

Table 2.11. Microstructural data for Sample 7

Microstructural Property	Value
Hardness(HV)	285
Grain Size (μm^2)	31.08
Average of KAM [degrees]	1.1302
Number of Precipitates($/mm^2$)	126607
Level of Rupture (t_r)	256.3 hours
Creep Life Fraction (t/t_r)	0.15
Temperature (°C)	650
Stress (MPa)	98

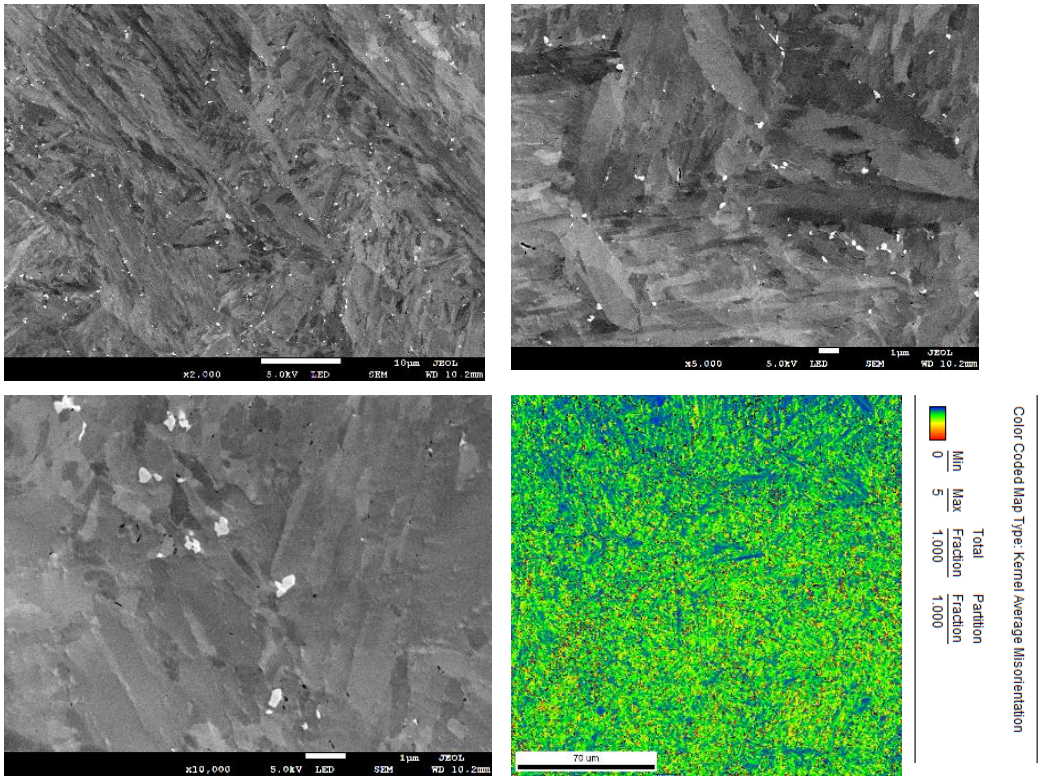

Figure 2.10. SEM Images for Sample 7 and corresponding EBSD Image (bottom right)

Table 2.12. Microstructural data for Sample 8

Microstructural Property	Value
Hardness(HV)	250
Grain Size (μm^2)	34.93
Average of KAM [degrees]	1.0015
Number of Precipitates($/mm^2$)	87723
Level of Rupture (t_r)	789.6 hours
Creep Life Fraction (t/t_r)	0.46
Temperature (°C)	650
Stress (MPa)	98

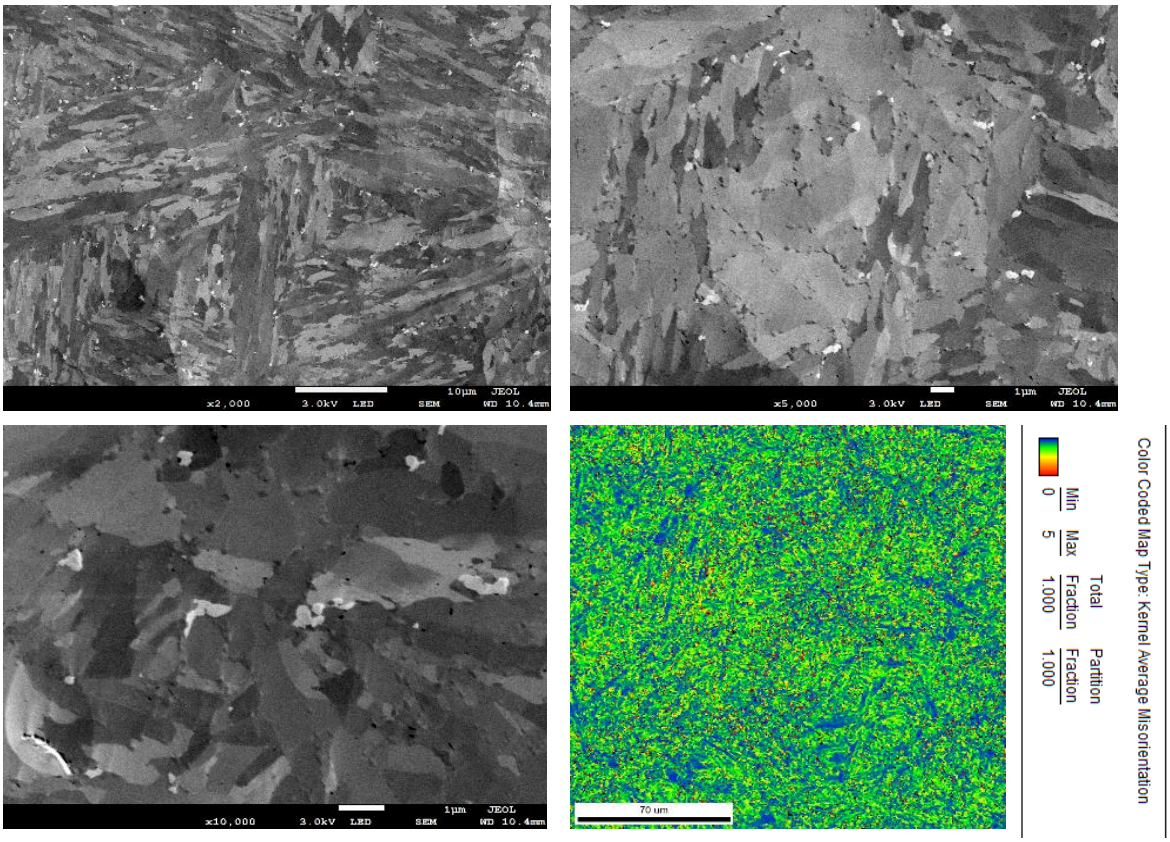

Figure 2.11. SEM Images for Sample 8 and corresponding EBSD Image (bottom right)

Table 2.13. Microstructural data for Sample 9

Microstructural Property	Value
Hardness(HV)	215
Grain Size (μm^2)	49.44
Average of KAM [degrees]	0.7425
Number of Precipitates($/mm^2$)	94407
Level of Rupture (t_r)	1736.8 hours
Creep Life Fraction (t/t_r)	1 (Ruptured)
Temperature (°C)	650
Stress (MPa)	98

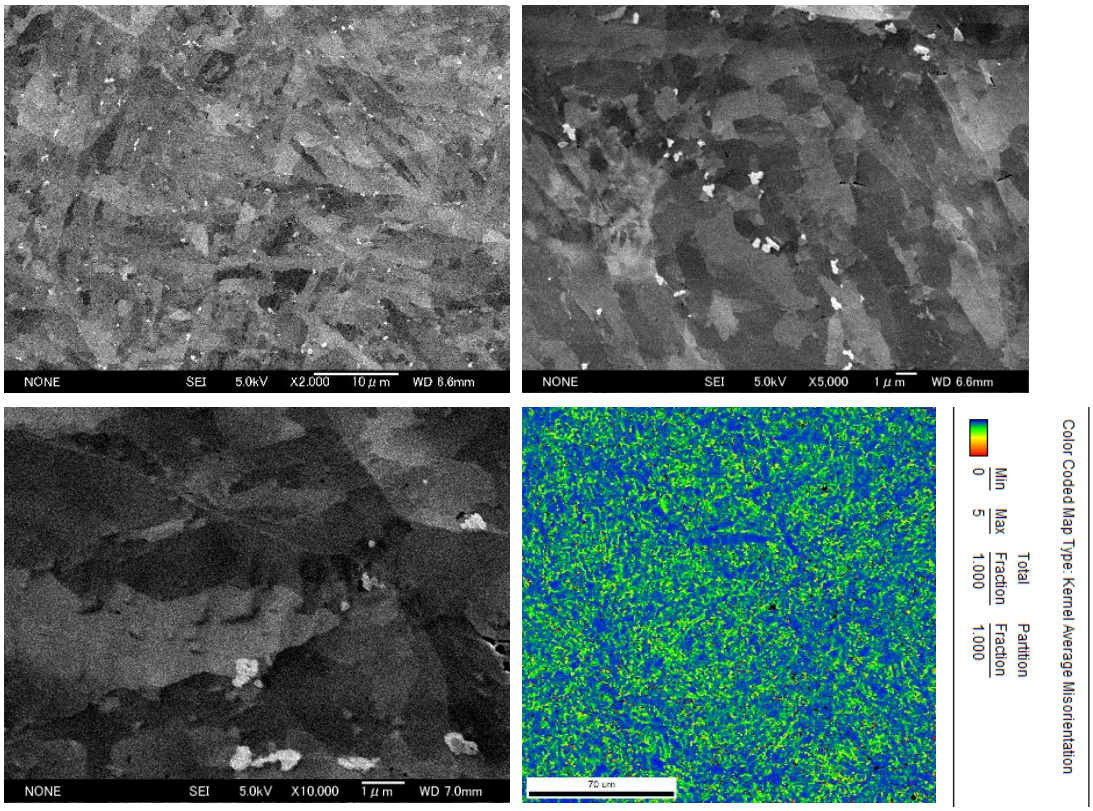

Figure 2.12. SEM Images for Sample 9 and corresponding EBSD Image (bottom right)

2.2.2. Data Analysis

As shown in Fig. 2.13 below, the effect on precipitations due to different stress and temperature conditions is evidently revealed. The precipitates in the images of the samples correspond to the carbide content in the materials. There are higher number of precipitates present in the lower temperature treated samples and the number of precipitates increase in this category of temperature as the rupture level increases. Additionally, in this category the size of the precipitates is much smaller than that of 650°C treated samples, however, there is also a decrease in the number of precipitates in 650°C treated samples. By looking at the images, it is also evident that the phenomena of recrystallization start to appear at higher temperature treated samples and the size of the crystal increase with the increasing temperature. For instance, in the virgin sample (Fig. 2.13 (a)), there is no crystallization observed unlike in the case of 650°C treated samples (Fig. 2.13(d)). The crystal size in the highest temperature treated samples is also bigger than that of 600°C treated samples. The relation between the evolution of number of precipitates and the LMP value is illustrated in Fig. 2.14.

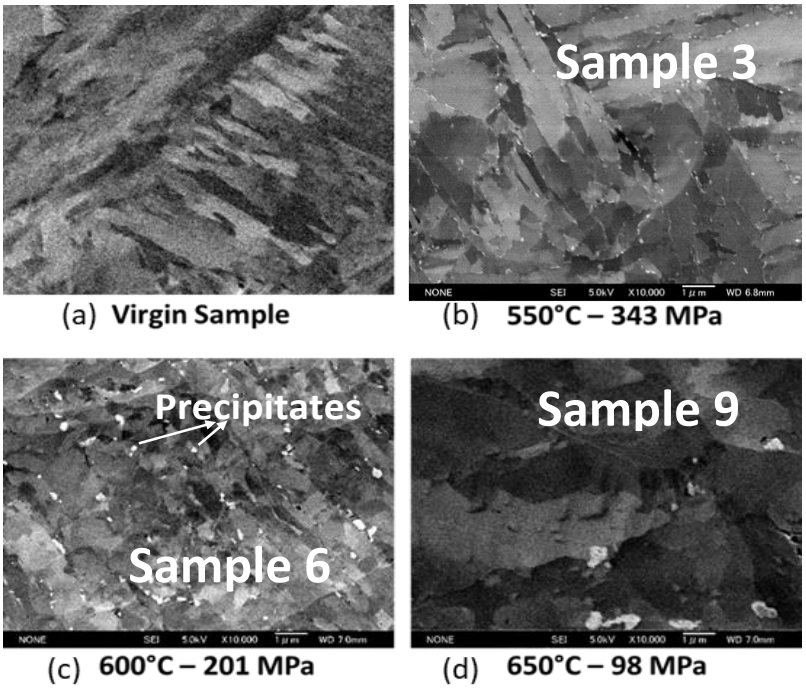

Figure 2.13. SEM images showing recrystallization of the samples and an increase in the crystal size with increasing temperature. The number and size of precipitates are also observable from these images. The precipitation number is given in per unit area(/mm2).

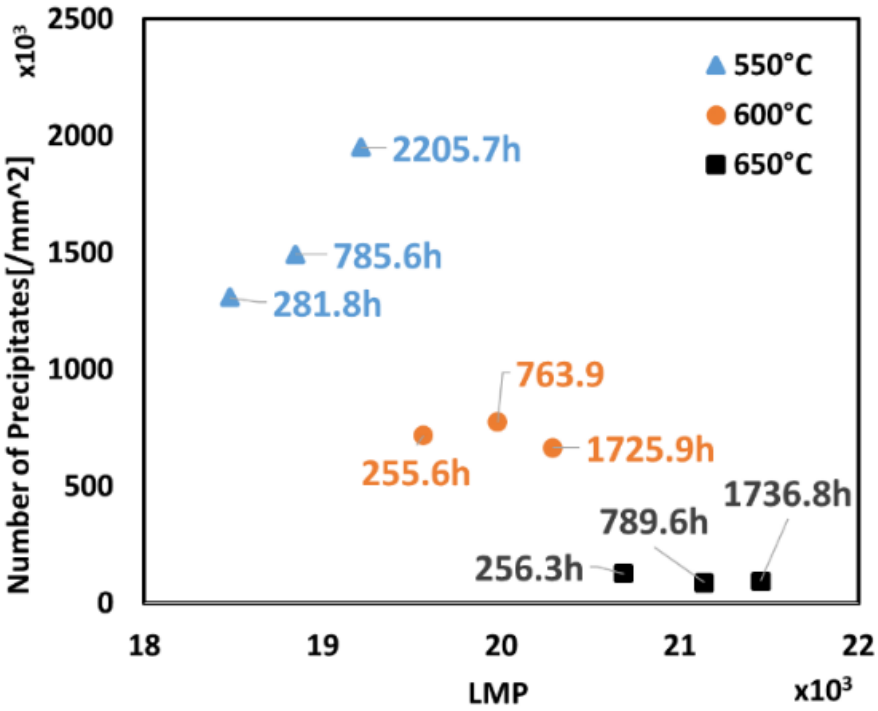

Figure 2.14. Evaluation of different samples based on the precipitation number versus the Larson Miller Parameter. The number of precipitates decreases with increasing temperature, whereas the size increases, as indicated by the SEM images.

Fig. 2.15 illustrates the effect of different temperatures on the above mentioned set of samples. Kernel Average Misorientation (KAM) of the ruptured samples along with that of the virgin sample is demonstrated in Fig. 2.16. The value of the KAM is calculated from the arithmetic mean that is associated with its log normal distribution. The KAM images show the distribution of dislocations in the samples when exposed to different testing conditions. For instance, using the color code shown in the Fig. 2.16, it is observed that the number of dislocations in the lower temperature treated samples is higher than that of higher temperature treated samples.

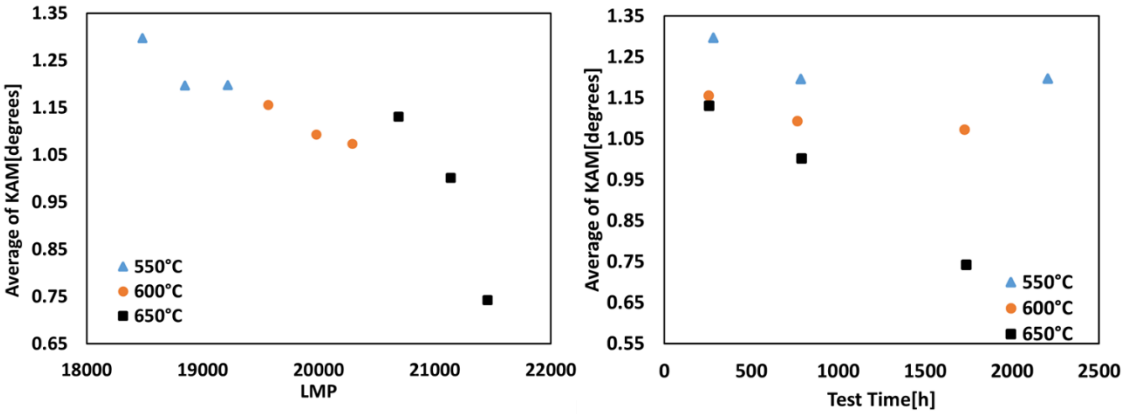

(a) Average of KAM vs. LMP showing larger variations in higher temperature samples

(b) Average of KAM vs. Test Time showing a sharp decrease in misorientation for higher temperature samples as the rupture approaches

Figure 2.15. Evaluation based on KAM against LMP and test time of the materials.

This effect corresponds to recrystallization phenomena. It is seen that there are larger variations in misorientation in higher temperature treated samples. The color bar shown in the right-hand side of Fig. 2.16 shows the extent of misorientation in the structure (blue: minimum misorientation, red: maximum (5°) misorientation). For example, consider Fig. 2.16(a) and (d).

Microstructural analysis during real-time NDT is very difficult, and the magnetic inspection techniques are quite sensitive to stress and temperature. Therefore, in upcoming chapters, a relation between the magnetic parameters derived from multiple techniques (Magnetic Incremental Permeability, B(H), Magnetic Barkhausen Noise) and the precipitations is established, with the aim of determining the effect of microstructure.

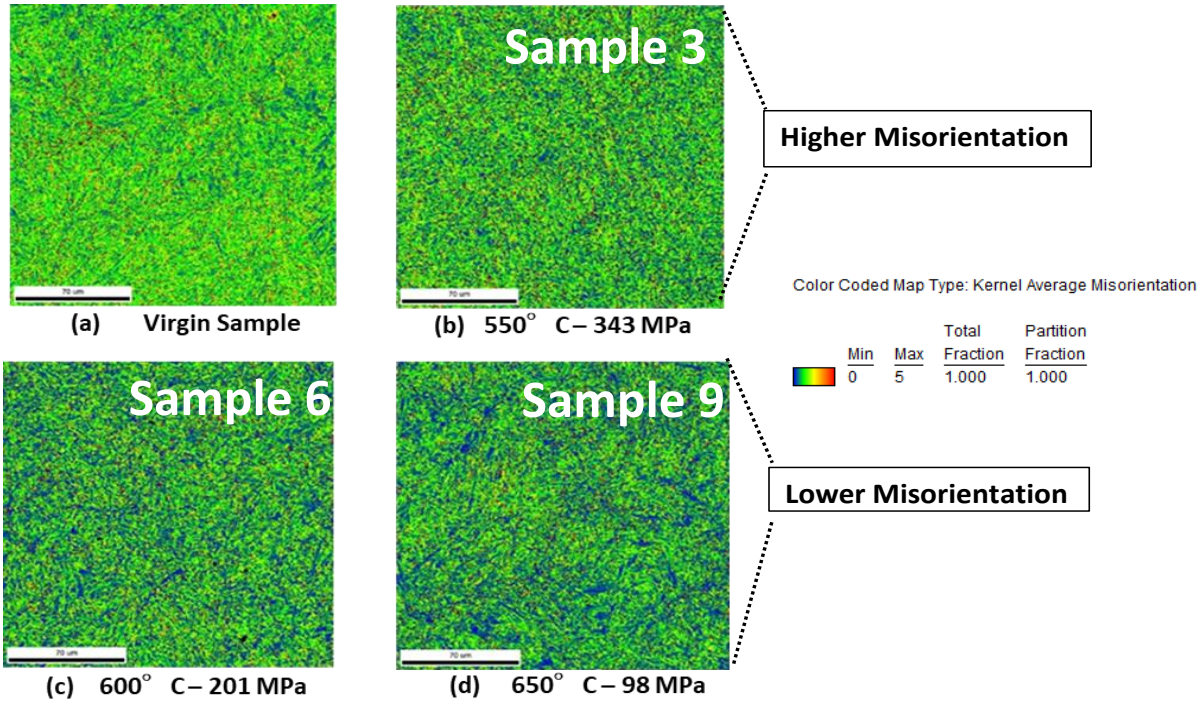

Figure 2.16. Kernel Average Misorientation (KAM) images (the size of the crystals increases with increasing temperature).

2.2.2.1. Analysis based on Hardness

Fig. 2.17 shows the hardness values plotted as a function of the Larson Miller Parameter (LMP), and the creep life fraction. The hardness is calculated from Vickers test [Moor] results. In Fig. 2.17, Hardness is evaluated against the LMP parameter in which it is quite evident that the Hardness of the samples decreases with the increase in the

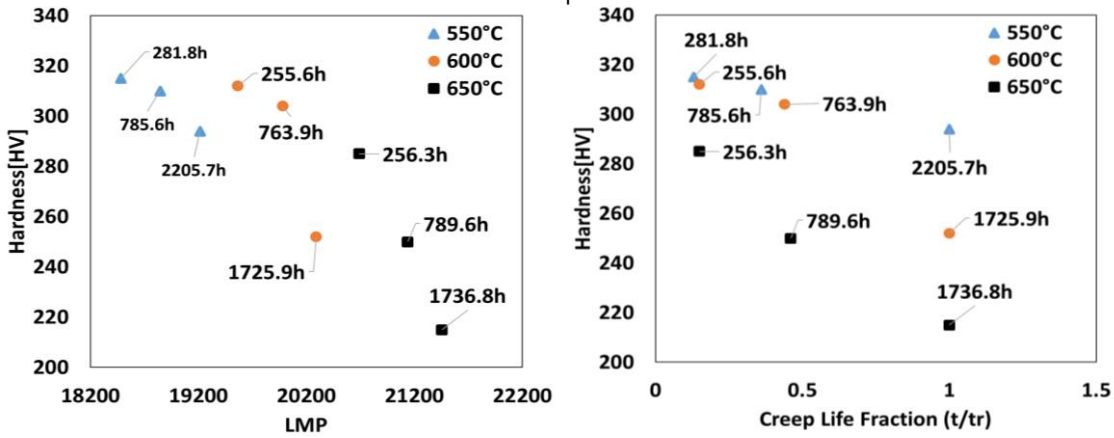

(a) Hardness vs. LMP demonstrating a decrease with the increase in temperature and Rupture time

(b) Hardness vs. Creep Life Fraction demonstrating a sharper decrease of hardness in higher temperature samples

Figure 2.17. Evaluation based on hardness

rupture level of the samples in all the three categories. However, for 650°C samples, the decrease is sharp in comparison to the 550°C samples. The similar trend can be seen in the second graph in Fig. 2.17 where hardness is evaluated against creep life fraction in which it can also be noticed that the rate of change of hardness is higher in higher temperature samples. The reason behind this is that the misorientation (related to KAM which can also be seen in Fig. 2.18) in the crystal structure of the materials decreases as the rupture increases. The results shown in the graph suggest that the hardness of the material is inadequate for investigating creep at different temperatures. Fig. 2.18 shows that Hardness might be an inadequate criterion to analyze precipitates in the samples. However, it is worth noticing that that the decreasing direction between 550°C and 650°C samples is opposite. This is due to the fact that for the former category the number of precipitates are dominant and for the latter, the size of the precipitates is dominant since, the precipitation number decreases as the temperature increases. It is also interesting to note that the variation in Hardness for 650°C samples is much higher when dislocations/misorientation are studied in relation to Average of KAM.

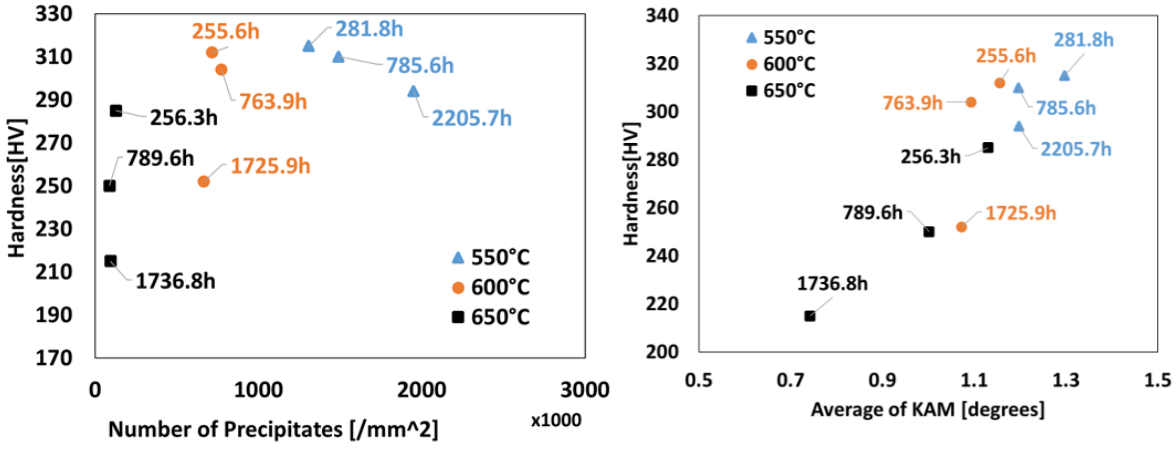

(a) Hardness vs. Number of Precipitates

(b) Hardness vs. Average of KAM

Figure 2.18. Evaluation based on microstructural data

2.2.2.2. Analysis based on Grain Size

During the microstructure analysis, the grain size for the samples was also investigated. Fig. 2.19 shows the evolution of grain size plotted against LMP. As the rupture level increases, the grain size decreases in case of 550°C samples whereas in case of 650°C the grain size increases with the increase in the rupture level. The similar trend can be seen in terms of creep life fraction (Fig 2.19) where the evolution of Grain size is in opposite direction between 550°C and 650°C samples.

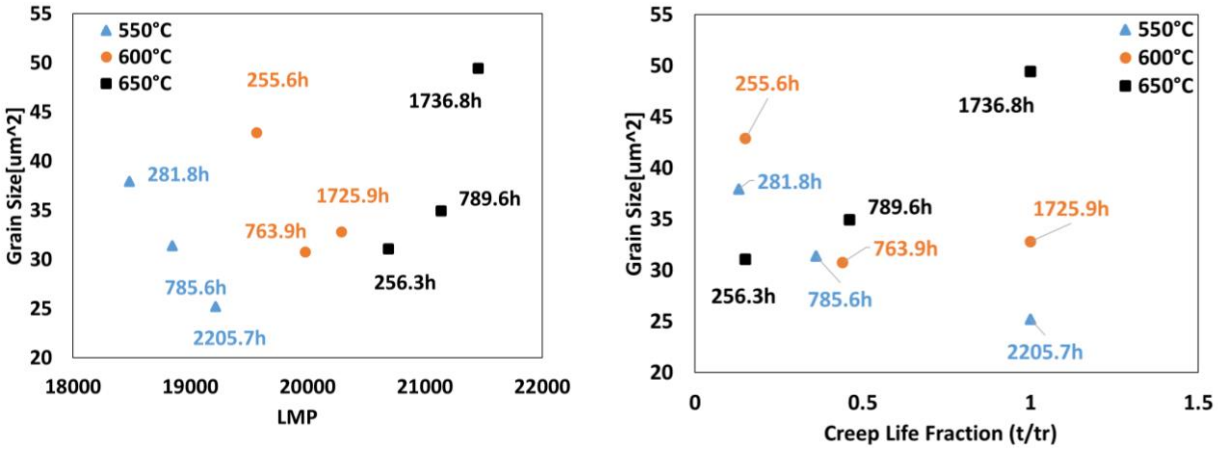

(a) Grain size vs. LMP demonstrating opposite evolution in case of higher and lower temperature samples

(b) Grain size vs. Creep Life Fraction demonstrating an increase in the grain size as the rupture level increases for higher temperature samples unlike lower temp. samples

Figure 2.19. Evaluation based on Grain Size

When it comes to the microstructure properties grain size is evaluated against the precipitation number analyzed. It can be seen in Fig 2.20 that the grain size is decreasing as the rupture level of the samples increases in case of 550°C samples along with the increase in the number of precipitates. However, in case of 650°C samples, the grain size increases with the increase in the rupture level at the same time with a decrease in the precipitation number. This is again due to the fact that for the 550°C samples, the number of precipitates are a dominant factor whereas for the 650°C samples, the size of the precipitates become significant.

Fig. 2.20 shows the comparison of grain size against the Average of KAM analysis. The grain size for the 550°C samples decrease with the increase in the rupture level along with the decrease in the degree of misorientation. It is also described in the following chapters that for the 550°C samples as the rupture level increases, the magnetic behavior of the samples becomes harder. This is due to the smaller sizes of the grain which needs higher amount of magnetization to orient domains along the direction of the magnetization.

For the case of 650°C samples, it is noticed that the grain size increases tremendously with the increase in the rupture level, although the degree of misorientation decreases (as is the case for 550°C samples). Since, the grain size is higher for this category of samples, the materials behave soft magnetic as is demonstrated in the following chapters. It is worth noticing that the change in degree of misorientation are much higher in higher temperature treated samples(650°C) as compared to the lower temperature treated samples(550°C). This higher change in misorientation is also observed in one of modeling parameters derived, in the following chapters.

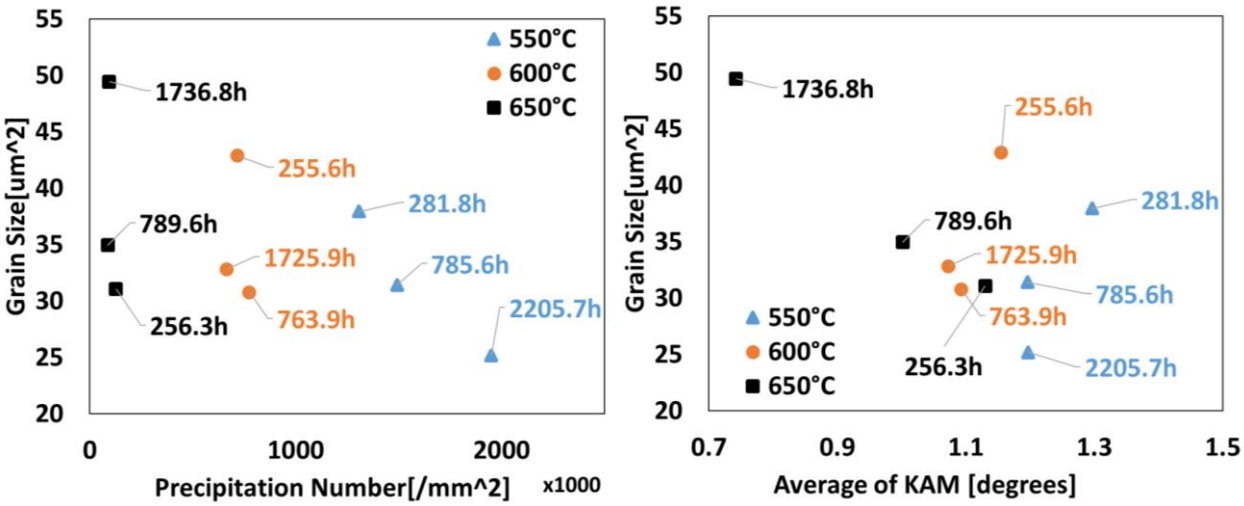

(a) Grain size vs. Precipitations demonstrating opposite evolution of precipitates for lower and higher temperature samples

(b) Grain size vs. Average of KAM demonstrating higher variations for higher temperature samples

Figure 2.20. Evaluation based on microstructural data

2.3. Summary

In this chapter, the microstructure analysis of the three categories of high chromium steel is investigated. Three different temperature effects are studied. Investigations reveal that the behavior of these samples is opposite in case of 550°C samples and 650°C samples. Properties like Hardness, Grain size are evaluated against the data derived from microstructural analysis (Precipitation number/Average of KAM) are studied. Further to this, the Microstructural properties are also studied in terms of the mechanical factors like Creep life fraction as well as Larson Miller Parameter (which combines the two mechanical factors like Stress and the thermal parameter Temperature). The results analyzed in this chapter show a large diversity in microstructural changes such as grain size, precipitates etc.) As a next step to understand and predict the microstructure of the materials, these data are evaluated in terms of experimental magnetic parameters (derived from Magnetic Inspection methods) which is very useful in field of Non-destructive testing. This will enable to predict the microstructure of the materials directly from the magnetic signatures without having done the microstructural analysis, where the samples have to be modified which is beyond the scope of Non-destructive testing.

References

[Garo] F. Garofalo, Fundamentals of creep and creep-rupture in metals. New York: Macmillan; 1965.

[Kass] M.E. Kassner, Fundamentals of creep in metals and alloys, 2nd ed. Amsterdam: Elsevier; 2009.

[Lars] F. R. Larson & J. Miller, *Transactions ASME*, Vol. 74, p. 765–771, 1952.

[Lupi] V. Lupinc, Bressers J, editor. Creep and fatigue in high temperature alloys. London: Applied Science Publishers; 1981. p. 7–40.

[Moor] P. Moore, Mechanical testing of welds, The Welding Engineers Guide to Fracture and Fatigue ,2015, Pages 113-141

[Mous] C. Moussa; About quantitative EBSD analysis of deformation and recovery substructures in pure Tantalum bout quantitative EBSD analysis of

deformation and recovery substructures in pure Tantalum. 36th Risø International Symposium on Materials Science. 2015.

[Muto] Y. Mutoh, Improving Fretting Fatigue Strength at Elevated Temperatures by Shot Peening in Steam Turbine Steel, Standardization of Fretting Fatigue Test Methods and Equipment, ASTM STP 1159, M. Helmi Attia and R.B. Waterhouse, Eds., American Society for Testing and Materials, Philadelphia, 1992, pp.119-209.

[Praj] S. Prajapati, Potential drop detection of creep damage in the vicinity of welds, NDT & E International, Volume 47, April 2012, Pages 56-65.

[Shib] A. Shibali, Creep and fracture in high temperature components: design and life assessment issues, in: Proceedings of 2nd ECCC creep conference. Lancaster, PA: DEStech Publications; 2009 pp. 402–413.

[Spos] G. Sposito, A review of non-destructive techniques for the detection of creep damage in power plant steels. NDT&E International. 2010.

[Trea] K.W.J. Treadaway, Studies of steel fracture by transmission and scanning electron microscopy, Building Research Station, Ministry of Public Building and Works, Garston, Watford, Herts, Journal of Microscopy, Vol. 89, Pt 2, April 1969, pp. 283-286

[Wood] S. Woodling, Influence of Surface Topography on the Effectiveness of Pulsed Light Treatment for the Inactivation of Listeria innocua on Stainless-steel Surfaces, Journal of Food Science 70(7), 2006.

CHAPTER 3

NONDESTRUCTIVE CHARACTERIZATION ON 12% Cr-Mo-W-V CREEP TEST SAMPLES: MAGNETIC INCREMENTAL PERMEABILITY AND HYSTERESIS ANALYSIS

The changes in the physical and mechanical properties of ferromagnetic materials are correlated to the magnetic properties of the materials as well. Such behavior can be observed using the electromagnetic inspection methods, such as eddy current testing (ECT) or advanced techniques based on ECT, such as Magnetic Incremental Permeability. In this chapter, an advanced Eddy current testing technique, Magnetic Incremental Permeability (MIP) is performed to evaluate the three categories of high chromium creep test steel samples which are treated with different creep test conditions, for instance, different temperatures and different levels of stress. From the previous chapter on Microstructure analysis, this microstructural information is then evaluated against the magnetic parameters that are derived from the standard MIP curves. Investigation in this approach helps to understand the microstructural changes in the samples corresponding to their creep level.

Every magnetic measurement can be used to extract some magnetic parameters which can further be co-related to the mechanical properties of the materials such as mechanical hardness, stress and strength etc. To perform this study there are already some commercially available non-destructive testing devices. 3MA-II (Micromagnetic Multiparameter Microstructure and Stress Analysis) has been developed at Fraunhofer Institute for Non-destructive testing and is currently used by many research institutes and industries on a large scale to ensure the quality of their production. The principle of 3MA-II is based on electromagnetic methods, thereby, deriving the testing statics during the magnetic hysteresis cycles, along with the electrical as well as magnetic parameters that are potentially influenced by the hardness, residual stress state as well as the microstructure of the materials under test.

In the Chapter 1, many different kind of testing techniques were introduced which are of prime interest in the field of non-destructive testing but are limited to only physical cracks. Particularly in this investigation, the type of defect that is considered is creep which is a major concern in the thermal and nuclear power industries. Whenever a material at high temperature is exposed to a mechanical load or stress, it leads to a deformation in the material state that is popularly known as creep. Creep is a resultant of several factors at the microscopic level such as recovery of crystalline stage, dislocations, an increase in the carbide precipitate density etc. which lead to the crack formation and consequently

to the material failure post to a certain threshold. Hence, creep poses a major challenge in the thermal and nuclear power industries for a smooth operation. Since, NDT lacks standards concerning the inspection methods to be incorporated, hence, sometimes this yields different results to different researchers making standardization of the conclusions difficult. What makes this investigation interesting is that three major advanced eddy current testing techniques have been applied to the same set of materials to reveal different measurements and information. The material that is creep degraded comes from a real time situation from the industry and this work is a high chromium material study (that is also rarely studied from the magnetic point of view).

In this chapter, one of the advanced eddy current testing techniques, Magnetic Incremental Permeability (MIP) is applied to the above mentioned materials. MIP has proven to be very sensitive to stress, different temperature treatments and to different levels of creep as demonstrated in this chapter. MIP has become highly popular among the researchers in the field of non-destructive testing in order to understand the degradation in the materials. It has been shown in this study, that MIP has provided considerable information correlated to the microstructure of the materials. Hence, it is a very beneficial and informative technique from the viewpoint of detection of creep.

In this chapter, dislocations, recovery of crystal stage and variations in the precipitations, in the high alloy steel (12% Cr-Mo-W-V steel, in this study) are investigated based on the AC magnetic properties of the steel. Following to this, the magnetic signatures based on MIP are then studied against different test times. In sections 3.1 and 3.2, the basics of MIP are detailed and optimization of the experimental set-ups is presented, respectively. The results are demonstrated in the section 3.4 where a correlation between the microstructural variations and the MIP signature curve is established. Additionally, Hysteresis measurements are also performed on these samples and it has been revealed that MIP provides more detailed information about the materials as compared to the Hysteresis measurements. Finally, the chapter is concluded in the section 3.9.

3.1. Magnetic Incremental Permeability (MIP)

The measure of a material's magnetic response to an applied external magnetic field is defined as the magnetic permeability of that material.

Although the shape of hysteresis curve B(H) may vary significantly depending on the material to materials but the magnetic flux density B and the magnetic field strength H are still correlated. On an exposure to a steady and static magnetic field to a ferromagnetic material, the reversible permeability measured with a small alternating magnetic field is defined as the MIP [Chen] (Fig. 3.1).

Mathematically, the MIP, μ_Δ , can be defined as [Mats]:

$$\mu_\Delta = \frac{1}{\mu_0}\frac{\Delta B}{\Delta H}, \tag{3.1}$$

Where, μ_0, ΔB, and ΔH are the permeability of air, incremental magnetic flux density, and incremental magnetic field, respectively.

By the measurement of the minor loop magnetic flux density during the process of magnetization, the respective magnetic incremental permeability (MIP) is calculated. Since, the microstructural features in a ferromagnetic material, for instance, the magnetic domains wall movements, are easily affected by any mechanical damage such as fatigue damage and plastic deformation, hence, the MIP method is considered as a very effective and potential non-destructive testing (NDT) technique for the evaluation of the residual stress, creep etc. [Chen].

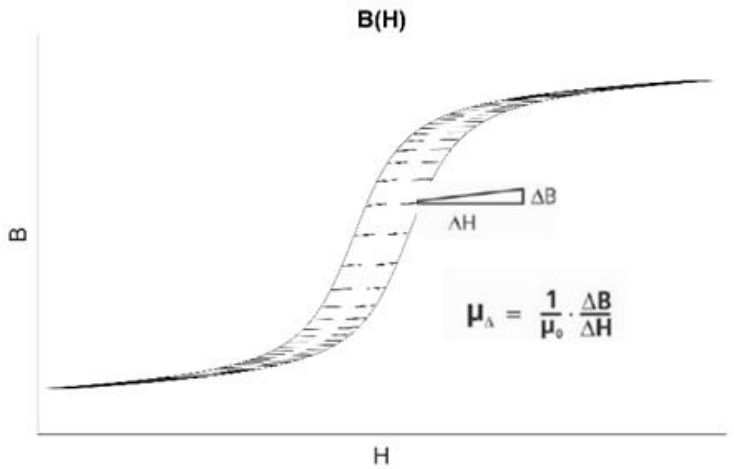

Figure 3.1. Magnetic Incremental Permeability depiction.

3.2. Experimental procedure

3.2.1. Using an Impedance Meter (LCR Meter)

For the optimization of the experimental set-up, two different experimental set-ups were investigated. Fig. 3.2 below shows the first approach in which the impedance of the coil is measured using an LCR meter (Impedance meter) for 12% Cr-Mo-W-V creep test samples. In this approach, the sample is applied with an external steady state magnetic field of 10kA/m (Sinusoidal, 0.1 Hz) using a U-shaped electromagnet. This tangential magnetic field along the direction of the sample is measured using a Hall effect sensor embedded inside the entire sensor set-up as shown in Fig. 3.3. Fig. 3.3 shows the pictorial description of the measuring set-up. The sensor is a transmitter-receiver type probe in which the transmitting coil (pancake coil) acts as an ECT coil to supply a high frequency 50kHz small alternating magnetic field. The pick-up coil (receiver coil) picks up the induced signal and feeds it to the LCR meter (model: ZM2375, NF Corporation) which measures the coil impedance. This coil impedance is recorded using the data acquisition system along with the Hall sensor output. When the coil impedance (which is proportional to the magnetic incremental permeability) is plotted against the steady state magnetic field applied (measured using Hall sensor), we get the typical butterfly loop (MIP signature curve, demonstrated in Fig. 3.6).

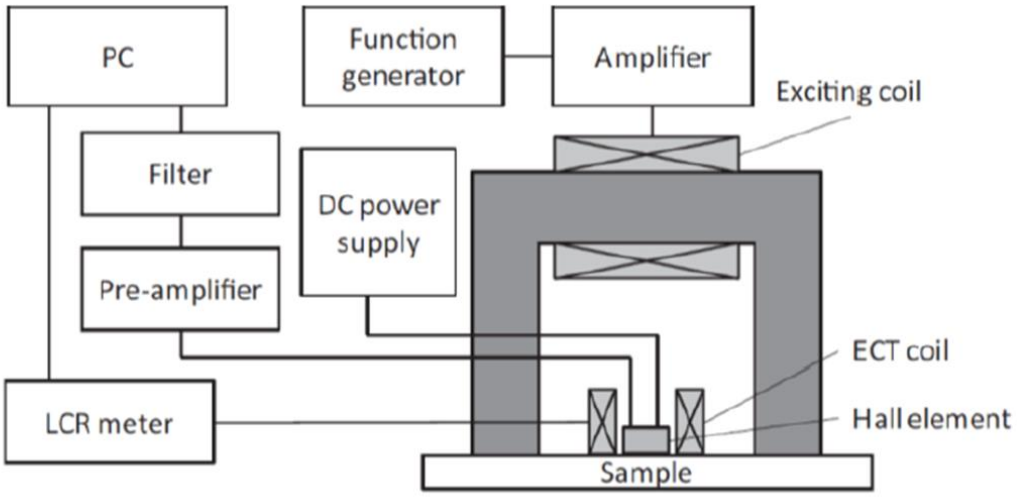

Figure 3.2. Schematic for measuring Incremental Permeability using LCR meter [IFS, Uchimoto Laboratory, internal document]

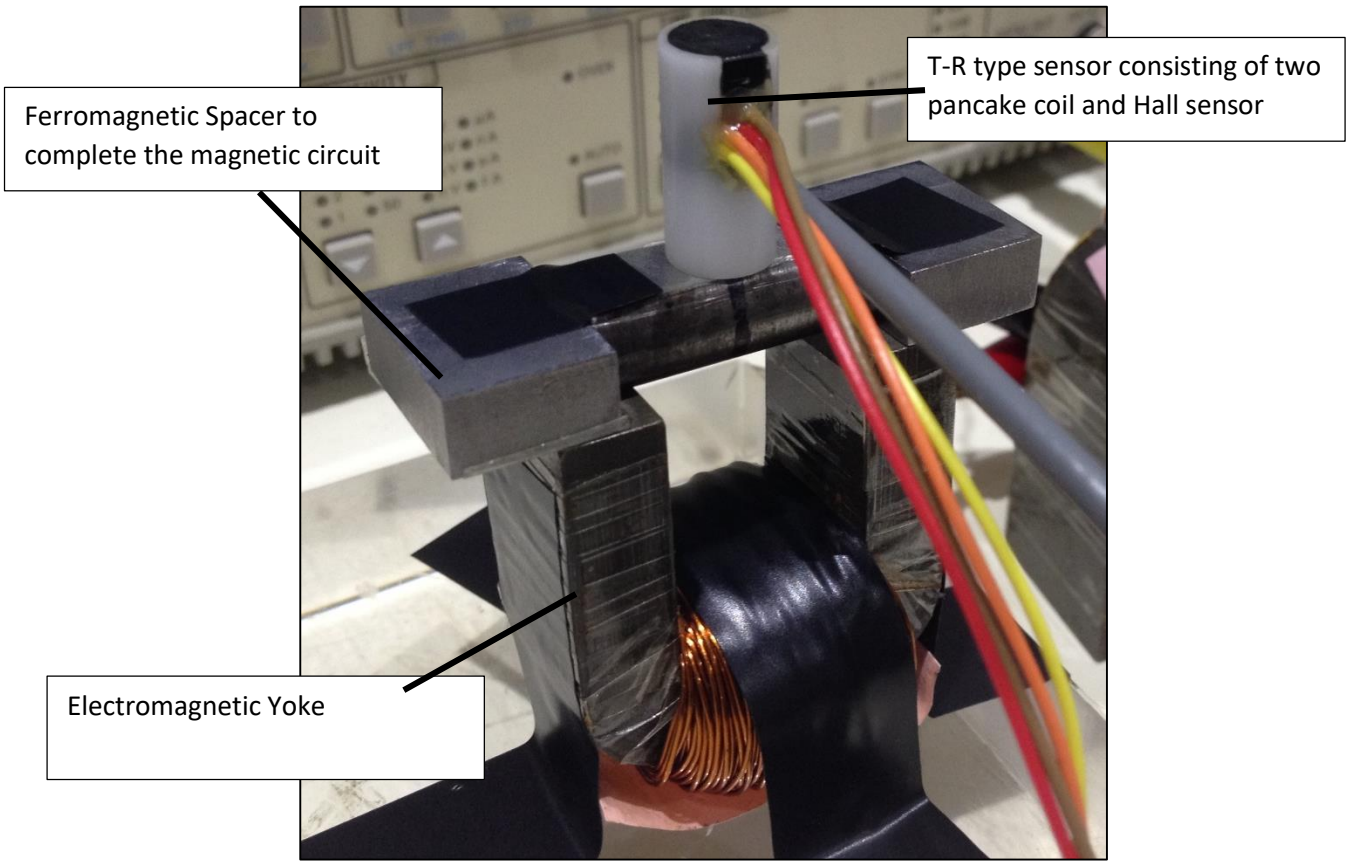

Figure 3.3. Measuring set -up (LCR meter)

3.2.2. Using a Lock-in Amplifier

Fig. 3.4. demonstrates the measuring set-up for measuring the Magnetic Incremental Permeability signals for the set of samples used in this study. A sinusoidal signal is used to magnetically excite the creep test samples with the help of a U-shaped electromagnet. As illustrated in the schematic of the sensor on the left-hand side of Fig. 3.5., a Hall sensor is included to measure the tangential component of the magnetic field strength *H*. As the sensor is transmitter-receiver type sensor, the upper coil is used as the transmitter coil to supply the high frequency AC component and the lower coil is used as the receiver coil to pick up the induced voltage. The AC component supplied by the transmitter coil is of low alternating magnetic field ΔH, which superimposes on the steady state component of the magnetic field supplied by the U-shaped yoke. The frequency chosen for the AC component of the magnetic field is 50 kHz. Other frequencies were also tried ranging from 20 kHz – 100 kHz, however there were no significant differences observed in the output signal. The output of the pick-up coil of the sensor is then fed to a digital lock-in amplifier (Model: LI 5640, NF Corporation).

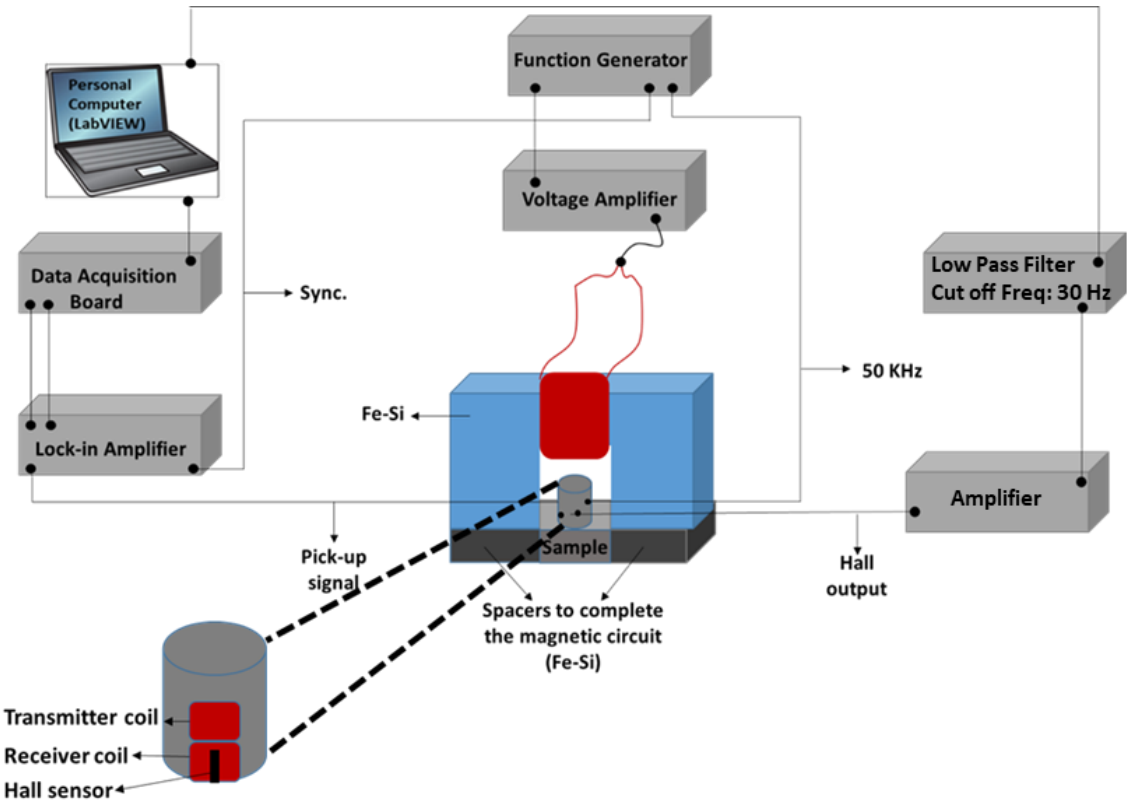

Figure 3.4. Schematic for measuring MIP using Lock in Amplifier

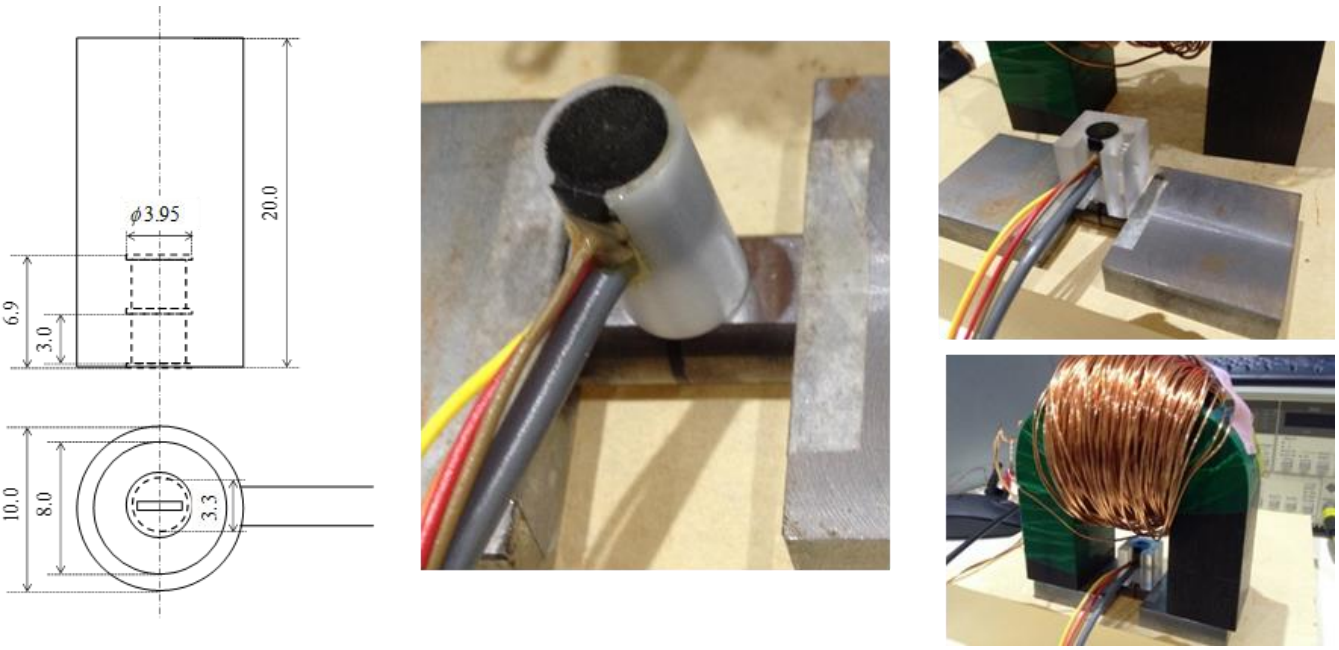

Figure 3.5. Probe set-up for the Magnetic Incremental Permeability measurement using Lock-in amplifier

The whole magnetization process and the respective effects are monitored and recorded using a digital lock-in amplifier that provides the amplitude of the output voltage which is proportional to the MIP.

3.2.3. LCR meter vs. Lock-in Amplifier for Magnetic Incremental Permeability Measurement

Fig. 3.6 below shows the comparison for measured MIP signature curves using an LCR meter (blue) and a digital lock-in amplifier (green). The graph clearly shows the signal output of a lock-in amplifier is much more stable and the signal to noise ratio is also better in comparison to the LCR meter output. Hence, for further measurements, the digital lock-in amplifier method is finalized to study and investigate the MIP curves for the 12% Cr-Mo-W-V creep test samples. It has to be noticed that there is always an offset in the voltage and impedance value measured as shown in Fig. 3.6. Although the offset contains information about the materials under test, for the comparisons between different samples, the offset has been removed and the initial value is set to 0 as shown in Fig. 3.7 onward.

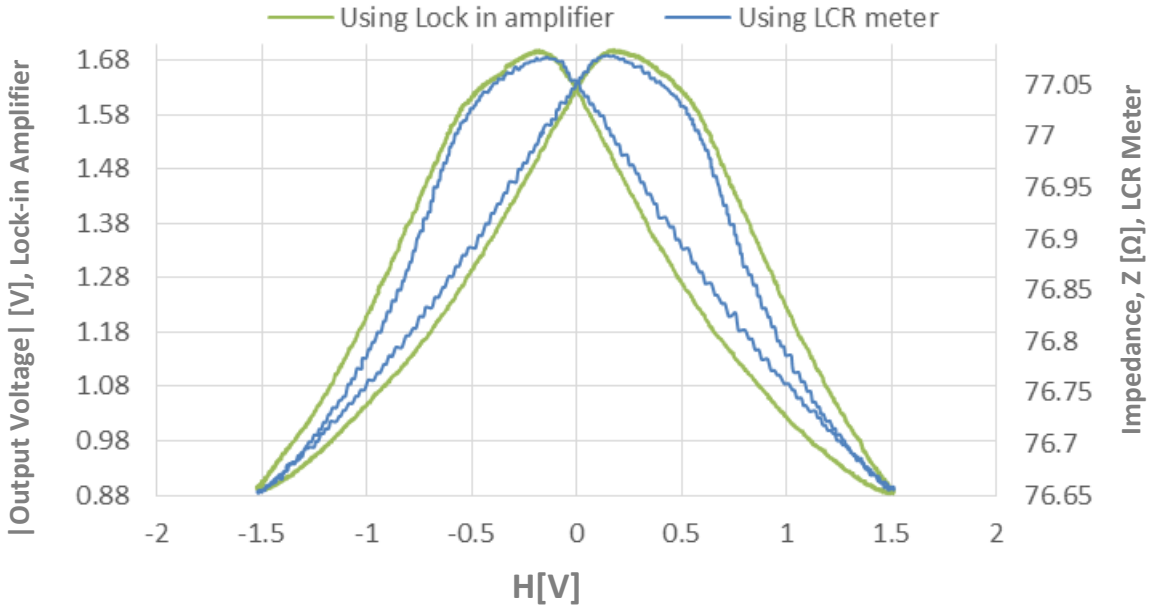

Figure 3.6. Comparison of measurements between LCR meter and Lock-in Amplifier

3.3. Amplitude and Frequency dependence

3.3.1. Frequency dependence

For the measurement of magnetic incremental permeability, two frequencies have to be considered, i.e., the excitation frequency for the magnetization of the material and the high AC frequency. The small resultant magnetic field as a result of AC component is used for superimposition on the steady state frequency.

Fig. 3.7 below shows the effect of different frequencies (low frequency component) associated to the net magnetic field strength H, tested on a virgin sample using a lock-in amplifier set-up. 5 different frequencies were tested and evaluated in order to find the optimal frequency for the measurements. As can be seen in the figure, MIP curves completely reverse for higher frequencies such as 1 Hz and 2 Hz. However, this reversal effect is also due to the material effect and the threshold for this effect will vary from material to material. 0.1 Hz being a lower frequency ensures maximum magnetisability of the material with lower losses, is chosen for the entire experimentation process.

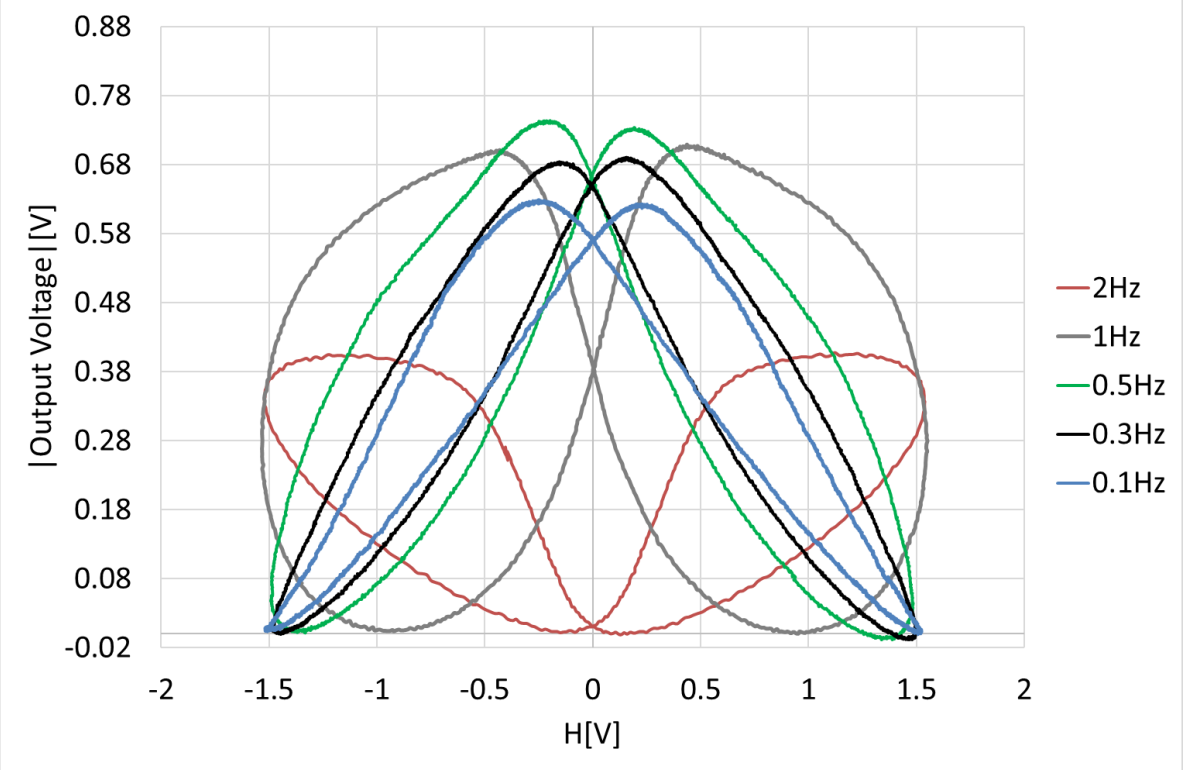

Figure 3.7. Frequency dependence tested on a Virgin Sample

As mentioned in the previous section, even the higher AC frequency component was varied, however, it did not show any significant changes and hence, 50 kHz was finalized for the AC component. For these measurements, the values of the time constant in the lock-in amplifier were also taken into consideration for each measurement.

3.3.2. Amplitude dependence

Fig. 3.8 below shows the amplitude dependence of the applied steady state magnetic field on the magnetic incremental permeability curves. The low frequency component chosen for this test is 0.1 Hz. The lower amplitude shows asymmetry in the curve and more than 10 kA/m shows saturation in the regions highlighted by the dotted circle. 10kA/m magnitude shows a good symmetry in the curve and a stable curve. Hence, 10 kA/m is chosen as excitation magnitude for the further experiments and studies on the 12% Cr-Mo-W-V creep test samples. It has to be noted that the output of the Hall sensor is measured in volts and in terms of kA/m using the calibration factor of 10000A/m = 1.5 Volts.

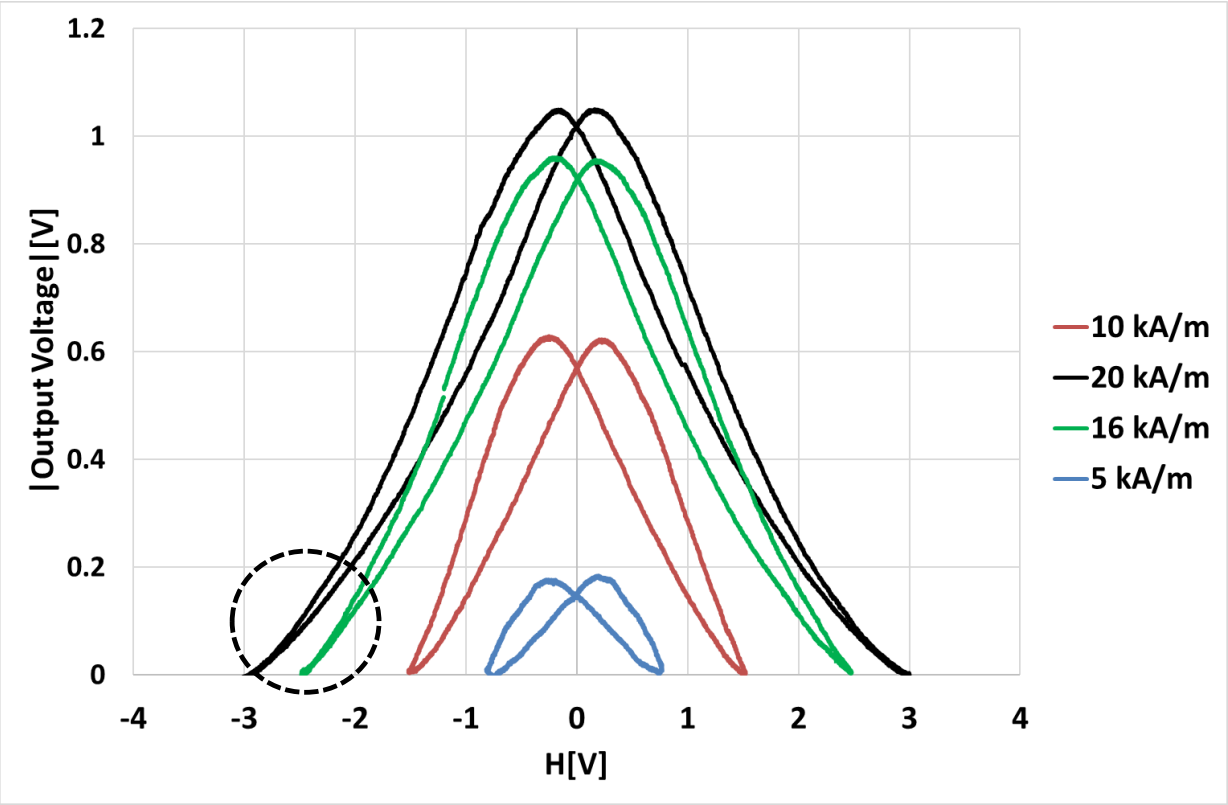

Figure 3.8. Amplitude dependence tested on a Virgin Sample

3.4. Magnetic Incremental Permeability Curves Analysis

Recalling the table from chapter 2 which illustrates the different conditions and parameters of different creep samples, an analysis of these curves is done in this section. Post to comparison of the effect of different frequencies, the excitation frequency of 0.1 Hz is chosen for all the following measurements demonstrated in this section as well as in the following sections. The excitation magnetic field of 10 kA/m is also employed for all these measurements.

Following to the experimental procedures mentioned in section 3.2., a typical butterfly loop is achieved, as shown in Fig. 3.10, which is known as the standard MIP curve. From these curves, various magnetic parameters can be derived, such as coercivity (Hc), Cross point, which corresponds to the remanence in the material, ΔV, which corresponds to the absolute value of the output voltage, corresponding to the incremental permeability. These parameters are then evaluated against the microstructural parameters shown in Chapter 2.

Table 3.1 Samples under test (Table from Chapter 3)

Sample number	Stress [MPa]	Temp [°C]	Test time [h]	Rupture level Ruptured:1
0	**0**	**0**	**0.0**	**0.0**
1	343	550	281.8	0.13
2	343	550	785.6	0.36
3	343	550	2205.7	**1.00**
4	201	600	255.6	0.15
5	201	600	763.9	0.44
6	201	600	1725.9	**1.00**
7	98	650	256.3	0.15
8	98	650	789.6	0.46
9	98	650	1736.8	**1.00**

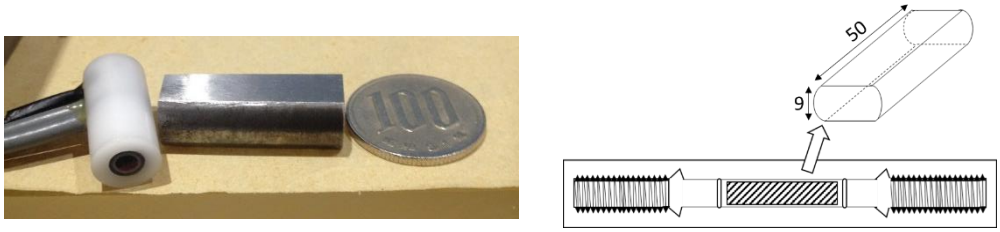

Figure 3.9. Sample under test

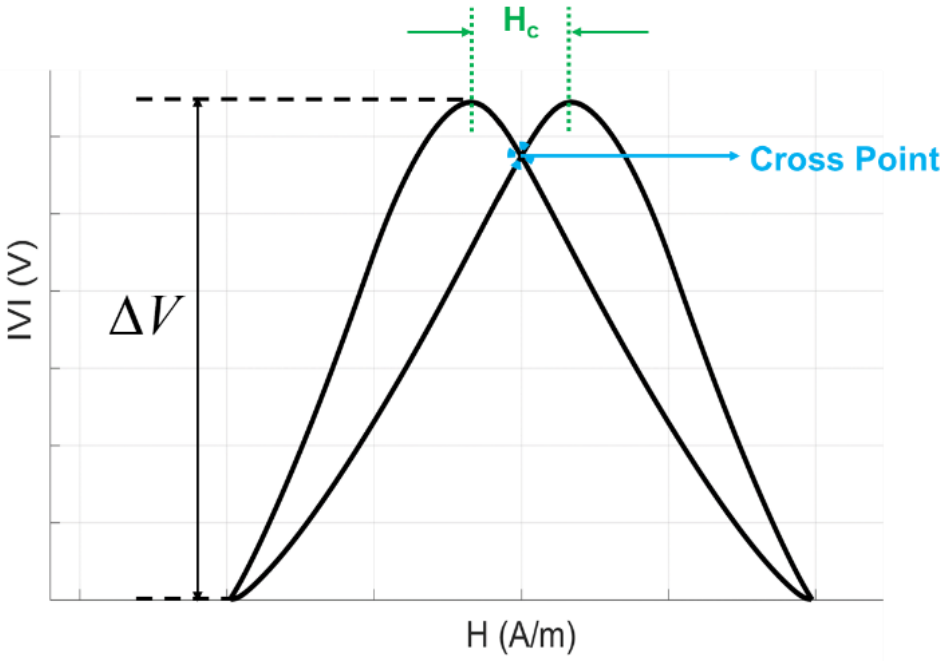

Figure 3.10. Depiction of a typical MIP curve with different magnetic parameters that can be derived from the curve

3.4.1. Evaluation based on different test times

In this section all samples are evaluated within each category of temperature with different test times (different levels of rupture) and the possible reason for the variations in the signature curves is illustrated in terms of microstructure.

- 550°C-343 MPa (Sample1-281.8 hours, Sample 2-785.6 hours, Sample 3-2205.7 hours)

Fig. 3.11 below demonstrates the variations in the evolution of MIP signature curve within the 550°C of samples, and similar stress, but with difference in their rupture levels. In this case it is quite evident that the cross point value of each curve drops as the test time of the material under test is higher. Sample 3 in this case, which is the ruptured sample in this category, has the value of cross point minimum and consequently, the absolute value of the output voltage (Magnetic incremental permeability) too. The reason for this drop in cross point value is because of the presence of carbide precipitates as shown in the image in Fig. 3.12. There are two important factors that affect the magnetic signal: number of precipitates and secondly, size of precipitates. In case of 550 °C samples, the number of precipitates are much higher in number in comparison to other

categories. This higher number results in more losses magnetically and hence more coercivity and less permeability in the material as the test time increases.

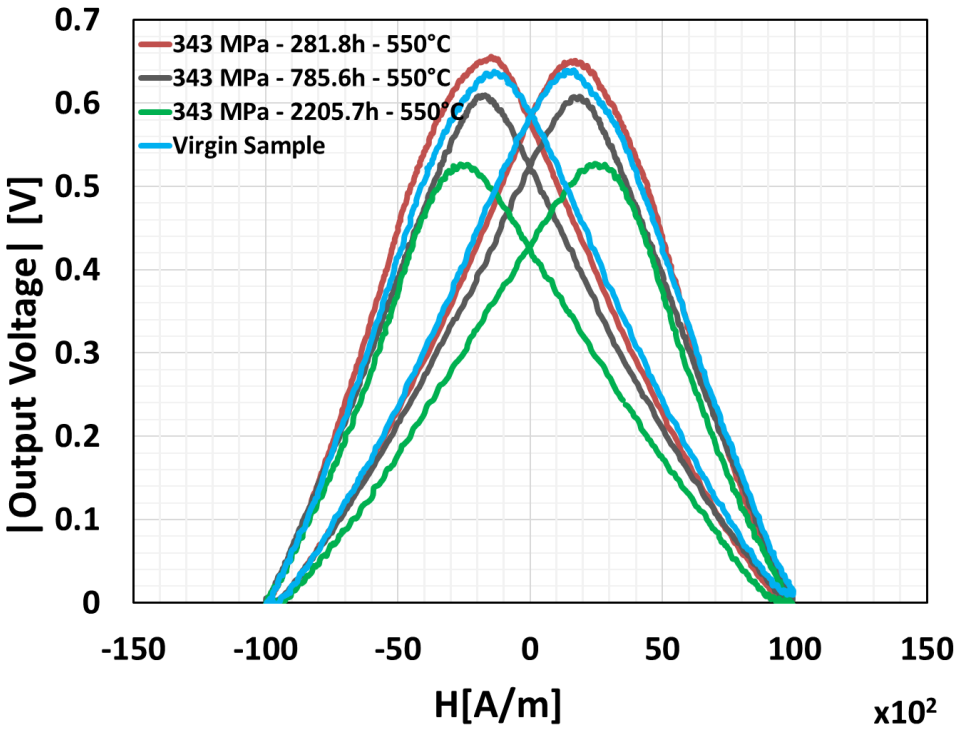

Figure 3.11. MIP curves with same temperature and different test times, for 550°C, denoting a decrease in the cross point with the increase in rupture level

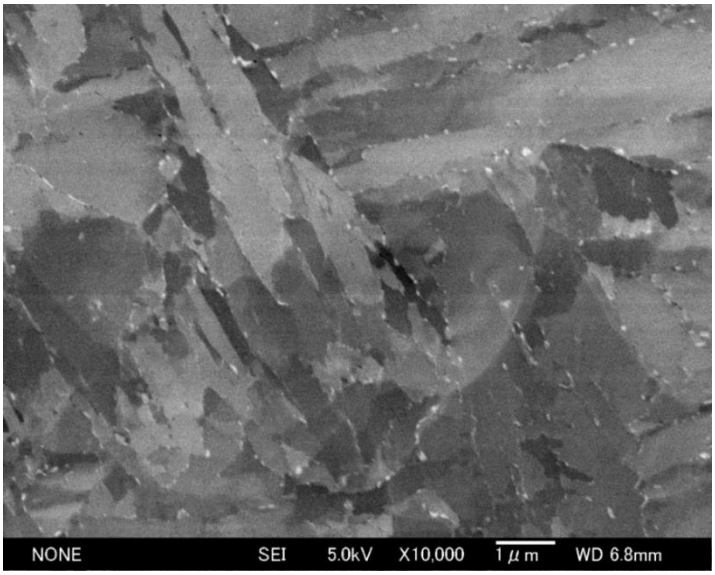

Figure 3.12. SEM Image for Sample 3

- 600°C- 201 MPa (Sample 4 - 255.6 hours, Sample 5 – 763.9 hours, Sample 6 – 1725.9 hours)

For 600°C samples, as depicted in Fig. 3.13, there is not much difference noticed in the cross point values. This almost negligible variation between the samples can be explained by looking at the Fig. 3.14, SEM image. In this Fig. the image is of Sample 6, ruptured. In this case, it can be observed that the number of precipitates has decreased and size of precipitates has increased. The effect is in the middle of two categories 550°C and 650°C. The individual values of cross point and coercivity (H_c) (magnetic parameters) have been evaluated in the following section 3.5.

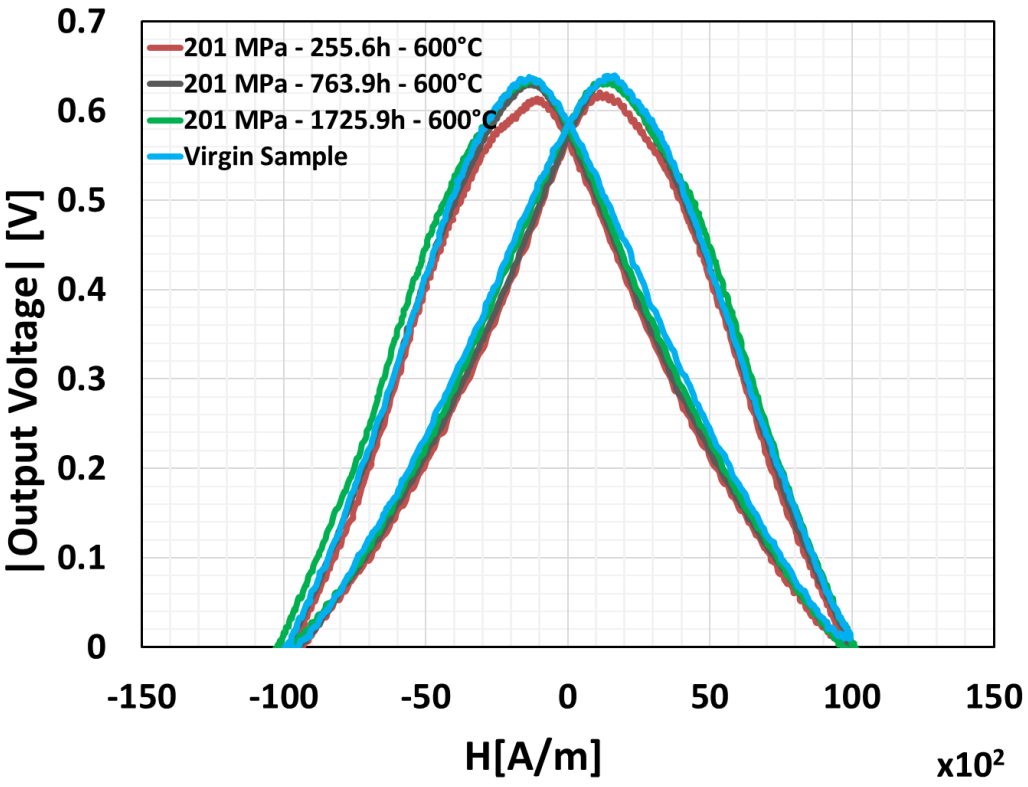

Figure 3.13. MIP curves, corresponding to a temperature of 600 °C and different test times, revealing a lower variation in terms of cross point.

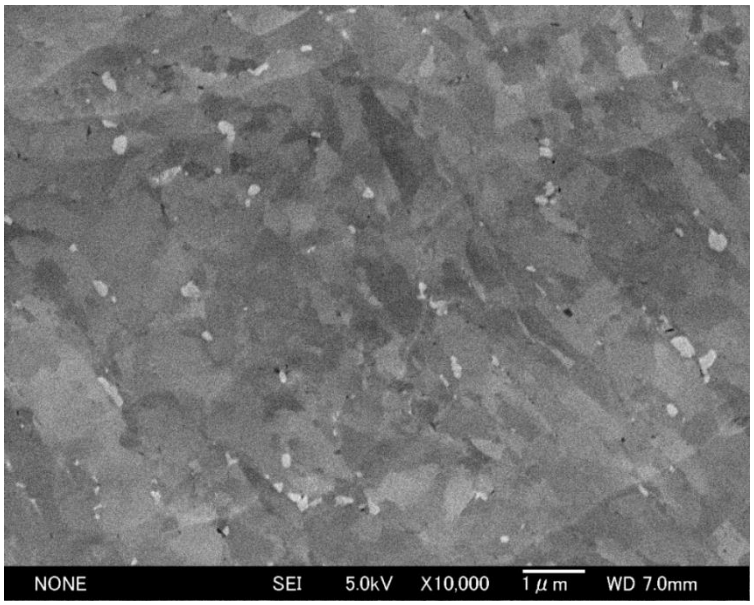

Figure 3.14. SEM Image for Sample 6

- 650°C- 098 MPa (Sample 7 - 256.3 hours, Sample 8 – 789.6 hours, Sample 9 – 1736.8 hours)

In Fig. 3.15 below, the MIP curves for the third category of samples, 650°C, are displayed. In this case, it is very evident that the effect observed is completely opposite to that of observed in the 550°C samples. The cross point and the equivalent absolute voltage increase as the test time increases. This is due to the fact that at higher temperatures, the number of precipitates reduce and their size becomes bigger,hence entirely an opposite evoution of magnetic parameters as compared to 550°C samples. Fig. 3.16 shows the SEM image of the Sample 9 (ruptured) highlighting the increased size of precipitates. It is also worth noticing that the MIP curve in this category show dual peak (at the highest amplitude of voltage). This probably due to the fact that at these higher temperatures, the materials behave in dual manner: Ferritic as well as Martensitic.

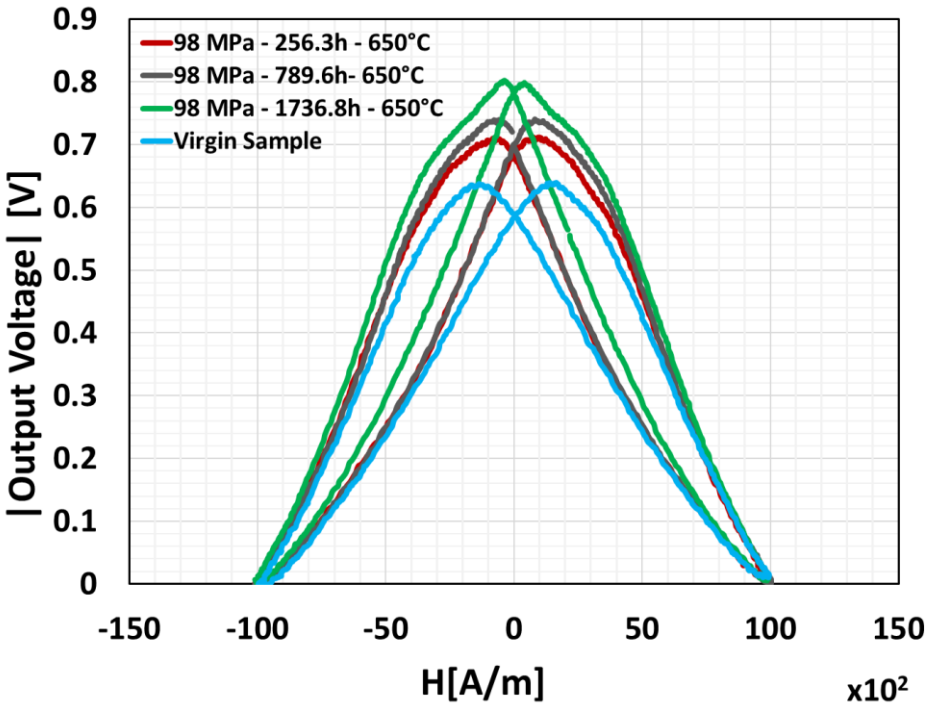

Figure 3.15. MIP curves, corresponding to a temperature of 650°C and different test times, revealing an increase in the cross point with increasing test time.

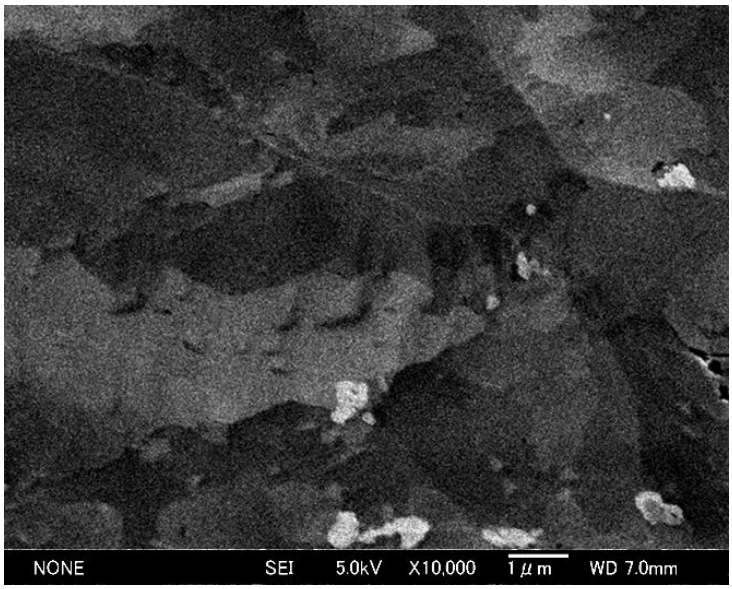

Figure 3.16. SEM Image for Sample 9

3.4.2. Evaluation based on different temperatures

Fig. 3.17 below shows the comparison of MIP signatures of the ruptured samples (Sample 3- Sample 6 – Sample 9) from each of the three categories (distinguished by varied temperature and stress treatmetns). As depicted in the figure, each curve can be characterized by quite distinct values in their coercivity (H_c) as well as distinct cross point values. The figure also demonstrates that the H_c values, with the increase in temperature,decrease. This also due to the fact at higher temperature, the material becomes extremely magnetically soft because of the reduction in the dislocations (demonstrated in Chapter 2). When the material becomes magnetically soft, it is obvious that the corercivity should fall and the permeability should increase as is the case stated in the Fig. 3.17.

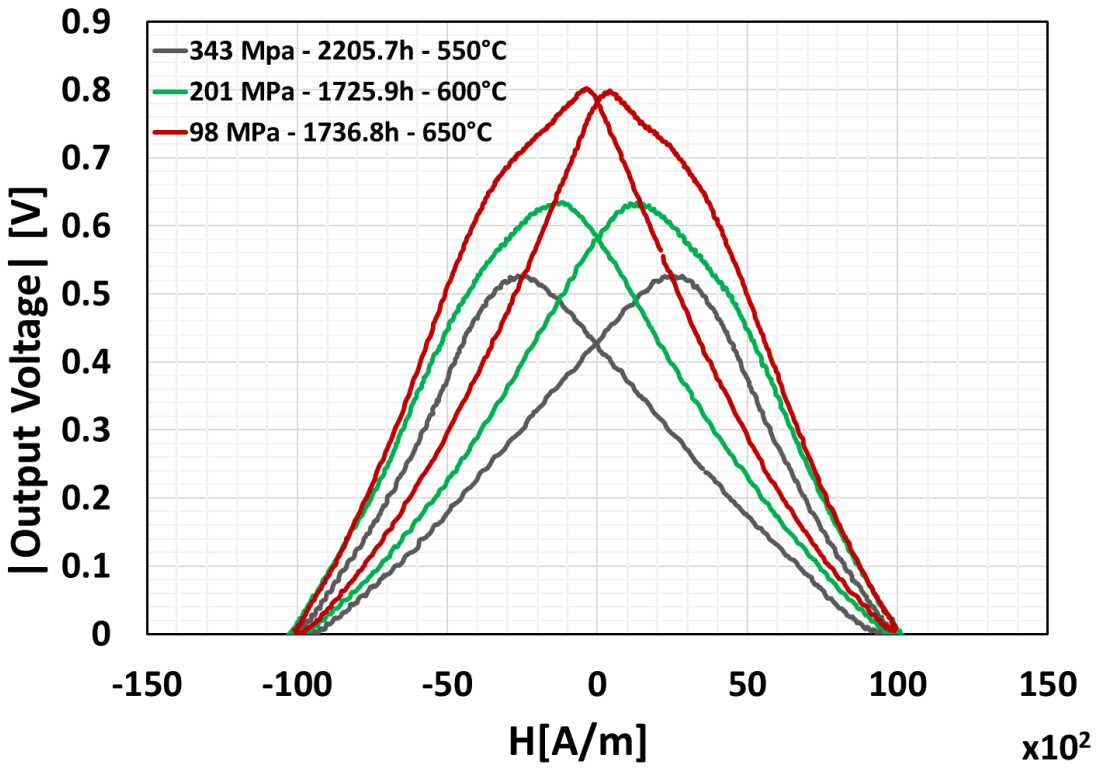

Figure 3.17. MIP curves for ruptured samples from each category

3.5. Magnetic Parameters versus Mechanical Parameters

In the previous sections, the typical MIP curves were analyzed, their shape, magnitude etc. From these curves, now, the magnetic parameters such as coercivity (H_c), remanence (Cross point), absolute value of output voltage corresponding to the permeability of the samples are derived. In this section, these derived magnetic parameters are evaluated against the mechanical parameters such as the stress the materials are exposed to, and Larson Miller Parameter (LMP, that considers the cumulative effect of temperature and test times). Fig. 3.18 below shows the cross point evaluation against the stress. For lower stress samples, as the rupture time increases, the cross point value increases, i.e., the remanence is higher in the samples that are degraded more due to creep and in case of higher stress samples, the cross point value falls as the sample nears the rupture level.

Fig. 3.19 shows the evaluation of coercivity versus the Larson Miller Parameter (the values of which are calculated in Chapter 2). It is quite evident that the coercivity in lower temperature samples increases with the increase in the test times, on the other hand, the coercivity for higher temperature decreases with the increase in the test times. It is also worth noticing that the trend of increase in lower temperature case is very similar to the trend of decrease in the higher temperature samples but in the opposite direction. This is due to the fact that the number of precipitates are prominent in the former case and the size of precipitates are dominant in the latter case.

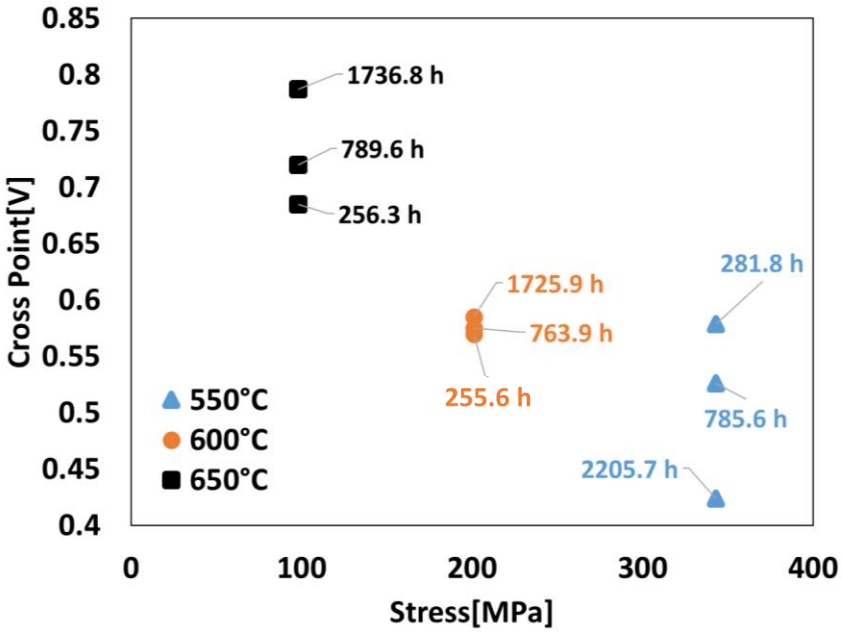

Figure 3.18. Cross point versus Stress

Additionally, within the same temperature category and for different test times, the value of the cross point against LMP decreases for 550°C samples and then increases partially for 600°C samples and further for 650°C samples as shown in Fig.3. 20 below. This may have resulted from the precipitation in the samples, as discussed in the previous sections. The trend of change in both lower and higher temperature is also opposite in this case as expected.

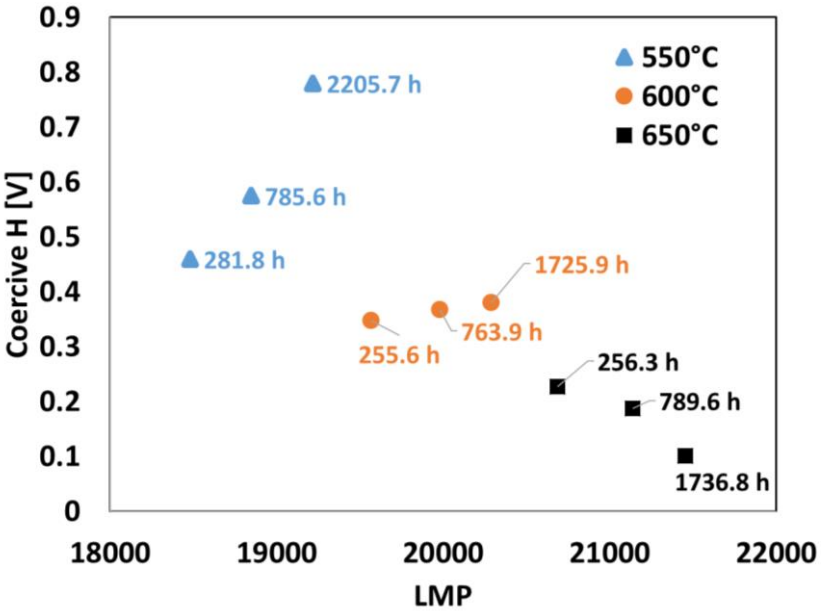

Figure 3.19. Coercivity versus LMP

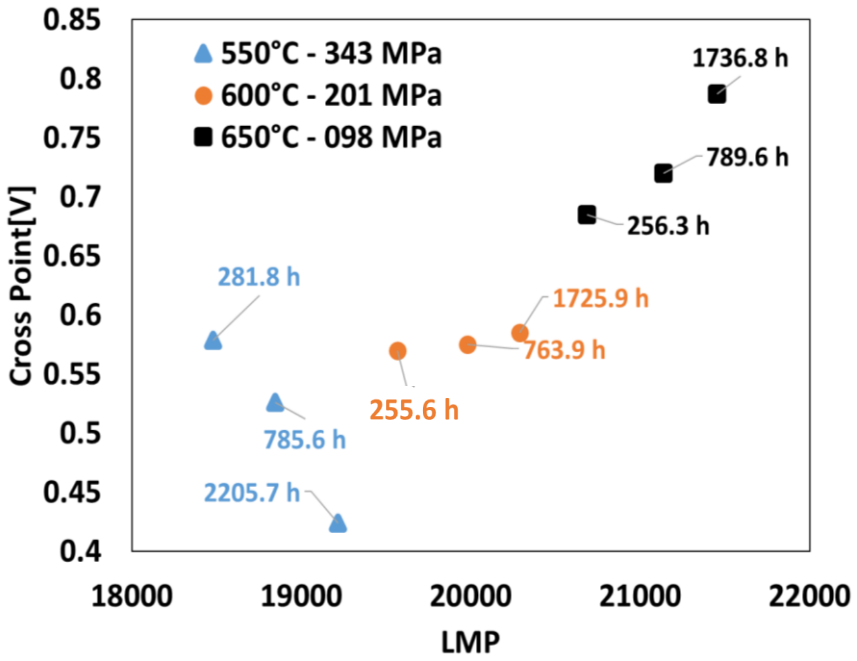

Figure 3.20: Cross point versus LMP

3.6. Magnetic Parameters versus Microstructure

In this section, the magnetic parameters derived from the MIP signals such as coercivity or cross point, are evaluated against the microstructure of the creep test samples. Their dependencies on the evolution of precipitates (Fig. 3.21-3.22) and on the misorientation (3.23-3.24) is checked. It is quite evident in the figures below that the evolution of magnetic parameters is similar to what was observed from the MIP signals previously. As explained previously, that Sample 1,2 & 3 (550°C) have more dominance from the increasing presence of number of precipitates as the rupture level increases, hence, more precipitates would mean more magnetically hard behavior. Therefore, it is seen that the coercivity increases as the number of precipitates increase for 550°C temperature treated samples. On the other hand, for 650°C temperature treated samples, the evolution is quite the opposite where the coercivity falls with the increase in the rupture level as number of precipitates only decrease and hence, the size of the precipitates become a dominant factor. For the 600°C temperature treated samples, hardly any differences are observed since, both number and size of the precipitates become equally dominant. From the misorientation point of view, it is seen in the Fig. 3.23-3.24, the KAM shows a stronger correlation majorly in the higher temperature treated samples only with larger variations. From the graphs it is seen that, if KAM has to be accessed from NDT signals, coercivity is an important factor. NDT signals show good and stronger correlation with the precipitates.

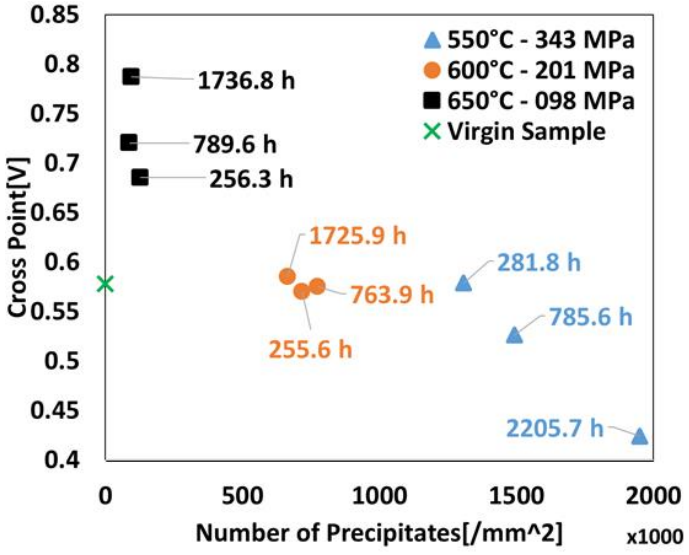

Figure 3.21. Cross point versus Number of Precipitates

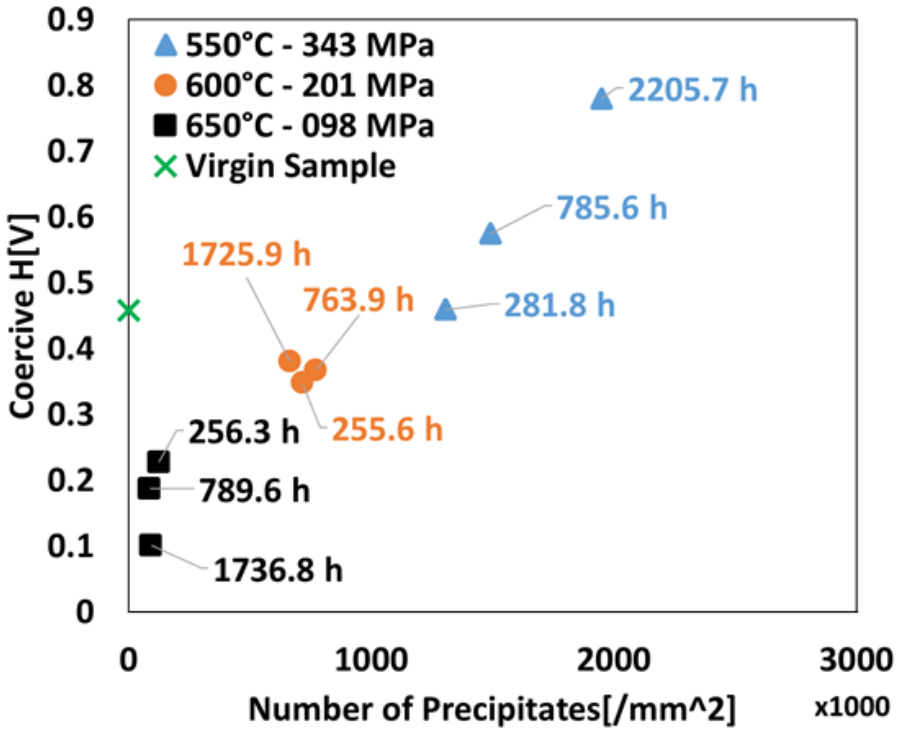

Figure 3. 22. Coercivity versus Number of Precipitates

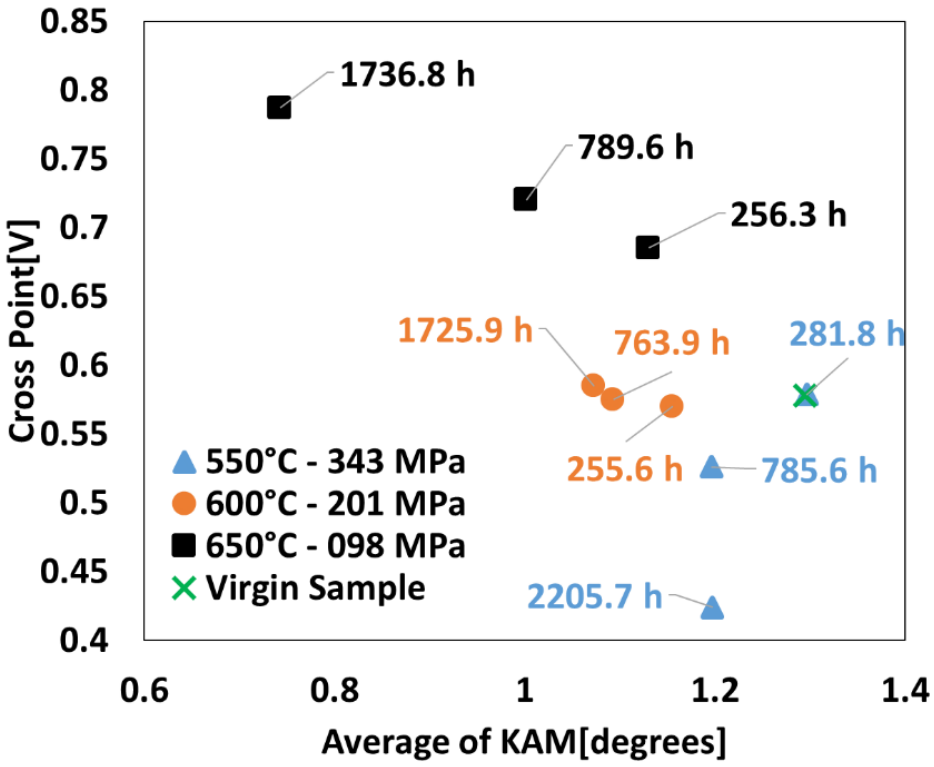

Figure 3.23. Cross point versus Average of KAM

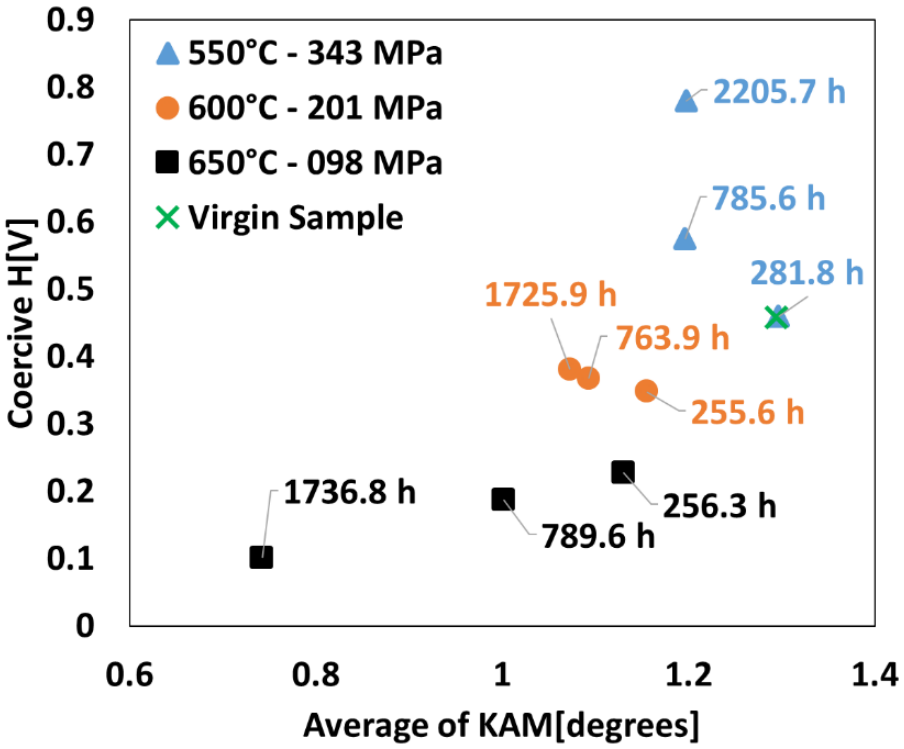

Figure 3.24. Coercivity versus Average of KAM

3.7. Hysteresis Measurements

In this section, the hysteresis loops for each sample are measured, observed and analyzed for the given set of 12% Cr-Mo-W-V creep test steel samples and a considerable conclusion is drawn as to why hysteresis might not be a good criterion to understand creep degraded samples but still some parameters are useful if we are not looking in-depth information.

When it comes to understanding and analyzing the ferromagnetic materials, hysteresis is the first inspection method. Many researchers have claimed that by just analyzing the shape and orientation of the hysteresis loop for a material under test, a lot of information can be revealed. However, one has to consider the factor, that hysteresis is a global information about the sample and not local. Hence, a lot of information that might be affecting the creep at the microstructural level, might be missed out. In general, the hysteresis measurements are performed using a VSM (Vibrating Sample Magnetometer) device for which a sample has to be of specific dimension, which limits to use this technique in the field of non-destructive testing, in real time situations. In addition to this, even if we want to measure the sample's magnetic response, in real time, the sample has to be surrounded by surrounding coils to record the induced voltage

corresponding to the induced Magnetic Flux density (B). By introducing the surrounding coils around the sample also limits this hysteresis measurment inspection method to be placed in the category of Non-destructive testing.

For these samples, to compare the hysteresis measurement (Global measurment) with the previously performed Magnetic incremental permeability,MIP, (local measurement) results, hysteresis loops are plotted. From these hysteresis loops, magnetic parameters are derived and then compared to the microstructure of the materials as described in Chapter 2.

3.7.1. Experimental Hysteresis Analysis

For these experiments, the sample is surrounded by a surrounding coil of 50 turns which was sufficiently enough to pick up the induced voltage corresponding to the Induced Magnetic Flux (B). The sample is magnetically excited with a sinusoidal external magnetic field H, of 10^4 Amperes/Meter with a frequency of 0.1 Hz, using a U-shaped yoke (similar yoke as used in MIP). Since the surrounding coild measures the induced voltage, B is calculated using the following procedure:

Applying the Lenz's law to the surrounding coil:

$$e = -n.\frac{d\phi}{dt} \tag{3.2}$$

Here e is the electromotive force, n the number of turns (50 in this case) and Φ the magnetic flux. Assuming the flux conservation inside the tested material:

$$\phi = B.S \tag{3.3}$$

Where S is the sample cross-sectional area, combining (1) and (2) gives:

$$e = -n.S.\frac{dB}{dt} \tag{3.4}$$

Finally, the average induction field B through the cross sectional area can be determined from:

$$B(t) = -\frac{1}{n.S}.\int_0^t e(t).dt \tag{3.5}$$

The time variation of the surface tangent magnetic excitation H(t) is directly measured using the Hall Effect sensor.

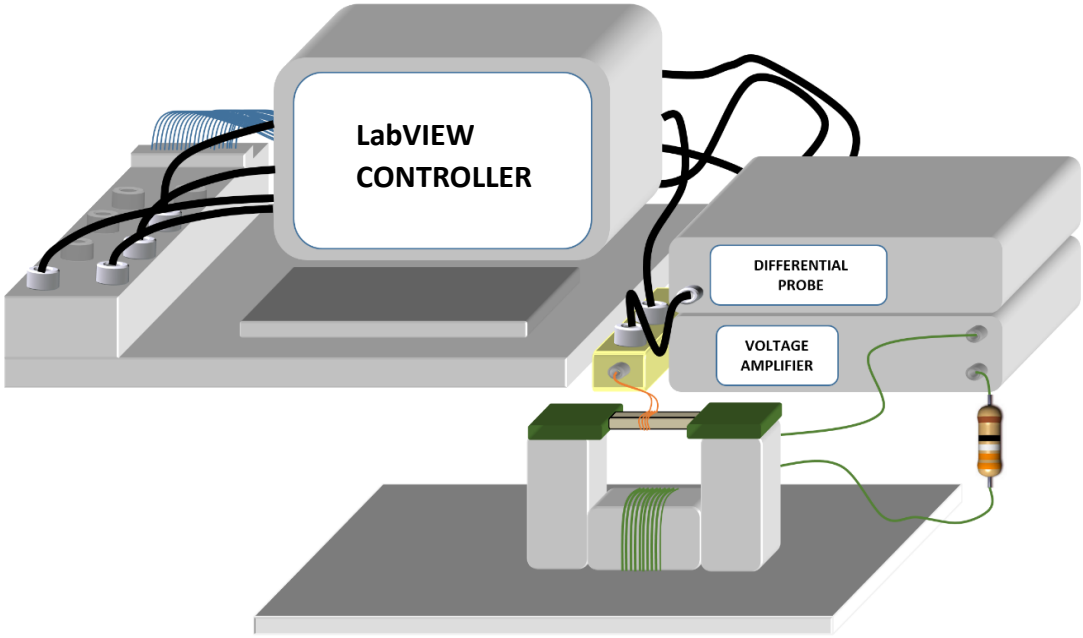

Figure 3.25. Hysteresis Experimental Set-up

This amplitude of magnetic field applied as well as the frequency are chosen to keep similar external parameters as in the case of MIP experiments. Fig. 3.25 shows the standard set-up.Fig. 3.26 below shows the comparison of hysteresis loops among the 550°C-343 MPa creep test samples with different levels of rupture times

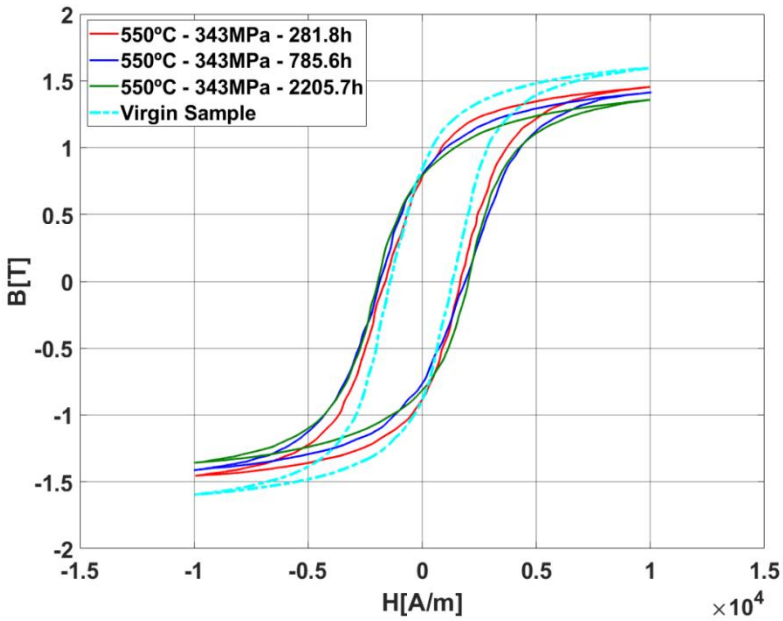

(a) Hysteresis comparison within the 550°C -343 MPa samples

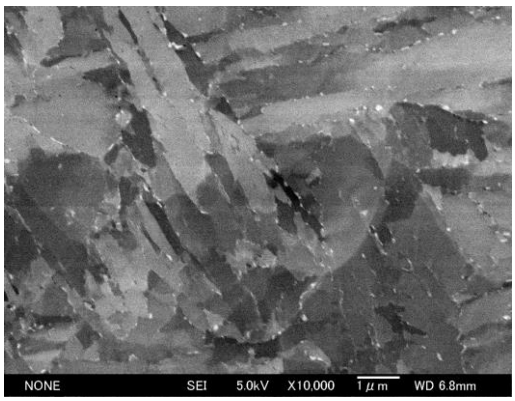

(b) The corresponding microstructure analysis for 550°C -343 MPa samples (in this case Sample 3)

Figure 3.26. Hysteresis comparison within the 550°C -343 MPa samples and the corresponding microstructure analysis

Recalling the analysis from MIP for the similar samples (Fig. 3.11), it is quite evident that the differences between the three samples is not so big in case of B(H) measurements as compared to the MIP measurements. This is quite acceptable physically, since, the MIP is a much more localized measurment which gives access to the state of the material at a deeper level in comparison to B(H) measurements. However, the trend is very similar. It can be observed clearly in Fig. 3.26 (top) that the coercivity is increasing as the rupture time increases which is completely justifiable in this case, since, at the microstructural level (Fig.3.26 (bottom)), there is an increase in the number of precipitates as the rupture level in the samples increase. This increase in the number of precipitates will make the material magnetically hard, hence higher coercivity. In addition this effect, the increase in the number of precipitates will also affect the induced magnetic flux in the materials. Hence, it can be observed that the induced B also falls with the increase in the number of precipitates.

Fig. 3.27(a) below shows hysteresis evolution for the cateogry of 600°C-201 MPa creep test steel samples as well as the corresponding microstructural image derived from SEM.

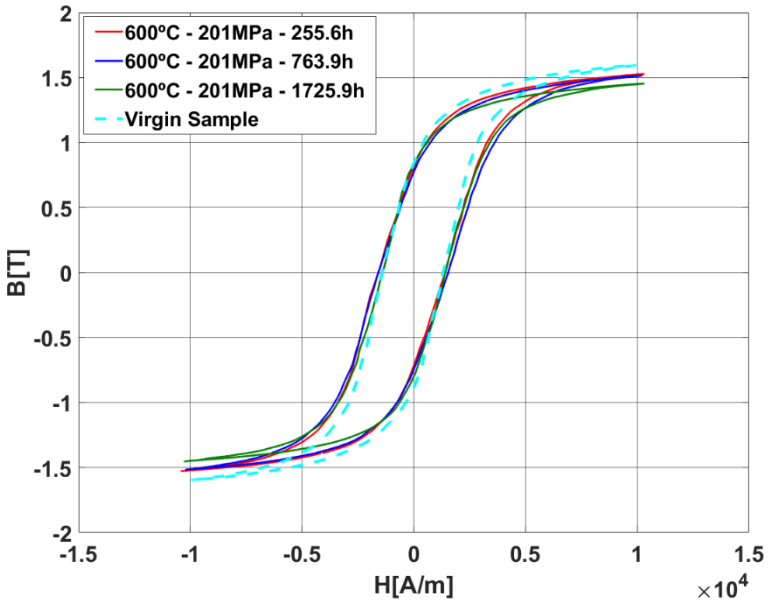

(a) Hysteresis comparison within the 600°C -201 MPa samples

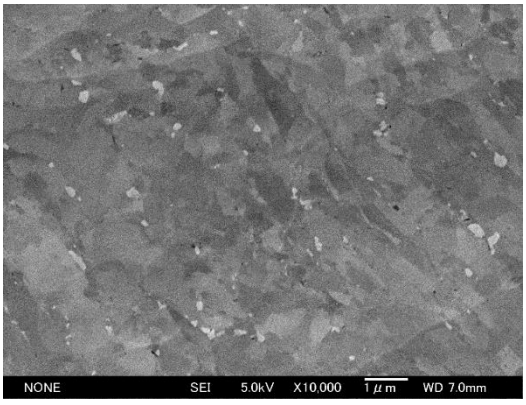

(b) The corresponding microstructure analysis for 600°C -201 MPa samples (in this case Sample 6)

Figure 3.27. Hysteresis comparison within the 600°C -201 MPa samples and the corresponding microstructure analysis

As was the case in MIP analysis (Fig. 3.13), not much differences are spotted since, this category is affected by both the number of precipitates as well as the size of the precipitates.

Similarly Fig. 3.28 below shows the comparison of samples from 650°C – 098 MPa creep test steel samples along with the correspoding SEM image. Fig. 3.15 can be recalled for the similar case from MIP analysis. Although the difference in case of Hysteresis curves within these three samples is not evident, MIP on the other hand showed much hihgher distinctions. However, it is still possible to observe that the coercivity falls with the increase in the rupture time as the number of precipitates are much lower in this case. It is still not an enough or adequate method to analyse creep degraded samples.

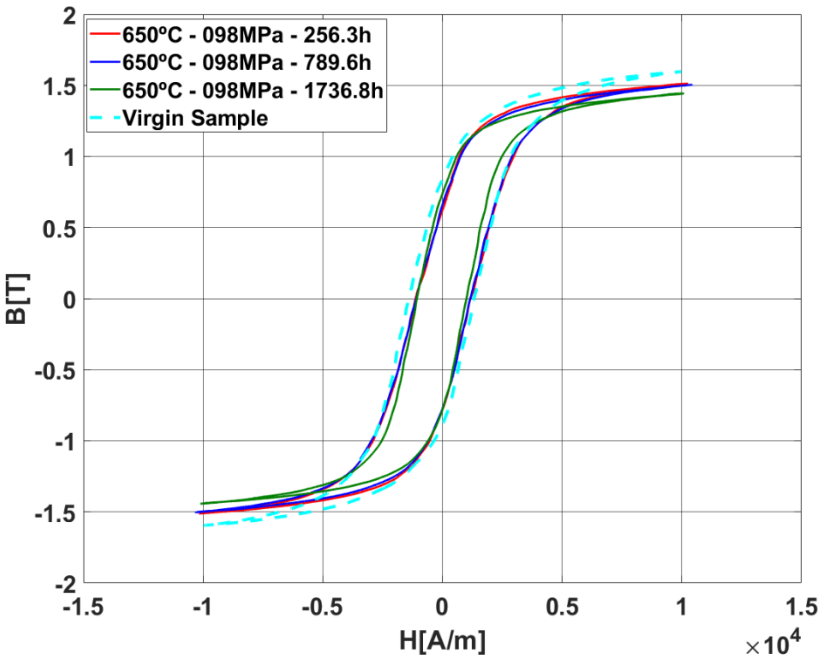

(a) Hysteresis comparison within the 650°C -98 MPa samples

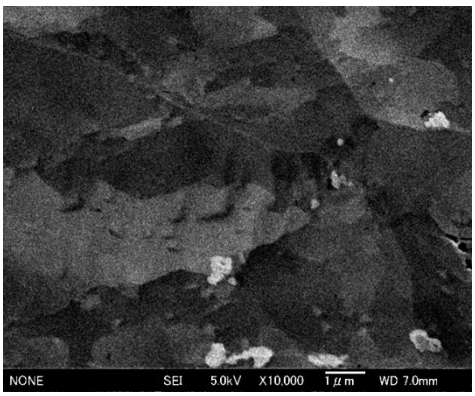

(b) The corresponding microstructure analysis for 650°C -98 MPa samples (in this case Sample 9)

Figure 3.28. Hysteresis comparison within the 650°C -98 MPa samples and the corresponding microstructure analysis

3.7.2. Ruptured Samples Analysis

Fig. 3.29 below shows the comparison of the ruptured samples (Sample 3 - Sample 6 - Sample 9), one from each category. When it comes to analysing the samples with different rupture times, within same temperature, it was shown in the previous section that B(H) analysis is inadequate. However, adding an extra parameter of temperature change, Fig. 3.29 shows that there is a distinction between the three ruptured samples. Since, the number of precipitates are lower in the higher temperature samples, the material becomes magnetically soft and hence, higher permeability-lower coercivity. It was also shown in Chapter 2 that Average of KAM is significant only in higher temperatures, hence, fewer dislocations at these temperatures are also the reason behind the lower coercivity. However, when compared to MIP, there is a much higher distinction observed in the same set of samples as presented in Fig. 3.17).

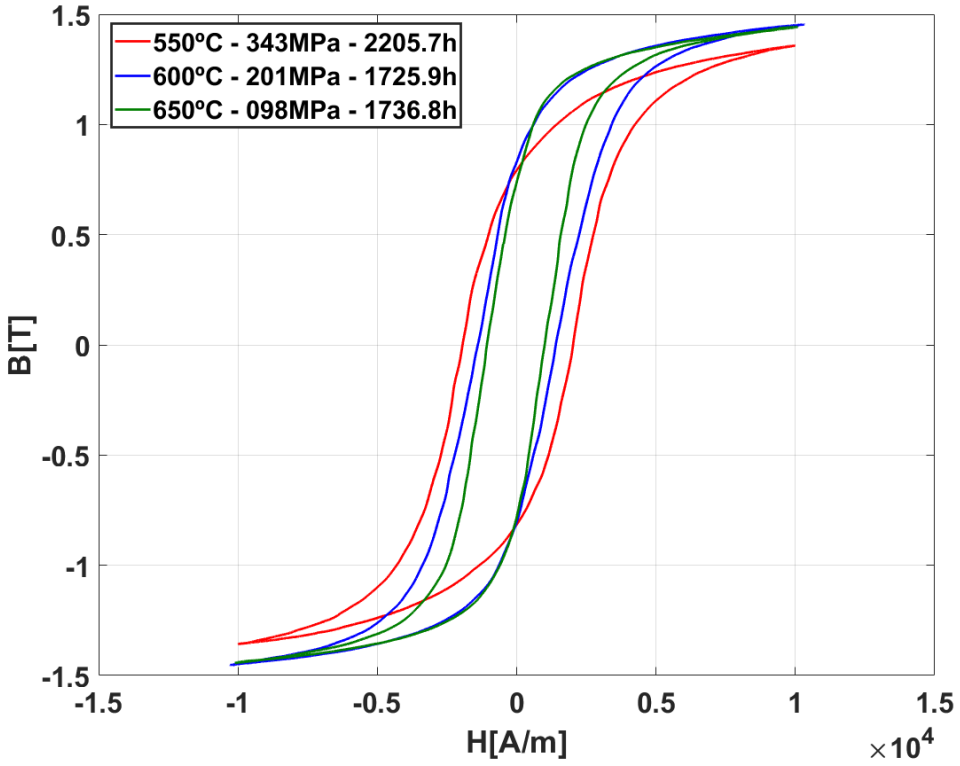

Figure 3.29. B(H) curves for ruptured samples

3.8. Magnetic Incremental Permeability versus Hysteresis Measurements

Hysteresis measurements are one of the first steps to investigate the properties of the materials when it comes to analyzing the ferromagnetic materials. In this study, as explained in the previous section, the surrounding coils were used to pick up the induced voltage proportional to the magnetic field B. Using the surrounding coils gives global access by averaging the information about the sample. Hence, the averaged information leads to losing of details about the sample. Fig. 3.26 -3.28 evidently show that the differences are not that distinct between the samples with the same temperature and different levels of rupture. However, in case of MIP, Fig. 3.11, 3.13 and 3.15 show the distinctions on a bigger scale for the same set of samples as compared to Hysteresis measurements. MIP being a local measure unlike Hysteresis, gives more local and detailed information about the samples' coercivity, remanence differences etc. When it comes to perform magnetic measurements, the Hysteresis measurements pose more challenges in terms of non-destructive testing, as one has to install the surrounding coils to investigate the materials and on top of that it provides the averaged information not certainly enough to assess the variations due to different creep levels as also shown in the previous section.

3.9. Summary

The aim of this chapter was to understand the kind of microstructural changes with effect to different treatments of the high chromium creep test steel samples. For a deeper investigation, an advanced technique 'Magnetic Incremental Permeability' was implemented to analyze the same set of samples. This technique helped to extract some magnetic parameters from the typical MIP curve from each sample. These parameters were then assessed with respect to the microstructural parameters change (Number of precipitates, recrystallization, Average of KAM corresponding to dislocations). Various assessments were formalized based on multiple mechanical / Microstructural / Magnetic parameters to interpret the behavior of the differently treated samples. From the microstructural point of view, the precipitation number showed a very good correlation with the magnetic parameters. It was revealed that the evolution of magnetic parameters for lower temperature samples is entirely opposite to the evolution of these parameters in case of high temperature samples. On the other hand, it was also observed that Average of KAM parameter exhibited a good correlation to the magnetic parameters only

in case of high temperature samples and the variation was much higher within the same set of samples as compared to the lower temperature treated samples.

Now that the experimental analysis is understood deeply in case of MIP measurements, from the NDT point of view, a modeling technique development is the next step that could help to understand the behavior in a deeper and understandable way. The modeling will not help understand the Physics behind but will also, help to reduce the tedious and expensive treatment of samples to get microstructural information (Once, microstructural analysis is done using SEM, EBSD, it doesn't remain anymore under the category of Non-destructive testing, since for this procedure the samples have to be in specific shape and size). Hence, the next chapter is about the techniques incorporated to model standard MIP curves first and then adapt them to the experimental data analyzed in this chapter.

CHAPTER 4

MAGNETIC INCREMENTAL PERMEABILITY NONDESTRUCITVE TESTING ON 12% Cr-Mo-W-V CREEP TEST SAMPLES: MODELLING AND PHYSICAL INTERPRETATION

It has been shown in the previous chapter that Magnetic Incremental Permeability has proven to be a very effective and informative method to evaluate the ferromagnetic materials non-destructively. Although, there exists a number of experimental ways to implement MIP; to make relevant and absolute conclusions about the measured quantities, it requires a lot of investigations and studies to propose certain standards because of the diversity in setting up experimental procedures. Since, such standards are missing in the NDT industry, an alternative solution is to propose simulation techniques to model MIP butterfly curves (making it independent of the experimental set-up). From these simulations, some modelling parameters could be derived to physically interpret the microstructure of the materials. Hence, as a next step as a continuation of the experiments presented in the previous chapter, modelling techniques to simulate MIP typical butterfly loops are presented in this chapter. Simulating MIP in itself is a very challenging task since, it involves dealing and simulating the minor loops that are a resultant of AC superimposed DC magnetic field during the process of magnetization and demagnetization. Different attempts are made to simulate the MIP curves and then an optimal model based on Jiles-Atherton theory is modified to adapt to the experimental data derived in the previous chapter. Derivation of modelling parameters from the butterfly loops based on J-A theory, establishes a physical relation with the microstructural properties of the materials such as dislocations, Kernel Average Misorientation, precipitation content.

4.1. Modeling Principles for Magnetic Incremental Permeability

Fig.4.1 below shows a schematic for the MIP experiments. To simulate the materials behavior under the magnetic incremental permeability situation, a mathematical model based on physical properties can be implemented. In a conventional approach, to take into account the magnetic field's distinct axial components and to be able to simulate the inhomogeneous distribution of the magnetic field, a full 3D magnetic model is required. Alternatively, by assuming the magnetic flux B and applied magnetic field strength H, as collinear, a simplified scalar analytical model, can be used as demonstrated in Fig.4.2 and in the zoomed part of Fig.4.1.

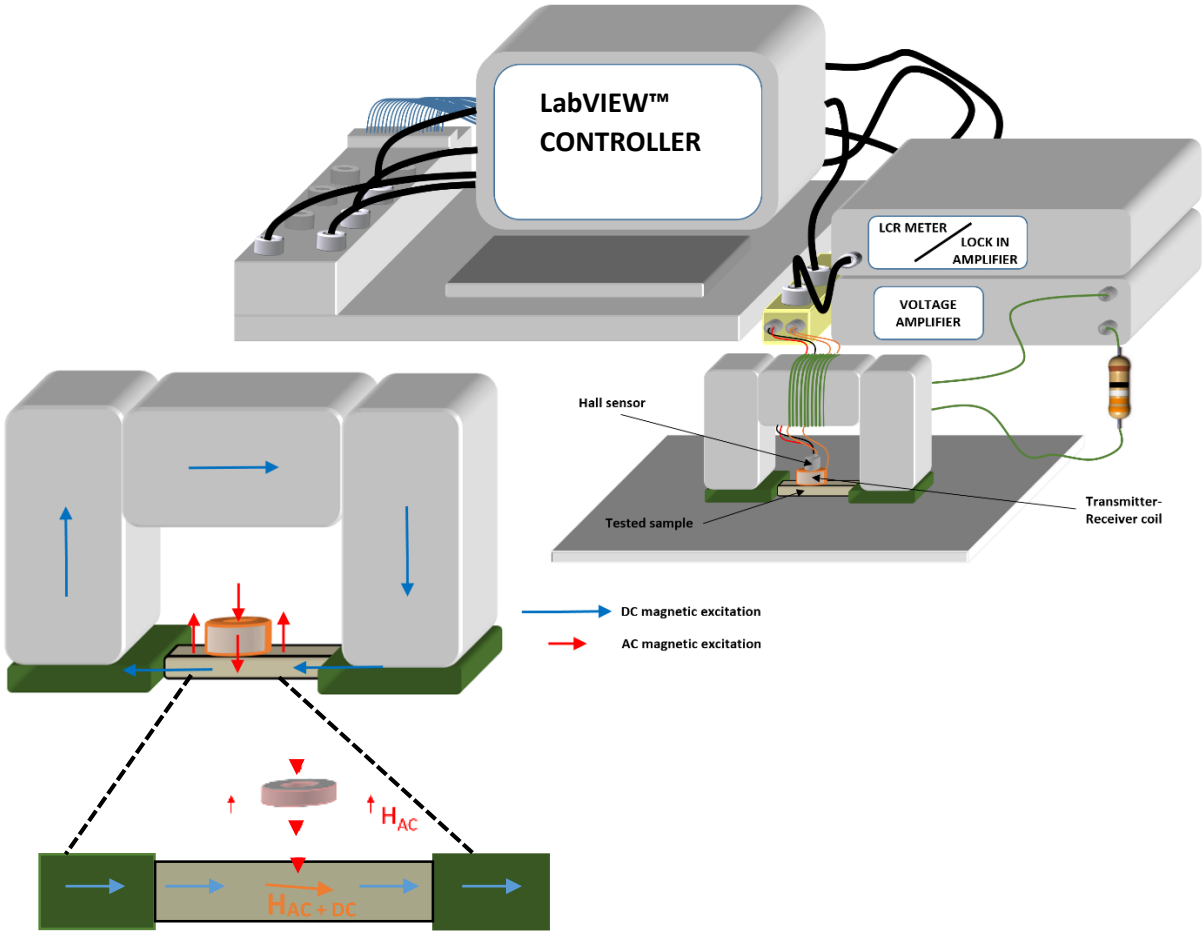

Figure 4.1. Illustration of the vector magnetic field distribution in the schematic experimental set-up for MIP.

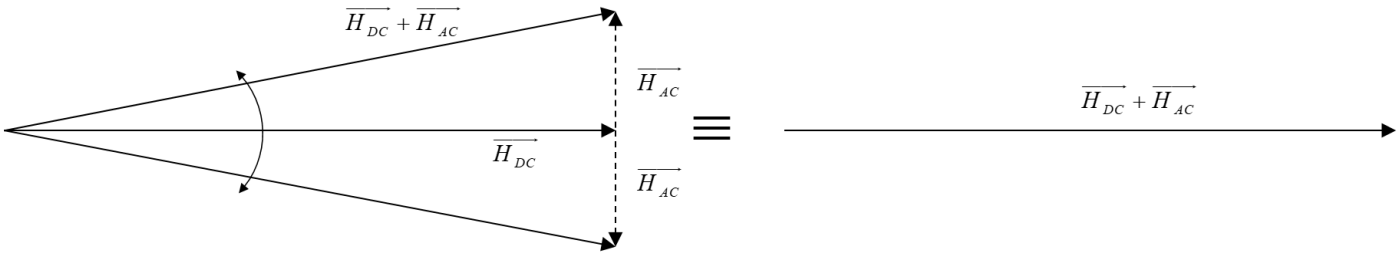

Figure 4.2. Illustration of the scalar approach

In a classical MIP experimental set-up, both AC and quasi-static (DC) magnetic excitations are both vectorially perpendicular quantities. However, the maximum amplitude of quasi-static magnetic excitation field is generally a thousand times higher in comparison to the AC magnetic excitation field. Hence, during the larger part of the quasi-static magnetizing process, the orientation of the cumulative vector excitation field $\vec{H}$ ($\overrightarrow{H_{DC}}$+ $\overrightarrow{H_{AC}}$ contribution) remains nearly constant.

As per this observation and for the simplification of the modelling scheme, the vector $\vec{H}$ is considered to be collinear to $\vec{B}$ vector (induction). On the basis of this assumption, a scalar approach is taken into account to simulate the materials magnetic behaviour, with the accurate scalar hysteretic material law. Additionally, the induced magnetization behaviour becomes homogeneously distributed in the materials under investigation, when operating on a low H_{DC} frequency. Consequently, the dynamic component of the excitation field H_{AC} has its effects at the areas near the pick-up coil on the surface of the sample. Since, the AC component has a very small amplitude, the permeability is assumed to be nearly constant, resulting to a direct proportionality between the measured output voltage amplitude and the permeability.

The amplitude of the magnetic field for the AC component is very weak. Even at 50 kHz, the local excitation slope dH/dt as a result of AC component is considered to be much lower than the maximum amplitude of dH/dt observed below the threshold of quasi static field. Although, when the AC dynamic contribution is considered during the minor loop conditions, it affects the phase shift among B and H [Mats, Mats1 and Duch] but it would still have an insignificant influence on the MIP signal (permeability modulus). As a result, the dynamic contributions are not considered in the following simulations. This assumption is legitimate since, it was validated experimentally in chapter 3; by varying the AC frequency component to both higher and lower, no significant effects were observed on the MIP signals. In this study, the focus is entirely on modelling the variations in the modulus of the permeability against the applied magnetic field (Resultant: MIP butterfly loop).

Since, the objective is the simulation of the typical butterfly loop $|\mu|(H)$, it is sufficiently enough to achieve the good simulations considering only the quasi-static contribution, for which there are two ways to simulate:

A. The Jiles-Atherton model is modified to address the accommodation issue (i.e., it requires multiple cycles to get the minor hysteresis loops stabilized) which is resolved by considering the AC component amplitude weak enough so as to neglect the hysteresis phenomena during the minor loop conditions.

B. An "applied H dependent" type modified model (for instance, the Preisach or the dry friction model). These models showcase the issue of congruency, which implies that the shape and the size of the resultant minor remanence loop predicted are not dependent on the system's magnetic state (Fig. 4.3), when a ferromagnetic material is cycled between the two magnetic excitation levels.

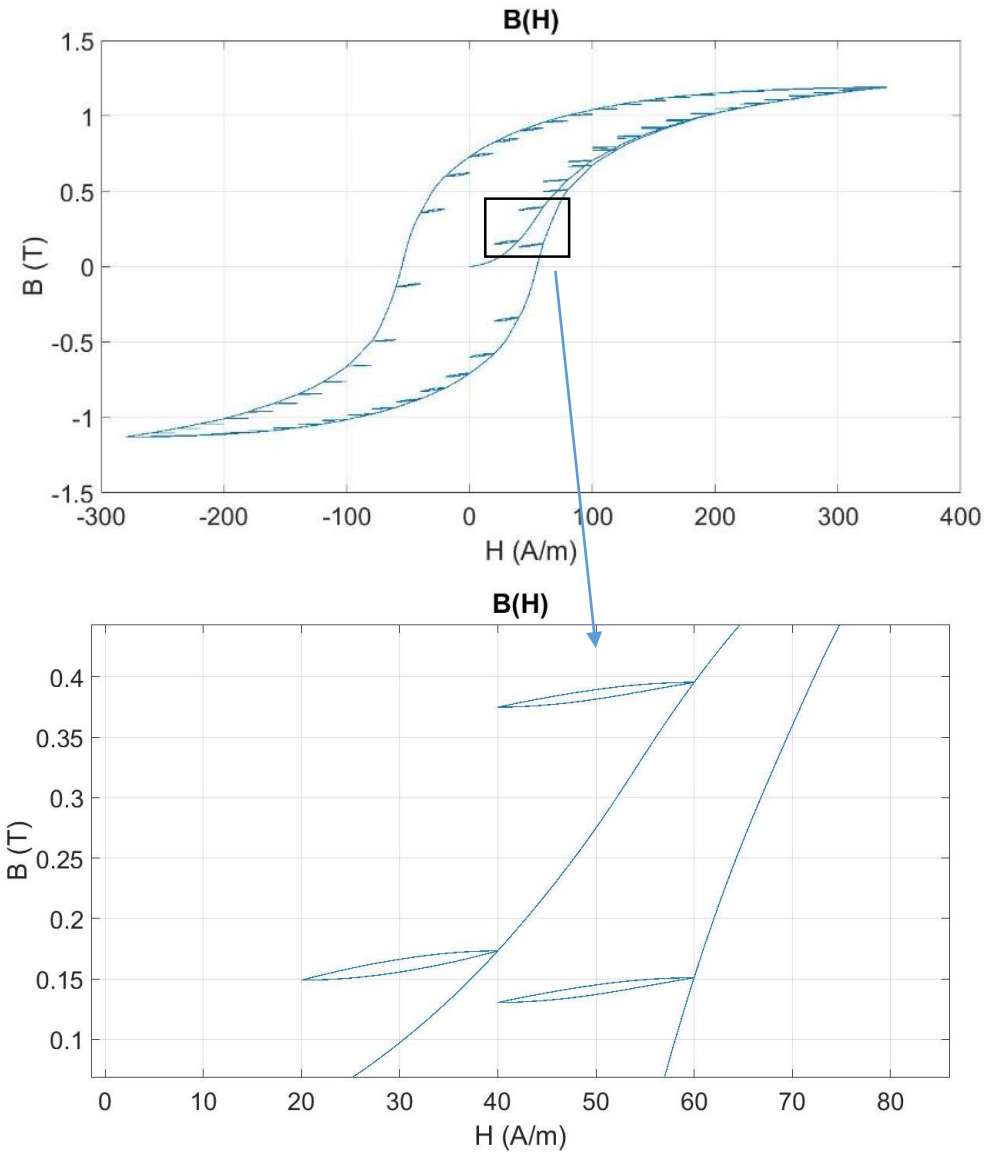

Figure 4.3. Illustration of the congruency issue

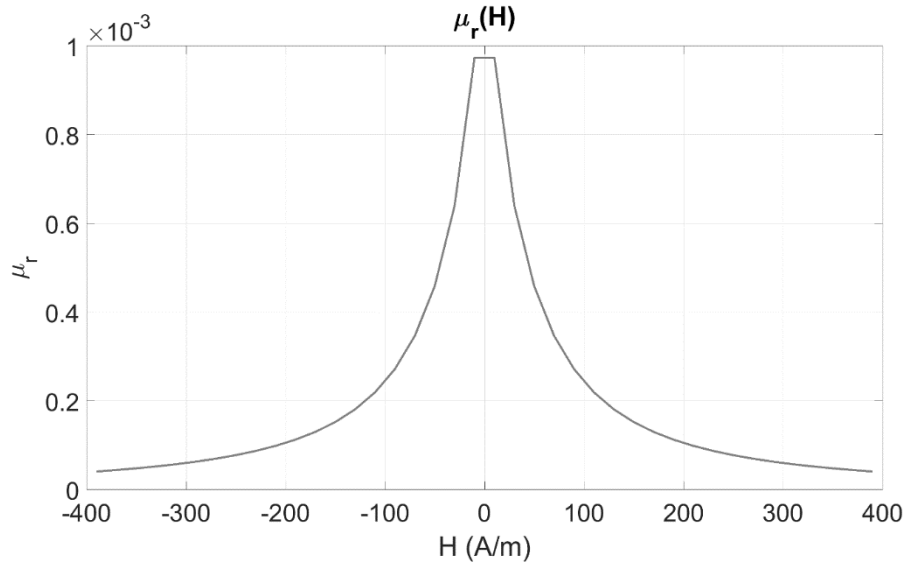

Figure 4.4. A single anhysteretic loop obtained using applied H dependent hysteresis model.

Hence, instead of getting a typical butterfly loop, it gets limited to a single anhysteretic curve due to congruency issue as shown below in Fig. 4.4. By replacing H as an input by $H_{eff} = H(t) + \alpha.M(t)$, the issue of above mentioned congruency can be resolved, where, H_{eff} is defined as the effective field, and α as the constant of proportionality between the magnetization and the average field, M is the sum of the reversible component and the irreversible component of the magnetization. This approach of solving the issue was proposed first by Della Torre and Kádár in [Torr, Torr1 and Cram], referring to this approach as the moving model approach that focused on adjusting the Preisach triangular distribution in a way such that it becomes stable. This is implemented by moving it along the axis at a 45° angle with respect to H+ axis by an amount that is proportional to the net magnetization in the medium. Consequently, the Preisach function P (H+, H-) is replaced by P (H+α.M, H-α.M). The resultant of this moving model approach is that the minor hysteresis loops become non-congruent and then the typical butterfly curve can be obtained as shown in Fig. 4.5. Considering the case of scalar model, α becomes equal to the magneto-metric demagnetizing factor average value along the axis of magnetization. Figure 5 below gives an illustration of the MIP butterfly loop obtained once the congruency issue is resolved.

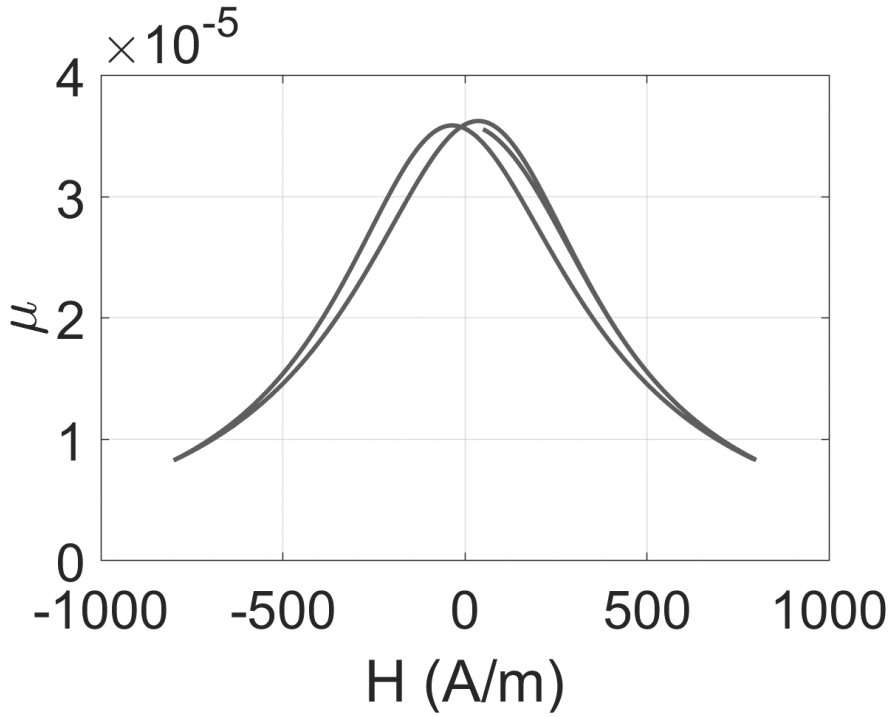

Figure 4.5. Butterfly loop obtained with a modified H dependent hysteresis model.

Finally, the two approaches (modified Jiles-Atherton model, modified H dependent models) are relevant. Since, the H dependent models are mathematical models, it is difficult to derive any relevant physical interpretation. Hence, in this study, the modified Jiles-Atherton model is chosen for its fixed number of parameters and their corresponding physical interpretation according to J-A theory.

4.2. The Jiles-Atherton model

Under a certain threshold frequency, the cumulative periodic value for the ferromagnetic losses become independent of the frequency which is also defined as the quasi-static state.

The Jiles-Atherton model considers mainly two contributions, namely, the domain walls translations and the domain walls bending. The Jiles-Atherton model has some certain interesting features which make it appealing for the modelling.

- It requires a low memory allocation.
- The model is entirely dependent on only 5 parameters.
- Each of the 5 parameters have an association with the microstructure and the value of these parameters can help in having a physical interpretation.

- Being a reversible model, it is relatively convenient to use B as an input instead of H for quasi-static models.

According to the Jiles-Atherton theory for ferromagnetic materials, the cumulative magnetization which is represented by M is composed of reversible magnetization(M_{rev}) as well as irreversible magnetization(M_{irr}). The magnetic domains rotation corresponds to the reversible magnetization whereas the domain wall displacements correspond to the irreversible magnetization.

$$M = M_{rev} + M_{irr} \tag{4.1}$$

Langevin equation [Lang] or by using a hyperbolic function, the anhysteretic magnetization M_{anh} can be described:

$$M_{anh} = M_s \left[\coth\left(\frac{H_e}{a}\right) - \frac{a}{H_e} \right] \tag{4.2}$$

$$M_{anh} = M_s \tanh\left(\frac{H_e}{a}\right) \tag{4.3}$$

In both equations (4.2) and (4.3), M_{anh} represents the anhysteretic magnetization, H_e represents the effective magnetic field, M_s represents the saturation magnetization and *a* is the anhysteretic magnetization shape parameter. According to Jiles-Atherton theory *a* = k_B.T / μ_0.m in which k_B represents the Boltzmann's constant, T, the temperature, and m describes the magnetic moment of a domain.

$$H_e = H + \alpha.M \tag{4.4}$$

In the above equation, H is the applied excitation field (tangential component), M represents the average magnetization of the sample. α represents the inter-domain coupling (see J-A theory) [Jile, Jile1, Jile2 and Zhan]. Equation (4.5) describes the link of anhysteretic, the irreversible and reversible magnetization.

$$M_{rev} = c(M_{an} - M_{irr}) \tag{4.5}$$

c is the coefficient of proportionality that can be determined by using the experimental results by calculating the ratio of the initial differential susceptibilities of the first magnetization curve and anhysteretic magnetization curves [Jile, Jile1, Jile2 and Zhan].

Equation (4.6) below represents the derivative of irreversible magnetization with effective field which is given by

$$\frac{dM_{irr}}{dH_e} = \frac{M_{anh} - M_{irr}}{k\delta} \tag{4.6}$$

The coefficient k is related to the pinning according to the Jiles-Atherton theory and it quantifies the energy on an average that is required to break the pinning site in a magnetic material during magnetization. δ represents the directional parameter that ensures that energy is always lost through dissipation [Jile, Jile1, Jile2 and Zhan].

$$\begin{cases} \delta = +1 & if \quad dH/dt \geq 0 \\ \delta = -1 & if \quad dH/dt < 0 \end{cases} \tag{4.7}$$

By combining the above equations, the main equation of the J-A model can be described as:

$$\frac{dM}{dH} = \frac{(1-c)\frac{dM_{irr}}{dHe} + c\frac{dM_{anh}}{dHe}}{1-\alpha(1-c)\frac{dM_{irr}}{dHe} - \alpha c\frac{dM_{anh}}{dHe}} \tag{4.8}$$

The differential equation represented in equation (4.8) allows to calculate the variations of the magnetization *M* with respect to applied magnetic field *H* variations. However, for some certain applications B imposed quasi-static model can be required. The details for the inverse version of the Jiles-Atherton model for the ferromagnetic materials can be found in [Sado, Leit], i.e. where the model input is *B*. The physical principles of the model remain similar but the main equation of this inverse Jiles-Atherton model is given by:

$$\frac{dM}{dB} = \frac{(1-c)\frac{dM_{irr}}{dB_e} + \frac{c}{\mu_0}\frac{dM_{anh}}{dH_e}}{1+\mu_0(1-\alpha)(1-c)\frac{dM_{irr}}{dB_e} - c(1-\alpha)\frac{dM_{anh}}{dH_e}} \tag{4.9}$$

With

$$\frac{dM_{irr}}{dB_e} = \frac{M_{anh} - M_{irr}}{\mu_0 k\delta} \tag{4.10}$$

And

$$B_e = \mu_0 . H_e \tag{4.11}$$

B_e represents the effective magnetic flux density.

4.2.1. The modified Jiles-Atherton model for the simulation of MIP

Fig. 4.6 demonstrates the issue of accommodation with the Jiles – Atherton model under unsymmetrical excitation H. Under the minor loops condition, the classical J-A model depicts a slower time for accommodation. It implies that the trajectory for magnetization between the turning points of a single minor loop does not close at its excursion's end (Fig. 4.6). It could be considered to be just a transient phase and a steady state could be reached when the ferromagnetic material is magnetically excited with a higher number of periods as illustrated in Fig. 4.7. This steady state attained is dependent on only H and not on the state of magnetization. As a result, the evolution of the modulus of the permeability $|\mu|$ versus H (MIP signature curve), instead of being a butterfly loop, is an anhysteretic curve as demonstrated in Fig. 4.8, which is far from the experimental observation.

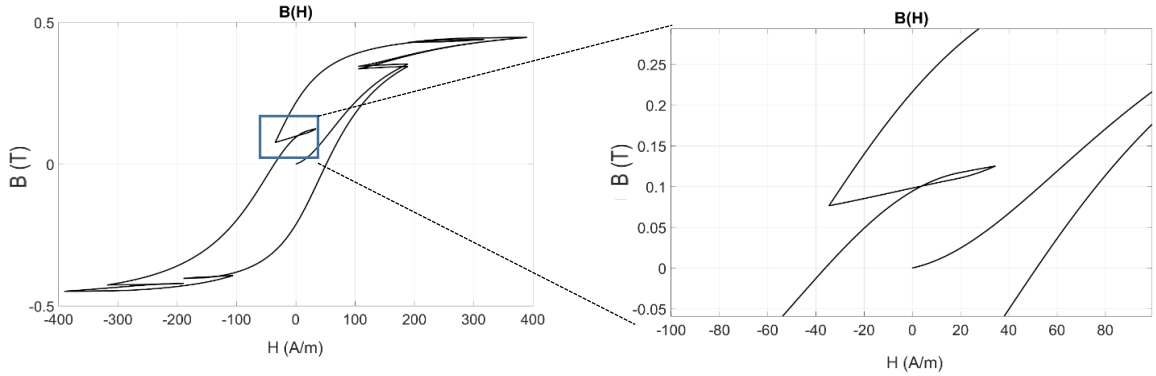

(a) Illustration of the accommodation issue with the J-A model under unsymmetrical excitation H.

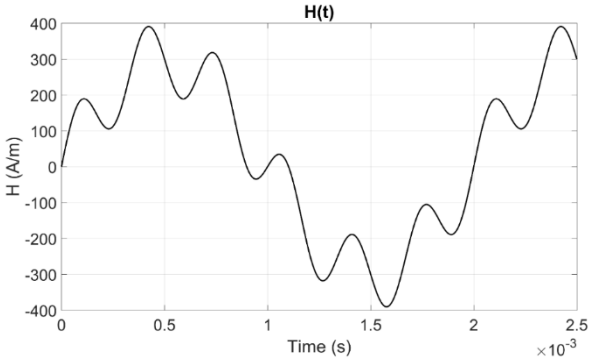

(b) Illustration of unsymmetrical excitation H.

Figure 4.6. Illustration of the accommodation issue with the J-A model under unsymmetrical excitation H.

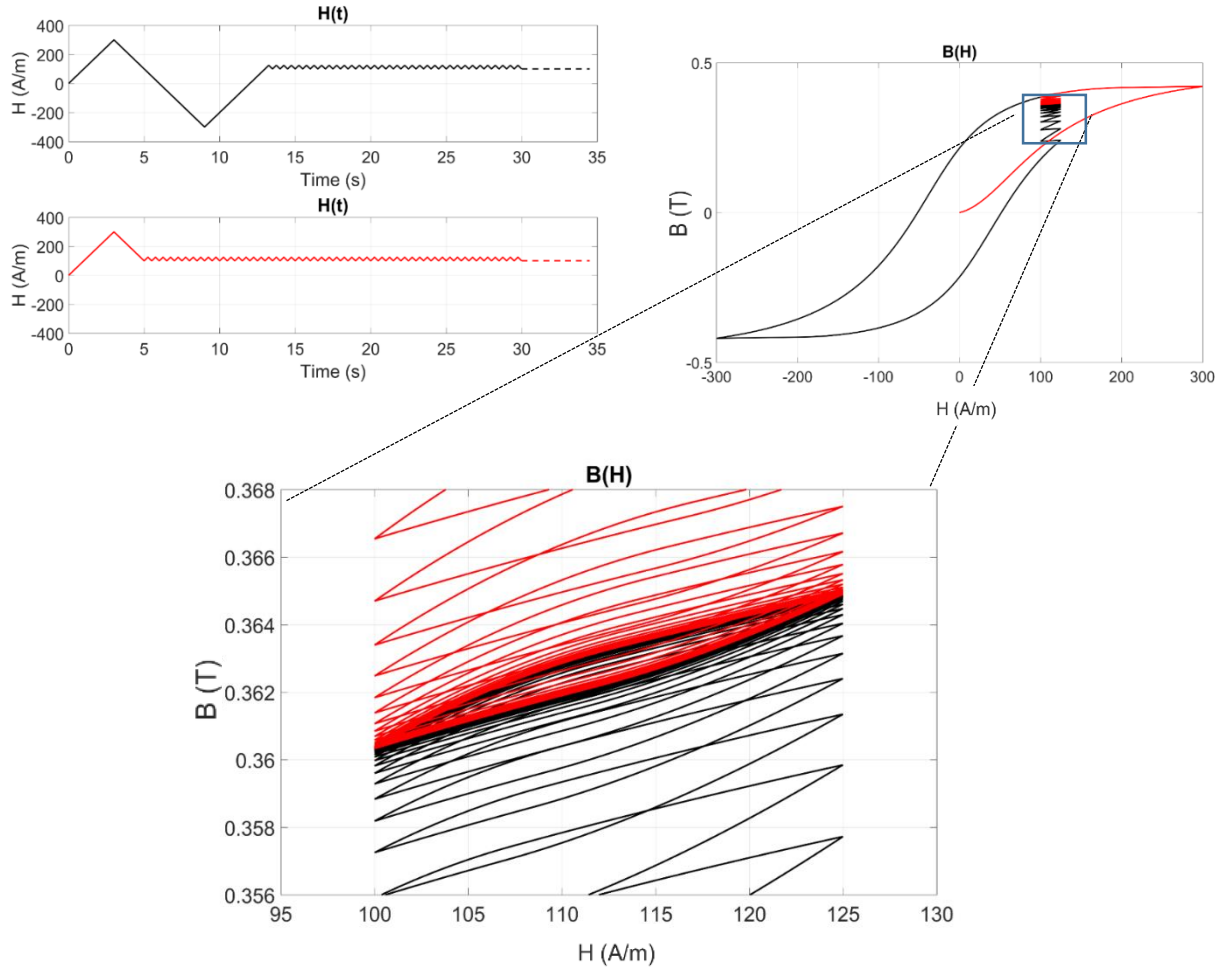

Figure 4.7. Illustration for the transient phase under minor loop situation with the J-A model

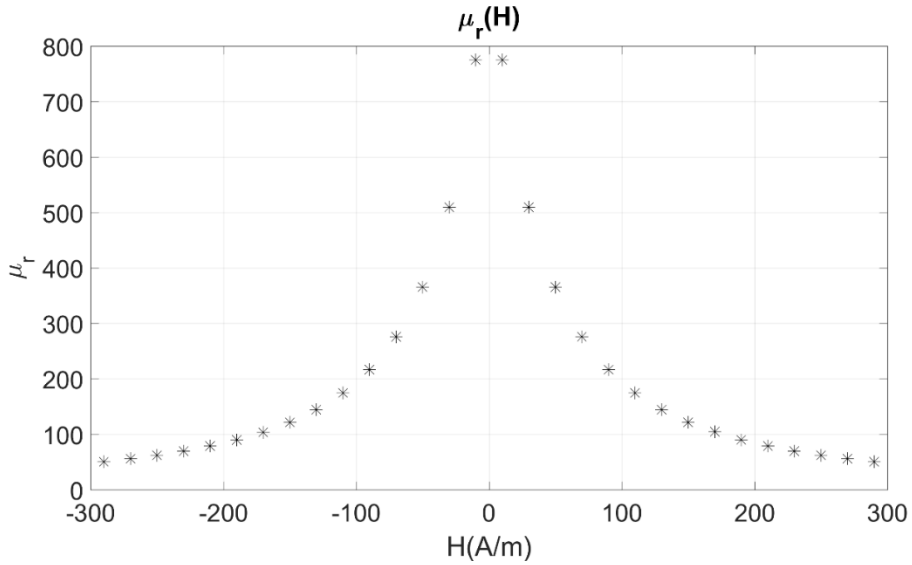

Figure 4.8. Illustration for the transient phase under minor loop situation with the J-A model.

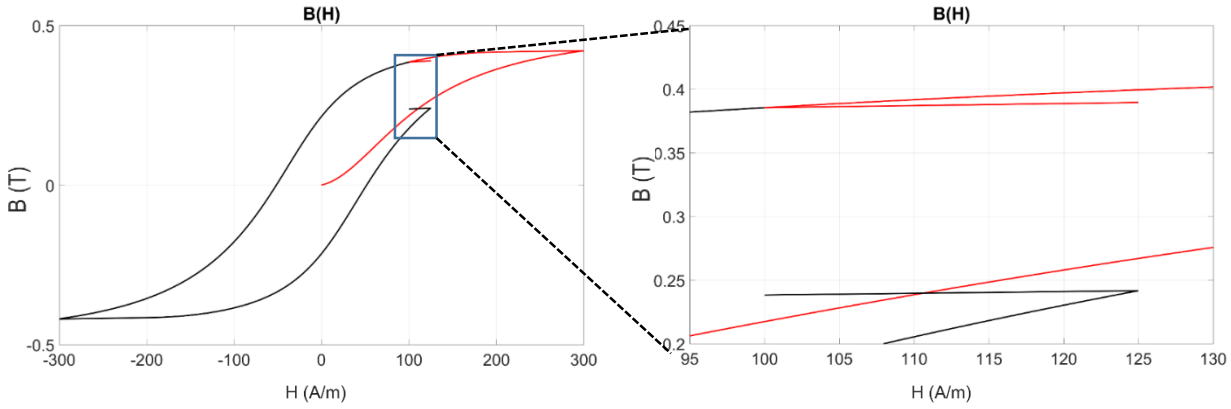

Figure 4.9. – Illustration for the single slope consideration under minor loops situation.

In order to solve this issue of accommodation, it is assumed that $\left|\overrightarrow{H_{AC}}\right|$ is weak enough and also by ignoring the hysteretic behavior of the minor cycles. In such a case, minor loops are then treated as a single slope as demonstrated also in [Gabi, Gabi1]. Fig. 4.9 illustrates the single slope behavior.

The $|\mu|$ versus H curve obtained with this approach is a typical MIP butterfly curve and resembles the experimental one. As a next step, the 5 J-A parameters are used as degrees of freedom in the simulation process.

4.3. Magnetic and electric quantities interdependence

From the empirical point of view, the information that can be extracted is the excitation magnetic field H(t) as well as the pick-up coil's voltage V(t). However, on the other hand, the numerical simulations provide the time variations of the magnetic quantities such as the magnetic excitation field H(t), the induced magnetic field B(t) and the permeability μ(t). Hence, a link between the magnetic as well as the electrical quantities must be established to validate the model for comparison with the experimental results.

To establish the link, a reluctance/impedance lump-type model typography is used. Both magnetic and air type reluctances are required for the inductance simulation. By considering the air reluctance to be highly superior to the magnetic reluctance, the number of equations can be reduced and finally a relation between the time variations of the real as well as the imaginary part of the complex permeability and the sensor voltage is established as follows:

$$V^* = j\lambda_1 + \lambda_2(-\mu'' + j\mu') \quad (4.12)$$

where λ_1, λ_2, are constants that are dependent on the nature and the geometry of the material. It can be seen in the equation above that the real part of the voltage is associated with imaginary part of the permeability and vice versa- the imaginary part of the permeability to the real part of the voltage. These constants can be derived by comparing the simulations and the experimental measurements using the results obtained from the virgin sample which is also considered as the reference sample in this case. Once these constants are set, they are kept same for all others simulations results for the rest of the samples.

4.4. Optimization of the modelling parameters

In order to perform these simulations, a total of 7 parameters must be evaluated – 5 parameters from the J-A model (Ms, a, α, k, c) and the two magnetic/electrical parameters(λ_1, λ_2). The latter are determined by comparing the simulations with the experimental data of the virgin sample. These parameters are conserved for the simulation of the rest of the samples. For the determination of Jiles-Atherton parameters, the first step is to calculate the average value H_i^{ave} of H_i^{inc} and H_i^{dec} for every given B_i of every sample's major hysteresis loop B(H):

$$H_i^{ave}(B_i) = \frac{H_i^{inc}(B_i) + H_i^{dec}(B_i)}{2} \quad (4.13)$$

where H_i^{inc}/H_i^{dec}stands for the value of H for the increasing or decreasing part of the major hysteresis loop. The $H_i^{ave}(B_i)$ curve that is obtained can be considered to be relatively closer to the actual anhysteretic curve. The two Jiles-Atherton anhysteretic parameters, M_s and a, are then calculated by fitting this curve to the simulated curve by using the curve fitting toolbox in Matlab™.

The first optimized and relatively accurate simulation results are obtained with insignificant variations in both the anhysteretic parameters M_s and a. Hence, both of these parameters are fixed and set. The optimization process then depends on the remaining 3

Table 4.1. Constant parameter values used in the simulation process

a(A/m)	M_s(A/m)	λ_1	λ_2
10020	2.00E+06	12.9	0.0453

parameters (α, k, c). Table 1 below shows the values of all the constant parameters used during the simulations.

As a final step in the optimization process, the comparisons between simulated and experimental MIP butterfly curves are used to calculate the remaining 3 J-A parameters. To calculate these parameters, a dedicated error function is proposed. The final value of these parameters, α, k and c, is chosen when their combination results in the minimum error function value:

$$dH/dt > 0, \qquad H \in [H_{\min}, H_{\max}]$$
$$Error = \sum_{i=1}^{n} abs\left(|\mu|_i^{\exp}(H_i) - |\mu|_i^{sim}(H_i)\right) \tag{4.14}$$

where μ^{exp} is the experimental modulus derived from the coil's voltage using equation 4.14 and μ^{sim} is the simulated one.

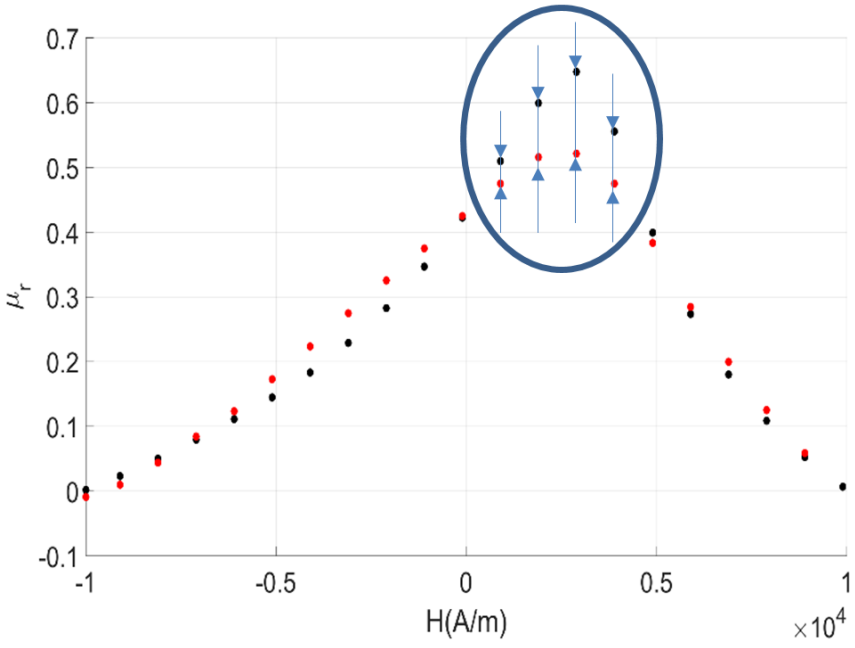

Figure 4.10. Illustration of optimization process

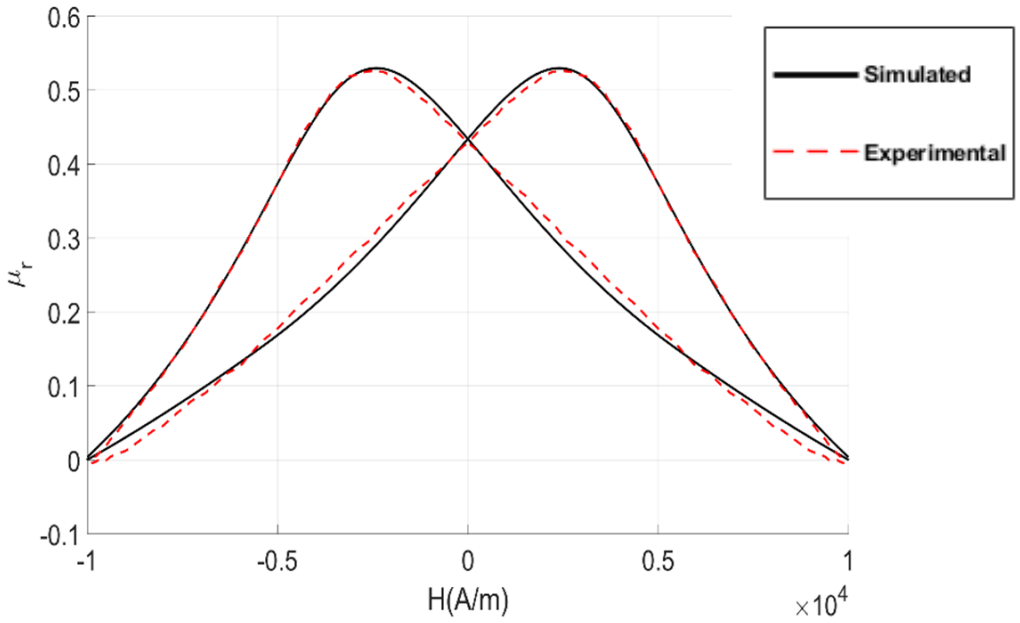

Figure 4.11 Illustration for the optimization process of fitting curves

Later in this study, a very similar function (equation 14) has been used to set the Jiles-Atherton model parameters for the case of Hysteresis B(H) measurements:

$$dH / dt > 0, \qquad H \in \left[H_{\min}, H_{\max}\right]$$
$$Error = \sum_{i=1}^{n} abs\left(\left|B\right|_i^{\exp}(H_i) - \left|B\right|_i^{sim}(H_i)\right) \tag{4.15}$$

Where B^{exp} is the experimental induction and B^{sim} the simulated one. Just as for the MIP case, considering the symmetry of the hysteresis cycle, the comparisons are performed on the increasing part of the curve (dH/dt>0), the combination of parameters is set when the error function reach its minimum.

4.5. Sensitivity check for derived parameters

From the curve fitting, a combination of J-A parameters is derived when the error function described in eq. 4.15 is minimum. These set of parameters are dependent on each other. Hence, to check the sensitivity of these parameters, one parameter is varied keeping the rest as constant. Fig. 4.12 illustrates the effect of each parameter on the curve fitting revealing high sensitivity. Even with a variation of 2%-3%, the fitting of the curve changes significantly.

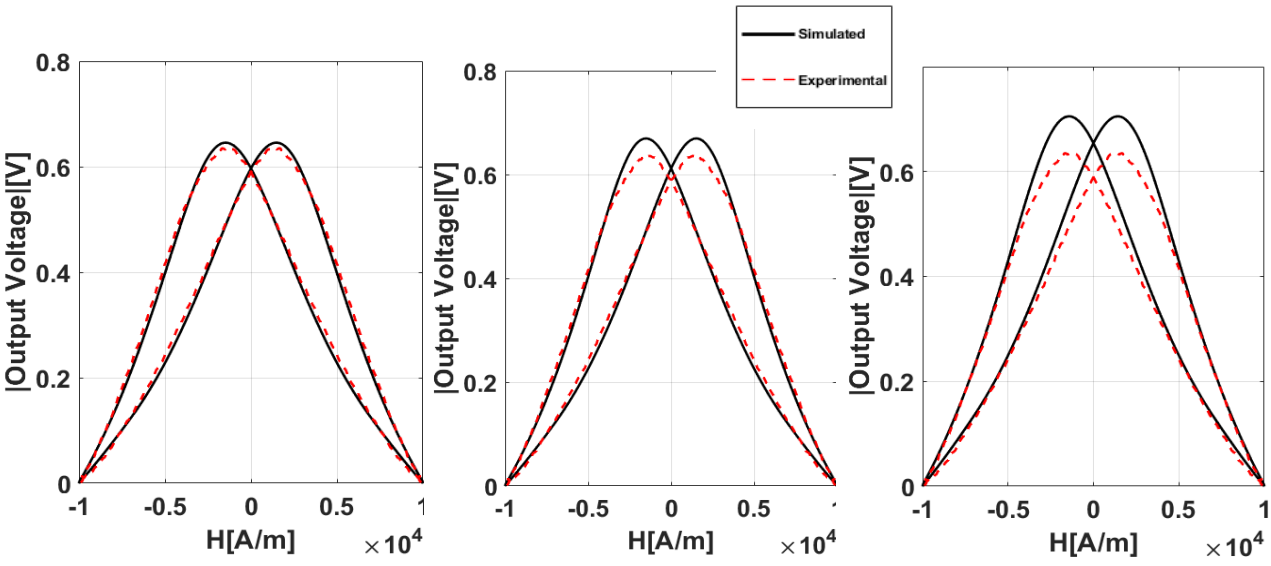

(a) Sensitivity check with parameter values, α=0.0104, c=0.32, k=3300

(b) Sensitivity check with parameter values α=0.0107, c=0.32, k=3300

(c) Sensitivity check with parameter values, α=0.0104, c=0.34, k=3300

Figure 4.12. Illustration of sensitivity for the set of J-A parameters post curve fitting

4.6. Results and discussion

Fig. 4.13 depicts a comparison of the simulated curves with the experimental results The modeled MIP curves showcase relatively a very good agreement to the experimental measurements obtained from the tested samples (although minor differences still exist in the coercivity region). The value of these parameters that are derived from optimization process are then evaluated against the microstructural data of the materials such as the number of precipitates and the average of KAM, as shown in Fig. 4.14 and Fig. 4.15.

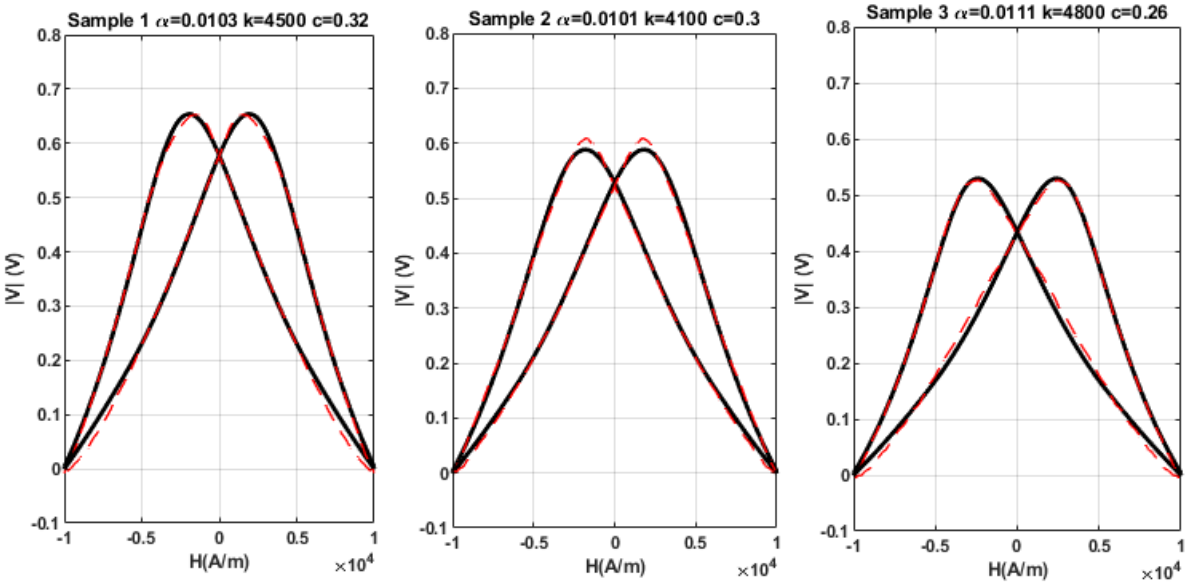

(a). Comparisons of simulated and measured MIP curves (Sample 1-3)

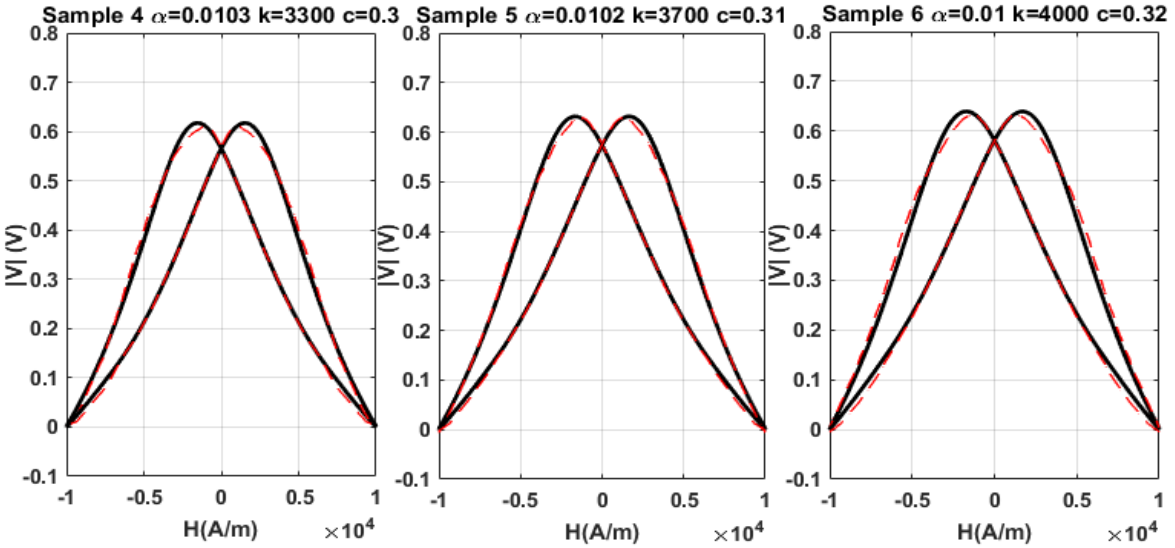

(b). Simulated and Experimental MIP curves (Samples 4-6)

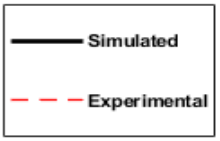

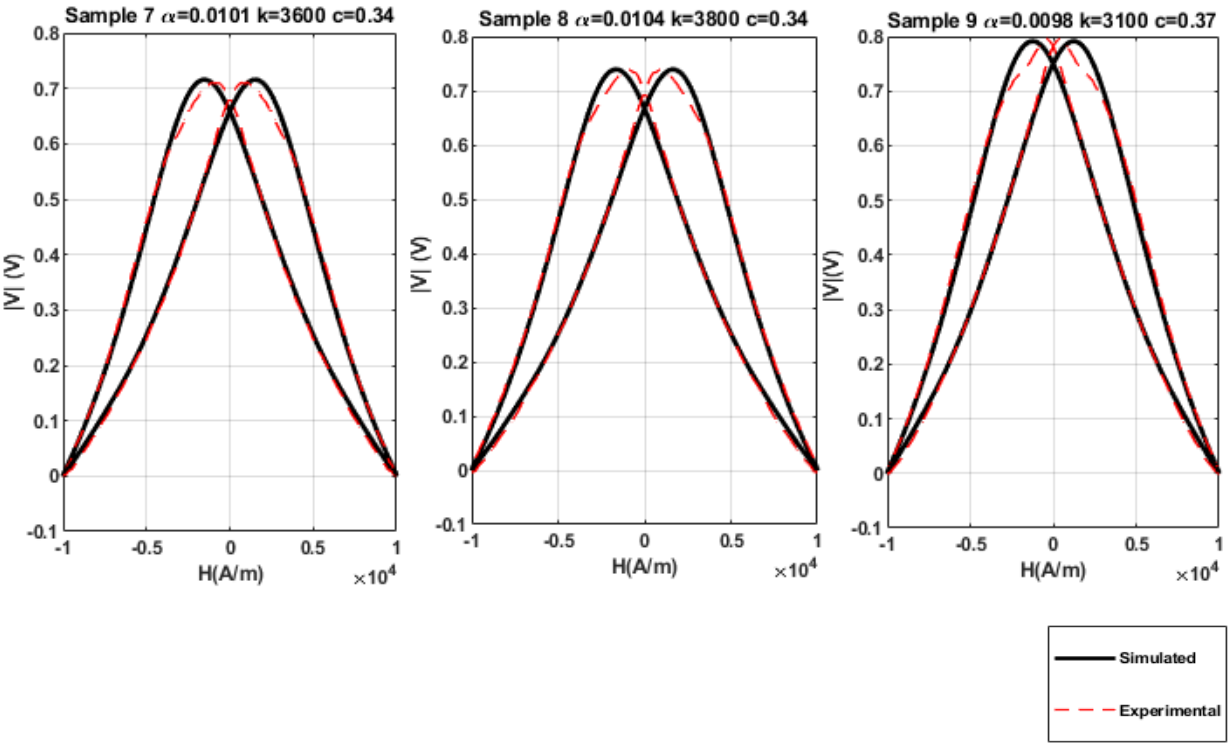

(c). Simulated and Experimental MIP curves (Samples 7-9)

Figure 4.13. Comparisons of Simulated and Experimental MIP curves (Samples 1-9)

4.6.1. Evolution of the Jiles-Atherton(J-A) parameters versus microstructure

4.6.1.1. J-A parameters vs. Number of Precipitates

Fig. 4.14 below illustrates the evolution of Jiles-Atherton model derived parameters against the materials' microstructure. One of the J-A model parameters, α, that represents the inter domain coupling according to the Jiles-Atherton theory, its evolution is shown in Fig. 4.14(a) against the precipitates. In Chapter 2, it was shown that in the category of 550°C temperature treated samples, the size of precipitates is smaller. As the size of precipitates is smaller in this case, it would imply higher interactions between the domains in the material, it would lead higher inter-domain coupling, hence a higher value of α, which is case demonstrated in the figure below. On the contrary for 650°C temperature treated samples, the size of the precipitates is much bigger which would lead to lesser interactions between the domain walls and hence lower value of α as demonstrated in the figure below.

The second J-A parameter evaluated here is *k*, which represents the average energy required to break the pinning site. In the category of 550°C temperature treated samples, there are a much higher number of precipitates per unit area than the samples from higher temperature category. These precipitates (representing the carbide content) sometimes can act as a pinning site and can play a vital role in the expansion of domain sizes. Hence, higher the number of precipitates higher would be the area of precipitates, and overall, it would require more energy to break the pinning site. Therefore, the value of k, is higher in the lower temperature treated samples. As was discussed in Chapter 2, the crystal size in the higher temperature treated samples is much larger than the lower temperature treated samples. Additionally, in the higher temperature treated samples, the misorientation are much lesser. This means that the permeability of these samples would be much higher and so would be the magnetic reversibility for these samples, which is represented by *c* according to J-A theory and is illustrated in the figure below.

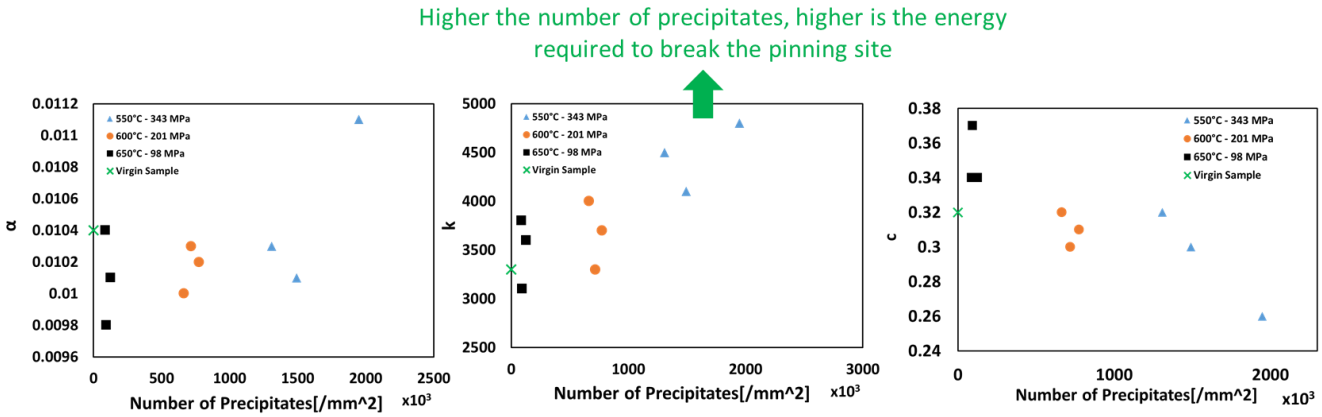

(a) Evolution of α vs. Precipitations

(b) Evolution k vs. Precipitations

(c) Evolution of c vs. Precipitations

α: inter-domain coupling in the magnetic material
k: average energy required to break pinning site
c: magnetization reversibility

Figure 4.14. Evolution of J-A parameters versus Number of Precipitates in case of MIP

4.6.1.2. J-A parameters vs. Average of Kernel Average Misorientation (KAM)

Fig.4.15 below illustrates the tendencies of J-A parameters against the Kernel Average Misorientation (KAM). In Chapter 3 it was demonstrated experimentally that KAM doesn't show much good correlations with respect to magnetic parameters. Similarly, in the model derived parameters, higher variations are observed only in higher temperature samples. Although, as we know from Chapter 2, 550°C temperature treated samples have higher misorientation and dislocation than that of higher temperature samples, this would also mean higher would be the energy required to break the pinning site which is also illustrated by the figure below (k parameter). As higher temperature treated samples have lesser misorientation, the magnetic reversibility would be much higher in this case as illustrated by the evolution of c in the figure below. Evolution of c against KAM is very similar to evolution of cross point against KAM studied in Chapter 3.

.

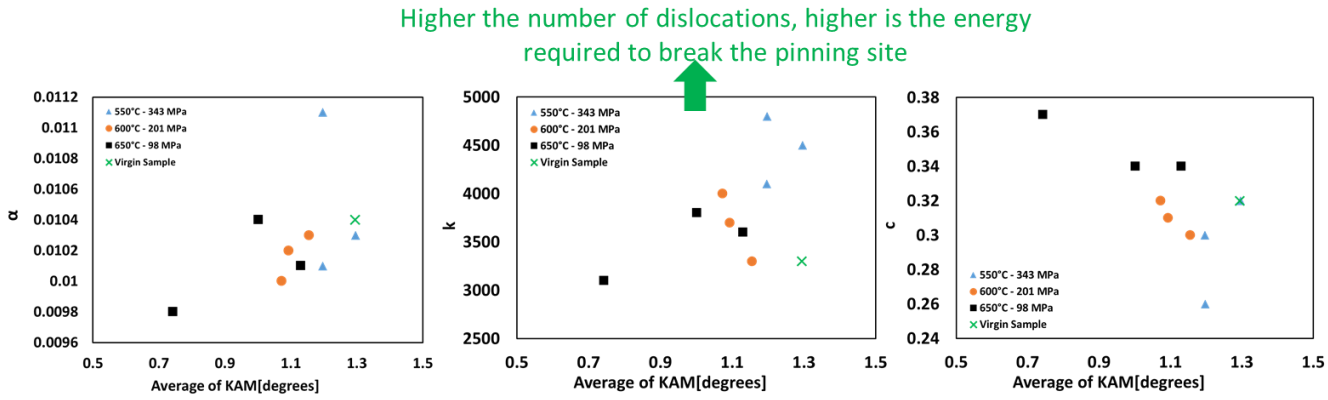

(a) Evolution of α vs. Average of KAM

(b) Evolution of k vs. Average of KAM

(c) Evolution of c vs. Average of KAM

α: inter-domain coupling in the magnetic material
k: average energy required to break pinning site
c: magnetization reversibility

Figure 4.15. Evolution of J-A parameters vs. Average of KAM

4.7. Modelling of B(H) curves

Following to the model optimization detailed in section 4.4., Hysteresis curves are simulated for each sample as below and the corresponding tables represent the derived parameters from the simulated curve

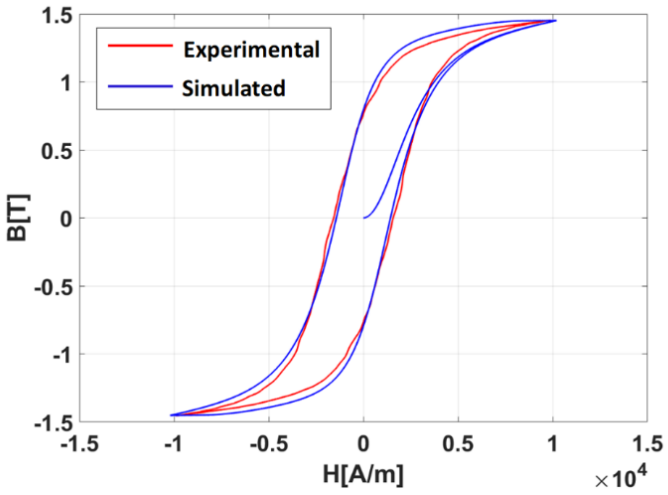

Parameter	α	k	c
Derived Value	0.0004	1300	0.0001

Figure 4.16. Simulated and Experimental Hysteresis cycle for Sample 1 and the corresponding derived J-A parameters

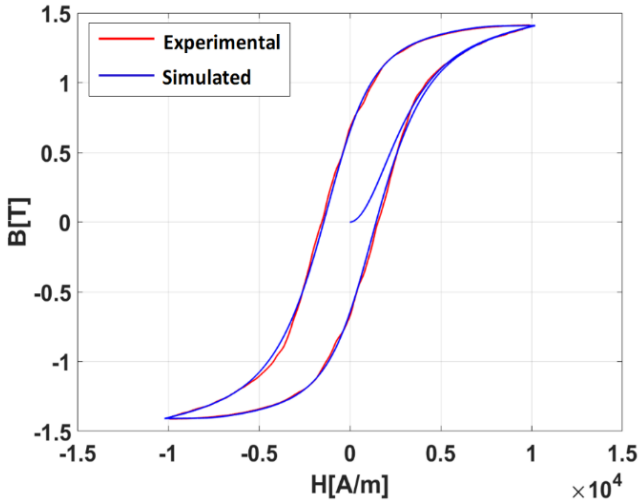

Parameter	α	k	c
Derived Value	0.0005	1400	0.0001

Figure 4.17. Simulated and Experimental Hysteresis cycle for Sample 2 and the corresponding derived J-A parameters

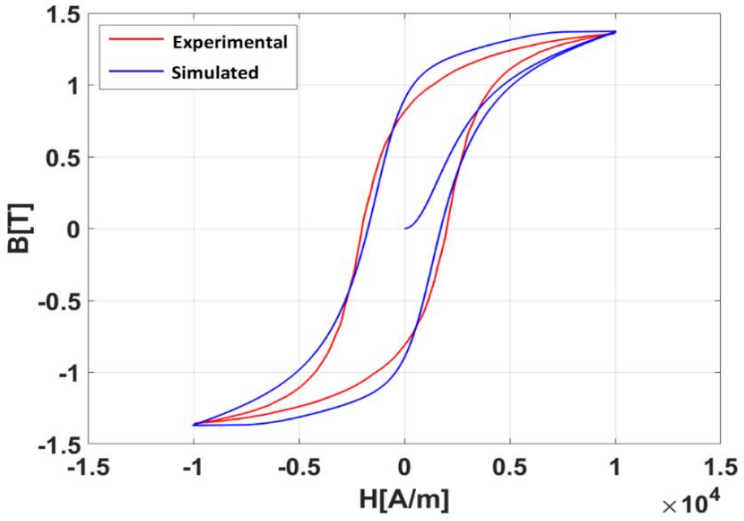

Parameter	α	k	c
Derived Value	0.0008	1700	0.001

Figure 4.18. Simulated and Experimental Hysteresis cycle for Sample 3 and the corresponding derived J-A parameters

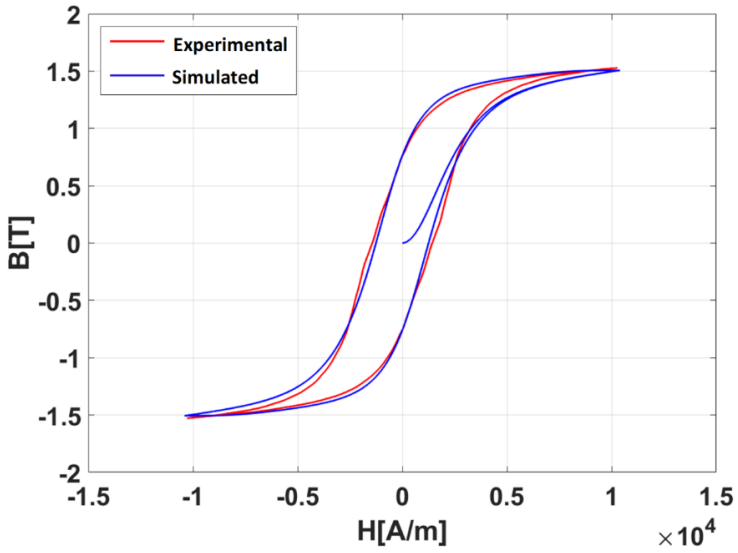

Parameter	α	k	c
Derived Value	0.0006	1600	0.001

Figure 4.19. Simulated and Experimental Hysteresis cycle for Sample 4 and the corresponding derived J-A parameters

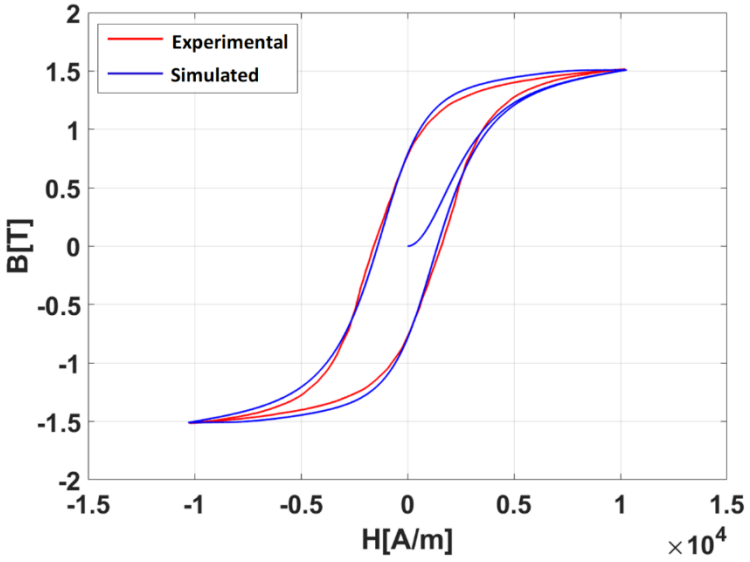

Parameter	α	k	c
Derived Value	0.00034	1600	0.01

Figure 4.20. Simulated and Experimental Hysteresis cycle for Sample 5 and the corresponding derived J-A parameters

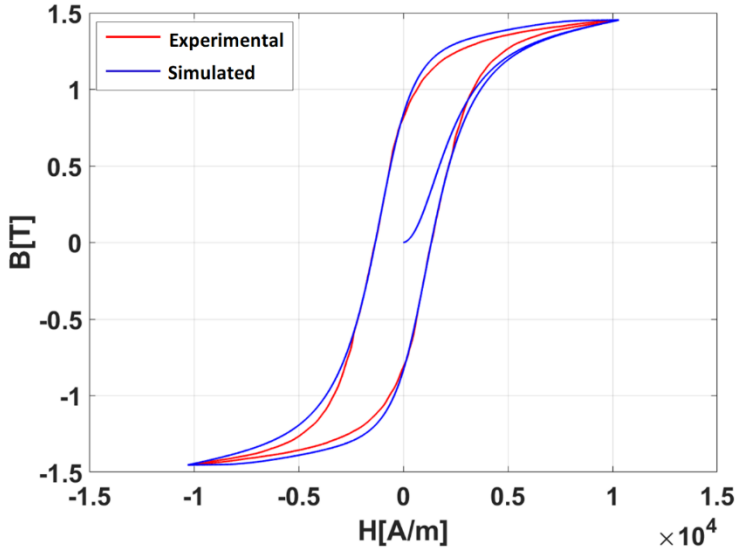

Parameter	α	k	c
Derived Value	0.0005	1720	0.001

Figure 4.21. Simulated and Experimental Hysteresis cycle for Sample 6 and the corresponding derived J-A parameters

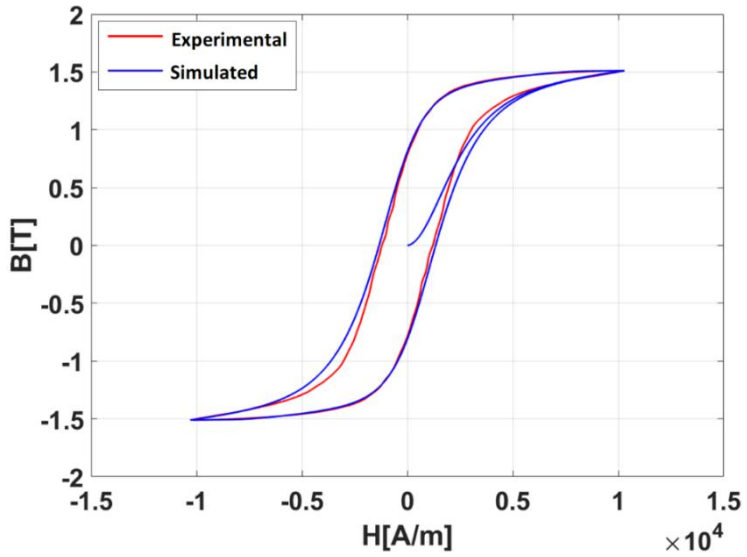

Parameter	α	k	c
Derived Value	0.0004	1510	0.14

Figure 4.22. Simulated and Experimental Hysteresis cycle for Sample 7 and the corresponding derived J-A parameters

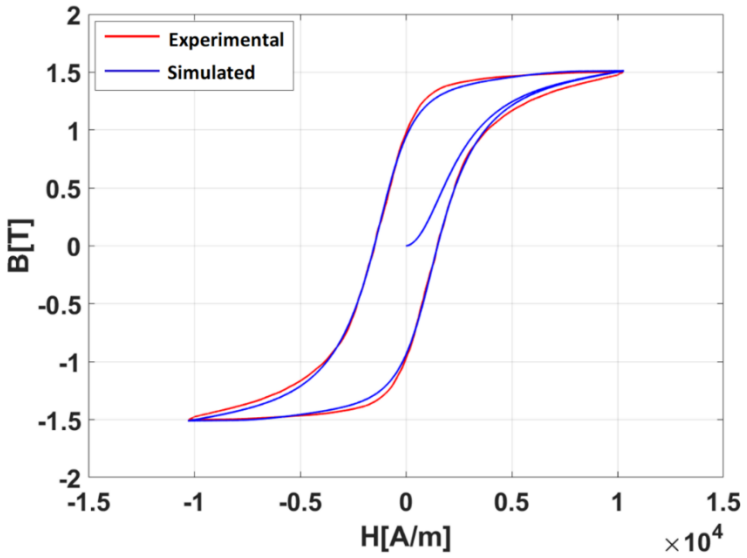

Parameter	α	k	c
Derived Value	0.0004	1490	0.06

Figure 4.23. Simulated and Experimental Hysteresis cycle for Sample 8 and the corresponding derived J-A parameters

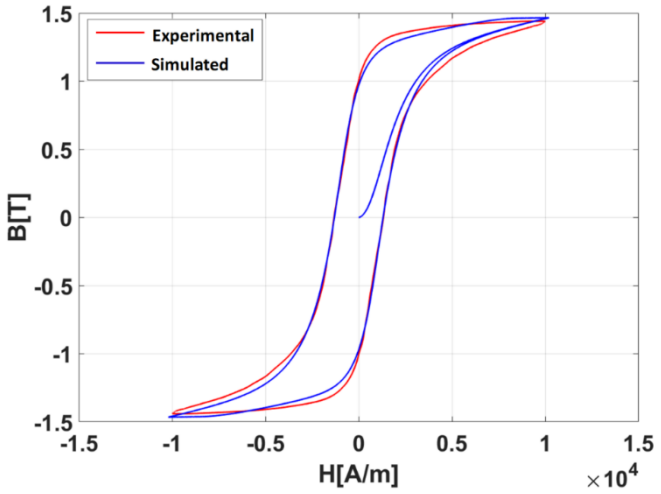

Parameter	α	k	c
Derived Value	0.00006	1300	0.001

Figure 4.24. Simulated and Experimental Hysteresis cycle for Sample 9 and the corresponding derived J-A parameters

4.8. Modelling Parameters (B(H)) versus Microstructure and Mechanical Properties

In this section the modelling parameters that are derived from the simulated hysteresis curves are evaluated against various parameters and a physical interpretation is drawn.

Out of all the parameters derived from the simulation, in B(H), α, is the only parameter that was the most relevant. Hence, in this section, the comparison of α versus Larson Miller Parameter(LMP), Number of precipitates and Average of KAM is given. Fig. 4.25 below shows the evolution of α with respect to LMP. As was evident in the previous experiments, it was noticed that the tendency of lower temperatures vs. higher temperatures is opposite. The ruptured samples are represented with a bigger mark. α is observed to be increasing with the increase in the LMP value for lower temperature treated samples whereas it is decreasing in case of higher temperature samples.

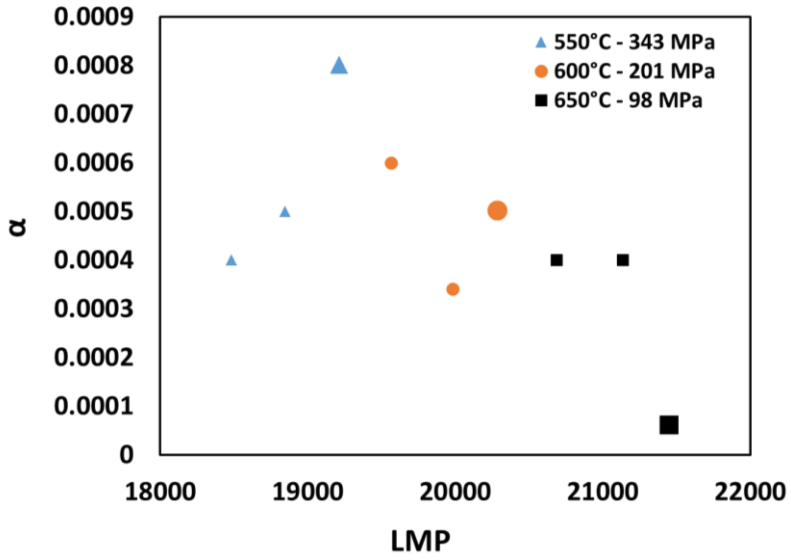

Figure 4.25. α versus LMP demonstrating the opposite behaviour in case of lower and higher temperature treated samples

Figure 4.26 below shows the comparison of α versus the number of precipitates. The physical meaning of α according the Jiles-Atherton theory is that it represents the extent of inter-domain coupling. Hence, lower the size of the precipitates in the material, higher would be the inter-domain coupling which is also the case represented by the Fig. 4.26 below. As mentioned in Chapter 2, Average of KAM was an inadequate parameter to analyse creep in samples, hence was the similar case in B(H) measurements. However, in the next section a correlation coefficient is shown for both MIP and B(H) for these parameters versus microstructure and the mechanical properties.

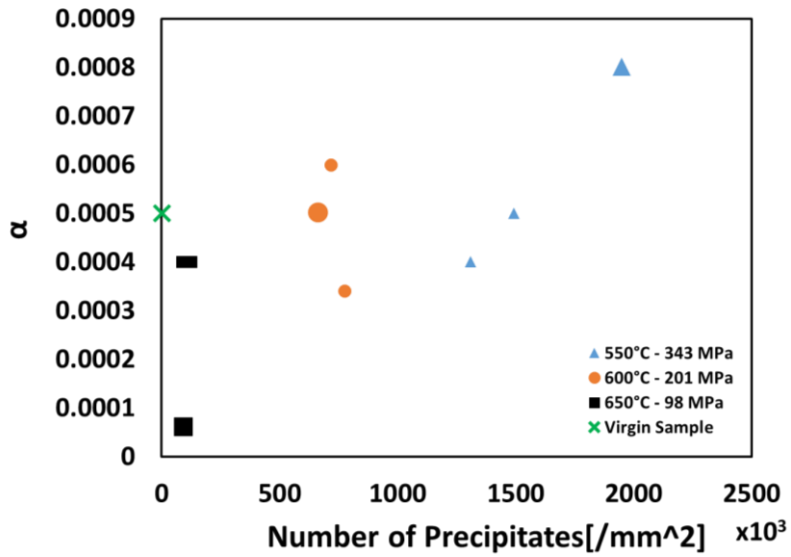

Figure 4.26. α versus number of precipitates demonstrating the opposite behaviour in case of lower temperature higher temperature samples

4.9. Pearson correlation coefficient analysis for MIP and B(H) derived modelling parameters

On fitting with the experimental data, multiple parameters can be accessed using the Jiles-Atherton model as described before. In order to validate the parameter and understand it well, a correlation is investigated among these parameters with respect to multiple microstructural parameters as well as mechanical parameters as shown in Fig.4.27-4.29. For this purpose, a well-known correlation coefficient is used, Pearson correlation coefficient, which can be defined as the measure of the strength of association within the two different variables. Mathematically,

$$\rho_{X,Y} = \frac{cov(X,Y)}{\sigma_X \sigma_Y} \tag{4.16}$$

Where, σ is the standard deviation of the variables (X,Y) and cov is the covariance.

In the figures below (Fig. 4.27-4.29), each of three parameters (α, k and c) are studied using the data based on MIP and B(H) measurements. Jiles-Atherton parameters were adjusted optimally for each and every sample for both MIP measurements as well as B(H) measurements.

The final objective of using the Pearson correlation coefficient is to be able to the assess the extent of correlation between the modelling parameters derived from MIP & B(H) with the microstructural changes occurring in the material as the creep time changes in the materials. Closer is the value of the correlation factor to 1/-1, higher is the correlation (either positive or negative). It is worth observing that the absolute value of the correlation factor in the case of Magnetic Incremental Permeability is closer to 1 for almost against all parameters. On the other hand, in the case of modelling parameters derived from B(H) simulations, the correlation is good and considerable only in the case of α parameter.

The possible reason and explanation is that the in case of B(H) measurements, access to the information about the first magnetization curve that is related to the magnetic reversibility coefficient (c) is lacking. This also implies that when B(H) measurement is performed, some information about the samples get missed out (average information) and MIP provides more information (since it is a very local and focussed

measurement) about the sample such as magnetic reversibility. Hence, variations of c and k limit the influence of the overall B(H) curve. On the contrary, Magnetic Incremental Permeability measurement investigates the local permeability with a bias magnetic field, and therefore, it is much more sensitive to all the three J-A parameters investigated. It is also worth noticing that the parameters which show positive correlation remain positive for both the measurements, MIP as well as B(H) and the negative ones remain negative throughout as well.

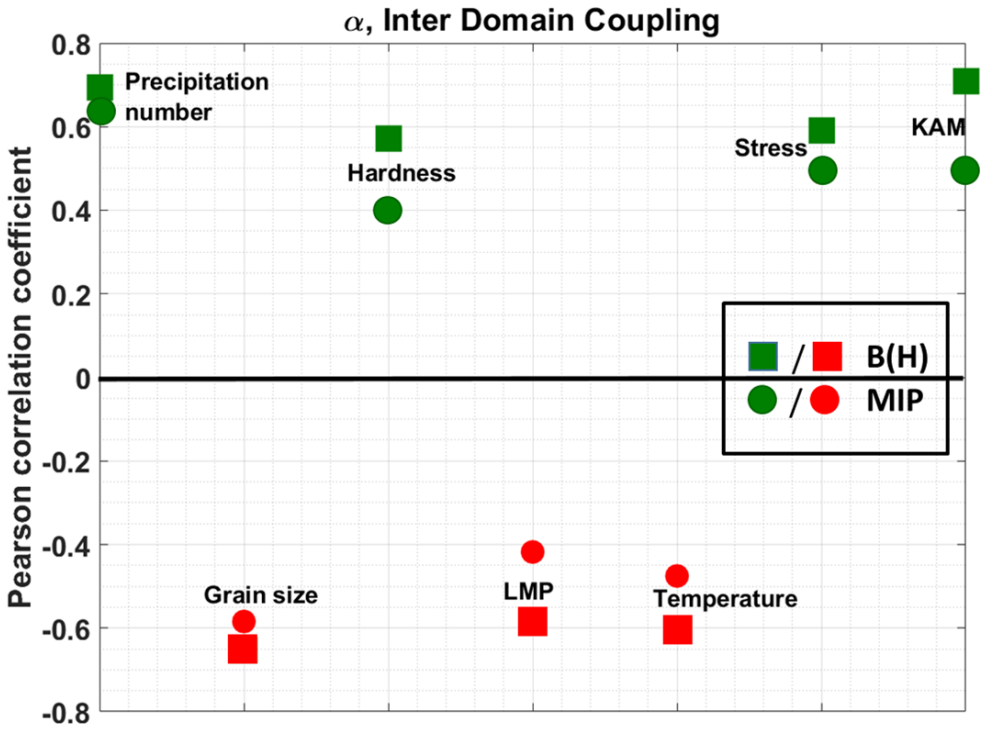

Figure 4.27. Pearson correlation factor for α with microstructural as well as mechanical parameters

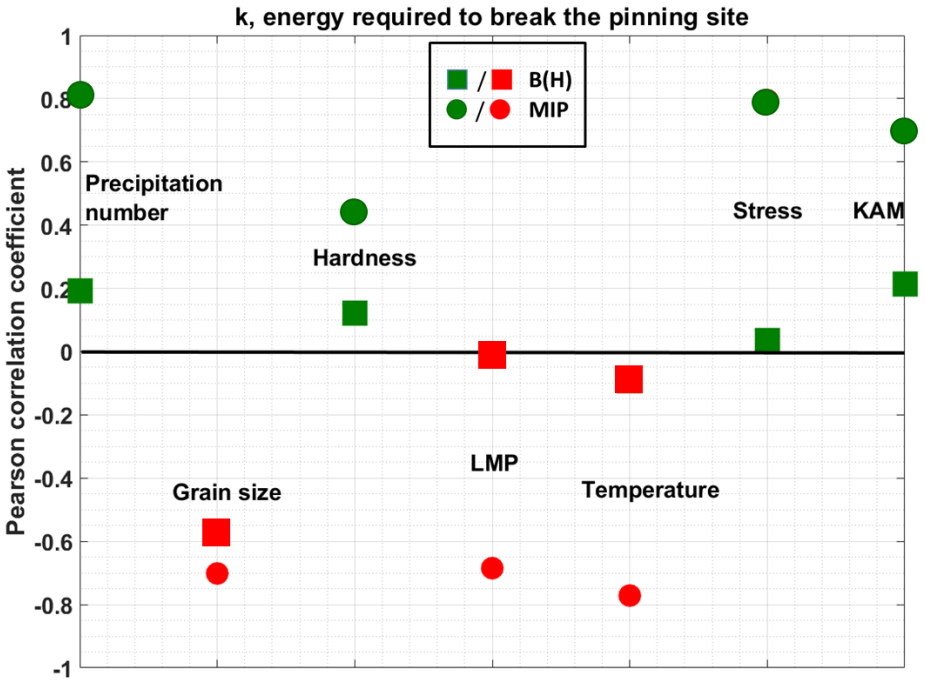

Figure 4.28. Pearson correlation factor for k with microstructural as well as mechanical parameters

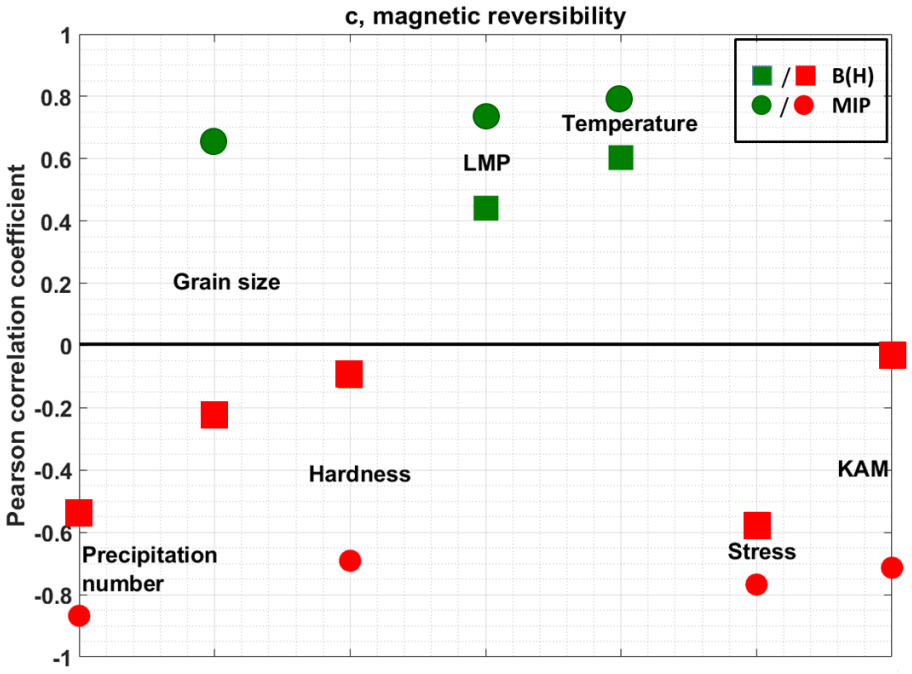

Figure 4.29. Pearson correlation factor for c with microstructural as well as mechanical parameters

4.10. Tendency of Modelling Parameters

Now that the modelling parameters have been derived and their correlation is established, it has to be noted that the absolute value of these parameters are not significant. These values will vary according to the experimental set-up involved. Hence, what is worth enquiring about is their tendency, how these parameters evolve. Following figures below show that these parameters show an opposite evolution behaviour as expected when lower and higher temperature samples are compared.

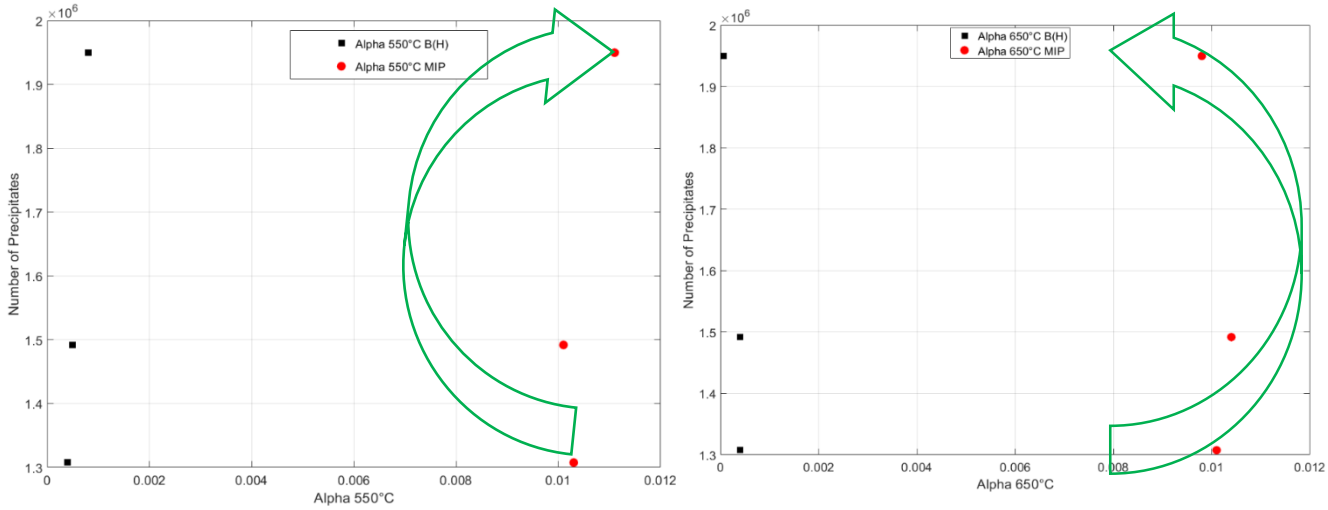

(a). Tendency of Alpha parameter in case of 550°C samples demonstrating similar tendencies in case of B(H) and MIP

(b). Tendency of Alpha parameter in case of 650°C samples demonstrating opposite tendencies to that of 550°C samples

Figure 4.30. Tendency of Alpha parameter in case of lower and higher temperature treated creep samples

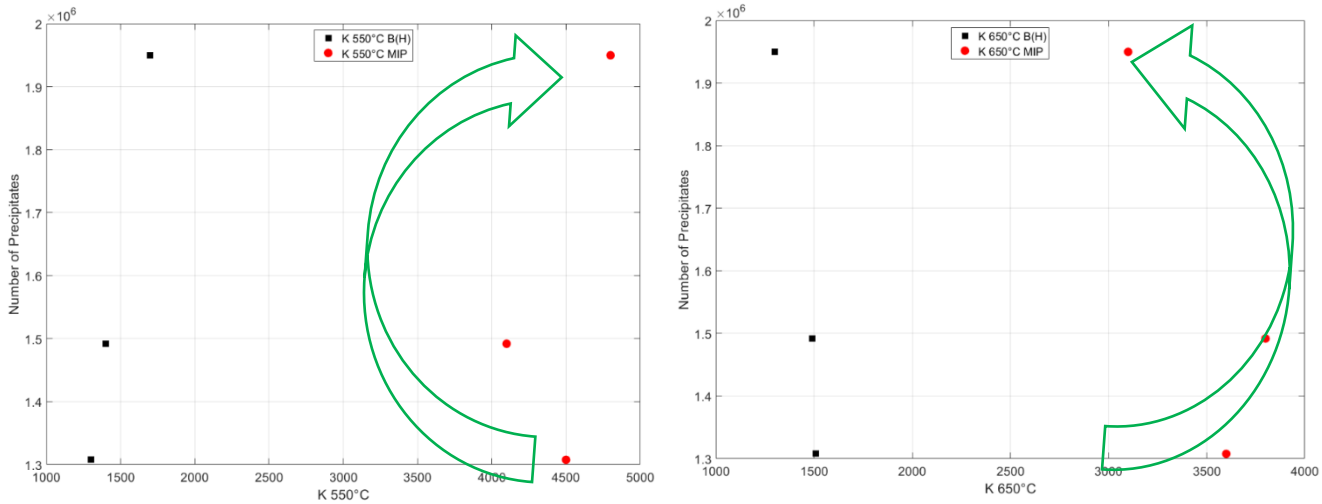

(a). Evolution of k parameter in case of B(H) and MIP for 550°C treated samples

(b). Evolution of k parameter in case of B(H) and MIP for 650°C treated samples

Figure 4.31. Tendency of k parameter in case of lower and higher temperature treated creep samples

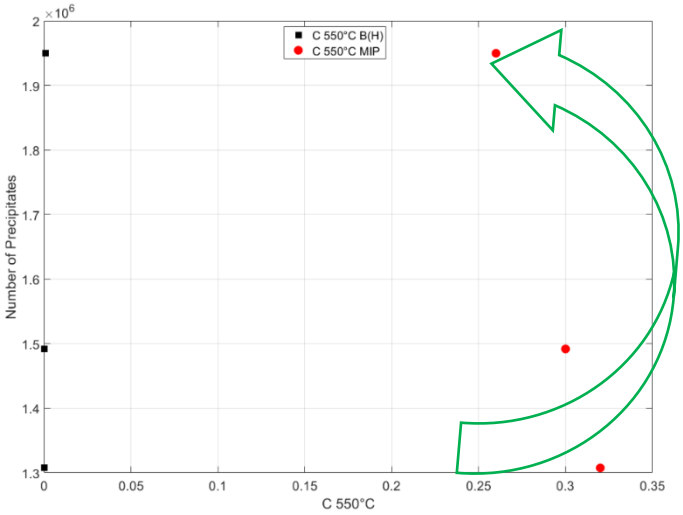

(a). Evolution of c parameter in case of B(H) and MIP for 550°C treated samples

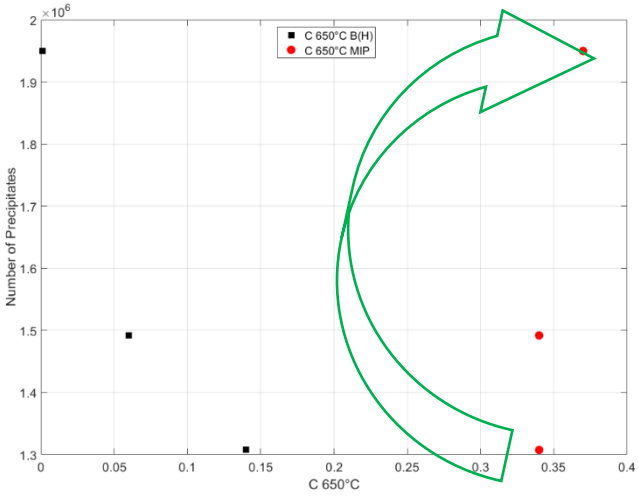

(b). Evolution of c parameter in case of B(H) and MIP for 650°C treated samples

Figure 4.32. Tendency of c parameter in case of lower and higher temperature treated creep samples

4.10.1. Tendency of Modelling Parameters based on rupture time

In the following Fig. 4.33, the tendency of evolution of parameters for lower, 550°C, and higher temperature, 650°C, is illustrated. It is quite evident that the parameters evolve in the opposite manner as expected from the behaviour of the materials. Fig. 4.34 also shows the evolution of parameters in case of B(H) samples for α.

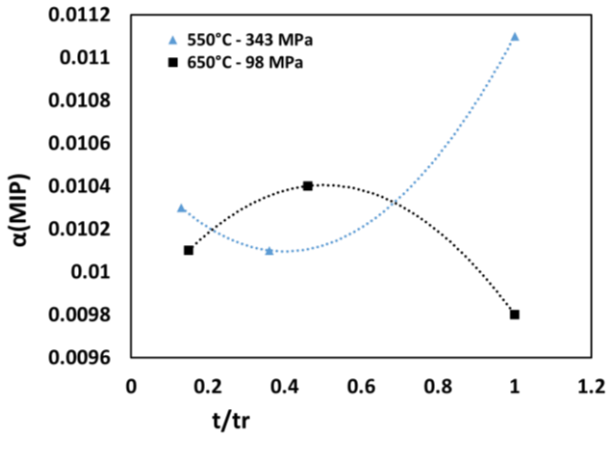

(a). Evolution of α parameter demonstrating opposite tendencies in case of 550°C and 650°C treated samples (in case of MIP)

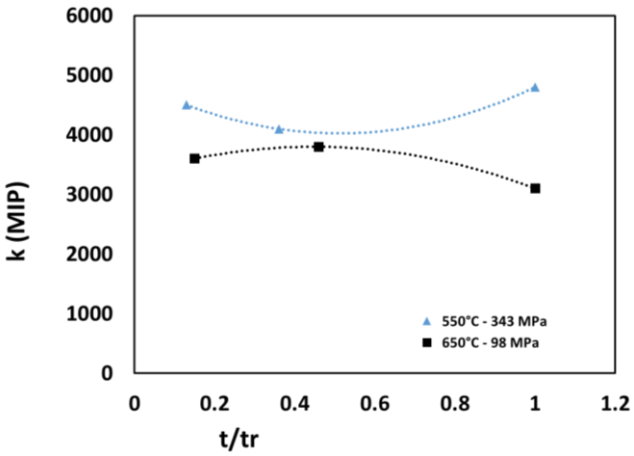

(b). Evolution of k parameter demonstrating opposite tendencies in case of 550°C and 650°C treated samples (in case of MIP)

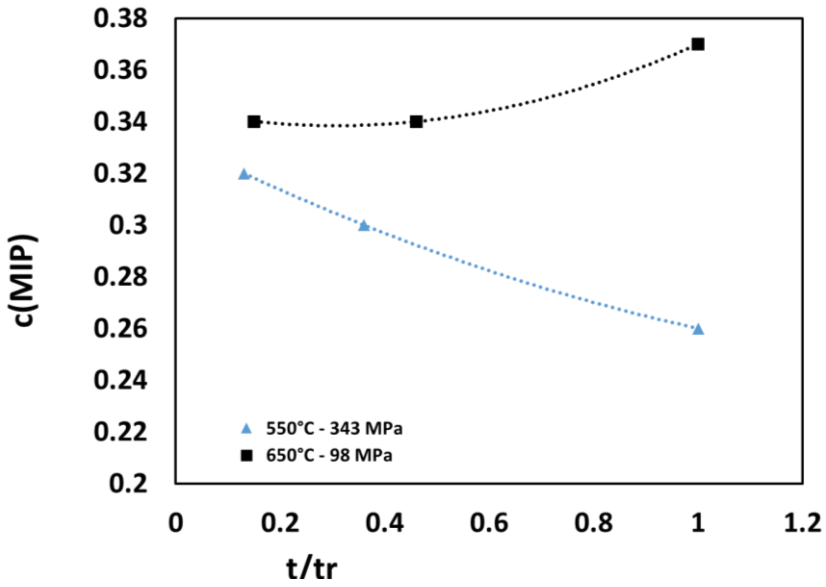

(c). Evolution of c parameter demonstrating opposite tendencies in case of 550°C and 650°C treated samples (in case of MIP)

Figure 4.33. Modelling parameters evolution versus rupture time for MIP

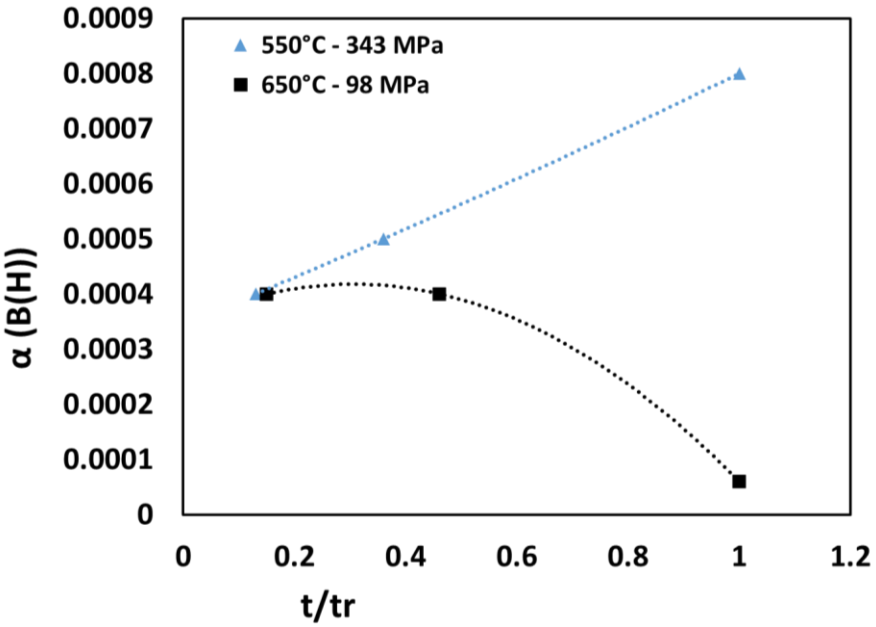

Figure 4.34. Evolution of α parameter versus rupture time for B(H) demonstrating opposite evolution for lower and higher temperature treated samples

4.11. Summary

In this chapter, Jiles-Atherton model was applied to magnetic signatures derived experimentally using MIP in chapter 3 on the same set of high chromium creep steel samples to further quantify the results obtained experimentally. Using Jiles-Atherton model and adapting it to magnetic signals gives access to three model parameters which are then investigated against the microstructure of the materials. To check the linearity relation between the derived model parameters and the microstructure of the materials, Pearson correlation coefficient was calculated for several cases to highlight which parameter shows better correlation to the microstructure. Jiles-Atherton parameters show a higher linear correlation to the microstructure particularly to the precipitations. Following to modelling on MIP curves, the hysteresis curves were modelled adapting the J-A model to B(H) signals obtained in chapter 3. It was observed that in case of Hysteresis measurements, only α shows a higher correlation with the precipitations. It was also observed that the absolute value of these parameters doesn't give information about the microstructural evolution in the materials but the tendency of the evolution of these parameters can help to quantify the information about the creep level in the materials. As a further step, in the next chapter, Magnetic Barkhausen Noise tests are performed on the same set of samples.

References

[Cram] H.A.J. Cramer, "A moving preisach verctor hysteresis model for magnetic recording media", vol. 88, iss. 1-2, pp. 194-204, 1990.

[Duch] B. Ducharne, G. Sebald, D. Guyomar, G. Litak, "Fractional model of magnetic field penetration into a toroidal soft ferromagnetic sample", Int. J. of Dyn. And Cont., pp. 1-8, 2017.

[Gabi] Y. Gabi, B. Wolter, A. Gerbershagen, M. Ewen, P. Braun, O. Martins, "FEM simulations of incremental permeability signals of a multi-layer steel with consideration of the hysteretic behavior of each layer", IEEE Trans. On Mag., vol. 50 n°14, 2014.

[Gabi1] Y. Gabi, A. Kedous-Lebouc, G. Meunier, B. Wolter, O. Geoffroy, P. Meilland, P. Labie, C. Guérin, O. Martins, "Assessment of 3MA technique potentiality for nondestructive evaluation of dual-phase steels using 2-D nonlinear FEM and taking hysteretic behavior into account", Proc. 19th Conf. Comput. Electromagn. Fields, pp. 48-48, Jul. 2013.

[Jile] D. C. Jiles and D. L. Atherton, "Theory of ferromagnetic hysteresis", J. Magn. Magn. Mater., vol. 61, no. 1–2, pp. 48–60, Sep. 1986.

[Jile1] D.C. Jiles, D. L. Atherton, "Theory of ferromagnetic hysteresis". J. of App. Phys., vol. 55, iss. 6, pp. 2115, 1984.

[Jile2] D. C. Jiles, "A self consistent generalized model for the calculation of minor loop excursions in the theory of hysteresis," IEEE Trans. Magn., vol. 28, no. 5, pp. 2602–2604, Sep. 1992.

[Lang] P. Langevin, Comptes Rendues, 1908, vol. 146 pg. 530.

[Leit] J. V. Leite, N. Sadowski, P. Kuo-Peng, N. J. Batistela, J. P. A. Bastos, "The inverse Jiles-Atherton hysteresis model parameters identification", IEEE Trans. Magn., vol. 39, pp. 1397-1400, May 2003.

[Mats] T. Matsumoto, T. Uchimoto, T. Takagi, G. Dobmann, B. Ducharne, S. Oozono, H. Yuya, "Investigation of electromagnetic nondestructive evaluation of residual strain in low carbon steels using the eddy current magnetic signature (EC-MS) method", J. of mag. and mag. mat., vol. 479, pp. 212-221, 2019.

[Mats1] T. Matsumoto, B. Ducharne, T. Uchimoto, "Numerical model of the Eddy Current Magnetic Signature (EC-MS) non-destructive micro-magnetic technique", AIP Advance, vol. 9, iss. 3, 2019.

[Prei] F. Preisach, "Über die magnetische Nachwirkung". Zeitschrift für Physik, 94: 277-302, 1935.

[Sado] N. Sadowski, N. J. Batistela, J. P. A. Bastos, M. Lajoie-Mazenc, "An inverse Jiles-Atherton model to take into account hysteresis in time stepping finite element calculations", IEEE Trans. Magn., vol. 38, pp. 797-800, Mar. 2002.

[Torr] E. Della Torre, G. Kadar, "Vector Preisach and the moving model", J. App. Phys., vol. 63, pp. 3004-3006, 1988.

[Torr1] E. Della Torre, "A Preisach model for accommodation", IEEE Trans. on Mag., vol. 30, iss. 5, pp. 2701-2707, 1994.

[Zhan] B. Zhang, B. Gupta, B. Ducharne, G. Sebald, T. Uchimoto, "Dynamic magnetic scalar hysteresis lump model, based on JilesAtherton quasi-static hysteresis model extended with dynamic fractional derivative contribution", IEEE Trans. on. Mag, iss. 99, pp. 1-5, 2018.

CHAPTER 5

MAGNETIC BARKHAUSEN NOISE NDT for 12% Cr-Mo-W-V CREEP TEST SAMPLES: CHARACTERIZATION, MODELLING & PHYSICAL INTERPRETATION

Micro magnetic NDT evaluate mechanical properties of the samples such as hardness, ageing level of materials. Barkhausen noise is very sensitive to mechanical changes as well as to residual stresses [Gaut, Yelb, Dobm and Altp]. It is legitimate to assume that the mechanical changes in the materials lead to microstructural changes as well as modifications of the magnetic behavior. Since these microstructural changes modify the domain wall movements, thereby, making Barkhausen Noise a very interesting technique to study creep phenomenon. The application of micro-magnetic non-destructive techniques (NDT) like measuring the magnetic Barkhausen noise (MBN) has increased extensively in the industrial field recently [Dobm]. This is majorly due to the improvement of the signal processing techniques that have enabled and simplified the online production monitoring [Altp]. However, its industrial development is limited because of the reproducibility of the raw signal mainly due to the acquisition process completed by high orders filters and huge gain amplifiers stages. Magnetic Barkhausen Noise Energy (MBN_{energy}) can be used to reconstitute local hysteresis cycles from Barkhausen noise measurement. This hysteresis cycles constitute good indicators for the understanding of the magnetization process and the influence of micro-structural and mechanical properties. The integration step filters the raw signal and give access to a stable image of the Barkhausen noise making it a much more efficient tool. In this chapter, MBN_{energy} method is applied for the evaluation of microstructural changes due to creep in the same set of high chromium steel samples which were investigated using MIP and B(H) testing techniques as detailed in the previous chapters. The motivation is to get the information about the microstructure from the magnetic parameters derived from the MBN signal. To avoid repeatability issues due to the sensor, lift off and sensibility, such as the quest of the most sensitive indicator, as per [Duch, Duch1], MBN_{energy} hysteresis cycles will be plotted and evaluated. MBN_{energy} hysteresis cycles are obtained by plotting the time integration of the square of the Barkhausen noise multiplied by the excitation field time derivation sign versus H, see equation 1 below:

$$MBN_{energy}(H) = \left(\int_0^T Bark(t)^2 . sign\left(\frac{dH}{dt} \right) dt \right)(H) \qquad (5.1)$$

Just as the classic hysteresis cycles, evolution of the average induction field B versus the tangent magnetic excitation H, MBN_{energy} hysteresis cycles area are related to an energy. Raw Barkhausen noise signal can actually be seen as the image of domain wall speed, by integrating the square of the signal as it is done in eq. 5.1 the area of the resulting hysteresis cycle is consequently the image of a kinetic energy. This energy is consumed by the domain walls during the magnetization process. After the experimental analysis, the magnetic signals are modeled using the theory of Jiles-Atherton by simulating under the quasi-static conditions. As shown in previous cases, the modeling parameters derived in case of MBN are analyzed and linked to the samples' microstructural information enabling physical interpretation.

5.1. Experimental procedure

Fig. 5.1 shows the experimental set-up schematic. The tested samples are magnetically excited using a sinusoidal magnetic excitation field driven with the help of a soft U-shaped magnetic lamination stack. The excitation frequency is set to 0.1Hz after optimization tests as explained in Chapter 3. The excitation magnetic field is feedback controlled to ensure a 10 kA/m maximum amplitude. The sensor used to pick up the Barkhausen Noise signal is made out of two pancake pick-up coils and a Hall Effect sensor

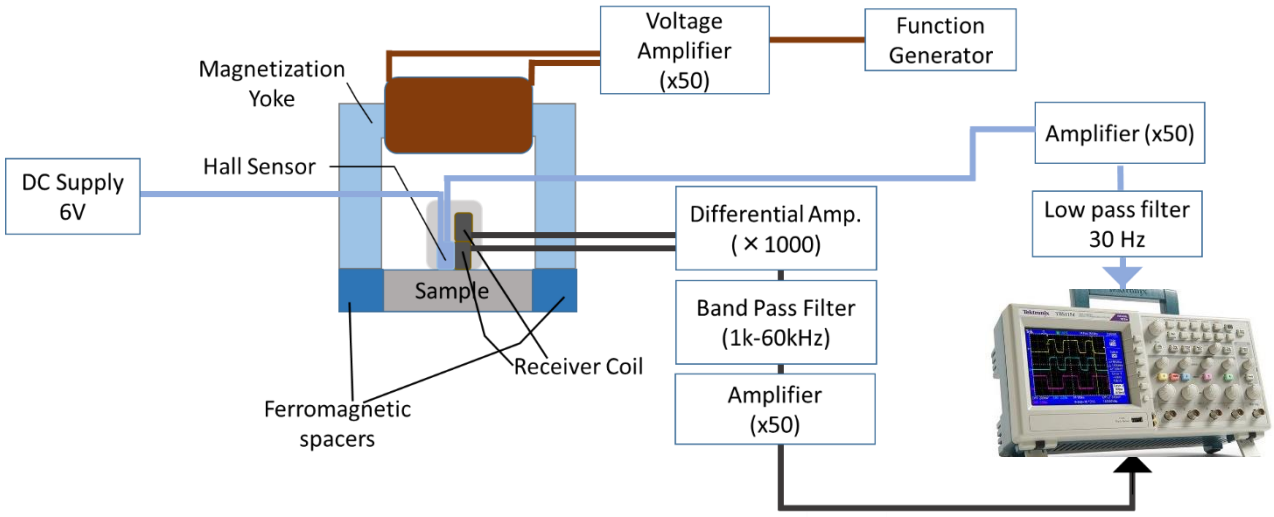

Figure 5.1. Magnetic Barkhausen Noise Measuring System (Schematic)

located inside (This sensor is the same as the one used in the case of MIP as shown in Chapter 3, the only difference being both the coils are used
to pick up the induced voltage instead of acting as Transmitter-Receiver type). The Hall sensor measures the tangential surface excitation field H. The output of the two pick up coils is transmitted to an electronic analog circuit. This circuit provides a first amplification of the differential Barkhausen signal by a factor of 1000 using a differential amplifier. Once amplified, this signal is fed to a band pass filter (BPF) of 1-60 kHz cut off frequency. The output of the BPF is amplified again by a factor of 50 before the oscilloscope acquisition. In parallel, the output of the Hall sensor is also amplified by a factor of 50 before its acquisition by the oscilloscope.

The raw MBN signal can be measured directly or processed as suggested by [Duch1] to get the $MBN_{energy}(H)$ curve. For this, in a second electronic circuit, the square of the Barkhausen noise is first calculated using an *AD633* analog multiplier, followed by a low noise operational amplifier *OPA2604* in an integration configuration ensuring the integration of this signal. A small reed relay *D31C2100* provides the reset function of the

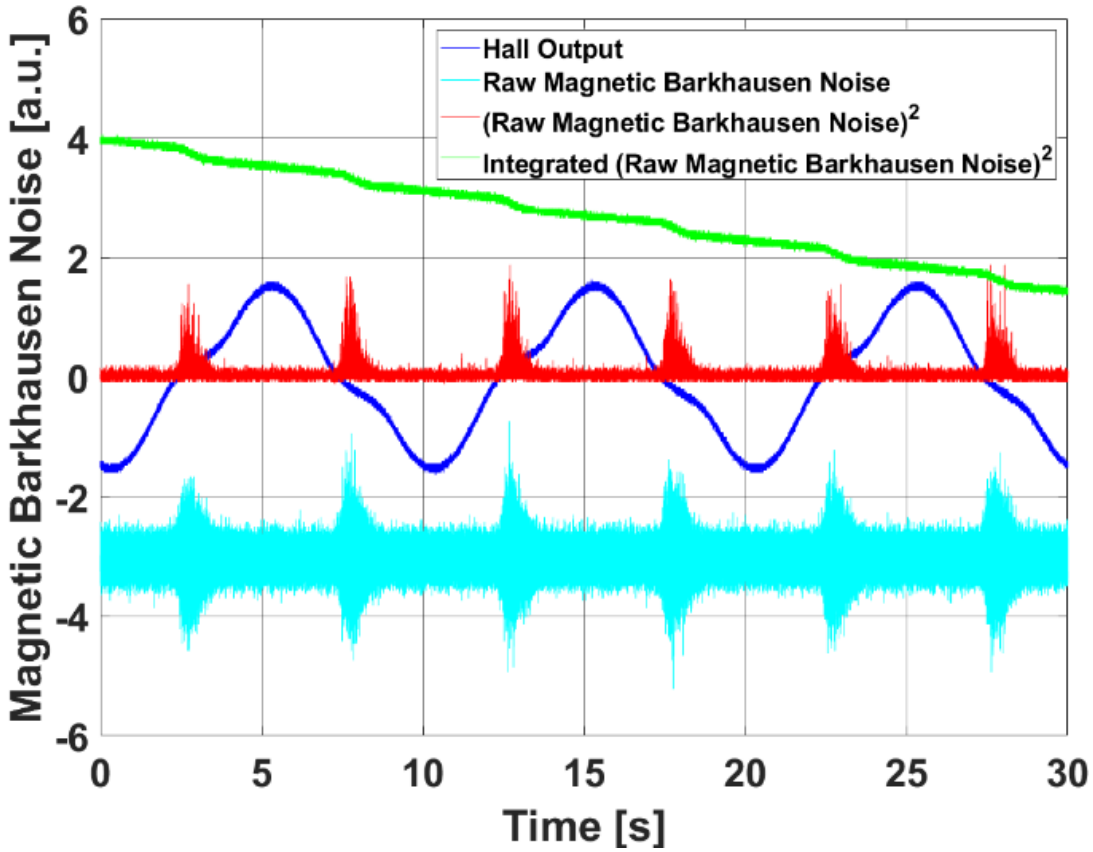

Figure 5.2. Data Acquisition for the Magnetic Barkhausen Noise Measurement system

integrator as soon as the acquisition is completed. Fig. 5.2 shows all the acquired signals by the oscilloscope.

Signal 1 (Blue) is the output of the Hall sensor. Signal 2 (Cyan) is the raw amplified magnetic Barkhausen noise. Signal 3 (Red) is the square of the MBN (Signal 2). Signal 4 (Green) is the integrated output of the Signal 3. A post processing numerical treatment is performed for the drift correction, the sign of the MBN_{energy} time derivation, the cycle symmetry and the final plot.

5.2. Experimental Results

Before proceeding to the results, below is the list of samples in Table 1, recalled from Chapter 2.

Construction of Hysteresis cycles from magnetic Barkhausen noise raw signals are called $MBN_{energy}(H)$ cycles. Fig.5.3 illustrates the different steps of this reconstruction. During the first step (b), the square of the raw signal is calculated. The resulting signal is multiplied to sign(dH/dt) which is 1 as H is increasing and -1 otherwise. A time integration is done right after as illustrated in Fig.5.3(c) and the offset is removed. Finally, a normalization step is performed to ensure equality between the absolute value of both the MBN_{energy} maximum and the minimum.

Table 5.1. List of Samples (Recalled from Chapter 3)

Sample number	Stress [MPa]	Temp [°C]	Test time [h]	LMP*
0	-	-	-	-
1	343	550	281.8	18479
2	343	550	785.6	18846
3	343	550	2205.7	19215
4	201	600	255.6	19565
5	201	600	763.9	19980
6	201	600	1725.9	20289
7	98	650	256.3	20686
8	98	650	789.6	21137
9	98	650	1736.8	21453

Larson Miller Parameter

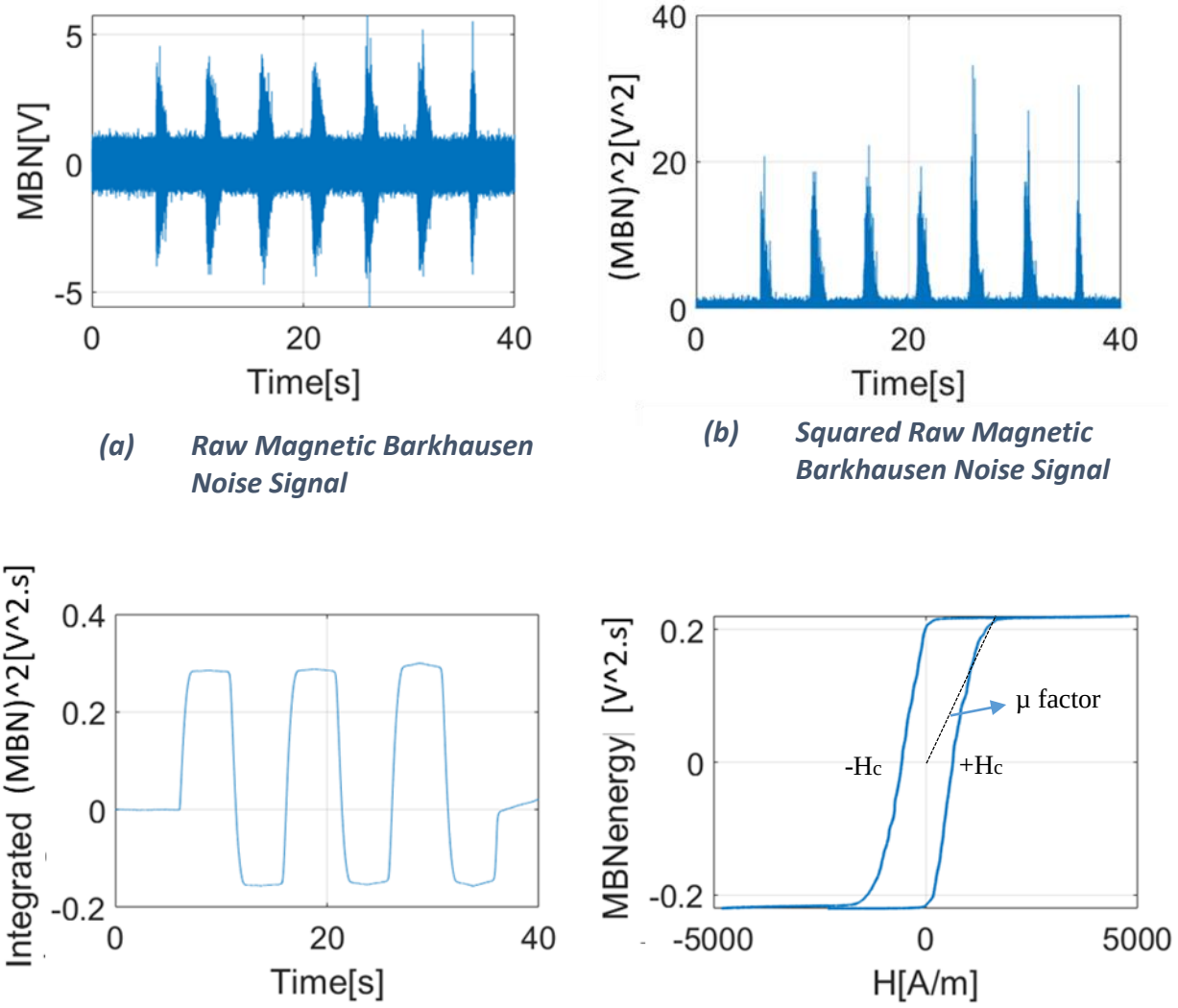

(a) Raw Magnetic Barkhausen Noise Signal

(b) Squared Raw Magnetic Barkhausen Noise Signal

(c) Offset removed Integrated MBN Signal

(d) Offset removed Integrated MBN Signal

Figure 5.3. Derivation of MBN_{energy} cycle from Raw Magnetic Barkhausen Noise

5.2.1. Experimental Data Analysis of 12%Cr-Mo-W-V Creep Test Samples

Fig. 5.4 shows the raw magnetic Barkhausen Noise signal for the three samples under the category of 550°C samples. The bottom figure in Fig.5. 4 shows the comparison of these three different sample via the reconstructed MBNenergy Hysteresis cycles from the raw MBN signal, using the technique presented in Fig. 5.3. From the raw signal in itself, the clear differences between the samples are observed. It is worth noticing that the amplitude of the raw signal falls as the creep increases. However, more information is specifically observed in the MBNenergy cycles. Clear differences among the saturation point of all the three samples are observed and it is also seen that the coercivity

tends to increase with the Ruptured sample in comparison to Sample 1. This is due to the presence of number of precipitates which are much higher in number making the samples magnetically hard as the rupture is approached.

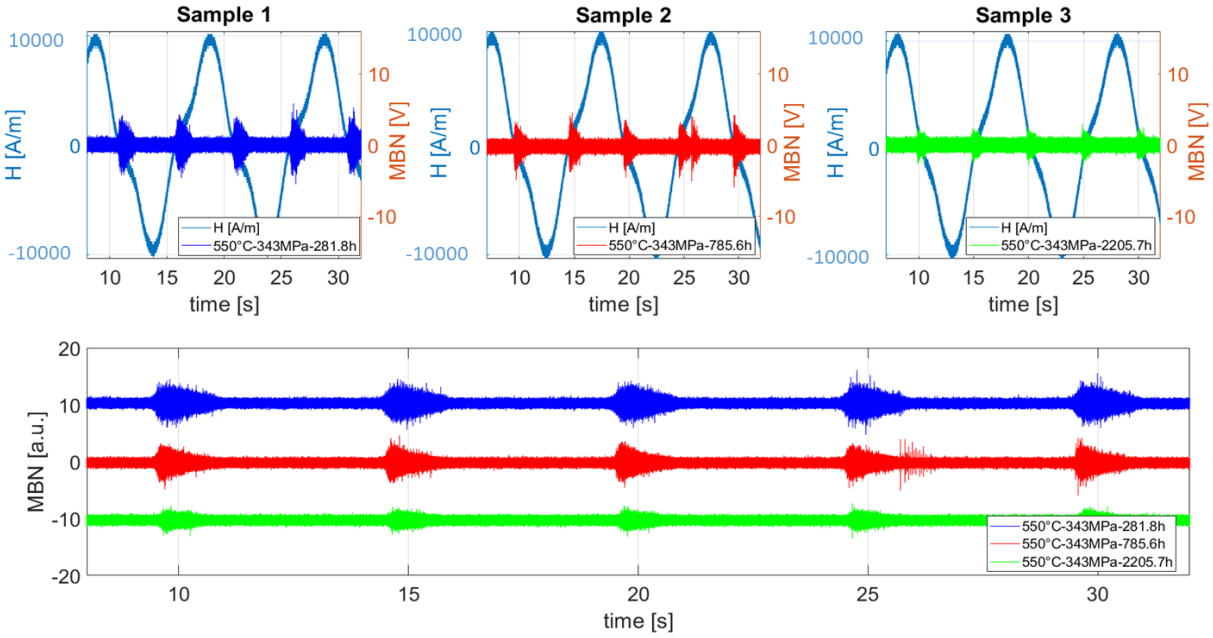

(a) Raw MBN signals for samples 1-3

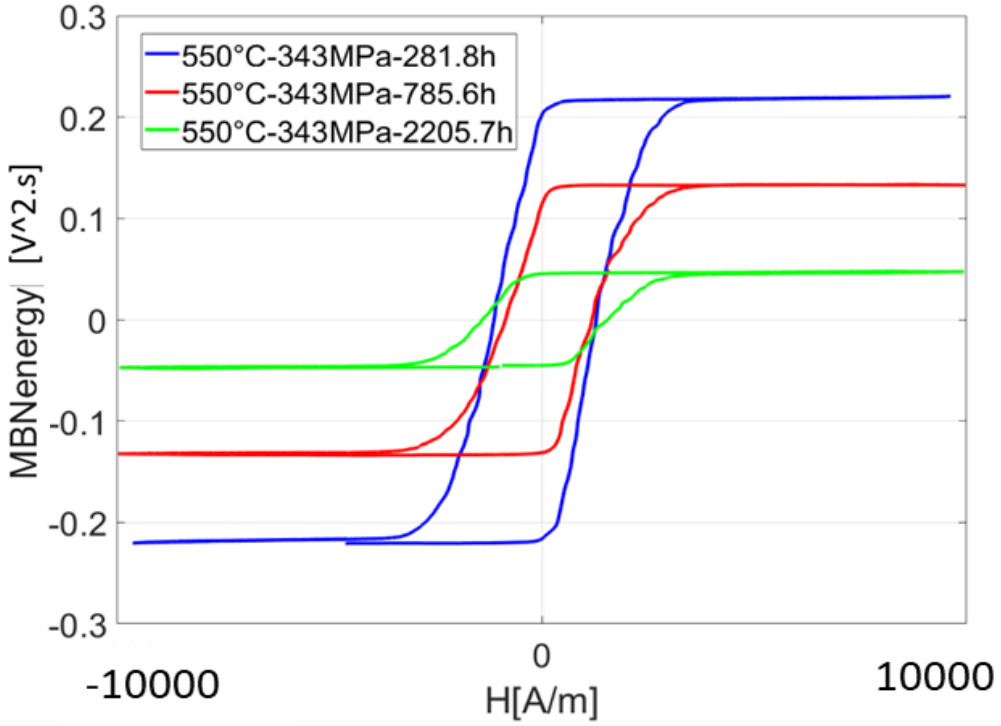

(b) Reconstructed MBN_{energy} cycles for samples 1-3

Figure 5.4. Raw MBN signal for Samples 1-3 and their respective reconstructed MBN_{energy} Hysteresis cycles (Bottom)

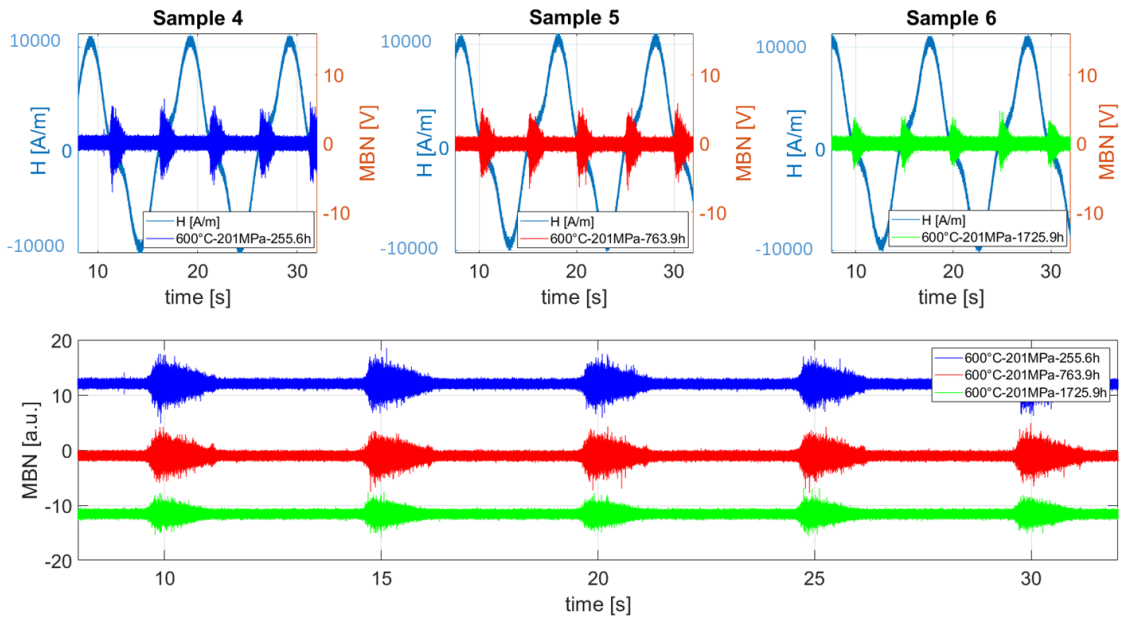

(a) Raw MBN signals for samples 4-6

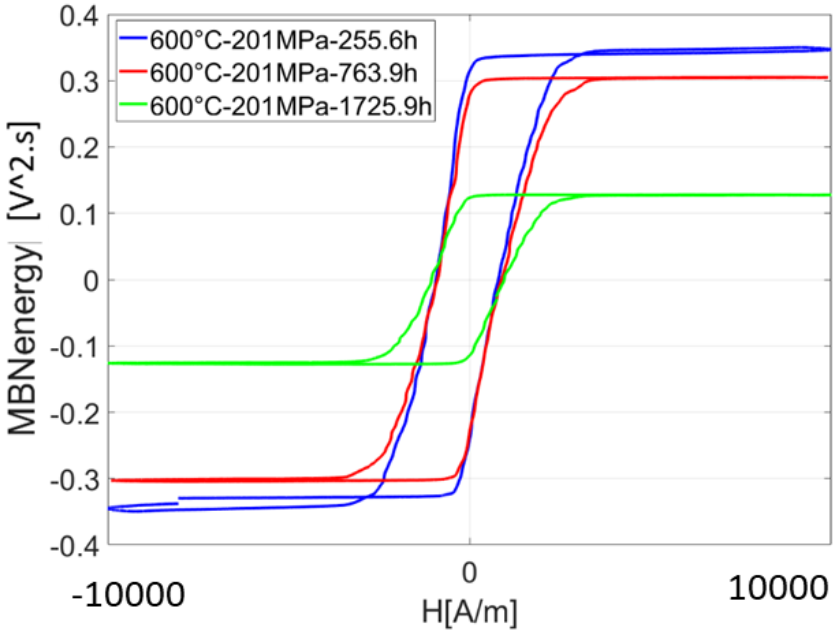

(b) Reconstructed MBN_{energy} cycles for samples 4-6

Figure 5.5. Raw MBN signal for Samples 4-6 and their respective reconstructed MBN_{energy} Hysteresis cycles (Bottom)

Fig. 5.5 above shows the comparison of the samples from 600°C category. As expected from Chapter 3&4, there are not much differences observed among the different samples, however, from the MBN_{energy} hysteresis cycles, the differences in the magnitude of MBN_{energy} is quite noticeable. It is also worth noticing that the MBN activity in the raw signals reduce over the time.

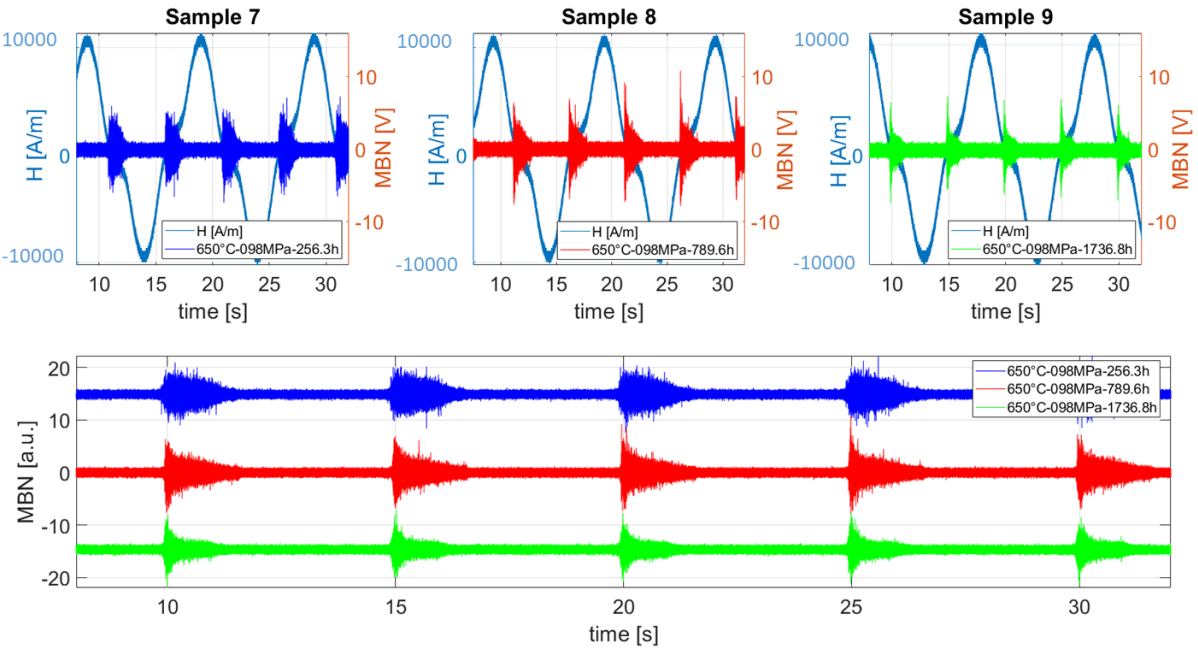

(a) Raw MBN signals for samples 7-9

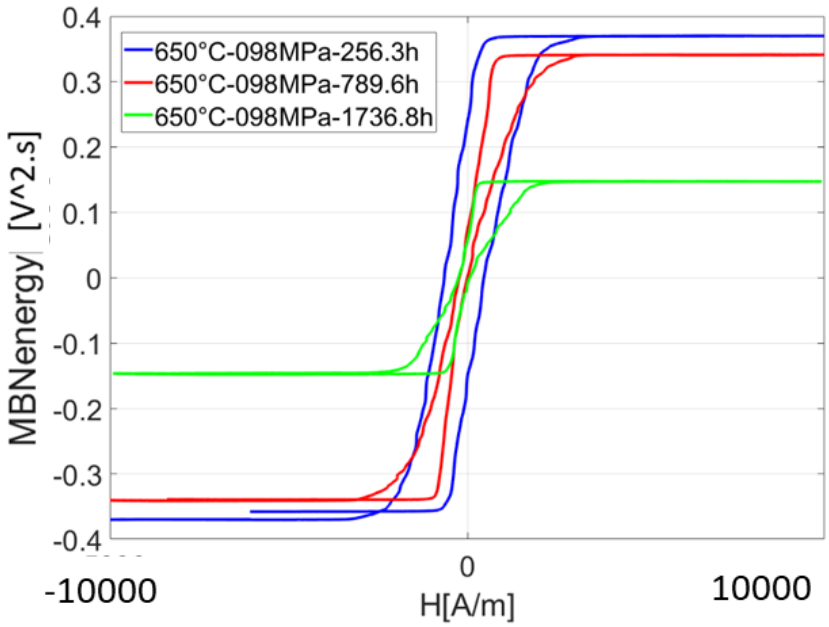

(b) Reconstructed MBN_{energy} cycles for samples 7-9

Figure 5.6. Raw MBN signal for Samples 7-9 and their respective reconstructed MBNenergy Hysteresis cycles (Bottom)

Fig. 5.6 above shows the comparisons for the 650°C category of samples. In contrast to the 550°C samples, here the amplitude of the MBN is increasing as the rupture level is increasing. It is also worth noticing in this case that the Barkhausen noise activity over time also decrease as the rupture is close. In this case, again in contrast to 550°C samples, the coercivity of the loops is also decreasing as the rupture nears.

5.2.2. Comparisons among the ruptured samples from the three different categories

Fig. 5.7 below shows the comparisons of the raw magnetic Barkhausen noise signals of the three ruptured samples from three different categories as well as their respective reconstructed MBNenergy Hysteresis cycles. As observed here, the peak to peak voltage amplitude of the Barkhausen noise raw increases with higher temperature treated samples. From a physical point of view this observation can be interpreted as a softening of the magnetic properties, increasing of the permeabalility and decreasing of the coercive fields absolute values, i.e, higher temperature treated samples gets magnetised and demagnetises faster in comparison to other samples. These interpretations are confirmed with the $MBN_{energy}(H)$ cycles figure (Fig. 5.7 bottom) below. As was observed in Chapter 2 (Microstructural Analysis), for 650°C, the number of precipitates are lower, which also makes possible for the easy domain wall movements ultimately leading to the easier orientation of the domains in the direction of the applied magnetic field and hence giving a higher and quicker magnetizability. It was also observed that between the similar temperature treated samples(Fig 5.4), as the rupture increases for the 550°C samples, the coercivity generally increases but for the 650°C samples (Fig. 5.6), the case is opposite in which the higher the rupture is, lesser is the coervity. This is possibly due to the effect of the precipitations. In 550°C, the number of precipitates is dominant and in case of 650°C the size of the precipitates is dominant. It also has to be noted that the on an average there are less misorientations/dislocations (KAM data can be referred to in Chapter 2) in the higher temperature treated samples and hence, quicker magnetization and higher permeability. Based on the Fig. 5.4-5.6, from the MBN_{energy} curves, some parameters such as coercivity factor corresponding to the similar coercivity from B(H) curves, Permeability(μfactor) using the slope of the curves, MBNenergy amplitude were extracted and correlated to the microstructure of the the materials. However, when considering the amplitude of MBN_{energy} curve, the absolute values for the same material may vary with different experimental set ups because of gain factor but

the relative relation between the samples will always remain constant.

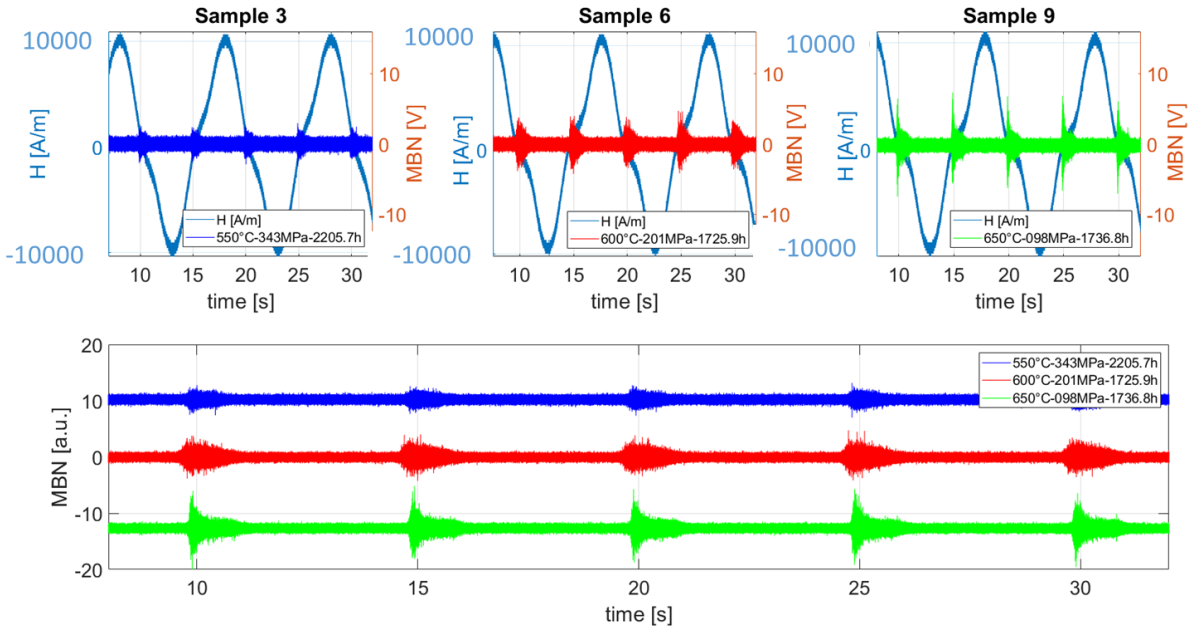

(a) Raw MBN signals for ruptured samples (Sample 3, 6 &9)

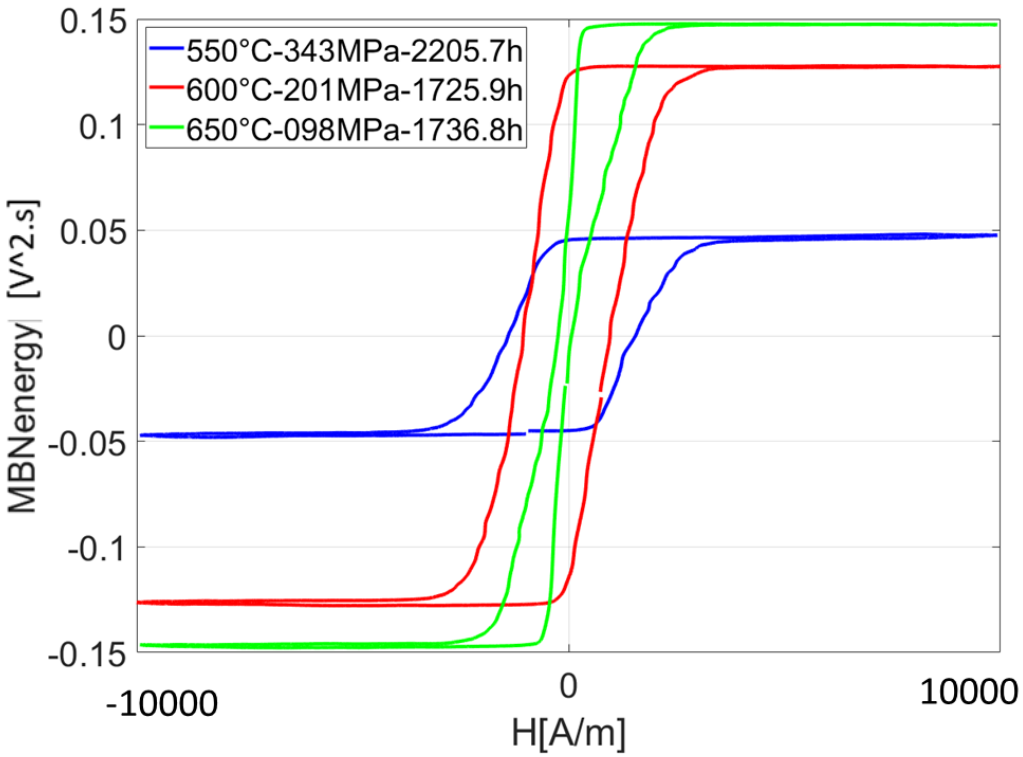

(b) Reconstructed MBN_{energy} cycles for ruptured samples (Sample 3, 6 &9)

Figure 5.7. Comparisons of Ruptured samples from three different temperature categories

5.3. Magnetic Parameters versus the microstructure

Fig. 5.8-5.9 below shows the correlation of magnetic parameters derived from MBN_{energy} curves with themicrostructural information of Precipitates(Fig. 5.8) and Dislocations (Fig.5.9).The use of Barkhausen noise measuring technique also demonstrates the effect of microstructural changes in the materials. The tendency of parameters is similar to that of MIP and B(H) results. The higher temperature samples behave in an opposite manner when compared to the lower temperature treated samples. As can bee seen the coercivity against the number of precipitates tends to increase at the rupture level due to larger number of precipitates which result in the magnetic hardening of the materials. On the other hand, for higher temperture treated samples, the coercivity falls with the decrease in the number of precipitates, which is due to the soft magnetic behavior of the materials.

KAM is an important factor from the materials science point of view, but to understand creep, KAM might or might not give a good correlation with the magnetic parameters. However, a bigger variation can still be noticed in the 650°C samples (which was the same case in MIP technique B(H) technique and even the modelling parameters derived from those techniques). The average dislocations definitely decrease in high temperature samples, hence resulting to higher permeability and magnetic reversibility. Even the slope, calculated from these curves did not show much relevance in accordance to creep time. Hence, when the material is tested using Barkhausen technique, coercivity is a good criterion and this was also verified with the model as demonstrated in Section

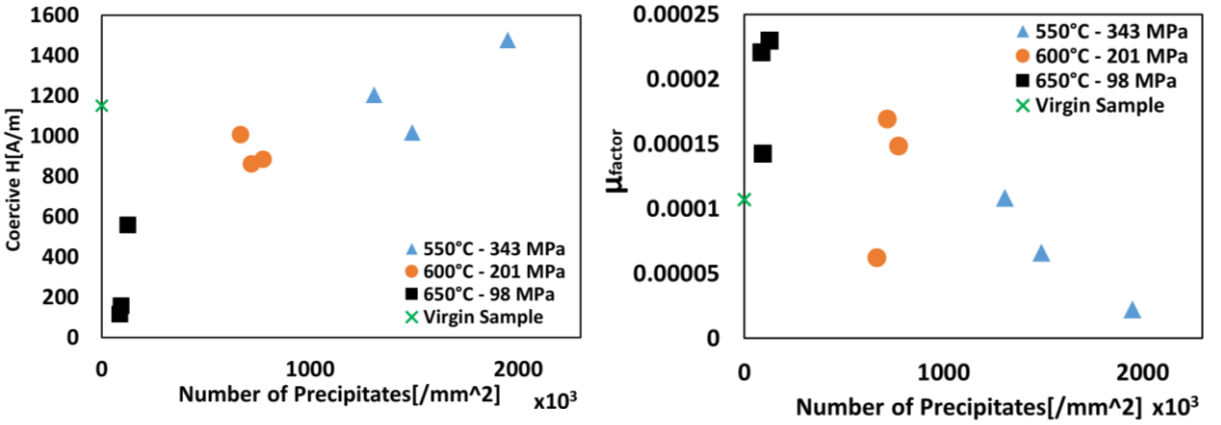

(a) Coercivity versus Precipitations

(b) Permeability factor versus Precipitations

Figure 5.8. Magnetic Parameters derived from MBN versus number of precipitates

5.4.

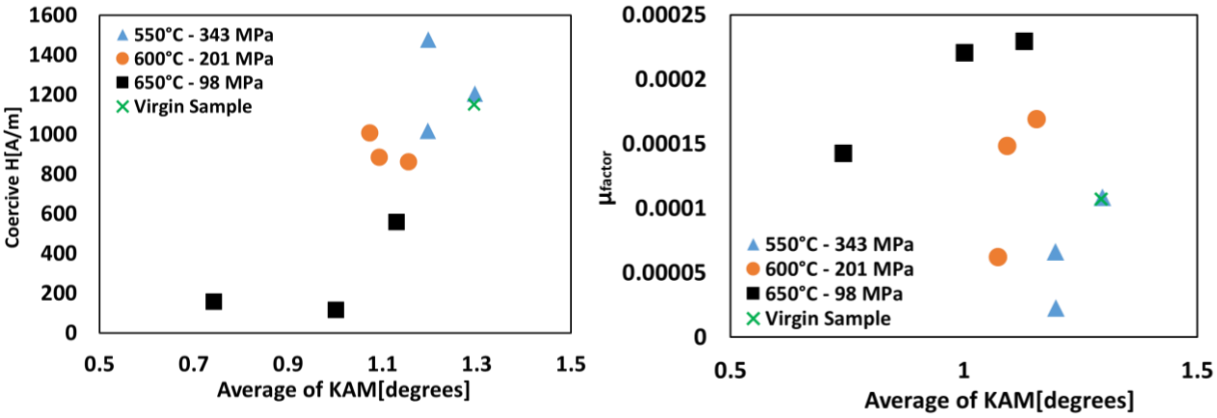

(a) Coercivity versus Average of KAM

(b) Permeability factor versus Average of KAM

Figure 5.9. Magnetic Parameters derived from MBN versus average of KAM

5.4. Jiles-Atherton hysteresis theory for the simulation of the MBN_{energy} hysteresis cycles

Following Jiles-Atherton model can be recalled from the previous Chapter 4 which allows to calculate the variations in the magnetization M with respect to H variations.

$$\frac{dM}{dH} = \frac{(1-c)\frac{dM_{irr}}{dHe} + c\frac{dM_{anh}}{dHe}}{1-\alpha(1-c)\frac{dM_{irr}}{dHe} - \alpha c\frac{dM_{anh}}{dHe}} \qquad (5.2)$$

5.4.1. A Jiles-Atherton-type approach for the simulation of the of MBN_{energy}(H) cycles

The motivation behind this simulation study is to derive a reliable parameter or a combination of parameters which hence, could be used to interpret about the microstructure of the material. Like detailed in Chapters 4 MIP gives good correlations for the three modelling parameters, α, k and c. Similarly, for the B(H) measurements, only α gives an interesting correlation. In this section the goal is to determine, which parameter/s could be reliable in case the measurements are performed using Magnetic Barkhausen Noise technique. Before the correlation step, the simulation process has to be run. For the MBN_{energy} hysteresis cycle, this process starts by the approximation of the experimental

MBN_{energy} anhysteretic curve. For this curve we have opted for a numerical estimation instead of experimental measurements as we know that the experimental procedure is hazardous and for barely almost all the classic soft magnetic materials no large differences can be observed between the estimated and the measured anhysteretic curves. Assuming the major hysteresis cycle as perfectly symmetrical, the MBN_{energy} anhysteretic curve can be calculated using the increasing part of the cycle and from equation (5.3).

$$H_i^{anhyst}(B_i) = \frac{H_i^{inc}(B_i) + H_i^{inc}(-B_i)}{2} \tag{5.3}$$

Here H_i^{inc} represents the H values for the increasing part of the major hysteresis cycle and H_i^{anhyst} the anhysteretic one. Ms and a, the Jiles-Atherton anhysteretic parameters are calculated right after by fitting the estimated anhysteretic curve to the simulated one using Matlab™ curve fitting toolbox. Finally, an optimization code based on the minimization of an error function (eq. 6.4) is run for the evaluation of the optimized α, k and c combination.

$$dH/dt > 0, \qquad H \in [H_{\min}, H_{\max}]$$
$$Error = \sum_{i=1}^{n} abs\left(\left| MBN_{energy} \right|_i^{\exp}(H_i) - \left| MBN_{energy} \right|_i^{sim}(H_i) \right) \tag{5.4}$$

5.4.2. Modelling Parameters derived from simulation of MBNenergy curves

Fig. 5.10 below gives as an illustration the comparison simulation/measure for sample 1 MBN_{energy} hysteresis cycle. It is demonstrated in the Fig. below that the modeling parameter (k in this case) are derived from the fitting of the simulated curve to the experimental one.

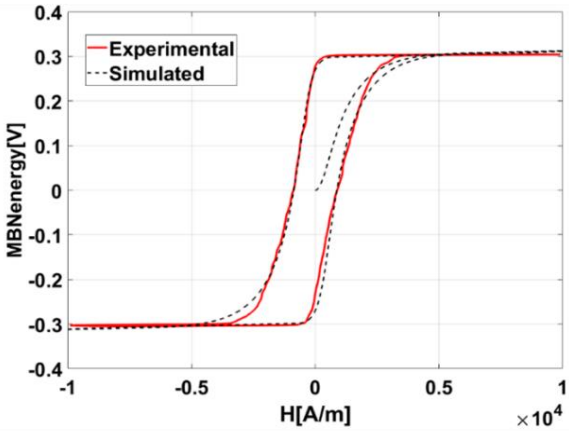

(a) Simulated and Experimental MBN_{energy} Curves for Sample 1

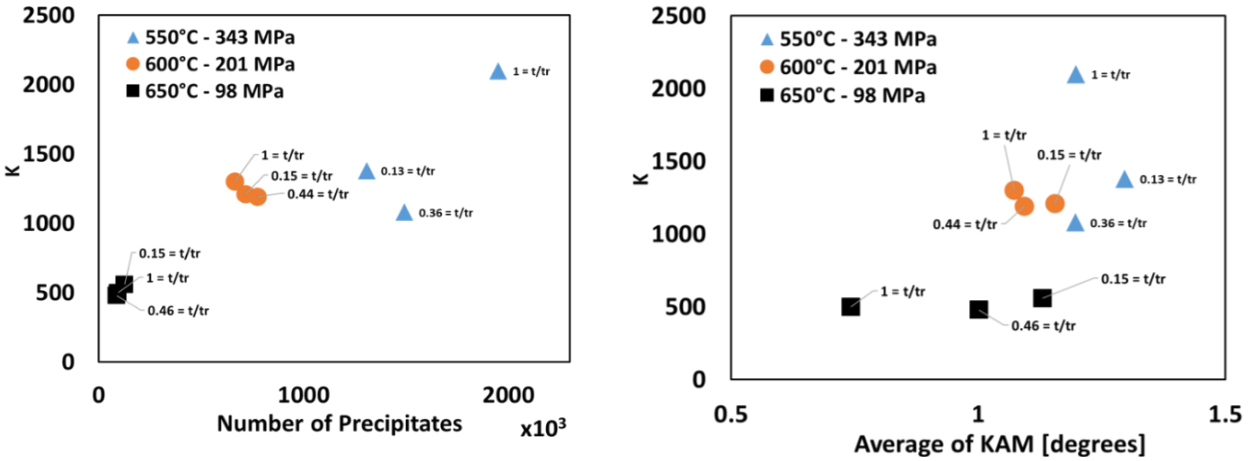

(b) Evolution of k parameter versus Precipitates

(c) Evolution of k parameter versus Average of KAM

Figure 5.10. Comparison of simulated and experimental curves for sample 1 MBN_{energy} cycle, variation of the k coefficient vs the number of precipitates, variation of the k coefficient vs KAM

Table 5.2 below shows the modelling parameters derived from the simulation based on the experimental data.

Table 5.2. Modelling parameters derived from simulation

Parameter	α	k	c
Sample 1	0.0015	1380	0.01
Sample 2	0.0018	1080	0.01
Sample 3	0.02	2100	0.01
Sample 4	0.0012	1210	0.01
Sample 5	0.0012	1190	0.01
Sample 6	0.0039	1300	0.01
Sample 7	2e-6	560	0.01
Sample 8	2e-6	480	0.22
Sample 9	2e-6	500	0.16

A fine analysis of the simulation parameters show that the coefficient k exhibits the most relevant correlation (Fig. 5.10), this is also verified by calculating the Pearson Correlation coefficient as shown in Fig. 5.11 (following the similar approach as in Chapter 4). k was evaluated with different parameters, (mechanical, magnetic and mathematical) and a correlation was studied using Pearson correlation coefficient as shown in Fig. 5.11 below. Closer the value of the factor to 1/-1 higher is the correlation (positive/negative).

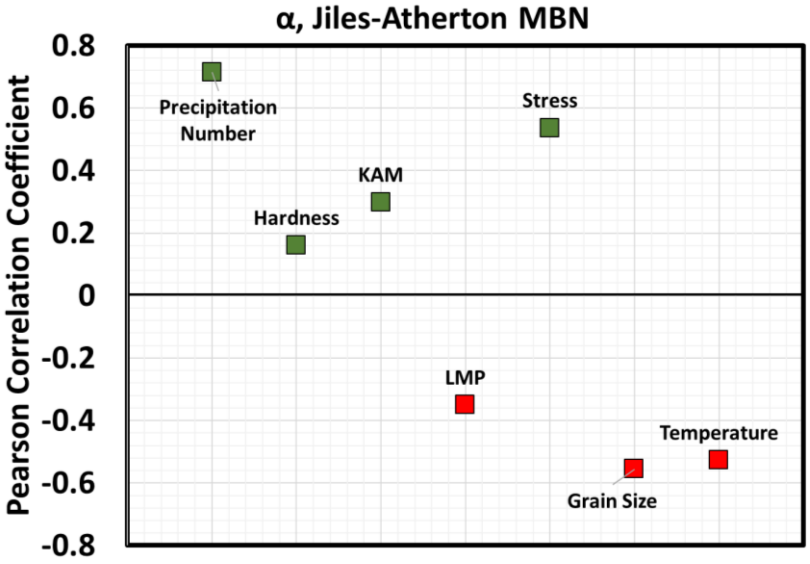

(a) Pearson correlation coefficient for α

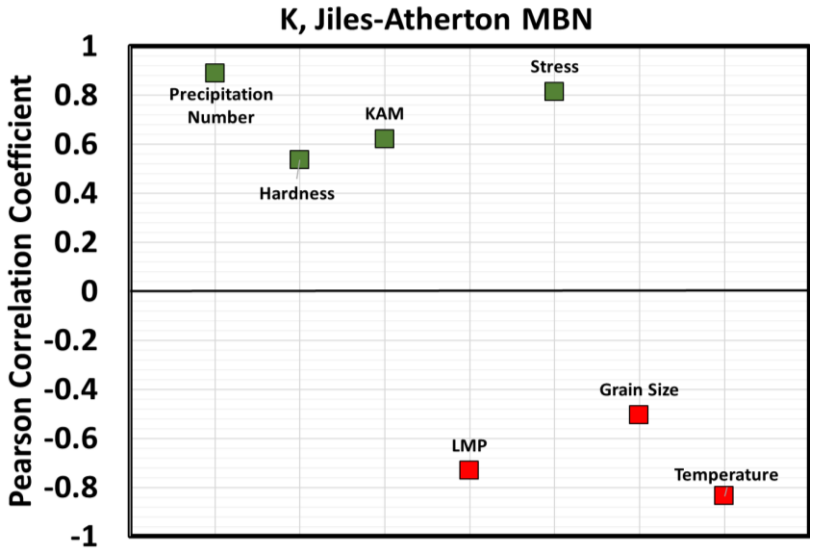

(b) Pearson correlation coefficient for k

Figure 5.11. Pearson coefficient for comparisons between simulation parameters (α, k) and micro-structural ones.

It has to be noted that all the J-A parameters are inter-related, i.e., each parameter changes with the change in the values of the others. Hence, the most stable parameter (k in this case) with variations in other parameters (α, c) is chosen which corresponds to the coercivity of the materials. Since, there are more dislocations and more precipitations (Chapter 2: Microstructural Analysis) in 550°C sample, it is well demonstrated in the Figure 5.10 above that the k factor is higher for this category. Comparing Fig. 5.8 which demonstrates coercivity vs. precipitates with k vs. precipitates in Fig.5.10, the tendency is quite similar. However, some variations are expected since, k also comprises of the effect of the variations from other parameters (α, c). The variation in the k parameter vs. creep life fraction t/t_r also is evaluated in Fig. 5.10 which also verifies that the evolution trend between 550°C samples and 650°C samples is opposite. However, the rate of change is also an important factor. In 550°C samples the rate of change of k with increase in rupture time is much higher (in the increasing direction) as compared to the rate of change in of k in 650°C samples which is very small (in the decreasing direction). From the precipitation point of view, the high temperature samples (650°C) do not show much variations, however, in terms of dislocations, the high temperature sample show a larger variation when k is analyzed with respect to average of KAM as illustrated in Fig.5.10. Magnetic as well as modeling parameters showed a larger variation with respect to KAM in terms in higher temperature treated samples (as detailed in previous chapters for MIP and B(H)) only which is the case in MBN technique too. It is also observed that in both B(H) and MBN other parameters like α is sensitive to only lower temperature samples and c is sensitive to only higher temperature samples. α represents the inter domain coupling which is higher for lower temperature samples since the size of the precipitates is smaller compared to higher temperature samples.

On the other hand, as can be seen in the Fig.5.8 the permeability is higher in higher temperature samples and hence the samples become soft magnetic leading to easy magnetic reversibility. Hence, c that represents the magnetic reversibility, is sensitive to higher temperature samples only as shown in Fig. 5.12.

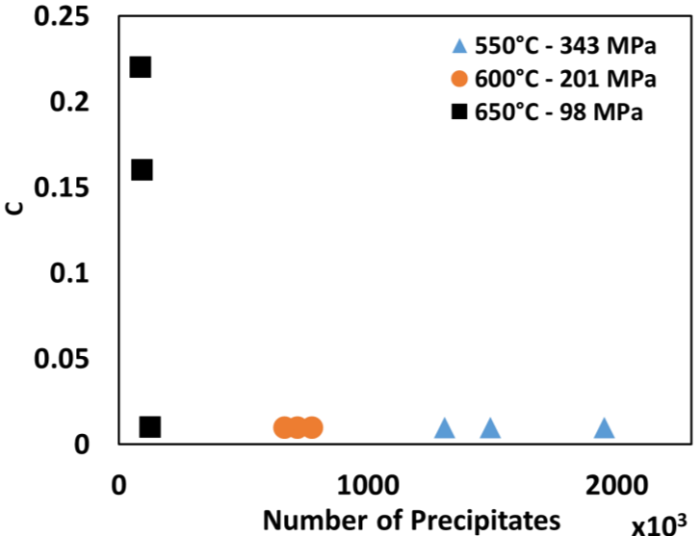

Figure 5.12. c versus number of precipitates

Fig. 5.13 below shows the evolution of the most reliable parameter k in case of Magnetic Barkhausen noise in relation to the rupture level. Although, there are minor discrepancies, but overall the tendency of evolution of this parameter in relation to coercivity factor derived from MBNenergy hysteresis cycles is very similar.

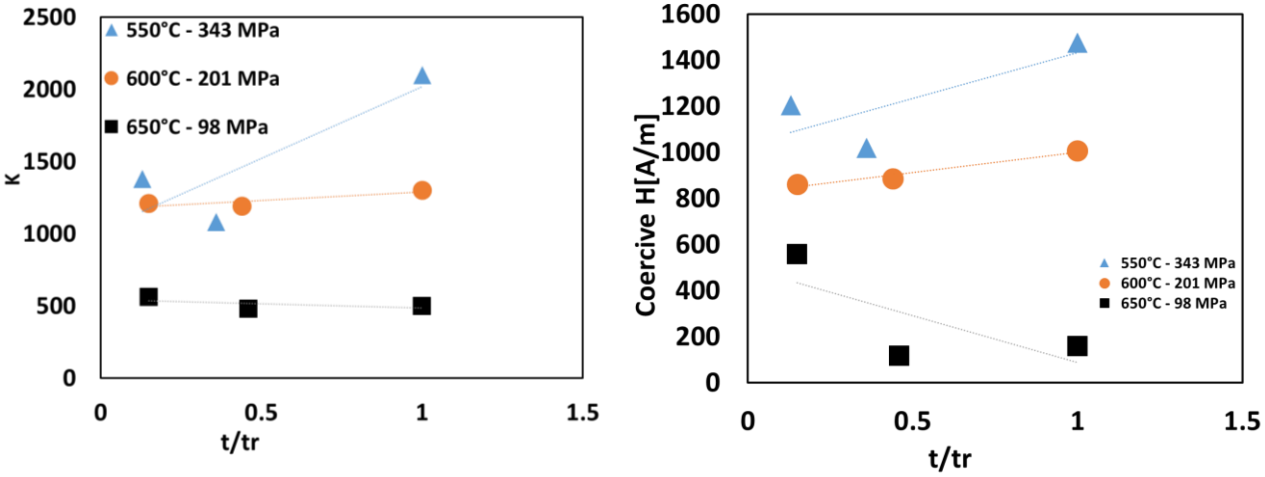

(a) Tendency of k versus rupture level for different temperature treated samples

(b) Tendency of coercivity versus rupture level for different temperature treated samples demonstrating similar evolution as k

Figure 5.13. Evolution of k and coercivity factor with respect to rupture level.

5.5. Summary

The focus in this chapter has been on micro-magnetic method Magnetic Barkhausen Noise for the evaluation of the micro-structural state of 12 Cr-Mo-W-V steel. Such micro magnetic analysis is of major interest as the micro-structural state is deeply connected to the flaws propagation in these structural steels and to serious consequences if not anticipated. As an image of the magnetic domain wall movements, the Barkhausen noise measurement is a micro magnetic non-destructive testing method of high potential and interest. In this study, instead of following the classic approach which consist on working directly from the raw signal, $MBN_{energy}(H)$ hysteresis cycles have been reconstructed and simulated. Working with these hysteresis cycles limit the reproducibility and the sensitivity issues such as providing a magnetic signature which can easily be simulated using the classic hysteresis models as the Jiles-Atherton one which has been used in this study. Once all the experimental tests and simulations are performed a fine analysis has been done in order to find correlations between the magnetic parameters (coercive field, permeability factor etc.), the J-A simulation parameters and the micro-structural properties.

References

[Altp] I. Altpeter, G. Dobmann, M. Kröning, M. Raboug, S. Szielasko, "Micro-magnetic evaluation of micro residual stresses of the IInd and III order", NDT&E Int., vol. 42, pp. 283-290, 2009.

[Dobm] G. Dobmann, I. Altepeter, B. Wolter, R. Kern, "Industrial applications of 3MA – Micromagnetic Multiparameter Microstructure and Stress Analysis", Electromagnetic Nondestructive Evaluation (IX), IOS Press, 2008.

[Duch] B. Ducharne, B. Gupta, Y. Hebrard, J. B. Coudert, "Phenomenological model of Barkhausen noise under mechanical and magnetic excitations", IEEE Trans. on. Mag, vol. 99, pp. 1-6, 2018.

[Duch1] B. Ducharne, MQ. Le, G. Sebald, PJ. Cottinet, D. Guyomar, Y. Hebrard, "Characterization and modeling of magnetic domain wall dynamics using reconstituted hysteresis loops from Barkhausen noise", J. of Mag. And Mag. Mat., pp. 231-238, 2017.

[Gaut] J. Gauthier, T.W. Krause, D.L. Atherton, "Measurement of residual stress in steel using the magnetic Barkhausen noise technique", NDT&E Int. vol. 31, iss. 1, pp. 23-31, 1998.

[Kleb] X. Kleber, A. Vincent, "On the role of residual internal stresses and dislocation on Barkhausen in plastically deformed steel", NDT&E Int., vol. 37, iss. 6, pp. 439-445, 2004.

[Stew] D.M. Stewart, K.J. Stevens, A.B. Kaiser, "Magnetic Barkhausen noise analysis of stress in steel", Cur. App. Phys., pp. 308-311, 2004.

[Yelb] H.I. Yelbay, I. Cam, C.H. Gür, "Non-destructive determination of residual stress state in steel weldments by magnetic Barkhausen noise technique", NDT&E Int. vol. 43, iss. 1, pp. 29-33, 2010.

CHAPTER 6

CONCLUSIONS

The major issue in the thermal power plants is the changes in the microstructure that occur over the time due to constant exposure of materials to high temperature and pressures. This implies that to study this evolution of microstructure the destructive imaging methods have to applied, which involve fastidious measurements and high equipment costs. Although, the imaging analysis gives a very quantitative microstructural data about the materials, it cannot be performed during its lifecycle. Hence, it is very interesting to correlate the NDT signals to the microstructural information. This will help in getting a tentative information about the material's state, by taking the NDT signals from time to time during the materials' lifecycle. In order to address this issue, in this thesis work, three different electromagnetic techniques are employed to investigate the high chromium Ferritic creep test samples subjected to different temperature and stress conditions. On the derivation of magnetic signatures, this information is used to interpret the microstructure, thereby avoiding the potential use of imaging techniques. In addition to that, a modelling technique is developed to simulate the magnetic signatures which provide access to modelling parameters. These modelling parameters are then correlated to the microstructure revealing the sensitivity information of each parameter with respect to each NDT technique used.

The first sub-objective of this thesis was to analyze the creep degraded high chromium Ferritic steels empirically using NDT techniques. As a first step, a sensitive technique based on Magnetic Incremental permeability (MIP) is employed to check the evolution of typical butterfly loops with respect to different test times, temperatures, Stress levels etc. This technique helps to determine several magnetic parameters from the curves which provide information about the magnetic state of the materials corresponding to the mechanical conditions. These parameters are evaluated versus different microstructural data which helps in understanding and predicting the potential changes in the microstructure of the materials due to creep. It is shown that these parameters are highly sensitive to the precipitation content in the materials and how their evolution changes in a different manner in case of differently treated samples. For instance, the magnetic reversibility (which is related to cross point in MIP curve) increases with the decrease in the number of precipitates (the material becomes soft magnetic). On the other hand, for grain misorientation analysis, it has been demonstrated in literature, that it is a very quantitative parameter to study creep. But in the tested samples, grain misorientation shows larger variations in case of high temperature samples only

(where the materials tend to become very soft magnetic due to large decrease of dislocations as the rupture level increases). However, if grain misorientation has to be studied, it is shown that the magnetic coercivity of the samples should be studied. Studying these signals can help in predicting the evolution of microstructure, thereby, making it a tentative alternative to the destructive method of imaging the microstructure.

Since, hysteresis is the standard curve to represent the magnetic behaviors of the materials, each sample is evaluated by measuring the respective B(H) curve. It is very interesting to note that, MIP signals show clear distinction between the samples as compared to their respective hysteresis curves. It implies that MIP provides much deeper information as compared to the B(H) measurements, which is actually an average information. To further compare the samples using a different micro-magnetic NDT technique, Magnetic Barkhausen Noise is employed, which studies the domain wall movements. It is shown that from MBN signals, coercivity shows a good correlation in terms of microstructure evolution and hence can be used in predicting the evolution of microstructural changes. The amplitude of the MBN_{energy} curves obtained during this experiments, shows that its amplitude always decreased when the rupture approaches.

As a part of the second sub-objective, as a next step, to further understand more the magnetic signals, different modelling techniques are tested for which the Jiles-Atherton model is finalized for understanding the physical behavior for the evolution of the given samples. This model helps to derive the modelling parameters such as α, k & c which according to Jiles theory have a physical meaning related to the microstructure. Each NDT technique used is modelled separately leading to a set of modelling parameters. For example, in case of α, which represents the inter-domain coupling, it shows that it is higher in case of lower temperature treated samples supporting the physics behind since, the size of the precipitates (which might act as a pinning site between the domains) is much lower in this case, and hence higher inter-domain coupling. The modelling parameters and their evolution show a very good agreement with the magnetic parameters evolution obtained experimentally.

The modelling technique is then adapted to Hysteresis measurements as well. As shown experimentally, the hysteresis cycles don't show stronger variations amongst different samples and it is also validated by the modelling parameters, since, B(H) shows a good correlation factor only in case of one modelling parameter, i.e., α.

MBN_{energy} curves obtained experimentally are then modelled and the derived modelling parameters are evaluated. *k* parameter which is associated with the coercivity shows a strong correlation with the microstructural properties of the materials.

All the modelling parameters obtained from MIP, B(H) and MBN curves are evaluated to determine the linearity relationship with the mechanical as well as the microstructural changes, using Pearson correlation coefficient calculation. In case of MIP, the all the three modelling parameters show a high correlation factor ranging between 0.6-0.85 particularly with precipitation content, highlighting strong correlations. In case of B(H) measurements, only α shows a good correlation with the microstructural properties and in case of MBN measurements, *k* parameter shows the high correlation factor close to 0.9. These modelling parameters are a potential tentative solution to overcome the issue of lack of standards in the field of NDT. Following Table 6.1. summarizes that which modelling parameter is sensitive in each measurement technique.

As a further step, these techniques are going to be tested on 9%Cr steel samples and the implementation of the modelling for the same will be checked. In order to predict the entire course of creep, furthermore, the samples of well-known history will be tested.

Table 6.1. Comparisons for different parameters' sensitivity corresponding to the NDT technique employed

Parameter/Technique	α	k	c
MIP	+++	+++	+++
B(H)	+++	-	+(only Higher temp.)
MBN	++	+++	+ (only Higher temp.)

List of Publications

Peer reviewed Journals (as first author)

- Space discretized ferromagnetic model for non-destructive eddy current testing, **B. Gupta**, B. Ducharne, G. Sebald, T. Uchimoto, **IEEE Transactions on Magnetics**, vol. 54, no. 3, pp. 1-4, March 2018.
- Magnetic Incremental Permeability Non-destructive Evaluation of 12 Cr-Mo-W-V steel creep test samples with varied ageing levels and thermal treatments, **Bhaawan Gupta**, Tetsuya Uchimoto, Benjamin Ducharne, Gael Sebald, Takamichi Miyazaki, **Journal of NDT&E International**, vol. 104, pp. 42-50, June 2019.
- Physical Interpretation of the Microstructure for aged 12 Cr-Mo-V-W Steel Creep Test Samples based on Simulation of Magnetic Incremental Permeability, **Bhaawan Gupta**, Benjamin Ducharne, Gael Sebald, Tetsuya Uchimoto, **Journal of Magnetism and Magnetic Materials,** vol. 486, September 2019 (In Press).
- Magnetic Barkhausen Noise Nondestructive Testing on 12% Cr-Mo-W-V Creep Test Samples: Characterization, Modelling and Physical Interpretation, **Bhaawan Gupta**, Benjamin Ducharne, Tetsuya Uchimoto, Gael Sebald, Takamichi Miyazaki, Toshiyuki Takagi, **Journal of Magnetism and Magnetic Materials,** November 2019 (In Press).
- Magnetic Sensor Principle for Susceptibility Imaging of Para- and Diamagnetic Materials, **Bhaawan Gupta,** Klaus Szielasko, **Journal of Nondestructive Evaluation 35(3)**, pp. 35-41, June 2016.

Peer Reviewed Journals (as co-author) – Complementary Activities

- Preisach's model extended with dynamic fractional derivation contribution, B. Zhang, **B. Gupta**, B. Ducharne, G. Sebald, T. Uchimoto, **IEEE Transactions on Magnetics***,* vol. 54, no. 3, pp. 1-4, March 2018**.**
- An improved sensor for the magnetic susceptibility imaging technique for detecting impurities in non-ferromagnetic materials, Ningxiang Yang, Xiucheng Liu, Pengfei Xing, **Bhaawan Gupta**, Jieming Yang, Jiaying Zhang, Benjamin Ducharne, Cunfu He, **Sensors & Actuators: A. Physical**, vol. 279, pp. 240-247, August 2018.
- Dynamic magnetic scalar hysteresis lump model, based on Jiles-Atherton quasi-static hysteresis model extended with dynamic fractional derivative contribution,

B. Zhang, **B. Gupta**, B. Ducharne, G. Sebald, T. Uchimoto, **IEEE Transactions on Magnetics**, vol. 54, no. 11, pp. 1-5, Nov. 2018.

- **P**henomenological Model of Barkhausen Noise Under Mechanical and Magnetic Excitations, Benjamin Ducharne, **Bhaawan Gupta**, Yoann Hebrard, J.B. Coudert, **IEEE Transactions on Magnetics**, vol. 54, no. 11, pp. 1-6, Nov. 2018.

- **L**ocal Measurement of Peening-Induced Residual Stresses on Iron Nickel Material Using Needle Probes Technique, Y. A. Tene Deffo, P. Tsafack, B. Ducharne, **B. Gupta**, A. Chazotte-Leconte, and L. Morel, **IEEE Transactions on Magnetics***,* vol. 55, no. 7, pp. 1-8, July 2019.

International Conferences Attended

(2016-2019) (in **Bold:** Presenting Author)

21st International Conference on the Computation of Electromagnetic Fields, COMPUMAG, Daejeon, Korea, June 2017.

- **Gupta, B.** Ducharne, G. Sebald, T. Uchimoto, Space discretized ferromagnetic model for non-destructive eddy current testing.
- **Gupta, B.** Ducharne, G. Sebald, T. Uchimoto, Magnetic lump model for the hysteresis frequency dependence of a polymer matrix.

18th International Symposium on Applied Electromagnetics and Mechanics, ISEM, Chamonix France, Sept. 2017.

- **B. Ducharne**, B. Gupta, G. Sebald, T. Uchimoto, Dynamic hysteresis lump model including fractional operators for the incremental permeability nondestructive testing.
- K. Szielasko, **B. Gupta**, B. Ducharne, M. Amiri, Magnetic Susceptibility Imaging as a New Approach towards Characterization and Testing of Para- and Diamagnetic Materials.

XXII International Workshop on Electromagnetic Non-Destructive Evaluation, ENDE, Paris France, Sept 2017.

- Gupta, **B. Ducharne**, G. Sebald, T. Uchimoto and Y. Hebrard, Characterization and Modeling of Magnetic Barkhausen Noise Envelope under both Magnetic and Mechanical Stress Excitation.

The 23rd International Workshop on Electromagnetic Non-Destructive Evaluation, ENDE, Detroit, USA, Sept. 2018.

- **Bhaawan Gupta**, Tetsuya Uchimoto, Benjamin Ducharne, Gael Sebald, Takamachi Miyazaki, Modelling and Experimental Magnetic Incremental Permeability Non-Destructive Evaluation of 12 Cr-Mo-W-V Creep Test Samples.

The Fourth International Conference on Maintenance Science and Technology (ICMST 2018), Tohoku University, Oct.2018.

- **Bhaawan Gupta,** Benjamin Ducharne, Tetsuya Uchimoto and Gael Sebald, Modelling and Experimental Magnetic Barkhausen Noise Non-destructive Evaluation of 12 Cr-Mo-W-V Steel Creep Test Samples.

The 24th International Workshop on Electromagnetic Non-Destructive Evaluation, ENDE, Chengdu, China, Sept.2019

- **Bhaawan Gupta**, Benjamin Ducharne, Tetsuya Uchimoto, Gael Sebald, Micromagnetic Non-Destructive Testing on High Chromium Creep Test Samples: Characterization, Modelling and Physical Interpretation.

Acknowledgements

The teams at Tohoku University and INSA-Lyon have been the most significant factor in finalizing this research work.

First of all, I would like to thank all the jury members, Prof. Laurent Daniel, Prof. Afef Lebouc, Dr. Klaus Szielasko and Dr. Anastassios Skarlatos for their very constructive feedback on my manuscript. I would also like to thank all the jury members from Tohoku University side, Prof. Toshiyuki Takagi, Prof. Kazuhiro Ogawa, Prof. Tetsuya Uchimoto, Prof. Gael Sebald for their very constructive feedback during the pre-defense of my thesis in Japan which has been very useful in finalizing this work. Their questions and comments during my defense gave a deeper perspective to my work and some new ideas to be implemented in future. I would like to further extend my gratitude to Klaus for supervising me before starting my Ph.D. and showing me how interesting the magnetic NDT is. His teachings were very productive during my research and I am highly grateful to him.

I owe a great deal of gratitude to my entire advising committee for giving me the freedom to make decisions about my work and of course trusting me with my choices. As a budding researcher, it built a lot of confidence in me. I hope to implement all the teachings from them in my career path and I hope to get an opportunity to work together with them in future through some projects.

I am highly grateful to Prof. Uchimoto, for introducing me to this opportunity of Double-Degree Ph.D. program between Tohoku University and INSA Lyon, which provided me a lot of international exposure and gave me a chance to enjoy Japanese as well French culture at the same time. His consistent approach to perfection and deeper analysis of results, made me learn technically, scientifically as well as on a personal level on my path of science. Discussions with him have always been to the point and very productive.

I also thank Prof. Gael Sebald, who has been from the very first day very supportive scientifically and personally to me. He was always easily approachable in the times when I needed some directions academically as well as personally during my stay in Japan. His visits to my experimental laboratory have been a very motivating factor for me to thrive for good results. 'It is normal to get lost sometimes during the Ph.D. but that time never goes wasted, you always end up learning something', these words from him have always been very inspiring for me and very useful in keeping my motivation high. Discussions with him have always been a learning experience, and helped me look into details better.

I owe a great deal of gratitude to my co-advisor Dr. Benjamin Ducharne, who has been a friend, mentor and a guide throughout this course of my thesis. From the very first day, Dr. Benjamin made sure that we had a friendly relationship which really helped me approach him very easily to clarify my doubts. During my stay in Japan, we had a lot of discussions on Skype which really helped me with the results obtained during the course of my thesis. His attitude of treating students as colleagues is tremendously remarkable. In case of any doubt, he would go out of the way to explain and clarify which I have always appreciated. I would like to thank him for giving me a very friendly and family-type atmosphere during the entire course of my thesis.

LGEF at INSA has been more like a family than a workplace, where I found comfort, lots of learning opportunities, not only professionally but also on a personal level. Thank you

Foamie, for inviting me to a party within two minutes of our introduction and breaking the ice. Thank you Thomas for the very quality and political discussions which I really enjoyed. Thank you Francesco, Yan, Ziyin for being wonderful partners in crime. I have learnt many things from you. Thank you Giulia for being a wonderful friend and colleague and also in contributing in my professional growth. Thank you for all the scientific and quality discussions we had. Thank you Laurence, Veronique, Fred, Quyen, Kaori and Zina for always being kind to me and willing to share the resources when I needed them. Thank you Laurent for allowing each one of us to grow and learn in this atmosphere under your direction. Thank you Pierre-Jean for your help in the instrumentation part of my research and for your jokes, that made the atmosphere lighter. Thank you for being a trainer to me in the days I attended gym with you. Thank you Mickael for being a very nice friend and colleague to me and conducting 'Fun with Science' experiments day with me on Fridays. It was indeed a memorable time. Thank you for the Naruko experience as well. Thank you Linjuan for being a nice friend and pulling my leg time to time and thank you for introducing me to Sichuan based food. Thank you Gildas for taking interest in my work and sharing your viewpoints with me after discussions. Thank you Jean-Yves, for giving me this opportunity to pursue my Ph.D. via the platform of ELyTMaX and time to time motivation. Thank you for all your kindness. Every discussion with you was easy, fun and informative.

I would like to thank you Evelyne for everything and being very patient with me dealing with French documents. You have always been kind to me throughout. Thank you for taking care of me. Without you, this boat would have been rudderless. It was because of you I could focus on my work without worrying about administrative stuff.

I would like to thank the entire team at Uchimoto Laboratory for making me feel welcomed and helping me with my research during my time at Tohoku University. I would like to all the members (Gael, Jean-Yves, Nicolas, Gildas, Chrystelle, Lucas, Sayaka and Kanako) of ELyTMaX at Tohoku University, Japan, for being a family for me in Japan and making my stay fun during my time in Japan.

I would also like to thank my best friends Sukumar and Ana for their constant support, motivation and good quality discussions about professional as well as personal growth.

I would like thank my sisters Saloni Didi and Moushmi for their constant support throughout my Ph.D. Moushmi, being a strict one really helped me keep track on my Ph.D. progress while Saloni Didi for teaching me how to handle stressful situations. I would also like to thank Saurabh Jeeju and Sahil Bhai for always guiding me in terms of career options during my Ph.D. and enlightening me with the future possibilities post Ph.D.

At last, my parents, Advocate Sudesh Kumar Gupta and Mrs. Sareshta Gupta, who have always been supportive to me during this course of work and throughout my life, I owe a great deal of gratitude to them. Their constant push and check have always been a motivating factor for me. At the end of the day, a telephonic call with them always relaxed me to the core. The quotations from famous writers shared with me by my parents during my childhood, came really handy throughout.

THESE DE L'UNIVERSITE DE LYON OPEREE AU SEIN DE L'INSA LYON

NOM : GUPTA
Prénoms : Bhaawan

DATE de SOUTENANCE : 23/09/2019

TITRE : Advanced Electromagnetic Non-Destructive Testing on Creep Degraded High Chromium Ferritic Steels : Characterization, Modelling and Physical Interpretation

NATURE : Doctorat

Numéro d'ordre: 2019LYSEI074

Ecole doctorale : ED MEGA (Mécanique-Energétique-Génie Civil-Acoustique)

Spécialité : Génie Mécanique

ABSTRACT: Under constant high temperatures and pressure, the material undergoes mechanical creep degradation which leads to microstructural changes. These microstructural changes if not monitored on time, can lead to some serious fatal accidents such as in power plants. To investigate these microstructural changes, the material has to be shaped in a certain specific shape and size to have the imaging analysis using Scanning electron microscopy, Electron backscatter diffraction etc. which are destructive in nature and involve high equipment cost. In order to overcome this issue, this thesis work, incorporates three different non-destructive techniques, to study the evolution of magnetic signatures with respect to the level of rupture they are exposed to. It is legitimate to assume that all the microstructural changes that occur in the material can be reflected in the corresponding magnetic signatures measured. The material that has been studied here is high chromium creep degraded steel which is used in the thermal power plant. The magnetic signatures are evaluated in terms of microstructural information to draw the conclusions. Some magnetic parameters from the curves, such as coercivity, magnetic reversibility are derived which show strong correlations with the microstructure. Similarly, techniques based on Hysteresis curves, and magnetic Barkhausen Noise are also implemented. To further quantify the results obtained from the magnetic signatures of the materials, a model has been developed to derive model parameters in order to physically interpret the microstructural changes. The modelling technique will help in overcoming the issue of lack of standards in NDT, irrespective of the experimental set-up involved. The parameters are compared to reveal sensitivity based on the technique. Finally, conclusion has been drawn to check which parameters are correlated to microstructure for a particular NDT technique used.

RESUME: Sous des températures et des pressions élevées constantes, les matériaux métalliques de structure subissent une dégradation mécanique par fluage qui entraîne des changements microstructuraux. Ces derniers, s'ils ne sont pas surveillés à temps, peuvent entraîner des incidents sérieux, notamment pour l'industrie énergétique (centrales électriques par exemple). Pour déterminer les changements microstructuraux, le matériau doit avoir une forme et une taille spécifiques pour que l'analyse des images obtenues par microscopie électronique à balayage, diffraction par rétrodiffusion d'électrons, etc. soit effectuée. Cette préparation demande à extraire le matériau à tester du système, et à le modifier pour la mesure. Afin de surmonter ce problème, ce travail de thèse intègre trois techniques non destructives différentes, pour étudier l'évolution des signatures magnétiques par rapport aux niveau de rupture auquel les matériaux sont exposés. Il est légitime de supposer que tous les changements microstructurels qui se produisent dans le matériau peuvent se refléter dans les signatures magnétiques correspondantes mesurées. Le matériau étudié ici est l'acier à haute teneur en chrome fortement dégradé par fluage, matériau utilisé principalement dans les centrales thermiques. Certains paramètres magnétiques, tels que la coercivité, la réversibilité magnétique, sont dérivés et montrent de fortes corrélations avec la microstructure. De même, des techniques basées sur les courbes d'hystérésis et le bruit magnétique de Barkhausen sont également appliquées. Pour quantifier davantage les résultats obtenus à partir des signatures magnétiques des matériaux, le modèle de Jiles-Atherton a été adapté à la simulation des signaux de contrôle non destructif. A l'inverse, la possibilité de déterminer les paramètres du modèle à partir des seules mesures de contrôle non destructif est démontrée. Cela apporte des éléments complémentaires à l'interprétation physique des changements microstructurels. La technique de modélisation peut aider en outre à résoudre le problème de l'absence de normes dans les essais non destructifs, quel que soit le dispositif expérimental utilisé. Les paramètres sont enfin comparés pour révéler la sensibilité de chacun d'entre eux aux changements microstructurels, et ce en fonction de chaque technique de contrôle non destructif utilisée.

MOTS-CLÉS: ELECTROMAGNETIC NON-DESTRUCTIVE TESTING, MATERIALS CHARACTERIZATION, HIGH CHROMIUM FERRITIC STEELS, CREEP, MAGNETIC INCREMENTAL PERMEABILITY, MAGNETIC BARKHAUSEN NOISE, HYSTERESIS, MICROMAGNETIC MODELLING

Laboratoire (s) de recherche : Laboratoire de Génie Electrique et Ferroélectricité (LGEF)

Directeur de thèse: Prof. Gael Sebald

Président de jury : Prof. Laurent Daniel
Composition du jury : Prof. Afef Lebouc, Prof. Laurent Daniel, Dr.-Ing. Klaus Szielasko, Dr. Anastasios Skarlatos

Advisors: Prof. Gael Sebald, Prof. Tetsuya Uchimoto, Associate Prof. Benjamin Ducharne